LEABHARLANN CHOLÁISTE NA TRÍONÓIDE, BAILE ÁTHA CLIATH | TRINITY COLLEGE LIBRARY DUBLIN
Ollscoil Átha Cliath | The University of Dublin

Terms and Conditions of Use of Digitised Theses from Trinity College Library Dublin

Copyright statement

All material supplied by Trinity College Library is protected by copyright (under the Copyright and Related Rights Act, 2000 as amended) and other relevant Intellectual Property Rights. By accessing and using a Digitised Thesis from Trinity College Library you acknowledge that all Intellectual Property Rights in any Works supplied are the sole and exclusive property of the copyright and/or other IPR holder. Specific copyright holders may not be explicitly identified. Use of materials from other sources within a thesis should not be construed as a claim over them.

A non-exclusive, non-transferable licence is hereby granted to those using or reproducing, in whole or in part, the material for valid purposes, providing the copyright owners are acknowledged using the normal conventions. Where specific permission to use material is required, this is identified and such permission must be sought from the copyright holder or agency cited.

Liability statement

By using a Digitised Thesis, I accept that Trinity College Dublin bears no legal responsibility for the accuracy, legality or comprehensiveness of materials contained within the thesis, and that Trinity College Dublin accepts no liability for indirect, consequential, or incidental, damages or losses arising from use of the thesis for whatever reason. Information located in a thesis may be subject to specific use constraints, details of which may not be explicitly described. It is the responsibility of potential and actual users to be aware of such constraints and to abide by them. By making use of material from a digitised thesis, you accept these copyright and disclaimer provisions. Where it is brought to the attention of Trinity College Library that there may be a breach of copyright or other restraint, it is the policy to withdraw or take down access to a thesis while the issue is being resolved.

Access Agreement

By using a Digitised Thesis from Trinity College Library you are bound by the following Terms & Conditions. Please read them carefully.

I have read and I understand the following statement: All material supplied via a Digitised Thesis from Trinity College Library is protected by copyright and other intellectual property rights, and duplication or sale of all or part of any of a thesis is not permitted, except that material may be duplicated by you for your research use or for educational purposes in electronic or print form providing the copyright owners are acknowledged using the normal conventions. You must obtain permission for any other use. Electronic or print copies may not be offered, whether for sale or otherwise to anyone. This copy has been supplied on the understanding that it is copyright material and that no quotation from the thesis may be published without proper acknowledgement.

MICRO-RAMAN INVESTIGATION OF Si, Ge AND CARBON RELATED NANOSTRUCTURES

By

Joanna Wasyluk

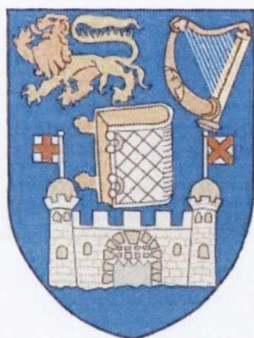

A thesis submitted for the degree of Doctor of Philosophy of the University of Dublin

Department of Electrical and Electronic Engineering
University of Dublin, Trinity College

TRINITY COLLEGE
10 APR 2012
LIBRARY DUBLIN
9379

Declaration

I, the undersigned, declare that this thesis in entirely my own work, except where otherwise accredited and it has not been submitted for a degree at any other university or institution. I furthermore agree that library may lend or copy this thesis upon request.

Abstract

The degradation in performance of silicon devices with scaling caused by fundamental silicon material limitations by the year of 2020 is forcing the semiconductor industry to consider extraordinary materials to replace silicon. Introducing new structures (like germanium on insulator), alteration of material properties in the channel region (such as SiGe alloys or strained Si), and replacement of Si (by graphene) are all being considered. Therefore a number of new materials are currently investigated by researches as a promising nano-material for "post-silicon electronics". The wide range of information on structural properties of these materials can be provided using Raman spectroscopic technique.

In this work, the technique of micro-Raman spectroscopy (MRS) has been employed to investigate properties of wide range of Ge and Si based materials such as strained Si layers, SiGe, SiGeC and ion implanted Ge layers as well as carbon related materials: SiC, diamond like carbon, a-C:Pt and graphene to determine their suitability for use in the development of nanotechnology. MRS is a powerful vibrational spectroscopy tool for investigation of very thin layers, which gives a unique combination of non-destructive analysis and high spatial resolution. In this study, micro-Raman spectroscopy is used as the primary technique to study Ge content and stress in SiGe virtual substrates as well as strain in s-Si cap layers for application in n-MOSFETs technology. The Raman and Infrared spectroscopy is also applied to determine the substitutional carbon content in SiGeC thin layers. The detailed investigation of the structural damage and electrical properties of ion implanted, bevelled Ge samples for smart cut technology is presented in this work by means of Raman mapping and Spreading Resistance profiling techniques.

The enhancement of Raman signal is experimentally observed and theoretically discussed for the carbon related ultra-thin films such as SiC and graphene. MRS is used to investigate different polytypism, structural quality and stress in SiC layers. MRS also provides information on number of graphene mono-layers. Raman area mapping is performed in this work in order to analyse the structural uniformity of graphene flakes. And finally, the detailed investigations of carbon like films and amorphous carbon films with Pt are presented in this work.

Acknowledgments

The research undertaken for this thesis was guided and encouraged throughout by Dr. Tatiana S. Perova, to whom the author would like to express her gratitude and sincere appreciation. The author would like to deeply thank to Dr. Perova for her time, encouragement and helpful discussions during all three years of studies.

The author also would like to thank to the various members of the MTL group for their help and interests: Elena Krutkova, Ana Baldycheva, Sergey Dyakov, David Adley and Victor Ermakov.

The author also wishes to record her appreciation to all collaborators, who supplied the author with the samples and shared their time on discussions: Dr. K. Lyutovich, Prof. E. Kasper, Prof. Ya-Hong Xie, Prof. F. Meyer, Prof. H. Gamble, Prof. M. Armstrong, Dr. P. Rainey, Prof. S. Kukushkin, Dr. D.W.M. Lau and Prof. D.G. McCulloch.

The author would like to acknowledge the financial support of IRCSET Ireland Postgraduate Award and ICGEE Ireland Bursary Award.

Finally, the author would like to express her thanks and appreciation to family and friends who provides me a good time and support through the PhD studies. Special thanks to Christina Cotter, Kate Mulholland, Lu He, Ho-Kei Chan, Neil Geary and Brian Rodriguez, who made valuable comments on English.

Table of Contents

1. Introduction to molecular spectroscopy 2

2.3. Molecular vibrations 2

2.4. Energy units and molecular spectra 6

2. Raman Spectroscopy 8

2.1. Historical background of Raman spectroscopy 8

2.2. Quantum theory of the Raman scattering effect 9

2.3. Classical theory and selection rules of the Raman scattering 12

2.4. Raman instrumentation and Raman spectra 16

2.5. Stress evaluation from Raman spectra 18

3. Infrared Spectroscopy 24

3.1. Introduction 24

3.2. Theory of infrared absorption 24

3.3. FTIR instrumentation and infrared spectra 26

4. Micro-Raman and Spreading Resistance analysis on ion implanted Ge for layer transfer applications 32

4.1. Introduction 32

4.2. Effects of hydrogen on defect formation and electric properties of the material 36

4.3. Experimental 39

4.3.1. Sample growth and description 39

4.3.2. Characterisation techniques 41

4.3.2.1. Spreading Resistance Profiling 41

4.3.2.2. Raman and Infrared spectroscopy 42

4.4. Results and discussion 43

4.4.1. Hydrogen implanted samples 45

4.4.2. Helium implanted samples 51

4.4.3. Germanium on sapphire 55

4.5. Conclusions 62

5. Composition and strain analysis in thin $Si_{1-x}Ge_x$ virtual substrates using micro-Raman spectroscopy and X-ray diffraction 67

5.1. Introduction 67

5.2. Structural properties of SiGe alloys 69

5.3. Experimental ... 72
5.4. Results and discussion ... 77
5.5. Conclusions ... 94
6. Raman and FTIR study of substitutional carbon incorporation in rapid thermal chemical vapour deposited $Si_{1-x-y}Ge_xC_y$ on Si (1 0 0) ... 97
6.1. Introduction ... 97
6.2. Experimental ... 99
6.2.1. Sample growth and description ... 99
6.3. Results and discussion ... 101
6.4. Conclusions ... 115
7. Micro-Raman investigation of SiC thin films grown by solid-gas phase epitaxy on Si(111) ... 119
7.1. Introduction ... 119
7.2. Phonon modes in Raman spectra for different polytypes of SiC ... 123
7.3. Experimental ... 125
7.3.1. Sample growth and description ... 125
7.3.2. Characterisation techniques ... 127
7.4. Results and discussion ... 128
7.4.1. Investigation of voids at SiC/Si interface and surface morphology ... 128
7.4.2. Investigation of different polytypes of SiC layers ... 131
7.4.3. Raman enhancement and micro-Raman mapping measurements ... 136
7.5. Conclusions ... 142
8. Ultraviolet and visible Raman analysis of thin a-C films grown by filtered cathodic arc deposition ... 145
8.1. Introduction ... 145
8.2. Experimental ... 149
8.2.1. Sample growth and description ... 149
8.2.2. Characterisation techniques ... 151
8.3. Results and discussion ... 152
8.4. Conclusions ... 165
9. Raman and Rutherford back-scattering study of a-C:Pt films ... 169
9.1. Introduction ... 169
9.2. Experimental ... 170
9.2.1. Sample growth and description ... 170

9.2.2. Determination of the Platinum content 171
9.2.3. Analysis of Raman spectra 171
9.3. Results 172
9.3.1. Rutherford backscattering 172
9.3.2. Raman scattering 173
9.4. Conclusions 177
10. Raman investigation of crystalline uniformity of graphene 180
10.1. Introduction 180
10.2. Atomic structures of single layer- , few layers- graphene and graphite 183
10.3. Experimental 184
10.3.1. Sample growth 184
10.3.2. Characterisation techniques 186
10.4. Results and discussion 187
10.4.1. Raman spectra of SLG, FLG and graphite 187
10.4.2. Investigation of structural uniformity of graphene using Raman area mapping technique 193
10.5. Conclusions 201
11. Conclusions and future work 206
10.1. Conclusions 183206
10.2. Future work 183208
Appendix I 211

List of Figures

Fig. 1.1. A diatomic molecule with a spring for a covalent bond......3

Fig. 1.2. Anharmonic and harmonic potential with energy states according to quantum mechanics......5

Fig. 1.3. Plane-polarized electromagnetic radiation......6

Fig. 1.4. Energy units for various portions of electromagnetic spectrum......7

Fig. 2.1. (a) Energy level diagram and (b) Raman intensities of the Rayleigh, Stokes and anti-Stokes Raman scattering......12

Fig. 2.2. Backscattering geometry with incident light polarized in the X direction and scattering light polarized in the Y direction Z(XY-Z)......15

Fig. 2.3. Schematic of an experimental setup of a Raman spectrometer......17

Fig. 2.4. Raman spectra of the crystalline bulk Si......18

Fig. 3.1. Basic components of a FTIR spectrometer......26

Fig. 3.2. Schematic of a Michelson interferometer......29

Fig. 3.3. FTIR spectra of bare Si wafers shown for float zone and Czochralski grown wafers......30

Fig. 4.1. Schematic of the Smart-Cut process......33

Fig. 4.2. (a) Microcracks and microvoids distributed in the peak-hydrogen concentration layer and (b) cracks with Ge–H bonds on the crack surfaces......37

Fig. 4.3. Schematic picture of the GeOS sample......41

Fig. 4.4. Schematic diagram of spreading resistance measurements on bevelled sample......42

Fig. 4.5. (a) SEM image of Ge sample implanted with $3x10^{16}$ atoms/cm^2 hydrogen dose and annealed at 450 ºC......44

Fig.4.6. White light interferometry surface profile of Ge sample, illustrating bevel and damaged region at the projected range......44

Fig. 4.7. Raman spectra in the range of Ge-Ge phonon mode for samples implanted with different dose of hydrogen and annealed at different temperatures......45

Fig. 4.8. Depth profiles of the Raman linewidth and carrier concentration from SRP for sample 2......47

Fig. 4.9. SRIM simulation of (a) a hydrogen ion distribution and (b) a damage in n-type Ge as a function of the target depth......47

Fig. 4.10. Raman maps of the Ge-Ge peak position, linewidth and peak intensity of (a-c) samples 2 and 2A and (d-f) samples 4 and 4A......48

Fig. 4.11. Raman linewidth and carrier concentration derived from SRP vs. depth into the sample..49
Fig. 4.12. Infrared absorption spectra of Ge substrate, Ge implanted with H and Ge implanted with H after annealing..51
Fig 4.13. (a) SEM image and optical microscopy image of Ge sample implanted with helium (sample B2)..52
Fig. 4.14. Raman line width and carrier concentration, derived from SRP, vs. depth into the sample B2..53
Fig. 4.15. Raman line width and carrier concentration derived from SRP vs. depth into the sample B3..53
Fig. 4.16. SRIM simulation of helium ion distribution and damage in Ge versus depth in Ge..53
Fig. 4.17. Raman maps of the Ge-Ge peak position, linewidth and peak intensity of (a-c) sample B2 and (d-f) sample B3..54
Fig. 4.18. SEM image of cross-section of GeOS device...56
Fig. 4.19. The optical microscopy image of (a) the corner and (b) the edge of the bevelled sample..57
Fig. 4.20. Optical microscopy images of different parts of sample Ge600C.............................57
Fig. 4.21. Raman spectra taken from different spot of sample Ge600.................................58
Fig. 4.22. Optical microscopy images of different locations of sample Ge800C.......................59
Fig. 4.23. Raman spectra taken from different spot of sample Ge800C...............................59
Fig. 4.24. Optical microscopy images of bevelled samples: (a) Ge600C and (b) Ge800C..60
Fig. 4.25. Raman maps of the Ge-Ge peak position, linewidth and peak intensity of sample GeOS annealed at (a-c) 600ºC and (d-f) 800ºC...61
Fig. 4.26. Raman spectrum of Ge structure: crystalline and amorphous................................62
Fig. 5.1. A cubic unit cell of crystal structure of silicon and germanium...............................69
Fig. 5.2. Lattice parameter a_{SiGe} of $Si_{1-x}Ge_x$ alloy calculated using Vegard's and Dismukes law for Ge content varies from 0 to 100%..70
Fig. 5.3. (a) A schematic diagram of a thin $Si_{1-x}Ge_x$ film to be grown on top of a thin bulk silicon layer..72
Fig. 5.4. Schematic of (a) SiGe virtual substrate and (b) of a strained-Si layer on an ultra-thin SiGe buffer..73
Fig. 5.5. Experimental Si-Si Raman band and the its fitting with (a) an asymmetric function and (b) mixture of Lorentzian and Gaussian functions...76

Fig. 5.6. (a) Raman spectra for SiGe/Si sample with R > 90% and different Ge content (b) Raman spectra for strained SiGe/Si sample with different Ge content..............................78
Fig. 5.7. (a) Si-Si, (b) Si-Ge and (c) Ge-Ge Raman peak position versus Ge content determined by HRXRD..80
Fig. 5.8. Raman shift of the Si-Si (a), Si-Ge (b) and Ge-Ge (c) peak as a function of Ge content..85
Fig. 5.9. Deviation of Ge content obtained from Raman and XRD data versus Ge content..86
Fig. 5.10. The various different baselines that can be chosen in calculating the intensities of the Si-Si, Si-Ge and Ge-Ge modes..87
Fig. 5.11. Intensities ratio versus Ge content...88
Fig. 5.12. (a) Raman spectra of sample 1797, 1669, 1799 and 1800 with increasing Ge content collected at 514 nm excitation wavelength..91
Fig. 6.1. FTIR spectra of samples 1105 and 1005..103
Fig. 6.2. Interference fringes obtained at resolution 0.5 cm^{-1} in FTIR spectra of samples 1105 and 805..103
Fig. 6.3. FTIR spectra for the first set of samples (SX) with a Ge content of 16% shown in the region of the Si-C band at ~605 cm^{-1}..104
Fig. 6.4. Integrated intensity of the Si-C infrared peak as a function of carbon content for all samples..105
Fig. 6.5. Raman spectrum of sample S4..106
Fig. 6.6. Raman spectra of samples 1005 and 805 shown in the region of the Si-C peaks..106
Fig. 6.7. The Raman peak position of the satellite C band (a) and the main C band (b) for the sets of samples studied in this work...107
Fig. 6.8. The ratio of the integrated intensities of the Si-C Raman peak to the Si-Si peak of the $Si_{1-x-y}Ge_xC_y$ layer as a function of substitutional carbon content..........................108
Fig. 6.9. The ratio of the peak intensities of the Si-C Raman peak to the Si-Si peak of the $Si_{1-x-y}Ge_xC_y$ layer as a function of substitutional carbon content..........................109
Fig. 6.10. Raman peak intensities ratio of the carbon satellite peak ($I(C_{sat})$) to the total intensity ($I(C_{tot})$) of the carbon local mode as a function of y........................110
Fig. 6.11. The Raman peak position of the Si-Si mode of the $Si_{0.9-y}Ge_{0.10}C_y$ layer as a function of C content..112
Fig. 6.12. The measured Raman peak position of Si-Si mode of the $Si_{1-x-y}Ge_xC_y$ layer for set SX and set X09 as a function of C content...112
Fig. 6.13. Raman shift of the Si-Ge mode of the SiGeC layers as a function of carbon content..113

Fig. 7.1. The tetrahedral bonding of a carbon atom with its four nearest silicon neighbours....120
Fig. 7.2. Site locations for C atoms in the (1100) plane....121
Fig. 7.3. Stacking sequence of 3C-, 4H- and 6H-SiC in (11 2 0) plane....121
Fig. 7.4. Schematic phonon dispersion curves of 3C, 2H and 4H polytypes....123
Fig. 7.5. Raman spectra of 3C, 2H, 4H and 6H- SiC measured at backscattering geometry....124
Fig. 7.6. Schematic model of void formation during SiC growth....126
Fig. 7.7. Scanning electron microscopy images of cross section of samples SiC/(111)Si: (a) sample FK 439, (b) sample FK 452....129
Fig. 7.8. Optical microscopy image of 3C-SiC layer with clearly seen void beneath (Renishaw)....129
Fig. 7.9. (a) SEM and (b) AFM images of the sample 424....130
Fig. 7.10. (a) SEM and (b) AFM images of the sample 501 with improved growth condition....130
Fig. 7.11. (a) SEM images of the sample AZ (3C-SiC on 6H-SiC substrate)....131
Fig. 7.12. Raman spectra of bulk 6H-SiC and sample AZ....133
Fig. 7.13. Low frequency acoustic phonon modes of 6H polytype of SiC measured with 514 nm excitation wavelength....134
Fig. 7.14. (a) Raman spectra of SiC layer grown on Si substrate measured at the void area and from outside the void area. (b) Fitting of TO-band spectrum, detected at the void, with functions (Lorentzian + Gaussian)....134
Fig. 7.15. Electron diffraction pattern of 3C-SiC layer on Si (111)....134
Fig. 7.16. Raman spectra of samples: FK 452, FK 469, FK 378, FK 389 measured with UV excitation wavelength....135
Fig. 7.17. (a) Top view of the sample of 3C-SiC obtained by optical microscopy. Results of Raman line-mapping for (b) peak position, (c) linewidth, and (d) peak intensity of the TO phonon mode for the 3C-SiC/Si sample....137
Fig. 7.18. The calculation results of the Raman intensity of the TO Si-C phonon mode versus the thickness of SiC layer with and without air void beneath....140
Fig. 7.19. Evolution of Si-C peak along four voids for sample FK 452....141
Fig. 7.20. (a) Raman area map of the Si-C peak intensity corresponding to (b) the optical microscopy image of mapped area....141
Fig. 8.1. Some allotropes of carbon: (a) diamond, (b) graphite, (c) lonsdaleite, (d–f) fullerenes (C60, C540, C70), (g) amorphous carbon, and (h) carbon nanotube....146
Fig. 8.2. The three bond hybridisations found in carbon: sp^3, sp^2 and sp^1....146
Fig. 8.3. Ternary phase diagram of bonding in a-C:H alloys....147

Fig. 8.4. The intrinsic stress measured as a function of ion energy for carbon thin films deposited with various Ar flow rates....153
Fig. 8.5. AES depth profiles for films grown using Ar flow rates of (a) 7 ml/min at 88 eV and (b) 15 ml/min at 159 eV....154
Fig. 8.6. Cross-sectional TEM image of an a-C film....155
Fig. 8.7. The density of carbon films as a function of (a) stress and (b) sp^2 content....155
Fig. 8.8. Radially averaged energy filtered diffraction patterns for a range of carbon films prepared at the energy and stress conditions indicated....157
Fig. 8.9. Visible Raman spectra (457 nm) (a) and UV Raman spectra of the a-C films (b) with different sp^3 content....158
Fig. 8.10. The G peak position as a function of sp^3 content measured by 457 nm (a) and 325 nm of excitation wavelength (b)....159
Fig. 8.11. The full width at half maximum (FWHM) of the G peak as a function of sp^2 content measured by excitation with 457 nm and 325 nm....160
Fig. 8.12. Dispersion of G peak position vs. excitation wavelength for selected ta-C and a-C samples....161
Fig. 8.13. Multi-wavelengths Raman spectra of a ta-C sample with ~70% sp^3....161
Fig. 8.14. The intensity ratio of the D to G peak as a function of the sp^3 content for visible excitation....162
Fig. 8.15. Raman peak intensity of the T band as a function of the sp^3 content....162
Fig. 8.16. The G-peak position (a) and G-peak FWHM (b) in the Raman spectra of films deposited under the indicated flow rates of Ar....163
Fig. 8.17. The sp^3 fraction as measured by EELS of a-C films prepared at room temperature as a function of stress, as measured by different groups....164
Fig. 9.1. Experimental (circles) and simulated (solid curve) spectra of H^+ ions with an initial energy of 242 keV scattered to an angle of 120° for sample 3....172
Fig. 9.2. (a) Raman spectrum of a-C films (sample 1) and of sample 4. (b) Raman spectrum of sample 3....174
Fig. 9.3. Peak positions of D and G bands versus Pt content....175
Fig. 9.4. FWHM of D and G bands versus Pt content....175
Fig. 9.5. The peak intensity ratio of the D and G bands versus the Pt content....177
Fig. 10.1. Scanning electron microscopy (STM) image of the atomic structure of a single layer of exfoliated graphene....181
Fig. 10.2. (a) A top view of the real space unit cell of monolayer graphene. (b) A top view of the real space of bilayer graphene (2-LG). (c) and (d) the unit cell of 2-LG and 3-LG graphene....184

Fig. 10.3. Optical micrographs of the nickel film surface after (a) 30 min and (b) 60 min of annealing.....185
Fig. 10.4. Schematic cross-section view of sample 1: graphene on Ni/SiO_2/Si, and sample 2: transferred graphene on SiO_2/Si.....186
Fig. 10.5. Schematic cross-section view of sample 3: graphene on Cu, and sample 4: transferred graphene on SiO_2/Si.....186
Fig. 10.6. Raman spectra of monolayer of graphene measured with an excitation wavelength of 488 nm.....188
Fig. 10.7. Optical microscopy image of graphene on SiO_2/Si.....188
Fig. 10.8. (a) Comparison of Raman spectra at 457 nm for bulk graphite and graphene. (b) Raman spectrum of disordered graphene.....189
Fig. 10.9. Evaluation of 2D Raman band measured with 514 nm excitation wavelength for (a) 1-LG, (b) 2-LG, (c) 3-LG, (d) 4-LG and (e) HOPG.....189
Fig. 10.10. Dispersion of the 2D peak for graphene on Ni/SiO_2/Si and SiO_2/Si.....190
Fig. 10.11. (a) First-order G-band process and one-phonon second-order DR process (b) for the D-band and (c) for the D'-band and two-phonon second-order resonance Raman spectral processes (d) for the double resonance 2D (G') process, and (e) for the triple resonance 2D (G') band process (TR) for monolayer graphene.....192
Fig. 10.12. Optical microscopy image of (a) graphene on Ni and (b) graphene on SiO_2/Si......193
Fig. 10.13. Raman area maps of graphene grown Ni/SiO_2/Si.....195
Fig. 10.14. Raman spectra from different spots of graphene on Ni measured at 488 nm of excitation wavelength.....196
Fig. 10.15. Raman spectra from different spots of graphene on SiO_2/Si.....196
Fig. 10.16. Raman area maps of graphene transferred from Ni/SiO_2/Si onto SiO_2/Si.....197
Fig. 10.17. Optical microscopy image of (a) graphene deposited on Cu and (b) graphene transferred onto SiO_2/Si.....198
Fig. 10. 18. Evolution of the 2D and G peaks for graphene on Cu with scanning distance.....198
Fig. 10.19. Raman area maps of graphene deposited on Cu.....199
Fig. 10.20. Raman area maps of graphene transferred from Cu onto SiO_2/Si.....200
Fig. 10.21. Evolution of the 2D and G peaks for graphene on Cu with scanning distance.....201

List of Tables

Table. 2.1. Polarisation selection rules for back-scattering from a (001) and (110) surface orientation....16

Table 2.2. Absorption coefficient (α) and penetration depth (d_p) in crystalline silicon for different wavelengths (λ) of the argon laser....21

Table 4.1. Doping and implant concentration and temperature of annealing for bevelled Ge samples implanted with hydrogen and helium....40

Table 4.2. The peak position, intensity and linewidth of the Ge-Ge band for sample Ge600C....58

Table 4.3. The peak position, intensity and linewidth of the Ge-Ge band for the sample Ge800C....59

Table 5.1. Thickness and composition for samples with s-Si on SiGe....74

Table 5.2. The calculated Ge concentration for samples, measured by XRD and Raman techniques....84

Table 5.3. Comparison of shift of Si-Si peak position in Raman spectra s-Si layer, obtained at different excitation wavelength and stress and strain calculation....90

Table 5.4. Strain in s-Si and in SiGe layers measured by XRD and Raman spectra analysis....93

Table 6.1. Structural parameters of the $Si_{1-x-y}Ge_xC_y$ thin films....100

Table 6.2. The Si-Si peak position of $Si_{1-x}Ge_x$ and $Si_{1-x-0.011}Ge_xC_{0.011}$ thin films with different Ge content....111

Table 6.3. The lattice constant, strain, Si-Si peak position and strain phonon coefficient for $Si_{1-x}Ge_x$ layers....115

Table 7.1. Raman frequencies of the optical and acoustic phonon modes for bulk 3C, 2H, 4H and 6H polytypes of SiC obtained by different groups....125

Table 7.2. Description of SiC samples....127

Table 7.3. Peak position, intensity and linewidth of TO and LO SiC phonon modes for samples AZ and 6H-SiC substrate....133

Table 7.4. Raman frequencies of acoustic phonon modes of 6H-SiC....133

Table 7.5. Peak position, intensity and linewidth of TO and LO SiC phonon modes for sample 452....135

Table 7.6. Peak position, intensity and linewidth of TO and LO Si-C phonon modes for different samples measured with UV excitation wavelength....136

Table 8.1. Typical physical properties for different forms of amorphous carbon thin films, diamond and graphite....148

Table 8.2. The operating parameters of the cathodic arc deposition system used to produce the three sets of samples....150
Table 8.3. Sample description of a-C films....150
Table 9.1. Parameters of the studied samples....170
Table 9.2. Pt concentration N, peak positions of D and G (Ω_D and Ω_G), FWHM of D and G bands (W_D and W_G), intensity ratio of D and G bands (I_D/I_G), and average size of graphene clusters (L_a) for the studied samples....174
Table 10.1. The peak position, intensity, and linewidth of the G and 2D bands for mono-layer of graphene measured with an excitation wavelength of 457 nm....190

Author's Publications

Peer Reviewed Publications:

1. P. Rainey, **J. Wasyluk**, T. Perova, R. Hurley, N. Mitchell, D. McNeill, H. Gamble, M. Armstrong, *Micro-Raman and spreading resistance analysis on bevelled implanted germanium for layer transfer applications*, accepted for publication to Electrochemical and Solid-State Letters in August 2010
2. T.S. Perova, **J. Wasyluk,** K. Lyutovich, E. Kasper, M. Oehme, K. Rode, A. Waldron, *Composition and strain in thin $Si_{1-x}Ge_x$ virtual substrates measured by micro-Raman spectroscopy and X-ray diffraction,* accepted for publication to JAP in August 2010
3. T.S. Perova, **J. Wasyluk**, S.A. Kukushkin, A.V. Osipov, N.A. Feoktistov, S.A. Grudinkin, *Micro-Raman mapping of 3C-SiC thin films grown by solid-gas phase epitaxy on Si(111)*, Nanoscale Research Letters **5** (2010), p. 1507
4. A.D. Remenyuk, T. Zvonareva, I.T. Serenkov, V.I. Sackarov, T.S. Perova, **J. Wasyluk**, *Ruserford Back-scattering and Micro-Raman spectroscopy of composite a-C:Pt films grown by magnetron co-sputtering of graphite and Pt targets*, Semiconductors, **44** (2010), p. 1074
5. **J. Wasyluk**, T.S. Perova, S.A. Kukushkin, A.V. Osipov, N.A. Feoktistov, S.A. Grudinkin, *Raman investigation of different polytypes in SiC thin films grown by solid-gas phase epitaxy on Si (111) and 6H-SiC substrates,* Silicon Carbide and Related Materials 2009, Materials Science Forum Vols., **645-648** (2010), p. 359
6. **J. Wasyluk**, T. S. Perova, D.W.M. Lau, M.B. Taylor, D.G. McCulloch, J. Stopford, *Ultraviolet and visible Raman analysis of thin a-C films grown by filtered cathodic arc deposition*, Diamond and Related Materials, **19** (2010), p. 514
7. **Joanna Wasyluk**, Tatiana Perova, Francoise Meyer, *Raman and FTIR study of substitutional carbon incorporation in rapid thermal chemical vapour deposited $Si_{1-x-y}Ge_xC_y$ on Si (1 0 0)*, J. Appl. Phys., **107** (2010), p. 023518
8. **Joanna Wasyluk**, Tatiana Perova, Francoise Meyer, *Determination of substitutional carbon content in rapid thermal chemical vapour deposited $Si_{1-x-y}Ge_xC_y$ on Si (1 0 0) using Raman spectroscopy*, Thin Solid Films **518** (2010) S151
9. D.W.M. Lau, J.G. Partridge, M.B. Taylor, D.G. McCulloch, **J. Wasyluk**, T.S. Perova, D.R. McKenzie, *Microstructural investigation supporting an abrupt stress induced transformation in amorphous carbon films,* J. Appl. Phys., **105** (2009), 084302

10. **J. Wasyluk**, D. Adley, T.S. Perova, A.M. Rodin, J. Callaghan, N. Brennan, *Micro Raman investigation of stress distribution in laser drilled via structures* – Appl. Surf. Sci. **255** (2009) 5546

Conference Proceedings and Conference Presentations:

1. **J. Wasyluk**, P. Rainey, L. McManus, T.S. Perova, R. Hurley, N. Mitchell, D. McNeill, H. Gamble, M. Armstrong, *Investigation of structural damage in ion implanted Ge samples for application in smart cut technology*, Proceeding of the Intel European Research and Innovation Conference, Leixlip, Ireland, 12-14 October 2010, p. 84 (poster presentation)
2. **J. Wasyluk**, *Raman mapping analysis of structural damage in ion implanted bevelled Ge samples for application in Smart Cut technology*, Proceeding of the 34[rt] Annual Symposium of Microscopical Society of Ireland, 25-27 August 2010, Belfast, p. 43 (oral presentation)
3. **J. Wasyluk**, T.S. Perova, C. Miao, Y. H. Xie, *Raman mapping analysis of graphene on Ni, Cu and SiO2/Si substrates*, the XIX International Materials Research Congress 2010 (IMRC 2010), 15-19 August 2010, Cancun, Mexico (poster presentation)
4. D. Adley, **J. Wasyluk**, T. Perova, *Investigation of surface roughness caused by crosshatched pattern in SiGe epilayers*, International Workshop on In Situ Characterization of Near-surface Processes", 30th May - 3rd June 2010, Eisenerz, Austria, p. 50.
5. **J. Wasyluk**, T.S. Perova, S.A. Kukushkin, A.V. Osipov, N.A. Feoktistov, S.A. Grudinkin, *Raman spectroscopy of SiC thin films grown by solid state epitaxy on Si (111)*, Proceeding of the 13th International Conference on Silicon Carbide and Related Materials, 11-16 October 2009, Nurnberg, Germany, p.I-184 (poster presentation).
6. **J. Wasyluk**, T. S. Perova, D.W.M. Lau, J.G. Partridge, M.B. Taylor, D.G. McCulloch, D.R. McKenzie, *Ultraviolet and visible Raman analysis of thin a-C films*, Proceeding of the 20th Diamond Conference, 6-10 September 2009, Athens, Greece, P2.8.28 (poster presentation).
7. **J. Wasyluk**, T.S. Perova, S.A. Kukushkin, A.V. Osipov, N.A. Feoktistov, S.A. Grudinkin, *Raman investigation of different polytypes of SiC layers grown on Si and SiC substrates,* Proceeding of the 33rd Annual Symposium of Microscopical Society of Ireland, 26-28 August 2009, Dublin, p. 43 (poster presentation).
8. **Joanna Wasyluk**, Tatiana Perova, Francoise Meyer, *Determination of substitutional carbon content in rapid thermal chemical vapour deposited $Si_{1-x-y}Ge_xC_y$ on Si (1 0 0) using Raman spectroscopy*, Proceeding of the 6th International Conference on Silicon Epitaxy and

Heterostructures, 17-22 May 2009, Los Angeles, California, USA, p.31 (poster presentation).

9. **J. Wasyluk**, D. Adley, T.S. Perova, H. Wadsworth, H.S. Gamble, K. Lyutovich and E. Kasper, *Investigation of Ge/Si Quantum Dots and Thin SiGe Layers Using a Combination of Surface Imaging Techniques and Micro-Raman Spectroscopy,* AFM Forum and Workshop, 20-21 November 2008, Dublin, P.14.
10. V. Sivan, L. Bui, A. Holland, **J. Wasyluk**, T. Perova, T. Priest, A. Mitchell, *Impurity free stress induced waveguides in lithium niobate* – Proceeding of European Conference and Exhibition on Optical Communication (ECOC), 21-25 September 2008, Brussels, p. 49.
11. **J. Wasyluk**, D. Adley, T.S. Perova, H. Wadsworth, H.S. Gamble, *Raman line and area mapping experiments for composition, stress and defects identification in SiGe structures*, Proceeding of the 32nd Annual Symposium of Microscopical Society of Ireland, 20-22 August 2008, Belfast, p. 23 (poster presentation).
12. **J. Wasyluk**, T.S. Perova, D.W.M. Lau, J.G. Partridge, M.B. Taylor, D.G. McCulloch, D.R. McKenzie, *Raman investigation of microstructure and stress induced in amorphous carbon films*, Proceeding of the 32nd Annual Symposium of Microscopical Society of Ireland, 20-22 August 2008, Belfast, p.24 (1st price for the Poster Presentation).
13. **J. Wasyluk**, D. Adley, T.S. Perova, A.M. Rodin, J. Callaghan, N. Brennan, *Micro Raman investigation of stress distribution in laser drilled via structures*, Proceeding of the European Material Research Society (E-MRS) conference 26-30 May 2008, Strasbourg, France, p. B-31 (poster presentation).
14. **J. Wasyluk**, R. A. Moore, A. Waldron, and T. S. Perova, *Characterisation of SiGe and SiGeC nanostructure materials*, Proceeding of the 30th Annual Symposium of Microscopical Society of Ireland, 30 August -1 September, Galway, Dublin, 2006, P25.

"...everything that living things do can be understood in terms of the jigglings and wigglings of atoms..."

R. P. Feymann[1]

[1]Feynman, R. P. (1963) Six Easy Pieces (Addison-Wesley, Reading MA), p 59.

1. Introduction to molecular spectroscopy

Molecular spectroscopy is a study of the absorption, emission, or scattering of electromagnetic radiation by atoms or molecules (or atomic or molecular ions) as a function of either wavelength or frequency. The most popular spectroscopic techniques are an infrared (IR) and Raman spectroscopy. The IR and Raman spectroscopy in general yield similar types of information. They both provide a means of studing pure rotational, pure vibrational, and rotation- vibration energy changes in the ground state of simple and even complex molecules.

The two methods are based on quite different physical principles. Infrared spectroscopy is mainly dealing with the absorption of energy by a molecule, ion, or radical from a continuum incident radiation or with the study of the emission of infrared radiation by species in exited states. In contrast, Raman scattering functions by an entirely different mechanism and depends on the collision of a quantum of monochromatic incident light with a molecule. This interaction photon-molecule leads to the frequency shift of the scattered light with respect to the incident light.

Not only do the mechanisms differ for the two techniques, but the criterion as to whether a particular transition will be observed in the infrared or Raman spectrum depends on widely different principles. For example, to be active in the infrared spectra, transitions must have a change in the molecular dipole moment associated with them. Raman activity criterion, however, depends on a change in the polarizability of the molecule. These two molecular characteristics are qualitatively inversely related.

The infrared and Raman techniques are unique in that they can be used to study gasses, liquids and solids. In contrast, X-ray diffraction is applicable only to the crystalline state, whereas nuclear magnetic resonance (NMR) spectroscopy is applicable largely to the sample in solution.

2.3. Molecular vibrations

Each atom has three degrees of freedom: it can move independently along each of the axes of the Cartesian coordinate system. If n atoms constitute a molecule, there are $3n$

degrees of motional freedom. Three of these degrees are translational and they involve moving of all atoms simultaneously in the same direction parallel to the axes of a Cartesian coordinate system. Another three degrees of freedom also do not change the distance between atoms and they describe rotation. The remaining *3n-6* degrees are motions, which change the distance between atoms: the length of the chemical bonds and the angels between them. Since these bonds are elastic, periodic motions occur. All vibrations of an idealized molecule result from superposition of *3n-6* non-interacting normal vibrations for nonlinear molecules. Linear molecules possess *3n–5* fundamental vibrational modes because only 2 degrees of freedom are sufficient to describe rotation.

Consider the vibration of a diatomic molecule in which two atoms with masses m_1 and m_2 are connected by a chemical bond represented as an elastic spring (Fig. 1.1).

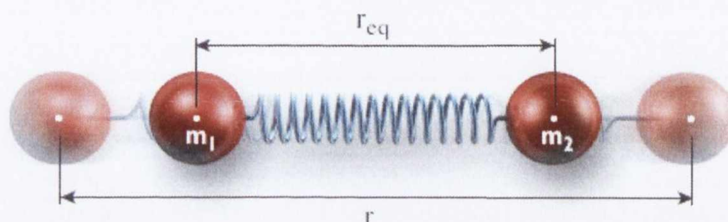

Fig. 1.1. A diatomic molecule with a spring for a covalent bond: m_1, m_2 - are the masses of atoms, r_{eq}, r – are the distances between two atoms.

The force F necessary to move the atom by a certain distance x from an equilibrium position, in accordance to Hooke's law, is expressed as:

$$F = -k \cdot (r - r_{eq}) = -k \cdot x, \tag{1.1}$$

where k is the force constant, and the minus sign indicates the directions of the force and the displacement are opposite to each other. According to Newton's law, the force is proportional to the mass m and its acceleration, the second derivative of the elongation with respect to the time t:

$$F = m \cdot \frac{d^2x}{dt^2}. \tag{1.2}$$

If we consider a diatomic molecule the mass m is called reduced mass (μ) of a diatomic molecule with the masses m_1 and m_2:

$$\frac{1}{m} = \frac{1}{\mu} = \frac{1}{m_1} + \frac{1}{m_2}. \qquad (1.3)$$

Above equations can be combined:

$$\mu \cdot \frac{d^2 x}{dt^2} = -k \cdot x. \qquad (1.4)$$

This second order differential equation possesses the following solution:

$$x = x_0 \cdot \cos(2\pi \nu t + \varphi), \qquad (1.5)$$

describing the motion of the atoms as a harmonic oscillation. Here ν is the vibrational frequency and φ is the phase angle. The second derivative of x by the time is found as:

$$\frac{d^2 x}{dt^2} = -4\pi^2 \nu^2 x_0 \cos(2\pi \nu t + \varphi) = -4\pi^2 \nu^2 x. \qquad (1.6)$$

Insertion into Eqn. (2.4) yields:

$$\nu = \frac{1}{2\pi}\sqrt{\frac{k}{\mu}}. \qquad (1.7)$$

Thus, we obtained an equation describing the frequency of the vibrations of a diatomic molecule.

The potential energy of a molecule, which obeys Hooke's law, is obtained by integrating Eqn. (2.1):

$$V = \frac{1}{2} kr^2, \qquad (1.8)$$

in which $r=x-x_e$, x_e is the Cartesian coordinate of the potential minimum. This is a parabolic potential which refers to harmonic oscillator. The atoms move with a definite frequency, according to the cosine function in Eqn. (2.6). The bonds in actual

molecules, however, are not obeying Hooke's law exactly. The force needed to compress a bond by a definite distance is larger than the force required stretching the bond. Graphs describing harmonic as well as real, anharmonic potentials are shown in Fig. 1.2. Anharmonic molecular potential is approximated by the Morse function:

$$V = D_e(1-e^{-\beta r})^2, \tag{1.9}$$

where D_e is the dissociation energy and β is a measure of the curvature at the bottom of the potential well.

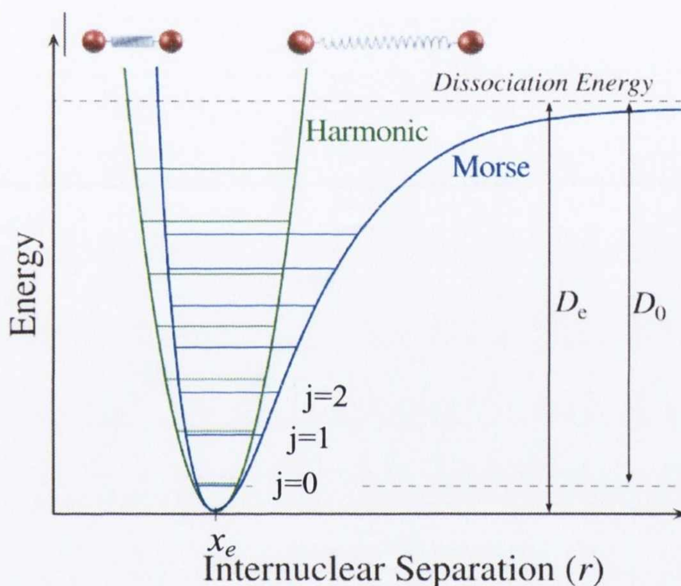

Fig. 1.2. Anharmonic (green line) and harmonic (blue line) potential with energy states according to quantum mechanics. r distance between the masses, x_e equilibrium distance, D_e and D are the theoretical and spectroscopic dissociation energies, respectively. The lowest energy level has the quantum number j=0, followed by j=1, 2, … .

According to classical mechanics, a harmonic oscillator may vibrate with any amplitude, which means that it can posses any amount of energy. Quantum mechanics, however, shows that molecules can only exist in definite energy states:

$$E_i = h \cdot \nu (j + \frac{1}{2}), \quad j = 0,1,2,... \tag{1.10}$$

while as for anharmonic potentials, the distance between energy levels decreases with increasing energy. If the Schrödinger equation:

$$\frac{d^2\psi}{dr^2}+\frac{8\pi^2\mu}{h^2}\left(E-\frac{1}{2}kr^2\right)\psi=0, \tag{1.11}$$

is solved with anharmonic potential from Eqn. (1.9), the eigenenergies of these states are as follow:

$$E_i=\hbar\nu(j+\frac{1}{2})-\chi_e\hbar\nu(j+\frac{1}{2})^2+..., \tag{1.12}$$

where χ_e is anharmonicity constant.

2.4. Energy units and molecular spectra

Figure 1.3 illustrates a wave of polarized electromagnetic radiation travelling in the *z*-direction. It consist of the electric component (*x*-direction) and magnetic component (*y*-direction), which are perpendicular to each other. The electric field strength (*E*) at a given time (*t*) is expressed by:

$$E=E_0\cos(2\pi\nu t), \tag{1.13}$$

where E_0 is the amplitude and ν is the frequency of radiation.

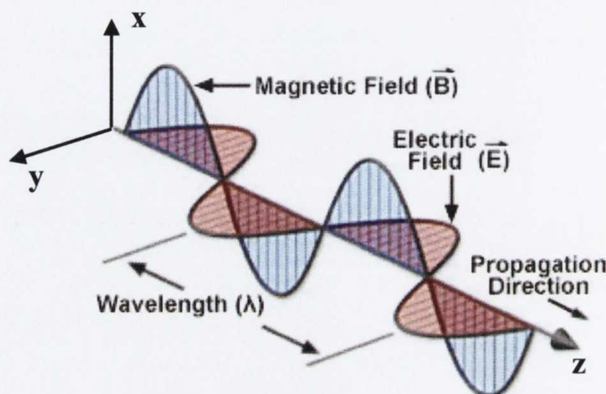

Fig. 1.3. Plane-polarized electromagnetic radiation.

In vibrational spectroscopy wavelength is measured in "wavenumbers", which is defined as:

$$\tilde{\nu} = \frac{1}{\lambda}(cm^{-1}) = \frac{\nu}{c}, \tag{1.14}$$

where c and ν is the velocity and frequency of light, respectively. The wavenumber is expressed in the units of cm^{-1}.

If a molecule interacts with an electromagnetic field, a transfer of energy from the field to the molecule can occur only when Bohr's frequency condition is satisfied. Namely,

$$\Delta E = E_2 - E_1 = h\nu = \frac{hc}{\lambda}. \tag{1.15}$$

Here ΔE is the difference in energy between two quantized states, h is Planck's constant (6.62×10^{-34} J/s), E_2 and E_1 are the energies of the excited and ground level, respectively. The wavenumber ($1/\lambda$) is proportional to the energy of transition. The molecule absorbs energy ΔE when it is excited from E_1 to E_2, and emits energy ΔE when it reverts from E_2 to E_1. As indicates in Fig. 1.4 the magnitude of ΔE is different depending upon the origin of the transition. In infrared and Raman spectra transitions appear in the range of 10^4 to 10^2 cm^{-1} and originate from vibrations of nuclei constituting the molecule.

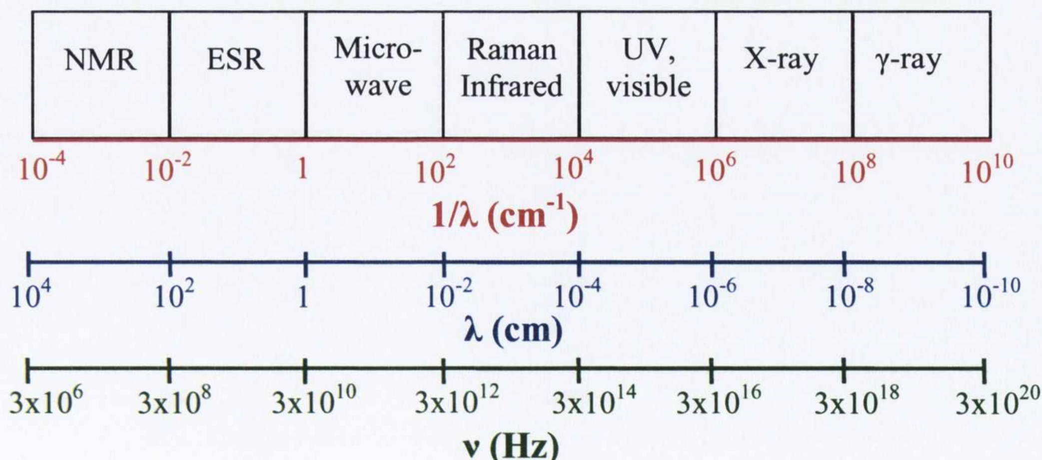

Fig. 1.4. Energy units for various portions of electromagnetic spectrum.

2. Raman Spectroscopy

2.1. Historical background of Raman spectroscopy

The genesis of Raman spectroscopy started in the first quarter of the 20th century when the scattering of monochromatic radiation with change of frequency was predicted theoretically by the Austrian quantum physicist, A. Smekal [1]. The scattering of light by various media had also been studied by Rayleigh in 1871 and Einstein in 1910 but no change of wavelength had been observed, with the sole exception of certain types of scattering in the X-ray spectral region observed by Compton [2]. With this background, many scientists were surrounding the idea of inelastic scattering, which was first reported by Indian scientist, Sir Chandrasekhra Venkata Raman and his co-worker Krishnan [3], and almost simultaneously by Landsberg and Mandelstam [4] in Moscow in 1928. Sir Raman used sunlight as the source and a telescope as the collector, the detector was his eyes. Two years later, C. V. Raman received the Nobel Prize in Physics for the discovery, which since then bears its name.

Gradually, improvements in the various components of Raman instrumentation took place. Early experimental work was directed toward improving the radiation sources. Various lamps of elements were developed (e.g., helium, bismuth, lead, zinc) [5-7] but they were unsatisfactory due to low light intensities. The mercury lamp, filtered to give essentially monochromatic radiation from one of the prominent mercury lines, became the standard source during the 1930s. Later in 1952, the mercury Toronto arc lamp became the ultimate source [8]. However, the decisive transformation in the quality of Raman spectra came with invention of the laser in 1960 [9], which was shortly applied as a monochromatic source. In fact, in 1962 Porto and Wood [10] reported the use of a pulsed ruby laser for exciting Raman spectra. The advantages of the laser included its capabilities for focusing onto a very small sample, thus enabling excellent spectra to be obtained routinely from materials in short supply. Although for many years the laser was the weaker component in terms of durability and reliability of the Raman instrument, during the 1970s most Raman instrumentation used Ar^+ lasers of appropriate stability for excitation with the lines of 488 nm and 514.5 nm, Kr^+, He-Ne,

cadmium and ruby lasers were also widely employed. More recently the Nd-YAG laser (1064 nm) has been also used for Raman spectroscopy.

Development in the optical train of Raman instrumentation took place in the early 1960s. It was discovered that a double monochromator removed stray light more efficiently than a single monochromator. Later, a triple monochromator was introduced. Holographic gratings appeared in 1968 [11], which added to the efficiency of the collection of Raman scattering in commercial Raman instruments.

Two major advances for Raman spectroscopy during 1980s and early 1990s were Fourier Transform Raman (FT-Raman) spectroscopy [12] and the use of Charge Coupled Devices (CCD) detection with dispersive Raman spectrographs [13-16]. FT-Raman instrumentation eliminated fluorescence interference for most samples, and placed easy-to-use Raman capability in the hands of much larger group of scientists. CCD detectors made dispersive Raman spectroscopy a fast technique collecting a complete spectrum in a few seconds or less.

Continuing advances in optical technology have made better filters, lasers, gratings, and spectrographs available to instrument manufactures. During the 1990s high-performance Raman instruments have became available that can be effectively used in non-laboratory environments by scientists and engineers.

2.2. Quantum theory of the Raman scattering effect

The quantum theory treats monochromatic radiation of frequency ν_0 as a stream of photons having energy $h\nu_0$ where h is a Planck's constant. When light is scattered from a molecule or crystal, most photons are elastically scattered with the same frequency (ν_0) as the incident photons. However, a small fraction of light (approximately 1×10^{-7} photons) is scattered at optical frequencies different from the frequency of the incident photons. The scattered radiation occurs in all directions and may also have observable changes in its polarization along with its wavelength.

The Raman effect can be described using an energy diagram shown in Fig. 2.1. The incident photon raises energy of the molecule from the ground state to a 'virtual state'. The virtual state is not a stationary energy state of the molecule in the quantum-mechanical sense, but rather a distortion of the electron distribution of a covalent bond.

The molecule immediately relaxes back to the original electronic state by emitting a photon. If the molecule returns to the vibrational energy level from which it started, as shown in Fig. 2.1 (a), the emitted photon has the same energy, and therefore, the same wavelength as the initial photon. No energy is transferred to the molecule. This is mentioned before Rayleigh scattering. The Stokes Raman scattering occurs if the molecule returns to a higher vibrational level. The emitted photon has less energy, and therefore a longer wavelength than the initial photon. The vibrational energy of the molecule is increased. If the molecule returns to a lower vibrational level, the emitted photon has more energy, and therefore a shorter wavelength than the initial photon. The vibrational energy of the molecule is decreased. This event corresponds to anti-Stokes Raman scattering. In general discussion, Raman scattering is usually assumed to be Stokes Raman scattering unless it is labelled as anti-Stokes. The kinetic energy of the photon and the molecule remains the same before and after the collision. If E represents the rotational, vibrational, and electronic energy of the molecule before a collision and E' represents the same values after the collision, then using the law of conservation of energy gives:

$$h\nu_0 + E = h\nu_s + E' \tag{2.1}$$

Rearranging Eqn. (2.1) gives:

$$\frac{E' - E}{h} = \nu_0 - \nu_s \tag{2.2}$$

The scattered radiation is classified as follows:

$$\begin{aligned} &E = E'(\nu_0 = \nu_s) \text{ Rayleigh scattering} \\ &E > E'(\nu_0 < \nu_s) \text{ anti-Stokes Raman Scattering} \\ &E < E'(\nu_0 > \nu_s) \text{ Stokes Raman Scattering} \end{aligned} \tag{2.3}$$

The intensities of Rayleigh scattered light and Raman scattered light are proportional to the number of molecules being illuminated. The Stokes and anti-Stokes Raman intensity shown by Fig. 2.1 (b) are therefore proportional to the number of molecules in the

lowest and in the next higher vibrational energy level, respectively. At thermal equilibrium the fraction of the molecules in one vibrational energy level relative to another is given by the Boltzmann distribution:

$$\frac{N_1}{N_0} = \left(\frac{g_1}{g_0}\right)\exp\left[-\left(\frac{\Delta E}{kT}\right)\right] \tag{2.4}$$

where N_1 – number of molecules in a higher vibrational energy level;

N_0 – number of molecules in a lower vibrational energy level;

g_1 – degeneracy of the higher vibrational level;

g_0 – degeneracy of the lower vibrational level;

ΔE – energy difference between the higher and the lower vibrational energy levels;

k – Boltzmann's constant;

T – temperature in K.

At thermal equilibrium the number of molecules in a lower vibrational energy level is always larger than the number of molecules in the next higher vibrational energy level. The anti-Stokes Raman intensity becomes vanishingly small relative to the Stokes Raman intensity for high energy vibrations, or low temperatures. Temperature of the sample can be determined from relative intensities of the Stokes and anti-Stokes Raman bands using Boltzmann equation [19-20].

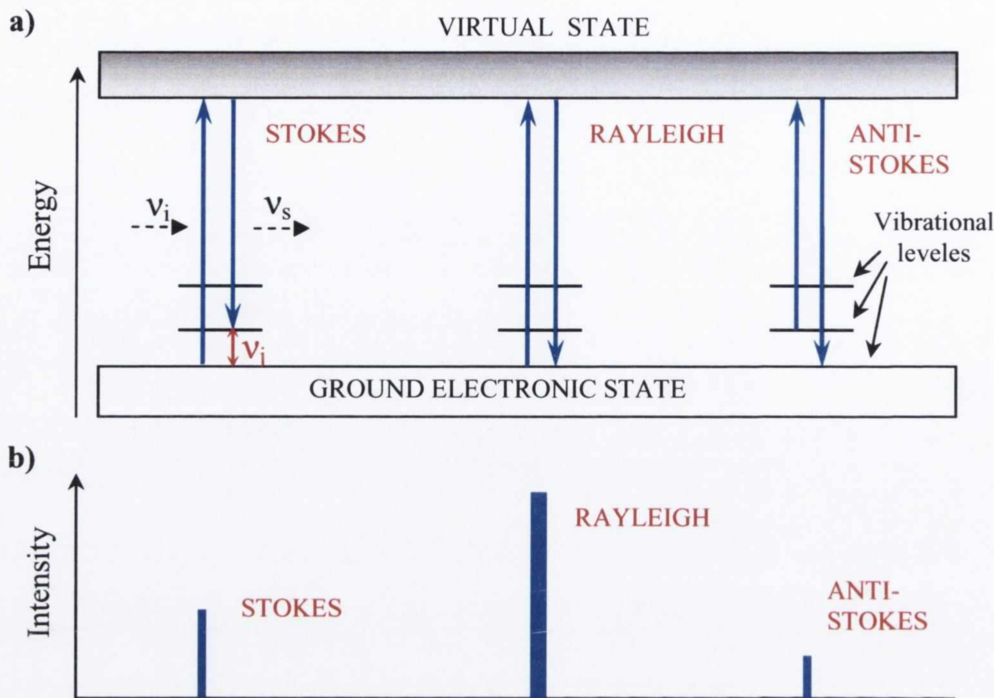

Fig. 2.1. (a) Energy level diagram and (b) Raman intensities of the Rayleigh, Stokes and anti-Stokes Raman scattering.

2.3. Classical theory and selection rules of the Raman scattering

The classical explanation of the Raman process is that the electric field of light interacts with the charges in a molecule, which in turn changes the frequency of light. When a molecule is introduced into electric field of strength E, an electric dipole moment P is induced in the molecule:

$$P = \alpha E, \qquad (2.5)$$

where α is the polarizability tensor of the molecule. The polarizability tensor, in general, is a function of the nuclear coordinates and hence of the molecular vibrational frequencies. When electromagnetic radiation of frequency ν_0 falls onto the molecule, it introduces a varying electric field, whose dependence on the time is given by:

$$E = E_0 \cos(2\pi\nu_0 t)\,; \tag{2.6}$$

where E_0 is amplitude of the electric field. Substituting Eqt. (2.2) into (2.1) yields the time-dependent induced dipole moment:

$$P = \alpha \cdot E_0 \cos(2\pi\nu_0 t)\,. \tag{2.7}$$

Thus, the electromagnetic radiation induces a varying electric dipole moment which then permits emission of light identical in frequency with that of the incident radiation. This is Rayleigh scattering.

However, if the polarizability varies slightly as the molecule vibration occurs, we can express this as:

$$\alpha = \alpha_0 + \left(\frac{\partial \alpha}{\partial Q}\right) \cdot dQ + \ldots, \tag{2.8}$$

where α is the polarizability of the molecular mode at equilibrium position and dQ is the normal coordinate describing the molecular vibrations. The dependence of the vibrational frequency ν_{vib} on the normal coordinate dQ is given by:

$$dQ = Q_0 \cos(2\pi\nu_{vib} t)\,, \tag{2.9}$$

where Q_0 is the normal coordinate of the initial position of the molecule. Combining (2.8) and (2.9) we get:

$$\alpha = \alpha_0 \cdot \left(\frac{\partial \alpha}{\partial Q}\right) \cdot Q_0 \cos(2\pi\nu_{vib} t)\,. \tag{2.10}$$

Finally, Eqt. (2.10) may be substituted into Eqt. (2.5), which yields:

$$P = \alpha_0 E_0 \cos(2\pi\nu_0 t) + \left(\frac{\partial \alpha}{\partial Q}\right) \cdot \alpha_0 E_0 \cos(2\pi\nu_0 t)\cos(2\pi\nu_{vib} t) \tag{2.11}$$

Using a trigonometric identity, the above relation may be recast as:

$$P = \alpha_0 E_0 \cos(2\pi\nu_0 t) + \left(\frac{\partial\alpha}{\partial Q}\right) \cdot \frac{\alpha_0 E_0}{2} \{\cos[2\pi(\nu_0 - \nu_{vib})t] + \cos[2\pi(\nu_0 + \nu_{vib})t]\} \qquad (2.12)$$

Examination of the above equation reveals that induced dipole moments are created at three distinct frequencies, namely ν_0, $(\nu_0 - \nu_{vib})$, and $(\nu_0 + \nu_{vib})$, which results in scattered radiation at these same three frequencies. The first scattered frequency corresponds to the incident frequency, hence is elastic scattering (Rayleigh), while the latter two frequencies are shifted to lower or higher frequencies and are therefore corresponds to inelastic processes. The scattered light in these latter two cases is referred to as Raman scattering, with the down-shifted frequency (longer wavelength) referred to as Stokes scattering, and the up-shifted frequency (shorter wavelength) referred to as anti-Stokes scattering. Thus, in Raman spectroscopy, the vibrational frequency (ν_{vib}) as a shift from the incident beam frequency (ν_0) is measured. Equation (2.12) also gives a gross selection rule for what are called Raman-active motions. The term $\partial\alpha / \partial Q$ must be non-zero. That derivative is the change in the polarizability with nuclear position. If that derivative equals zero, the entire second term is zero and there will be no Raman scattering. Thus, a molecular motion will be Raman-active only if the motion occurs with a changing polarizability.

In most Raman set-ups, a back-scattering geometry is employed, which means that the same lens is used for focusing the laser onto the sample and collecting the scattered light. As in Fig. 2.2, the laser beam is directed along the Z axis and the light scattered in the –Z direction is collected. In this example, the incident light is taken to be polarized in the X direction while the scattered light is said to be polarized in the Y direction. This set up can be represented using Portos notation as Z(XY)-Z. The Raman scattering efficiency, I, depends on the polarization vector of the incident (e_0), scattered (e_s) light, and is given by:

$$I = C\sum_j \left| e_0 \times R_j \times e_s \right|^2, \qquad (2.13)$$

where C is a constant and R_j is the Raman tensor of a phonon j. The values of R_j are obtained from theoretical consideration [17,18]. They are second-rank tensors, which are used to calculate the polarization selection rules.

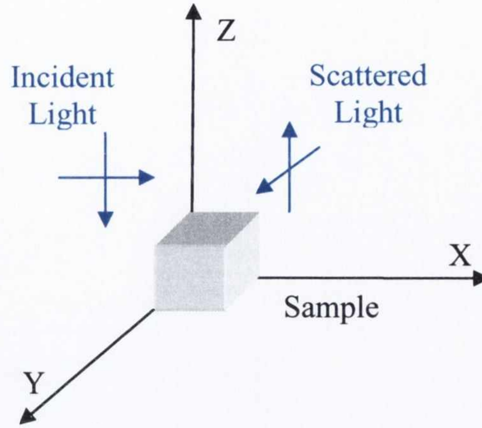

Fig. 2.2. Backscattering geometry with incident light polarized in the X direction and scattering light polarized in the Y direction Z(XY-Z).

In silicon, there are three Raman tensors [18]. In the crystal co-ordinate system x =[100], y =[010] and z= [001], they are given by:

$$R_x = \begin{pmatrix} 0 & 0 & 0 \\ 0 & 0 & d \\ 0 & d & 0 \end{pmatrix} \qquad R_y = \begin{pmatrix} 0 & 0 & d \\ 0 & 0 & 0 \\ d & 0 & 0 \end{pmatrix} \qquad R_z = \begin{pmatrix} 0 & d & 0 \\ d & 0 & 0 \\ 0 & 0 & 0 \end{pmatrix} \tag{2.14}$$

For back-scattering from a (001) surface, R_x and R_y represent scattering by transverse optical (TO) phonons polarized along x and y respectively, while R_z corresponds to scattering by longitudinal optical phonons (LO) polarized along z. The combination of equations (2.13) and (2.14) determines which Raman phonons can be detected for a given crystal orientation of the sample and incident and scattered light polarization. Table 2.1 shows which of the three modes can be observed for different polarization directions. It follows from this table that for back-scattering from a (001) surface only the z polarized phonon (LO) would be observed in Raman spectrum. In the absence of stress in silicon, the three optical modes of silicon have the same frequency of 520cm^{-1}.

Table. 2.1. Polarisation selection rules for back-scattering from a (001) and (110) surface orientation.

Polarization		Visible		
e_i	e_s	R_x	R_y	R_z
Back-scattering from (001)				
(100)	(100)	-	-	-
(100)	(010)	-	-	X
(1-10)	(1-10)	-	-	X
(110)	(1-10)	-	-	-
Back-scattering from (110)		-	-	X
(1-10)	(001)	X	X	-
(1-10)	(1-10)	-	-	X
(001)	(001)	-	-	-

2.4. Raman instrumentation and Raman spectra

Raman spectra were registered in back-scattering geometry using a micro-Raman Renishaw 1000 system equipped with a Leica microscope. Different excitation sources were used: the 457, 488 and 514 nm lines of an Ar+ laser and the 633 nm line of a HeNe laser. Some additional measurements were obtained with a Jobin-Yvon LabRam HR800 micro-Raman system with excitation source of 325nm (HeCd laser).

A typical Raman system consists of the following basic components: (1) an excitation source (laser), (2) optics for sample illumination, (3) a double or triple monochromator, and (4) a signal processing system consisting of a detector, an amplifier, and an output device (computer). The schematic of the Raman setup is shown in Figure 2.3. A number of stages are involved in the acquisition of Raman spectrum. A sample is placed on the motorized X-Y stage in the sample chamber and the laser light after passing through various polarizers and filters is focused onto the sample through the lens. The scattered light is collected using the same lens (backscattering geometry) and is returned to the spectrometer, where it is passed through the notch filter to its way to monochromator. The holographic notch filter supressed an intense Rayleigh scattered signal. Monochromator slit widths are set for desired spectral resolution. The monochromator,

which consists of diffraction grating, effectively rejects stray light and serves as a dispersing element for incoming radiation. In the Renishaw system, the 1800 lines/mm grating is used providing a spectral resolution of ~ 1 cm^{-1}. Finally, the Raman shifted radiation is detected with a charge-coupled device (CCD), which is linked to a desktop computer, and software algorithms are then used to analyze and plot the spectra.

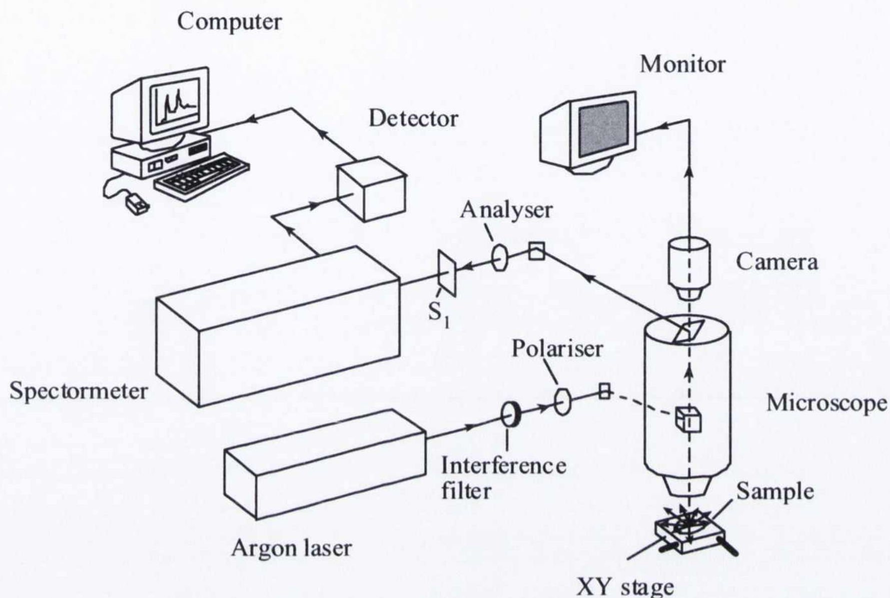

Fig. 2.3. Schematic of an experimental setup of a Raman spectrometer.

The obtained Raman spectra were analyzed with GRAMS software. A mixture of Lorentzian and Gaussian functions was used to characterize the Raman peaks. The parameter of the Raman peaks are:

- Peak position
- Peak intensity
- Full width at half maximum (FWHM)
- and its symmetry.

Figure 2.4 shows a representative Raman spectrum of crystalline bulk silicon, which is used to calibrate the Raman system. Examining the vibration of Si lattice, the vibration can be either perpendicular to the bond of the Si lattice (TO phonon mode), or in the line with the bond, which is known as LO phonon mode. The first order Raman spectrum of stress free Si has a single line at about 520 cm^{-1}, which corresponds to triply degenerated phonon in the sense that this frequency is the same for all three

phonon modes, one longitudinal (LO) and two transversal (TO_1 and TO_2). The position, linewidth and shape of the Raman peak are sensitive to the presence of strain, structural defects, temperature, chemical composition and concentration of carriers.

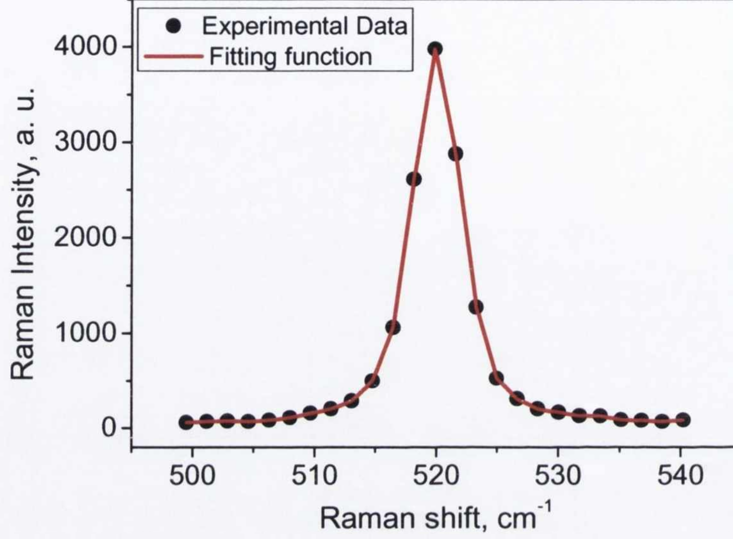

Fig. 2.4. Raman spectra of the crystalline bulk Si.

2.5. Stress evaluation from Raman spectra

Mechanical strain or stress may affect the frequency of the Raman mode. One of the first papers addressing theoretically the effect of stress on the Raman mode was that by Ganesan et all [21]. It was shown that frequencies of the three optical modes in the presence of the strain, to terms linear in the strain, can be obtained by solving the following secular equation [21,22]:

$$\begin{vmatrix} p\varepsilon_{11}+q(\varepsilon_{22}+\varepsilon_{33})-\lambda & 2r\varepsilon_{12} & 2r\varepsilon_{13} \\ 2r\varepsilon_{12} & p\varepsilon_{22}+q(\varepsilon_{11}+\varepsilon_{33})-\lambda & 2r\varepsilon_{23} \\ 2r\varepsilon_{13} & 2r\varepsilon_{23} & p\varepsilon_{33}+q(\varepsilon_{11}+\varepsilon_{22})-\lambda \end{vmatrix}=0 \quad (2.15)$$

Here *p, q* and *r* are material constant, so called phonon deformation potentials. They describe the changes in the 'spring constant' of the $q \cong 0$ optical phonon with strain and can be determined experimentally by applying external stress to the material under

study [28-30]. The secular equation is referred to the system of crystallographic axes, x = [100], y = [010] and z = [001]. Diagonalization of the secular matrix yields the set of three eigen-vectors of the optical phonons in the presence of strain. The difference between the Raman frequency of each mode in the presence of stress, ω_j (*j=1,2,3*), and in the absence of stress, ω_{j0}, can be calculated from the eigenvalues λ_j:

$$\lambda_j = \omega_j^2 - \omega_{j0}^2 \quad \text{or} \quad \Delta\omega_j = \omega_j - \omega_{j0} \approx \frac{\lambda_j}{2\omega_{j0}} \tag{2.16}$$

Using Hooke's law to define the uniaxial stress along the [100] direction of silicon, the strain tensor components can be calculated. This gives: $\varepsilon_{11} = S_{11}\sigma$, $\varepsilon_{22} = S_{12}\sigma$ and $\varepsilon_{33} = S_{12}\sigma$, where S_{ij} elastic compliance tensor elements of Si. Solving Eqns. (2.15) and (2.16) leads to:

$$\Delta\omega_1 = \frac{\lambda_1}{2\omega_0} = \frac{1}{2\omega_0}(pS_{11} + 2qS_{12})\sigma \tag{2.17}$$

$$\Delta\omega_2 = \frac{\lambda_2}{2\omega_0} = \frac{1}{2\omega_0}(pS_{12} + q(S_{11} + S_{12}))\sigma \tag{2.18}$$

$$\Delta\omega_3 = \frac{\lambda_3}{2\omega_0} = \frac{1}{2\omega_0}(pS_{13} + q(S_{11} + S_{12}))\sigma \tag{2.19}$$

The Raman tensors and mode polarization vectors are not changed. So, for back scattering from a (001) surface, only the third Raman mode is observed (Table 2.1, Eqn (2.15)), and the relation between the shift of this mode and the stress is given by equation (2.13). Using for crystalline silicon: S_{11}=7.68x10^{-2} Pa^{-1}, S_{12}= −2.14x10^{-12} Pa^{-1} and $p = -1.43\omega_0^2$, $q = -1.89\omega_0^2$, $r = -0.59\omega_0^2$ [22], we find:

$$\Delta\omega_3\,(cm^{-1}) = -2\times10^{-9}\,\sigma(Pa) \tag{2.20}$$

In the case of biaxial stress in x-y plane, with stress components σ_{xx} and σ_{yy} this becomes:

$$\Delta\omega_3 = \frac{1}{2\omega_0}\left(pS_{13} + q(S_{11} + S_{12})\right)\cdot\left(\sigma_{xx} + \sigma_{yy}\right) \tag{2.21}$$

or

$$\Delta\omega_3\,(cm^{-1}) = -4\times10^{-9}\left(\frac{\sigma_{xx} + \sigma_{yy}}{2}\right)(Pa) \tag{2.22}$$

Thus, compressive stress (σ negative) will result in an upward shift of the Raman peak, while tensile stress (σ positive) corresponds to a downward shift. Whether the Raman frequency of certain material changes more or less with stress depends on the material parameters (S_{ij}, p, q, r). For example, for silicon under uniaxial stress in the [100] direction, a peak shift of 1 cm^{-1} corresponds to a stress of about 500 MPa (Eqn (2.14)). With a very sensitive and stable instrument, it is possible to detect peak shifts of about 0.05 cm^{-1}, from which it follows that the minimal detectable stress level in silicon is about 25 MPa and the strain level is about 10^{-4}.

The Raman signal originates from a volume defined by the wavelength and the diameter of the laser beam. A shorter laser wavelength gives information on the stress closer to the surface. Some information on the change of the stress with depth can be obtained by using different wavelengths. The total scattered light intensity integrated from the surface to a depth d, I_S, is given by [23]:

$$I_S = I_0 D\int_0^d e^{-2\alpha}dx = \frac{I_0 D}{2\alpha}\left(1 - e^{-2\alpha d}\right) \tag{2.23}$$

while that from the depth d to infinity is given by

$$I_d = I_0 D\int_d^\infty e^{-2\alpha}dx = \frac{I_0 D}{2\alpha}e^{-2\alpha d} \tag{2.24}$$

I_0, D and α are the incident light intensity, the Raman scattering cross section and the photo-absorption coefficient of silicon respectively. If one assumes that the penetration depth, d_p, is given by the depth that satisfies the relationship $I_d/(I_S+I_d)=0.1$, then this depth is given by:

$$d_p = \frac{-\ln 0.1}{2\alpha} = \frac{2.3}{2\alpha}. \qquad (2.25)$$

The absorption coefficient of silicon for the 514.5 nm (2.41 eV), 488 nm (2.54 eV) and 457.9 nm (2.71 eV) wavelength of the argon laser is obtained, using a third-degree interpolation, from [24] and, using equation (2.19), the penetration depth in crystalline silicon is found to be 770 nm, 570 nm and 320 nm respectively. These results are summarized in Table 2.2.

Table 2.2. Absorption coefficient (α) and penetration depth (d_p) in crystalline silicon for different wavelengths (λ) of the argon laser.

λ, nm	$10^{-3}\alpha$, cm^{-1}	d_p, cm^{-1}
514.5	14.96	770
488	20.18	570
457.9	36.43	320

References

1. A. Smekal, The quantum theory of dispersion, Naturwissenschaften, 11, 873 (1923)
2. A. Compton, A quantum theory of the scattering of X-rays by light elements, Phys. Rev., 21, 483 (1923)
3. C.V. Raman and K.S. Krishnan, The optical analog of the Compton effect, Nature, 121, 711 (1928)
4. G. Landsberg and L. Mandelstam, A novel effect of light scattering in crystals, Naturwissenschaften, 16, 557 (1928).
5. F. P. Kerschbaum, Z. Instrumentenk 34, 43 (1914)
6. B. Veskatesachar, L. Sibaiya, Indian J. Phys. 5, 747 (1930)
7. J. H. Hibben, "The Raman Effect and Its Chemical Applications" Reinold Publishing Corp., New York, 1939
8. H.L. Welsh, M.F. Crawford, T.R. Thomas, and G.R. Love, Can. J. Phys., 30, 577 (1952)
9. T.H. Maiman, Stimulated optical radiation in ruby, Nature, 187, 493 (1960)
10. S.P.S. Porto and D.L. Wood, Ruby optical maser as a Raman source, J. Opt. Soc. Am., 52, 251 (1962)
11. J. R. Ferraro, R. Jarnutowski, D. C. Lankin, Spectroscopy 7, 30 (1992)
12. T. Hirschfeld, B. Chase, Appl. Spectrosc. 40, 133 (1986)
13. C. A. Murray, S. B. Dierker, J. Opt. Soc. Am. A 3, 2151, (1986)
14. Y. Wang, R. L. McCreery, Anal. Chem. 61, 2647 (1989)
15. M. J. Pelletier, Appl. Spevtrosc. 44, 1699 (1990)
16. L. D. Barron, L. Hecht, W. Hug, M. J. MacIntosh, J. Am. Chem. Soc. 111, 8731 (1989)
17. M. Cardona, "Light Scattering in solid II", ed. M. Cardona and G. Güntherodt, Berlin: Springer, (1982)
18. R. Loudon, Adv. Phys. 13, 428-80 (1964)
19. M. Malyj, J. E. Griffiths, Appl. Scpectrosc., 37, 315 (1983)
20. S. D. Rassat, E. J. Davis, Appl. Scpectrosc., 48, 1498 (1994)
21. S. Ganesan, A. A. Maradudin, J. Oitmaa, Ann. Phys., 56, 556 (1970)
22. E. Anastassakis, A. Pinczuk, E. Burstein, F. H. Pollak and, M. Cardona, Solid State Commun., 8, 133 (1970)
23. J-I. Takahashi, T. Makino, J. Appl. Phys. 63, 87 (1988)

24. D. E. Aspnes, A. A. Studna, Phys. Rev. B 27, 985 (1983)

3. Infrared Spectroscopy

3.1. Introduction

Fourier-Transform Infrared (FTIR) spectroscopy is an optical characterisation technique that provides information about the chemical bonding or molecular structure of materials, whether organic or inorganic. Simply, it is the absorption measurement of different infrared (IR) frequencies by a sample positioned in the path of an IR beam. The main goal of IR spectroscopic analysis is to determine the chemical structural fragments within molecule, known as functional groups. Different functional groups absorb characteristic frequencies of IR radiation. Using various sampling accessories, IR spectrometers can accept a wide range of sample types such as gases, liquids, and solids. Thus, IR spectroscopy is an important and popular tool for structural elucidation and compound identification.

Infrared spectrometers have been commercially available since the 1940s. At that time, the instruments relied on prism to act as dispersive elements, but by the mid 1950s, diffraction grating has been introduced into dispersive machines. The most significant advances in infrared spectroscopy however have come as a result of the introduction of Fourier-Transform spectrometers. This type of measurement employs an interferometer as a basic optical element and exploits the well-established mathematical process of Fourier-transformation. Fourier-Transform Infrared spectroscopy has dramatically improved the quality of infrared spectra and minimized the time required to obtain data.

In this chapter, the theory of infrared absorption and the instrumentation of the Fourier-transform infrared spectroscopy are presented.

3.2. Theory of infrared absorption

The Infrared spectroscopy is based on the interaction of electromagnetic radiation with a molecular system, in most cases in the form of absorption of energy from the incident beam. Infrared radiation is absorbed by molecules and converted into energy of molecular vibration. When the radiant energy matches the energy of a specific

molecular vibration, absorption occurs. The absorption of infrared light induces transition between the vibrational energy levels given by Eq. (1.12) in Chapter 1. As it was shown in Fig. 1.2, the energy levels of the anharmonic oscillator are not equidistant. When a molecule is raised from the ground vibrational state (*j=0*) to the first excited vibrational state (*j=1*), it is said to undergo a fundamental transition. According to Eq. (2.12) the wavenumber of this transition is given by:

$$\tilde{\nu}(0 \rightarrow 1) = \frac{\nu_0}{c}(1 - 2\chi_e) \tag{3.1}$$

where χ_e is anharmonicity constant. The intensity of an infrared absorption band is proportional to the square of the change in the molecular electric dipole moment μ caused by a normal coordinate q:

$$I_{IR} \propto \left(\frac{\partial \mu}{\partial q}\right)^2. \tag{3.2}$$

In other word, a normal mode is infrared active, if this mode alters the dipole moment of the molecule and thus fulfils the following requirements:

$$\frac{\partial \mu}{\partial q} \neq 0. \tag{3.3}$$

This is a selection rule for infrared spectroscopy. The vast majority of molecules have infrared bands in the spectral range between 400 and 4000 cm^{-1}. Most of the intense features in any mid-infrared spectrum can be assigned to fundamental transition. As a consequence of anharmonicity, transition from the ground state to higher excited state (*n=2,3,4*...) also occurs. This type of transition is called an overtone transition. For example, the overtone transition from *n=0* to *n=2* appears at a wavenumber of:

$$\tilde{\nu}(0 \rightarrow 2) = 2\frac{\nu_0}{c}(1 - 3\chi_e). \tag{3.4}$$

Overtones can be recognized because they give a rise to very weak absorption bands, often at about twice the wavenumber of a fundamental transition.

3.3. FTIR instrumentation and infrared spectra

Fourier-transform infrared spectroscopy is based on the idea of the interference of radiation between two beams to yield an interferogram. The latter is a signal produced as a function of the change of pathlength between the two interactive beams. The two domains of the distance and frequency are interconvertible by the mathematical method of Fourier-transformation.

Infrared spectra were registered at normal incidence of light using a Digilab FTS 6000 spectrometer with a Globar source, a KBr beam splitter, and a mercury cadmium telluride (MCT) detector.

The typical FTIR spectrometer consists of three basic components: radiation source, interferometer, and detector. The schematic of the FTIR setup is shown in Fig. 3.1. The radiation emerging from the source is passed through interferometer to the sample before reaching the detector. Upon amplification of the signal, in which high-frequency contribution has been eliminated by filter, the data are converted to the digital form by analog-to-digital converter and transferred to the computer for Fourier transformation.

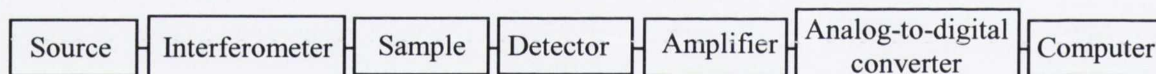

Fig. 3.1. Basic components of a FTIR spectrometer.

The most common interferometer used in FTIR spectrometry is Michelson interferometer [1], which consists of two perpendicularly plane mirrors (one of each can move in a direction perpendicular to the plane) and beamsplitter (semi-reflecting film). The schematic of a Michelson interferometer is shown in Fig. 3.2. The role of the interferometer is to divide radiant beams, generate an optical path difference between the beams, and then recombine them in order to produce repetitive interference signals measured as a function of optical path difference by a detector. If a collimated beam of monochromatic radiation of wavelength λ passed into an ideal beamsplitter, 50% of the

incident radiation will be reflected to the fixed mirror (M1), while other half of the beam will be transmitted to the other mirror (M2). The reflected part of the beam travels to the fixed mirror M1 through the distance L, is reflected there and coming back to the beamsplitter after the total path length 2L. The same happens to the transmitted radiation. However, as the mirror M2 is not fixed at the same position L but can moved very precisely back and forward around L by the distance x, the total path length of the transmitted part is accordingly $2(L+x)$. Thus, when the two parts of the beam recombine at the beamsplitter they posses an optical path length difference of $\delta=2x$. Since the two beams are spatially coherent, they interfere on recombination. Naturally, only half of the radiation entering the interferometer can get out to the detector, half is reflected back towards the input. The beam which emerges from the interferometer at 90° to the input beam is called transmitted beam and this is a beam detected in FTIR spectrometry.

In the case of a monochromatic ray, the two beams of radiation interfere constructively if their optical retardation is multiple of the wavelength λ:

$$\delta = 2x = n\lambda \text{ with n=0,1,2,3...} \tag{3.5}$$

and destructively if δ in an odd multiple of $\lambda/2$:

$$\delta = 2x = (2n+1)\frac{\lambda}{2}. \tag{3.6}$$

The beam, modulated by the movement of the mirror M2, leaves the interferometer, passes through the sample, and is finally focussed on the detector. The signal actually registered by the detector is the radiation intensity of combined beams as a function of the retardation δ. For a source of monochromatic radiation with frequency v, the intensity at the detector is given by the equation:

$$I_D(\delta) = \frac{1}{2} S(\tilde{\nu}) \cdot [1 + \cos(2\pi\tilde{\nu}\delta)] \tag{3.7}$$

where $S(\tilde{\nu})$ is the intensity of the monochromatic source. It can be seen that $I_D(\delta)$ is composed of a constant (*dc*) component and a modulated (*ac*) component. Only *ac*

component is important in the spectroscopic measurements and it is referred to as the interferogram:

$$I_D(\delta) = S(\tilde{\nu})\cos(2\pi\tilde{\nu}\delta). \tag{3.8}$$

A plot of light intensity versus optical path difference is called an interferogram. The interferogram is a function defined in the time domain. If the movable mirror is moved at a constant velocity V, the retardation is simply:

$$\delta = 2Vt. \tag{3.9}$$

And the interferogram is given by:

$$I_D(\delta) = S(\tilde{\nu})\cos(2\pi\tilde{\nu}2Vt). \tag{3.10}$$

Therefore, the signal is measured by the detector as a sinusoidal wave with the frequency $2\tilde{\nu}V$. If the sample absorbs the radiation at this frequency, the amplitude of the sinusoidal wave is reduced by the value proportional to the amount of absorbed energy by the sample. Next, a mathematical operation known as Fourier transformation converts the interferogram (a time domain spectrum) to the final IR spectrum, which is the frequency domain spectrum (intensity versus frequency).

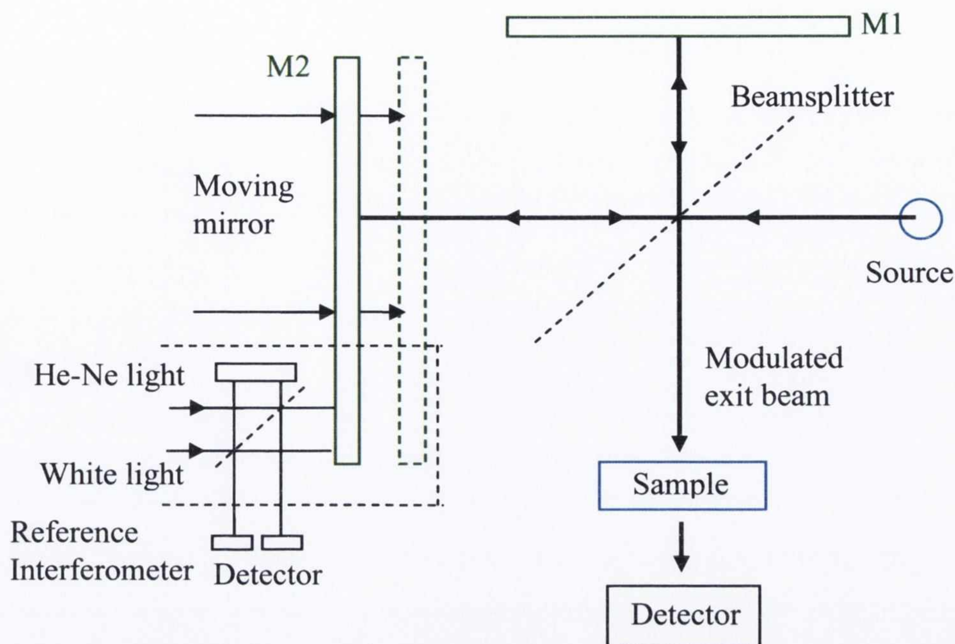

Fig. 3.2. Schematic of a Michelson interferometer.

IR absorption information is generally presented in the form of a spectrum with wavelength or wavenumber as the x-axis and absorption intensity or percent transmittance as the y-axis. If the sample has a concentration c, and the path length of source beam in this sample is b, then the fundamental equation governing the absorption of radiation as a function of transmittance is:

$$T = I / I_0 = 10^{-abc} . \qquad (3.11)$$

where I_0 and I are the intensity entering the sample and transmitted by sample, respectively. The constant a is called the molecular absorptivity at the specific frequency. This equation is usually transformed to the logarithm form:

$$\log_{10}(I_0 / I) = abc . \qquad (3.12)$$

The term $log_{10}(I_0/I)$ is called the absorbance (A). Then, for a single compound in a homogeneous medium, the absorbance at any frequency is expressed as:

$$A = abc\,. \tag{3.13}$$

This is the absorption law which is called the Bouguer–Beer–Lambert law or, commonly, Beer's law. It states that the intensities of absorption bands are linearly proportional to the concentration of each component in a homogeneous mixture or solution. The absorbance A is also alternately given by:

$$A = \log_{10}(1/T)\,. \tag{3.14}$$

The transmittance spectra provide better contrast between intensities of strong and weak bands because transmittance ranges from 0 to 100% T whereas absorbance ranges from infinity to zero. The Fig. 3.3 shows representative IR absorption spectra of two Si wafers grown by the Czochralski and Float Zone methods. The intense band at ~ 614 cm^{-1} belongs to Si-Si phonon of Si crystalline lattice while the band at ~1100 cm^{-1} corresponds to stretching mode of Si-O defect mode. As can be seen from Fig. 3.3 the better quality Si wafer with less oxygen impurities is grown using the Float zone method. Therefore, FTIR spectroscopy supplies information on interstitial oxygen in different materials. Moreover, IR absorption can also be used to provide information relating to film thickness, doping concentration [2], or substitution carbon content [3].

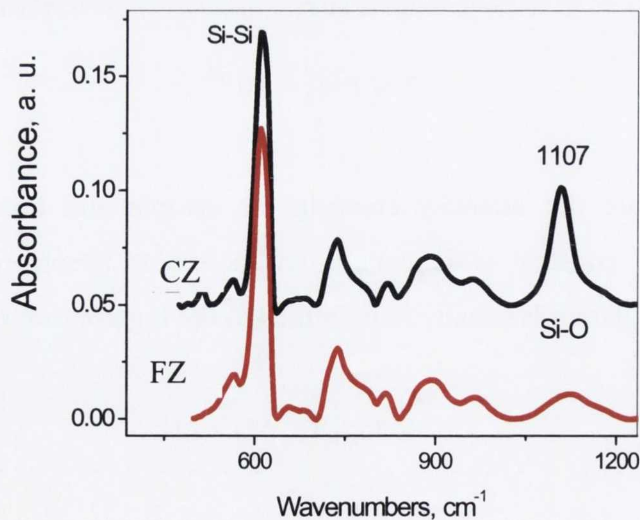

Fig. 3.3. FTIR spectra of bare Si wafers shown for float zone (FZ) and Czochralski grown (Cz) wafers.

References

1. A. Michelson, Phil. Mag. 31, 338 (1891); 34, 280 (1892)

2. S. W. Lim, Y. Shimogaki, Y. Nakono, K. Tada, H. Komiyama, J. Electrochem. Soc., 146, 4196 (1999)

3. J. Wasyluk, T. Perova, F. Meyer, J. Appl. Phys., 107, 023518 (2010)

4. Micro-Raman and Spreading Resistance analysis on ion implanted Ge for layer transfer applications

4.1. Introduction

The degradation in performance of silicon metal-oxide semiconductor (MOS) devices with scaling caused by fundamental Si material limitations is forcing the semiconductor industry to consider extraordinary techniques and materials. Changes in structure (various forms of double-gated devices), alteration of material properties in the channel region (SiGe alloys or strained silicon), and replacement of silicon (new GaAs gate dielectric) are all being considered. In view of the challenges of introducing any of the preceding technologies into full manufacturing, other options that reuse much of the silicon infrastructure and processing are attractive. For those requirements, pure Ge is considered as a good candidate. Compared with Si, Ge has higher free charge carrier mobility and a lower dopant activation temperature [1]. The availability of good quality, bulk Ge wafers as large as 200 mm, driven by the solar cell industry for space applications is also an advantage. However, Ge technology suffers from a potentially fatal flaw-increased leakage because of the lower bandgap, which now appears possible to overcome in part through the use of Ge-On-Insulator (GOI) substrates that up to now have not been commonly available.

To fabricate GeOI the well-known in Si industry Smart Cut [2] technology is used. Smart Cut is a revolutionary technique used to transfer ultra-thin single crystal layers of wafer substrate material onto another surface (mechanical support). This method is widely applied in Silicon-On-Insulator (SOI) technology. Differing from traditional layer-transfer techniques, which are based mainly on wafer bonding and etch-back or on epitaxial lift-off, the Smart Cut approach uses a thermal activation process as an “atomic scalpel”. It literally slices the wafer horizontally, lifting off a thin layer from the donor substrate and placing it onto a new substrate. Inherently, this process offers better control, and a single donor substrate can be reused many times for further layer transfers. The transferred layer thickness is pre-determined by the cleavage zone created via ion implantation of hydrogen, helium, argon, etc. A schematic process of Smart Cut technology is shown in Figure 4.1 with hydrogen implantation in Ge as an

example. Wafer A, capped with a dielectric layer (Plasma Assisted PACVD grown SiO_2 to protect the Ge surface during implantation), is exposed to hydrogen implantation at room-temperature with a dose in the range 10^{16}–10^{17} cm^{-2} in order to introduce a thin layer with hydrogen ions of sufficiently high density. At this stage hydrogen decorated defects (microvoids) are formed at a depth equals to the implantation range. The second step consists of chemical cleaning and hydrophilic bonding at room temperature of wafer A to a handle wafer B by van der Waals forces. The handle wafer serves as a stiffener and often is covered with SiO_2 layer. Next, the two bonded wafers (A and B) are annealed. During the first stage, a crystalline rearrangement and coalescence of the hydrogen-decorated defects into larger structures occurs in the hydrogen-implanted region. A thin damaged layer appears at the depth of the maximum hydrogen ion concentration in the implanted wafer A, which splits into two parts yielding a GeOI structure and the remainder of wafer A.

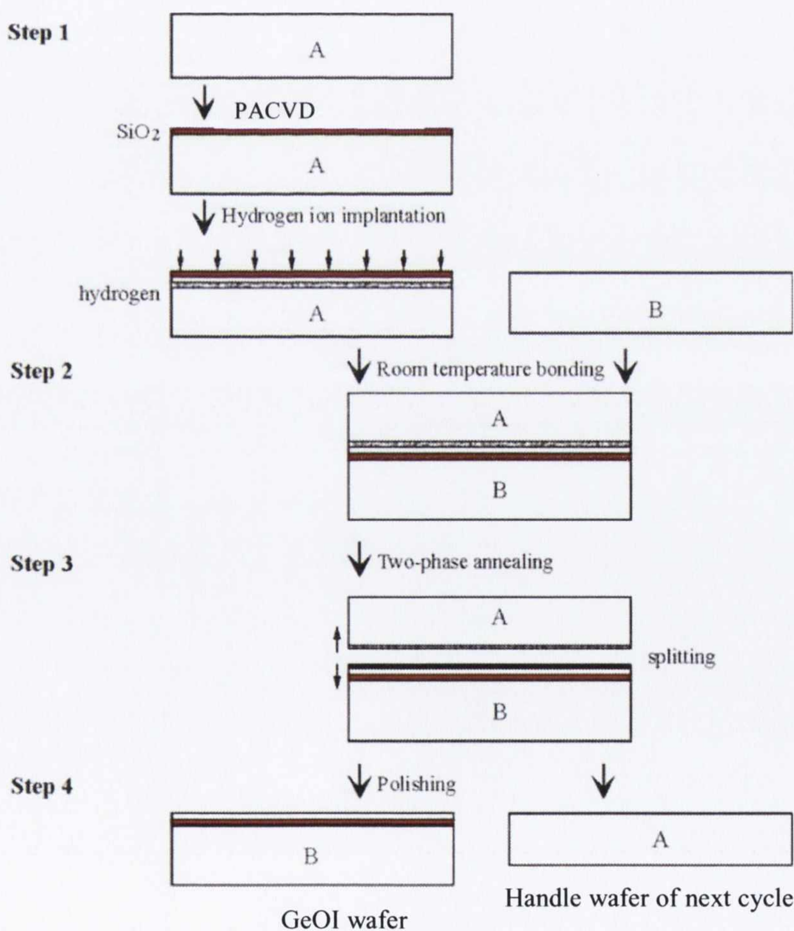

Fig. 4.1. Schematic of the Smart-Cut process [3].

The subsequent high-temperature thermal treatment removes radiation defects in the germanium layer and strengthens the chemical bonds between the two wafers. The last step consists of polishing of the top germanium layer by a chemical-mechanical method to obtain a surface quality comparable to germanium prime wafers. Thus, as a result of the process, a GeOI wafer and a residual wafer A are obtained, and the latter can be used again as a donor wafer (see Fig. 4.1).

The history of smart cut technology starts from SOI which was first introduced in the 1970s as a niche substrate technology for military or space applications. In these early days, Bonded and Etched-Back Silicon-On-Insulator (BESOI) and Separation by Implantation of Oxygen (SIMOX) were the dominant SOI fabrication technologies. However, they were not very well suited to high-volume, commercial production. After a brief period using SIMOX implantation techniques to fabricate SOI wafers, the founders of Soitec pioneered a new wafer bonding technique, Smart Cut, which was developed at CEA-LETI. Smart Cut based manufacturing of Soitec's SOI wafers, which are sold under the tradename UNIBOND, ramped up in the mid 1990s. The first industrial implementation of SOI was announced by IBM in August 1998 [4]. Smart Cut technology significantly enlarges the field of engineered composite substrates combining different thin layer materials to address the requirements of the most diverse applications. At present, beyond Germanium on Insulator, other materials such as Silicon-On-Quartz, Strained-Silicon-on-Silicon and Silicon Carbide-On-Insulator are engineered using the Smart Cut. This flexibility of the Smart Cut technology in development of hetero-composite substrates extends its applications to photonics, opto-electronics, and high frequency and high power devices. The choice of insulator depends largely on the intended application; sapphire being used for radiation-sensitive applications and silicon dioxide preferred for improved performance and diminished short channel effects in microelectronics devices [5]. The benefits of Smart Cut are numerous: it is scalable to any wafer size, it allows multiple exfoliations of a donor substrate, it uses standard IC manufacturing equipment and the thicknesses of the transferred layer and buried oxide are tunable.

During the Smart Cut process of GeOI, germanium layers are typically transferred at 250-400°C [6], depending on various factors, including the dose of hydrogen used, and thermal expansion coefficients of the handle and donor substrates. Silicon is, largely, the substrate of choice for handle wafers in a GeOI process, but silicon and

germanium do not have matching thermal expansion coefficients. If the top germanium layer is thick enough to impose strain on the substrate stack, the splitting temperature and subsequent thermal budget often need to be minimised to avoid wafer breakage. Therefore, if many defects still existed after splitting, a handle substrate that is closely thermally matched to Germanium would provide the opportunity for higher temperature annealing. Sapphire and Germanium substrates are thermally matched, and Germanium-On-Sapphire substrates have already been demonstrated as a suitable platform for high frequency devices [7].

Raman spectroscopy has been extensively applied to study ion-implanted semiconductors, since the shape of Raman lines for lattice vibrations is indicator of structural disorder induced by ion implantation. Raman spectra of post-irradiated Si [8,9], Ge [10] and GaAs [11,12] have been studied. Bevelling is a well known technique which is used for preparing samples for spreading resistance profiling (SRP). It can also be useful in Raman spectroscopy analysis, where there is a requirement to probe deep into materials or to probe multilayer or graded layer structures. The depth profiling of composition and strain using Raman spectroscopy has been presented for bevelled $Si/Si_{1-x}Ge_x/Si$ structures in Refs. [13,14]. Raman analysis on GaAs bevelled samples formed by chemical etching [15] and polishing [16] has been also reported. Germanium has much larger absorption coefficient in the visible range of spectra compared to Si. The penetration depth of laser light at 633 nm in Ge is around 80 nm – several times smaller than the projected range of ions (in this work ~300 nm). Therefore, without applying the bevelling method we will be able to get information only from the damaged region near the surface and not from the projected range. The Raman analysis of damage at the Ge surface caused by H implantation has been undertaken by Ishioka [10].

This chapter reports for the first time on the Raman analysis of bevelled, ion implanted germanium samples. The bevelling allows Raman measurement to be performed in depth profiling of Ge samples with nano-scale resolution. Different types of germanium substrates implanted with hydrogen and helium as well as Ge-On-Sapphire (GeOS) substrates, made by bonding a hydrogen-implanted Ge substrate to a thermally oxidized sapphire wafer, are studied in this work for structural properties relevant to device fabrication. The implanted Ge and completed GeOS samples were characterized for structural quality, stress, film uniformity, resistivity and carriers'

concentration, using optical microscopy, micro-Raman spectroscopy and SRP technique. A Raman mapping technique was applied to investigate the influence of different process conditions, such as annealing temperature, type and dose of implanted ions, on the structural quality of the Ge layer.

4.2. Effects of hydrogen on defect formation and electric properties of the material

The two main keys of the Smart Cut technology are to generate a large number of microdefects (microcracks and microvoids) concentrated in a very thin layer in the implanted wafer by hydrogen ion implantation and to split the bonded wafer system later by thermal annealing. Therefore, an insight into the nucleation of microcavities associated with hydrogen implantation is necessary in order to gain a fundamental understanding of this complicated nanoscale process involving chemical reaction, bond decohesion, and mechanical deformation and fracture. The effect of implanted hydrogen on defect nucleation within Si was well explained by several research groups [17-19]. Both Si and Ge have a diamond cubic crystal structure with bond lengths of 2.352 Å for Si and 2.450 Å for Ge [20], an indirect bandgap and similar characteristics of isolated H-stabilized defects [21,22]. The dissociation energy of the Si-H monohydride bond is 2.5 eV, whereas for the Ge-H monohydride bond the dissociation energy is 1.9 eV [21,22]. Since ion implantation in Si is studied in larger extent than in Ge, a comparison with Si is always useful to explain the behaviour of light ion related defects in Ge. As in many respects [23], at the microscopic level, similar mechanisms for the formation of H defects are likely to occur in both materials [24-26]. Based on this, a model of H implantation in Si is going to be used in this work to explain H implantation in Ge. The unit cell of Ge can be divided into eight cube-shaped sub-cells of identical size, with edge length, a/2. Each of the four sub-cells has a body-centred Ge atom whereas the other four sub-cells do not. This means that in each unit cell of a germanium crystal there are four intrinsic voids (interstitial spacing vacancies). The voids size is much larger than a hydrogen ion. Therefore, most hydrogen ions implanted are trapped in these inherent voids, which serve as sources of larger defects. The trapped hydrogen atoms combine with Ge atoms and form Ge–H bonds. The implantation process pushes more and more hydrogen ions into the voids, causing an increase of internal pressure in

the voids. The trapped hydrogen atoms diffuse and segregate near the peak implantation region during thermal annealing, forming microvoids filled with H_2 molecules and coated with atomic hydrogen captured at broken and dangled Ge bonds at the pore surface and at the crack tip (see Fig. 4.2). Presence of molecular hydrogen in Ge as well as Ge-H bonds has been demonstrated by means of Infrared [27] and Raman spectroscopy [28]. It has been also demonstrated that more efficient damage is produced in Ge than in Si for similar implant conditions [29]. Microcracks and platelets in the implanted zone in Ge were experimentally observed by transmission electron microscopy (TEM) in Ref. [30]. The high pressure inside the microcavities, which is magnified significantly due to the high temperature in thermal annealing, is the driving force for nucleation and expansion of defects, which further leads to splitting of the wafer. The effect of splitting of a wafer along the damaged (or porous) layer is based on the phenomenon of growth and coalescence of microvoids towards the platelets, which occurs mainly parallel to the surface of the wafer [26,31,32]. In Ref. [26] it was demonstrated that although the distribution of (001) and {111} platelets is similar in both Si and Ge, the {111} platelets have been found to be either larger and/or higher density in Ge than in Si. This leads to the conclusion that lower energy is needed to form platelets in Ge than in Si. This is in agreement with the threshold fluence for abundant blistering which has been found to be lower for Ge than for Si [33].

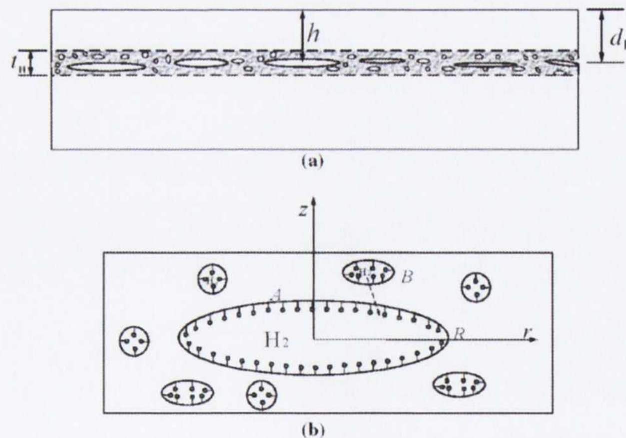

Fig. 4.2. (a) Microcracks and microvoids distributed in the peak-hydrogen concentration layer and (b) cracks with Ge–H bonds on the crack surfaces. t_H is the thickness of the hydrogen implanted area and d_H is a depth of the peak implantation.

A very important consequence of ion implantation is the creation of lattice damage such as vacancies, interstitial-type defects and even the formation of amorphous regions [26,34]. These defects can give rise to local deformation of the crystal structure, i.e. elastic stress. Applying a too high dose of hydrogen in materials can also induce negative effects such as blistering, swelling, flaking and exfoliation. Although some discrepancies are observed at the atomic scale (e. g. the passivation of the cavities seems to take a place via monohydrides in Si and by both mono- and di-hydrides in Ge [24]), available results suggest that at the microscopic level the formation of the platelets and their evolution toward micro-cavities is similar in Ge and Si at a temperature normalized with respect to the melting temperature [26]. It seems to be the same also for interstitial-related defects [26]. It should be emphasized that these similarities observed for light ion implantation are no longer valid when increasing the ion mass [26].

Radiation damage is known to cause donor [35] and acceptor [36] states in the band gap of many semiconductors, through the formation of vacancies and interstitials, which, on annealing, interact with hydrogen, oxygen or dopant atoms already present in the lattice structure. In one example, Auret et al. [37] implanted germanium with heavy ions, indium, and the more chemically inert xenon, and concluded that, after some annealing, the electronic properties of implantation induced defects were independent of the implanted species. However, it is known that hydrogen is specifically noted for its chemically reactivity in semiconductors and it is therefore generally considered to be more prone to create defects. In the case of silicon, it is known that hydrogen and defects frequently interact, to become stable defects which would otherwise anneal out at relatively low temperatures [38]. It has been suggested that, contrary to the case with silicon, where hydrogen is amphoteric (it always counteracts the prevailing conductivity), interstitial hydrogen could act as an acceptor state in germanium [39,40]. This may be an argument for developing a layer transfer process based on hydrogen-helium co-implants, with a high ratio of helium. While the hydrogen implantation and its influence on electronic properties are well understood for silicon, in the case of Ge there are still many unresolved issues. In recent years, several studies on electrically-active hydrogen-implant related defects in germanium have been performed using deep level transient spectroscopy (DLTS) [41]. These studies generally involved implant

doses at or below 10^{14} atoms/cm^2. It would appear necessary to examine implant doses, several orders of magnitude higher, similar to that used in a smart-cut process.

4.3. Experimental

4.3.1. Sample growth and description

Germanium samples used in this study were n-type, Sb-doped and p-type, Ga-doped <100> wafers with varying resistivities. The samples were given an HF-based clean, then coated with a 300 nm thick layer of PACVD SiO_2 from a silane precursor. This layer was then densified by annealing in a nitrogen ambient at 600°C for 2 hours. Wafers were then implanted with various fluences of hydrogen (ranging from 3 to 6×10^{16} atoms/cm^{-2}) or helium (3×10^{16} atoms/cm^{-2}) with implantation energies (H+: 75KeV; He: 105KeV) selected for a projected range of ~300 nm into the germanium substrate. Substrates were aligned at a 7° angle and kept at close to ambient temperature throughout the implantation. Wafers were then cut into smaller samples for analysis. Detailed description of germanium samples analyzed in this work is shown in Table 4.1. Samples for SRP and Raman measurements were prepared at Solecon Laboratories [16], by bevelling at various shallow angles ranging from 0.0025 rad to 0.006 rad, in a diamond grit, to achieve a final roughness of 0.4-0.8 nm RMS. Samples were mounted on a bevelling block, and then the bevel is created by attaching the block to a special bevelling jig following by grinding an angled surface against a diamond embedded glass surface. The glass plate was lubricated with oil to help flush the debris from the bevel. Once the bevelling was completed the sample was cleaned and ready for SRP and Raman measurements.

GeOS samples were fabricated with a hydrogen implantation dose of 7×10^{16} cm^{-3} (see Table 4.1). After implantation the oxide layer on Ge was preceed with chemical mechanical polishing (CMP) in order to have a smooth oxide surface before bonding to handle wafer. Next, the oxide surface was cleaned with nitric fumic acid in order to remove any residue from the surface. The Ge wafer was annealed at 400 °C for 2 hours to simulate an ion-cut process. After transferring the Ge to the sapphire support the

samples were processed with post split anneals at 600 °C and 800 °C for two hours. As a final step, an oxide layer was grown on the top of GeOS. The structure of the samples is presented in Fig. 4.3 and it consists of: ~0.3 μm SiO_2 (top layer) / ~0.5 μm Germanium / 0.6 μm SiO_2 (buried layer) / 500 μm sapphire. The bevelled angle for these samples was also estimated from the surface profile results (see Appendix I). They are in good agreement with the angles reported by *Selecon Lab*.

Table 4.1. Doping and implant concentration and temperature of annealing for bevelled Ge samples implanted with hydrogen and helium. The bevelled angle data were provided by *Selecon Labs*.

Sample (Bevel angle)	Background Germanium doping concentration	Implant dose conditions	Description
Hydrogen implantation			
2 (α=0.0026rad)	n-type (Sb) $8\times10^{14}/cm^3$	3×10^{16} atoms/cm^2, 75KeV	Annealed at 450 °C and bevelled
2A			Annealed at 450 °C and bevelled and then annealed at 600 °C
4 (α=0.003rad)	p-type (B) $6\times10^{16}/cm^3$	6×10^{16} atoms/cm^2, 75KeV	un-annealed
4A			Annealed at 200 °C after bevelling
Helium implantation			
B2 (α=0.0056rad)	n-type (Sb) $2\times10^{15}/cm^3$	3×10^{16} atoms/cm^2, 105KeV	Annealed at 400 °C/2h
B3 (α=0.006rad)			Annealed at 300 °C/4h then 600 °C/2h
GeOS hydrogen implantation			
GeOS600 (α=0.0023rad)	n-type (Sb) $2\times10^{16}/cm^3$	7×10^{16} atoms/cm^2, 75KeV	600 °C/2h
GeOS800 (α=0.0016rad)			800 °C/2h

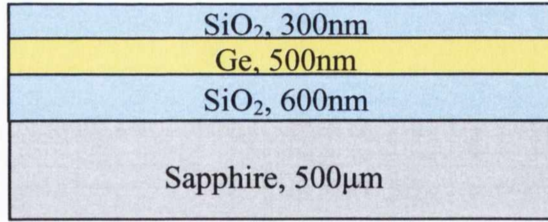

Fig. 4.3. Schematic picture of the GeOS sample.

4.3.2. Characterisation techniques

4.3.2.1. Spreading Resistance Profiling

SRP, also known as Spreading Resistance Analysis (SRA), is a technique used to analyze resistivity vs. depth in semiconductors. Knowing the resistivity of the semiconductor, dopant concentration can be calculated based on the following equation:

$$\rho = (Ne\mu)^{-1} \tag{4.1}$$

where: ρ is resistivity in ohm-cm, N is net dopant concentration in atoms/cm^3, e is electronic charge in coulombs, μ is majority carrier mobility in cm^2/volt-sec. Measuring electrical resistivity is therefore a viable way of determining dopant concentrations. SRP measurements and carrier concentration calculations were made at *Solecon Labs.* Two tungsten carbide tips spaced within 20 μm of each other were used for scanning along the beveled region and taking a measurement at step increments every 4-8 μm. For example, with a bevel angle of 0.002 rad and a step increment of 5 μm, the depth increment is 0.01 μm. Five mV are applied across the probes and the resistance (called spreading resistance) is measured (see Fig. 4.4). The resistance encountered within the slab of sample is:

$$R = \frac{\rho}{2a} \tag{4.2}$$

where: R is the measured resistance in ohms and a is the radius of the contact area of the tip with sample in cm. Most of the resistance occurs very close to the electrical contact allowing the local resistivity to be determined. The probes produce a negligible probe to silicon resistance (nearly ohmic contact) over the entire resistivity range for both p-type and n-type (rich in holes and rich in electrons, respectively). Keeping the resistance of wiring and the spreading resistance within the probe tips to a minimum, the measured resistance is almost exclusively from $R = \rho / 2a$ for silicon samples at least $2a$ thick. With the aid of calibration resistivity standards, ρ can be determined at each probing by the probe pair.

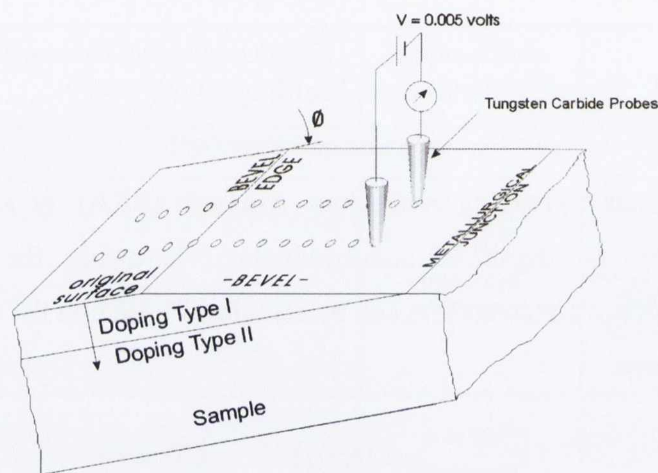

Fig. 4.4. Schematic diagram of spreading resistance measurements on bevelled sample [42].

4.3.2.2. Raman and Infrared spectroscopy

The micro-Raman scattering measurements were carried out at room temperature in the backscattering geometry using RENISHAW 1000 micro-Raman system. A HeNe laser at 633 nm and with power of 5 mW was used as an excitation source to avoid sample heating. The Raman line mapping measurements were taken in the static mode with 10s exposure time and 1 accumulations. The laser spot was focused on the sample surface using a 50x objective with short-focus working distance. Line mapping measurements were performed at a distance along the bevelling surface ranging from 0 to ~ 400 μm with a step size of few microns, where zero corresponds to the starting point of the measurements (see Fig. 4.5). In order to compare Raman data with SRP, the mapping

distance (d_m) was recalculated to distance in depth from sample's surface (d_p) using the trigonometric function, $sin\alpha = d_p/d_m$. The Raman spectra were fitted with mixture of Gaussian and Lorentzian function to obtain the position, intensity, and linewidth of the detected Ge-Ge peak.

FTIR transmission measurements on Ge samples were performed at normal incidence of light in the spectral range from 6000 to 400 cm^{-1} using a Fourier transform Digilab FTS 6000 spectrometer with a Globar source, a KBr beam splitter and a mercury cadmium telluride (MCT) detector. Due to the small size of samples, the microsampling Perkin-Elmer attachment has been used for measurements, which allows one to focus the infrared (IR) beam into a spot size of ~ 3-5 mm in diameter. The spectra were collected with 8 cm^{-1} resolution and 128 scans were averaged for each spectrum in order to improve the signal-to-noise ratio.

4.4. Results and discussion

Figures 4.5 and 4.6 show a scanning electron microscopy (SEM) image and a white light interferometry surface profile of Ge sample implanted with $3x10^{16}$ atoms/cm^2 hydrogen dose and annealed at 450ºC. The structural damage caused by implanted hydrogen at the projected range is clearly observed in Figs. 4.5 and 4.6. A dose of 3×10^{16} atoms/cm^2 is slightly below the threshold of blistering for germanium and typically provide not sufficient hydrogen to form blisters large enough to be visible at the surface. Consequently this is beneficial for analysis, as both SRP and Raman analysis would be detrimentally affected by the surface roughening caused by blisters. However, bevelling reveals some defects and cavity formation at the projected range, due to clustering of molecular hydrogen. Raman spectra measured at the projection area for different Ge samples are presented in Fig. 4.7. The strong peak observed at around 300 cm^{-1} is assigned to the longitudinal optical (LO) phonon mode. The full width at half maximum (FWHM) and intensity of Ge-Ge Raman peak are indicators of crystalline quality of the structure. The FWHM increases and peak intensity decreases, as the number of implant-related defects increase. The integrated intensity of the Ge-Ge Raman peak decreases remarkably with increasing ion fluence, as shown in Fig. 4.7.

This decrease in the integrated intensity can be explained in terms of an increase in the absorption coefficient due to the defect formation [9].

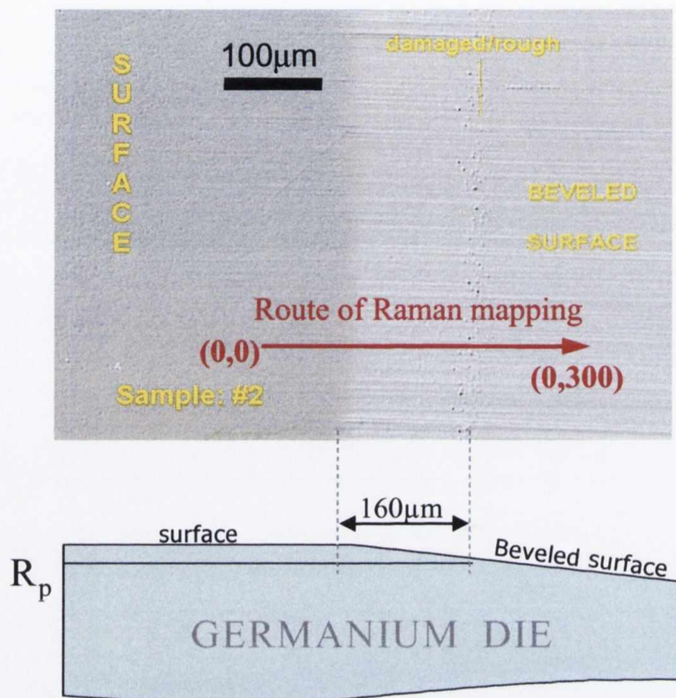

Fig. 4.5. (a) SEM image of Ge sample implanted with $3x10^{16}$ atoms/cm^2 hydrogen dose and annealed at 450 °C. The red arrow indicates the direction and distance of Raman line mapping. (b) Schematic picture of cross section of a bevelled Ge sample.

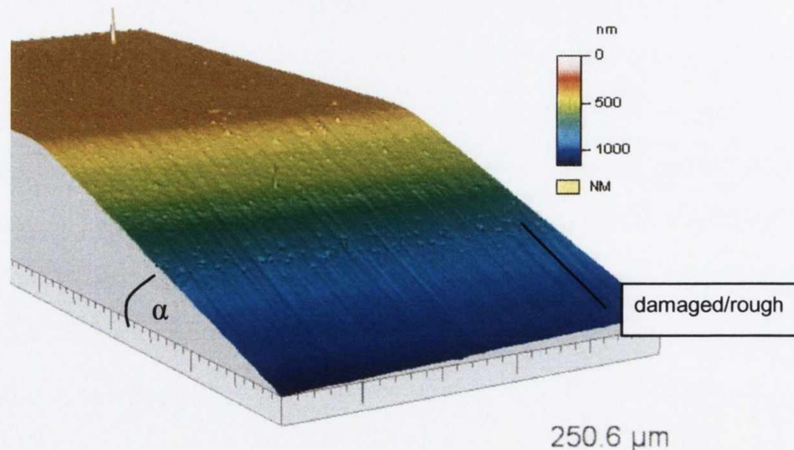

Fig.4.6. White light interferometry surface profile of Ge sample, illustrating bevel and damaged region at the projected range.

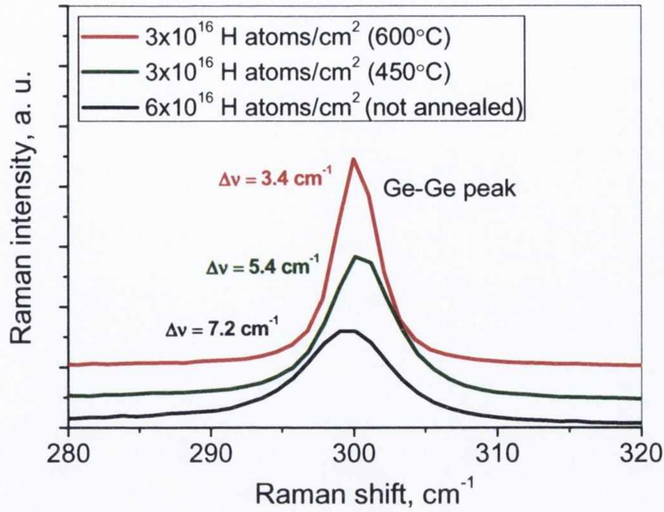

Fig. 4.7. Raman spectra in the range of Ge-Ge phonon mode for samples implanted with different dose of hydrogen and annealed at different temperatures. Δv indicates the value of the full width at half maximum.

As can be seen from Fig. 4.7, the largest linewidth ($\Delta v = 7.2 cm^{-1}$) is observed for sample 4, implanted with the largest hydrogen dose without any subsequent anneals. The FWHM of the Ge-Ge peak decreases to 5.4 cm^{-1} for sample 2A implanted with a smaller H dose and annealed at 450ºC. After further annealing of the same sample at higher temperature (~600ºC), the linewidth of the Ge-Ge peak reaches the value corresponds to that for bulk crystalline quality Ge. This indicates that due to the high temperature annealing, structural defects caused by hydrogen implantation have vanished and the Ge structure is fully recovered.

4.4.1. Hydrogen implanted samples

In Figure 4.8 (a), the depth profiles of the Raman linewidth and carrier concentration are presented for sample 2 implanted with 3×10^{16} hydrogen atoms/cm^2 and annealed to 450 ºC. The peak of ~1×10^{17} acceptors and the maximum linewidth of Ge-Ge peak (~5.8 cm^{-1}) is observed at the projected range of ~320 nm below the sample surface. Sample 2 was implanted with a dose slightly below the threshold of blistering for germanium. For the sample annealed at 450 ºC, as can be seen in Fig. 4.1, the defects

are clearly observed at the projected range by optical microscopy. Raman line-mapping results show the maximum linewidth of the Ge-Ge Raman peak exactly at the projected range ~320 nm (see Fig 4.8 (a)). The value of ~320 nm was also confirmed by SRIM simulation presented in Fig. 4.9. Figure 4.9 (a) illustrates the hydrogen ion distribution in Ge with a SiO_2 capping layer. The distribution of vacancies (damage) caused by ion implantation is simulated in Fig. 4.9 (b). For the sample annealed at 600 °C, SRP shows that the carrier concentration decreases by about one order to 1×10^{16} acceptors/cm^3, while the Raman linewidth profile is flat and corresponds to the high crystalline quality region of the un-implanted Ge wafer (see Fig. 4.8(b)). Original Raman maps of the Ge-Ge peak position, linewidth and peak intensity for samples 2 and 2A are presented in Figs. 4.10 (a-c). At the bevelling region for sample 2, the Ge-Ge peak position shifts slightly to the higher frequencies (about 0.2 cm^{-1}), which leads to the conclusion, that bevelling itself introduces the relatively small compressive stress in the structure. There are no observed changes in peak position between bevelled and projection regions. This is due to the annealing process, which introduces the relaxation of stress in the Ge lattice caused by the implanted hydrogen. After annealing of the bevelled sample at 600 °C, the Ge structure is fully relaxed as the Ge-Ge Raman peak is observed at ~300 cm^{-1}. This leads to the conclusion that post-bevelled annealing repairs the structural damage caused not only by the H implantation but also by the bevelling process. This conclusion is agreement with Raman maps of the linewidth and the peak intensity, presented in Figs. 4.10 (b) and 4.10 (c), respectively. The FWHM of the Ge-Ge peak for sample 2A is equal to ~3.6 cm^{-1} and it stays the same at the surface, bevelled region and projected area. Peak intensity increases significantly after additional annealing proving that the structural damage in Ge sample is recovered. The FWHM of Ge peak for sample 2 at the bevelled region increases (~ 0.4 cm^{-1}) compared to the sample surface (see Fig. 4.10 (b)). Again, this change in the linewidth can be assigned to the surface roughness introduced by the bevelling itself. The larger increase in linewidth (~0.6 cm^{-1}) observed at the projection area indicates that some defects and roughness due to the cavity formation at the projected range have been introduced by accumulated hydrogen.

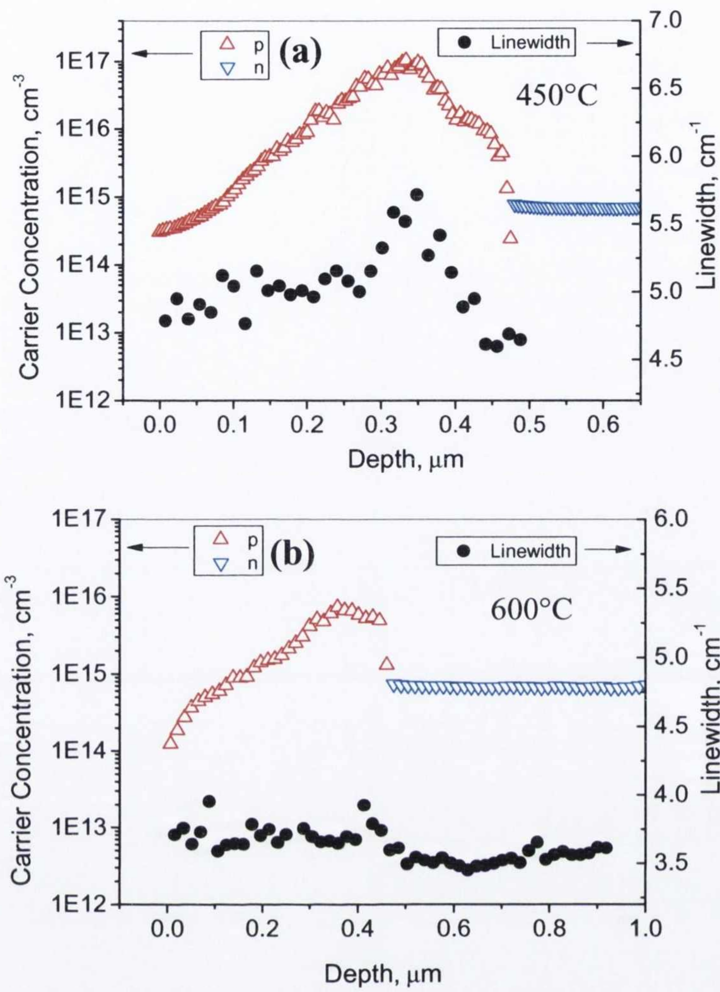

Fig. 4.8. Depth profiles of the Raman linewidth and carrier concentration from SRP for sample 2 implanted with 3×10^{16} hydrogen atoms/cm^2 and annealed to (a) 450 °C and (b) 600 °C.

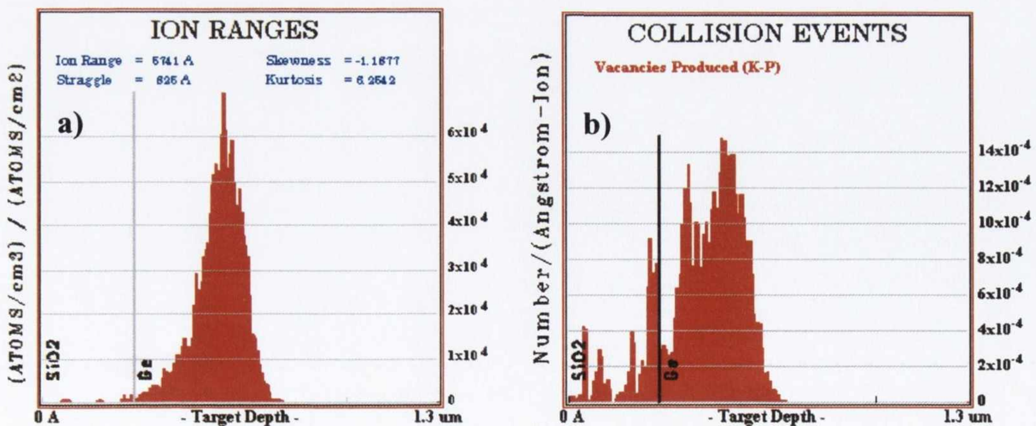

Fig. 4.9. SRIM simulation of (a) a hydrogen ion distribution and (b) a damage in n-type Ge as a function of the target depth.

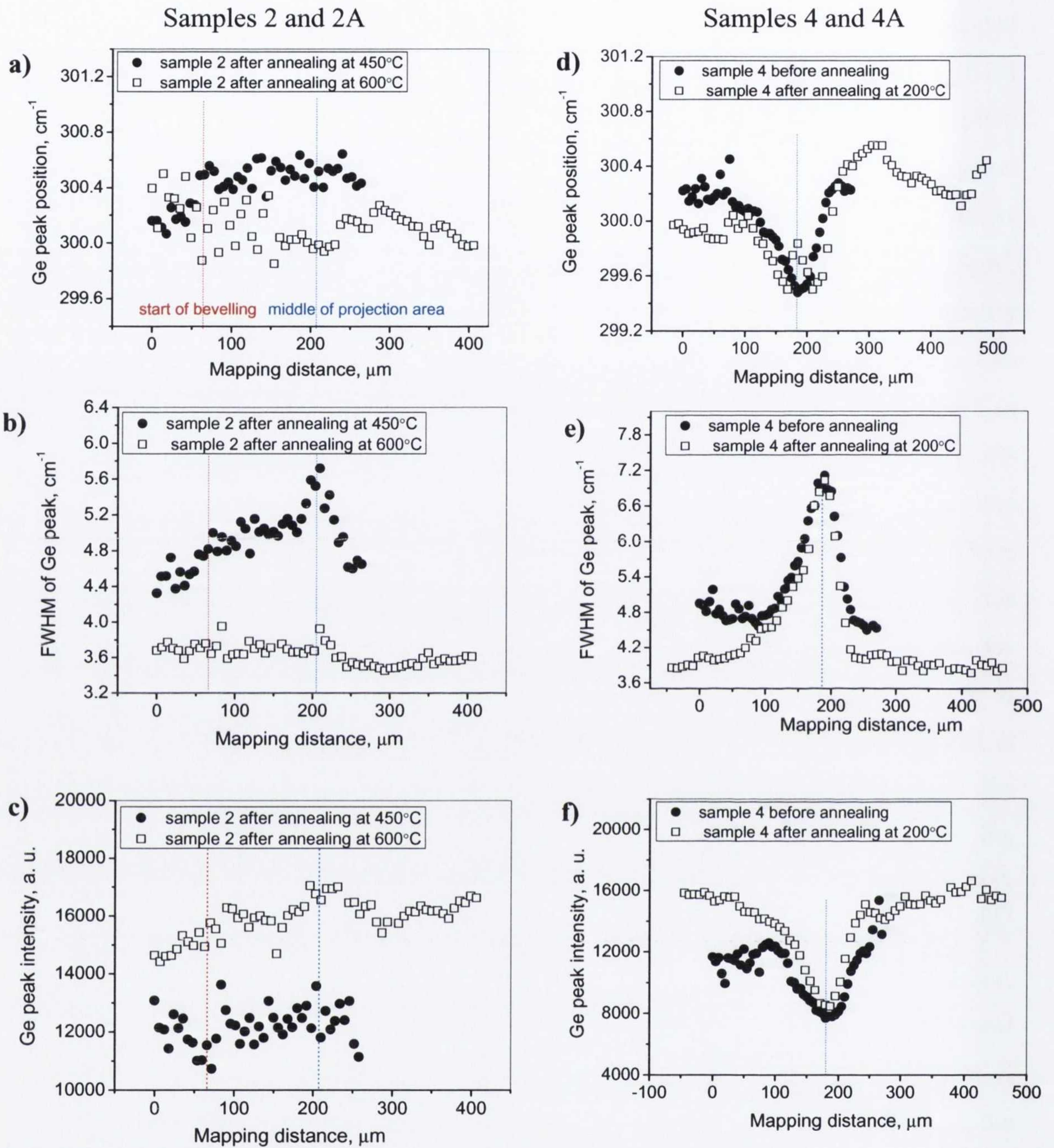

Fig. 4.10. Raman maps of the Ge-Ge peak position, linewidth and peak intensity of (a-c) samples 2 and 2A and (d-f) samples 4 and 4A. Red and blue lines indicate the start of the bevelling and the middle of projected range, respectively.

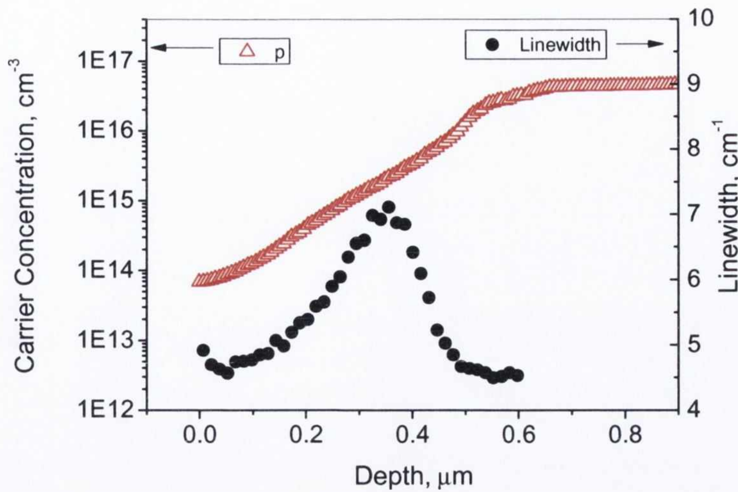

Fig. 4.11. Raman linewidth and carrier concentration derived from SRP vs. depth into the sample, for a 6×10^{16} atoms/cm^2 hydrogen implant into germanium without annealing.

In Figure 4.11, the map of Raman linewidth and the carrier concentration are plotted for a sample implanted with hydrogen dose of 6×10^{16} atoms/cm^2, without any subsequent anneals. SRP shows a high resistivity region running from the surface to the projected range, while Raman shows a FWHM of 7 cm^{-1}, corresponding to a projected range of ~370 nm. The projected range was estimated from SRIM simulation. The dose of hydrogen used for sample 4 is a typical dose for a germanium smart cut process, e.g. for splitting at or around 400 °C. It was not possible to get meaningful data from the annealed high dose implant sample due to blistering. The lack of annealing for this sample also hides the presence of acceptor states, as follows: the resistivity along the bevel, measured from tungsten probes is a function of the majority carrier concentration, N (see Equ. 9.1). However, defects that impair crystal quality cause a reduction of mobility, and therefore an increase in resistivity. This would explain the drop in carrier concentration in the implanted un-annealed sample, shown in Fig. 4.11. The higher background concentration also shows more clearly the drop in mobility caused by un-annealed implant damage, stopping around 0.7 μm deep. Figures 4.10 (d-f) present the Raman maps of the Ge-Ge peak position, linewidth and peak intensity for samples 4 and 4A. The Ge-Ge peak shift (about 0.7 cm^{-1}) to a lower frequency is observed at the projected area for the implanted but not annealed sample. This indicates the presence of tensile stress in the structure. The linewidth of the Ge-Ge peak increases significantly (~ 2.4 cm^{-1}) at the projection area, corresponding to the defects introduced in the Ge lattice by hydrogen atoms. The peak intensity decreases at the projection

region. Sample 2 was annealed after bevelling at a temperature of 200 °C. As can be seen from Figs. 4.10 (d-f), the temperature of 200 °C was too low to introduce any structural changes at the projected range during the annealing process. However the temperature of 200 °C was high enough to lead to the structural recovery of the damage caused by the bevelling process outside the projected range. The distribution of the Ge-Ge peak linewidth at the projection region is asymmetrical. The linewidth increases at the distance of 100 μm, reaches the maximum value at the middle of the projected range and then decreases twice faster at the distance of 50 μm. The region closer to the surface from the peak ion concentration has more damage than the region below the depth of max ion concentration. This distribution of damage corresponds exactly to the asymmetric ion and damage distribution in Ge simulated in SRIM program. Sample 4 was implanted with molecular hydrogen at 150 keV (1.5×10^{16} molecules/cm^2). The SRIM cannot perform molecular implantation thus the simulation was performed for H+ atoms at 75 keV. The SRIM simulation for 1000 hydrogen ions is presented in Fig. 4.9.

The presence of molecular hydrogen and Ge-H bonds can be confirmed by Raman spectroscopy [28,43]. These measurements were performed with a special geometry and polarization configuration where the incident laser beam was set at an angle of 40°/60° with the sample normal [28,43]. The Renishaw micro-Raman setup does not allow for this configuration, however, the presence of hydrogen within the Ge structure was detected in this work using Fourier Transform Infrared spectroscopy. Figure 4.12 presents the infrared absorption spectrum of the bulk Ge and the subtracted spectra of the Ge implanted with 3.5×10^{16} H_2 and the Ge implanted and annealed at 450 °C for 2 hrs. As can be seen from Fig. 4.12 the band around ~2000 cm^{-1} is observed for Ge samples implanted with H. This band can be deconvoluted into three bands around 1990, 2020, and 2050 cm^{-1} [44-48]. These three feature correspond to the stretching of Ge-H bonds in GeH_n ($n=1$-3) groups. The very weak Ge-H band is also observed for bulk un-implanted Ge. This indicates some small presence of hydrogen due to the wafer growth. The Ge-H band increases in intensity and shifts to lower frequency after annealing of implanted sample, which is in agreement with the evolution of Ge-H band presented in Ref. [49]. Additional weak bands observed at low frequency in Fig. 4.12 are not related to Ge-H bonds but they are not fully compensated rotational bonds of water vapour present in the chamber.

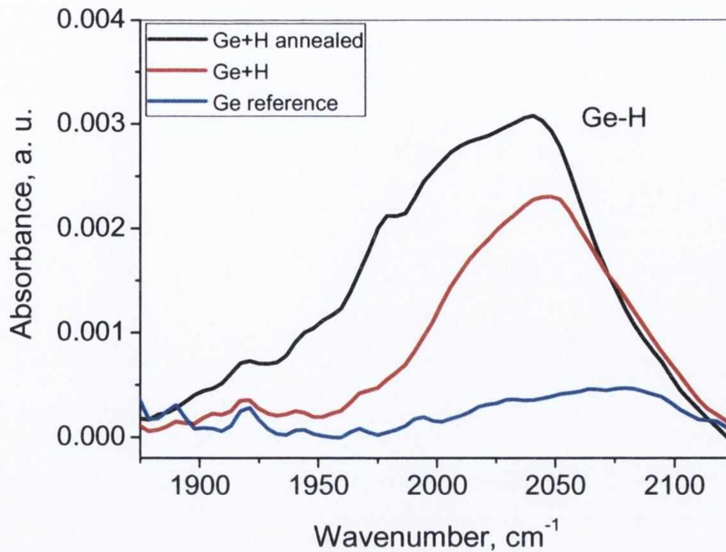

Fig. 4.12. Infrared absorption spectra of Ge substrate, Ge implanted with H and Ge implanted with H after annealing.

4.4.2. Helium implanted samples

Two Ge samples implanted with the helium dose of 3×10^{16} atoms/cm^2 were also analysed by Raman spectroscopy and SRP. Figure 4.13 presents the SEM and optical microscopy images of the sample surface. The bevelling region is clearly observable in Fig. 4.13 (a). In Figures 4.14 and 4.15, the maps of Raman linewidth and carrier concentration are plotted for these samples annealed at 400 ^{o}C (sample B3) and annealed at 300 ^{o}C and then at 600 ^{o}C (sample B2). Fig. 4.14 shows a SRP peak of 1×10^{17} acceptors at the projected range and a second peak, deeper into the substrate. Figure 4.15 shows that these deeper features disappear after 600 ^{o}C annealing. For silicon, it has been observed that helium implants produce a slight increase in self interstitials, which anneal out at moderate heat [50]. It is also known that interstitial defects are more likely to occur beyond the projected range, while vacancies generally occur in the region above the projected range [51]. Raman linewidth mapping on the sample annealed at 400ºC shows a corresponding peak at the projected range (see Fig. 4.14). The increase in FWHM of the Ge-Ge band about ~1.25 cm^{-1} is observed at the projected range. Any significant changes in linewidth of the Ge-Ge peak are not detected for the second SRP peak with a carrier concentration of ~10^{16} atoms/cm^3. For

sample B3, the carrier concentration decreases at the projection range to 2×10^{15} atoms/cm^3. No evidence of amorphization, due to the ion implantation was observed.

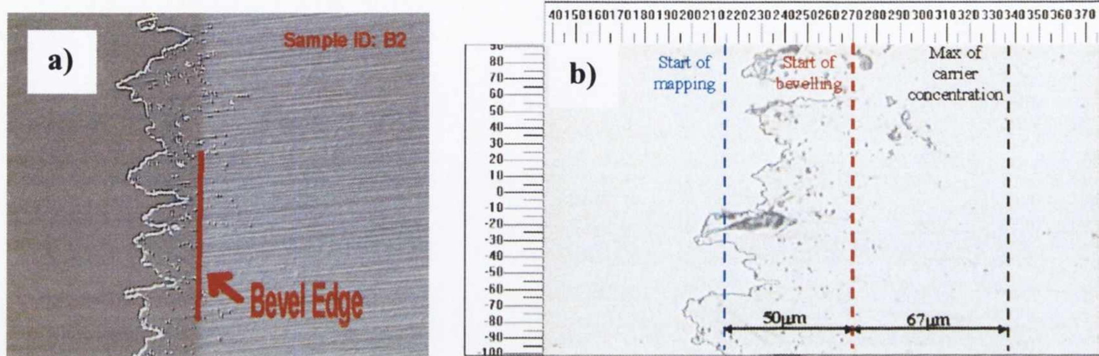

Fig 4.13. (a) SEM image and optical microscopy image of Ge sample implanted with helium (sample B2).

As with silicon, it is very difficult to induce blistering through helium implantation in germanium, even at doses of several $\times10^{17}$ atoms/cm^{-2}. Note that the background antimony concentration estimated from SRP graphs for the helium implanted sample B3 (~2×10^{15} cm^{-3}) is higher than in the sample implanted with hydrogen shown in Fig. 4.8 (8×10^{14} cm^{-3}). Comparing the number of acceptors present after H and He implants and annealing at 600 °C, at first glance, the number of acceptors present appears lower for helium. However, the measured carrier concentration is the sum of background Sb concentration and shallow acceptors, and when the compensation by n-type Sb is deducted; the acceptor amounts are quite comparable. Figure 4.17 presents the Raman maps of peak position, linewidth and intensity of the Ge-Ge band for samples B2 and B3. The compressive stress and drop in the peak intensity are observed at the projection range for sample B2 whereas Raman mapping of sample B3 after annealing at 600°C does not show any significant changes in the Ge-Ge peak (see Fig. 4.12 (d-f)). Based on Raman mapping results, the middle of projected range (maximum damage) for sample B2 is observed at a depth of 0.33 µm, which corresponds exactly to the value obtained by SRIM simulation presented in Fig. 4.16.

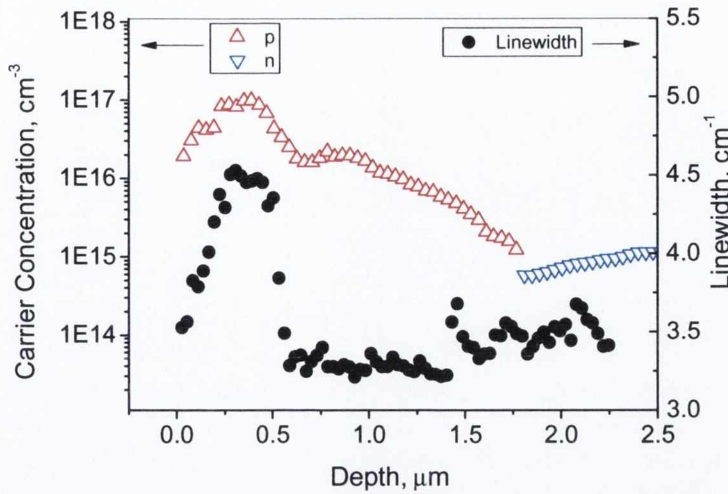

Fig. 4.14. Raman line width and carrier concentration, derived from SRP, vs. depth into the sample for a 3×10^{16} atoms/cm^3 helium implant into germanium after annealing at 400 °C (sample B2).

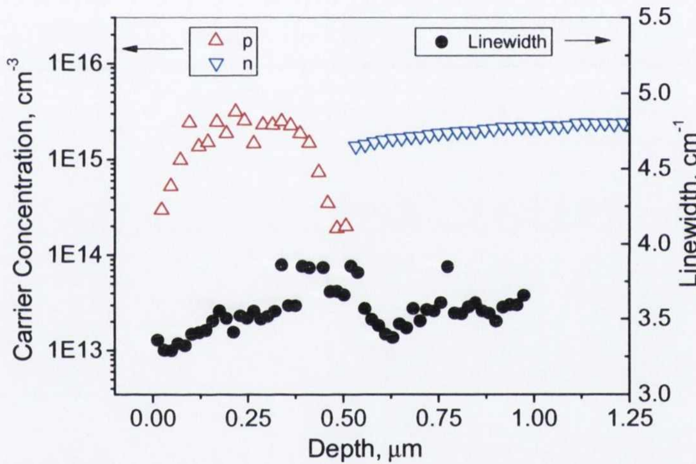

Fig. 4.15. Raman line width and carrier concentration derived from SRP vs. depth into the sample, for a 3×10^{16} atoms/cm^2 helium implant into germanium, after annealing first at 300 °C and then at 600 °C (sample B3).

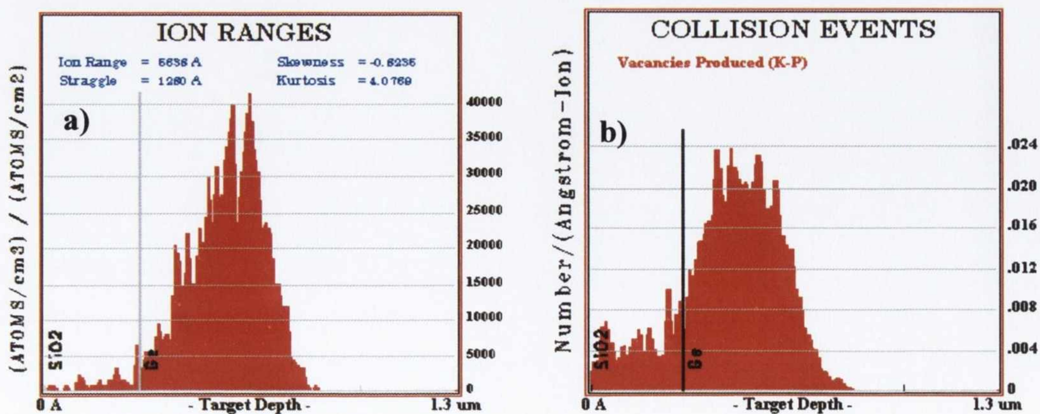

Fig. 4.16. SRIM simulation of helium ion distribution and damage in Ge versus depth in Ge.

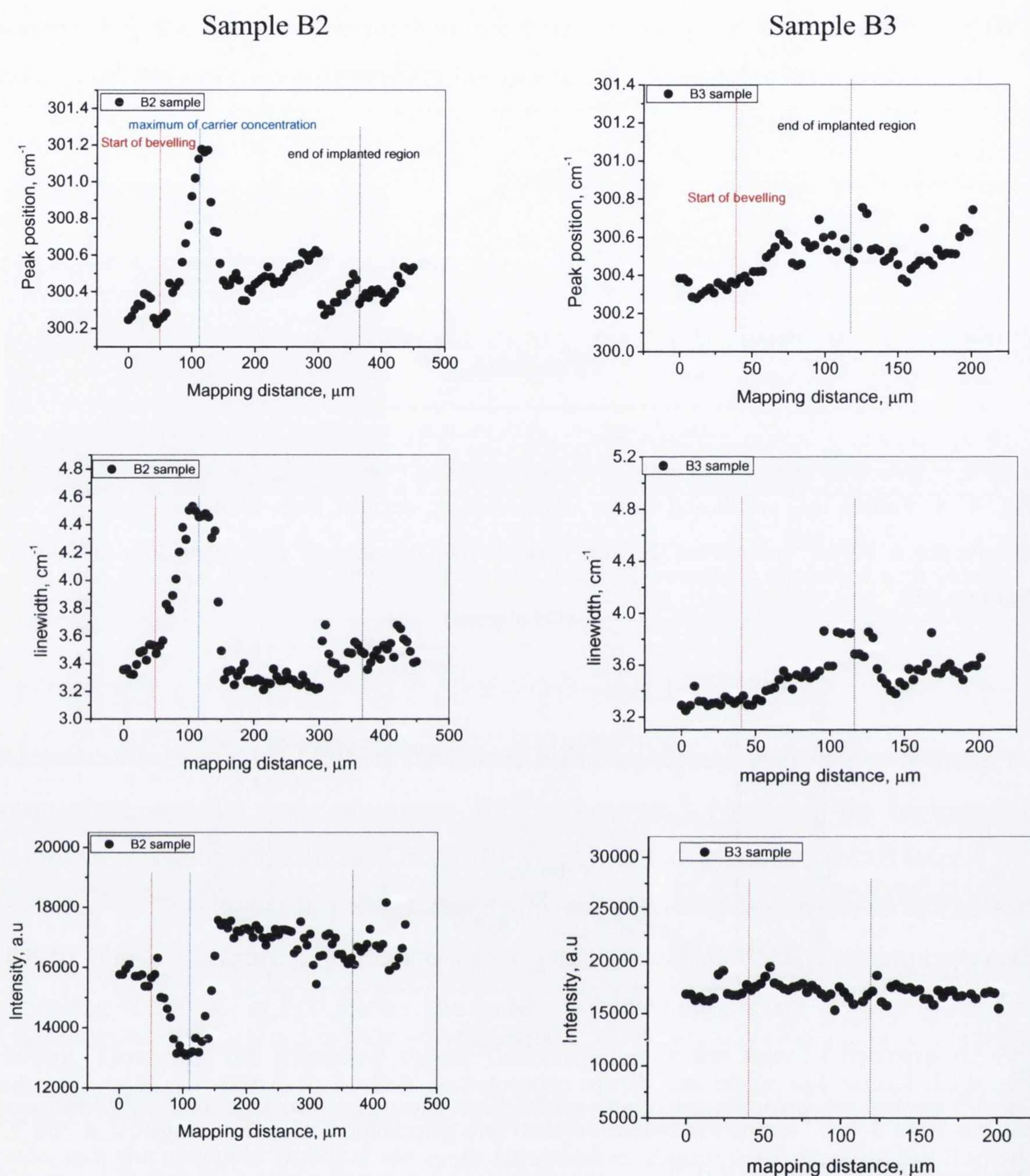

Fig. 4.17. Raman maps of the Ge-Ge peak position, linewidth and peak intensity of (a-c) sample B2 and (d-f) sample B3. Red and blue lines indicate the start of the bevelling and the middle of projected range, respectively.

Considering hydrogen and helium implants in Ge, the number of acceptor states present in the sample, in and around the projected range, after 300 °C /400 °C annealing is 3 times the number of ions implanted. Then, on annealing to 600 °C, this number drops by one order of magnitude. The exact nature of these more stable defects (e.g. whether V-H, V-O, V-Ge, V-Sb) is difficult to determine using SRP or Raman, but the Raman

results suggest that they are not amorphized germanium, but rather point defects left behind after the re-crystallisation process. Considering Figs. 4.10 and 4.17, the Raman linewidth suggests an intact crystal structure at the surface of the sample. Therefore, seeding of solid phase epitaxy could be provided from this top surface as well as the bulk. This has been reported as resulting in "clamshell defects" [52] where the two parallel re-growth planes meet, around the projected range of implant. Whatever the nature of the complexes remaining after annealing at 600 ^{o}C, they are not detectable with Raman, due to their low concentrations. Comparing Fig. 4.8 with Figs. 4.14 and 4.15, it is perplexing that the number of acceptors produced by implantation of the same atomic dose is similar for He and H, given that mass of He is 4 times the mass of H, and for these doses and energies, SRIM predicts the level of damage produced by helium to be 20 times higher than that for hydrogen. A tentative suggestion might be that, for He there should be few if any chemical interactions between the implanted ion and host atom, therefore all the acceptor states remaining after annealing at 400 ^{o}C are due to damage alone. Comparing 400 ^{o}C and 600 ^{o}C, annealing causes a marked reduction in end of range effects for He, which may be related to damage.

4.4.3. Germanium on sapphire

Ge layers after smart cut transfer are analysed in this section. While germanium can be bond directly to sapphire after transfer, it is necessary to employ an intermediate dielectric layer to ensure good electrical properties at the buried interface to germanium. It is preferable that the intermediate dielectric layer is deposited on the germanium before bonding. Thin ~ 20 nm SiO_2 layers give less stable interfaces, which is attributed to the out diffusion of GeO through the thin oxide resulting in an increase in fast surface states and a reduction in mobility. To ensure the absence of microvoid generation during the post bond anneal it is preferable to employ a thick SiO_2 layer at the bond interface to allow out-diffusion of water vapour [53]. Thus, in circumstances where it is not appropriate to deposit a thick layer on the germanium, SiO_2 is also deposited on the sapphire surface before bonding. This is the case in the present investigation. The structural geometry of devices before the growth of the SiO_2 on the top of Ge layer is presented in Fig. 4.18.

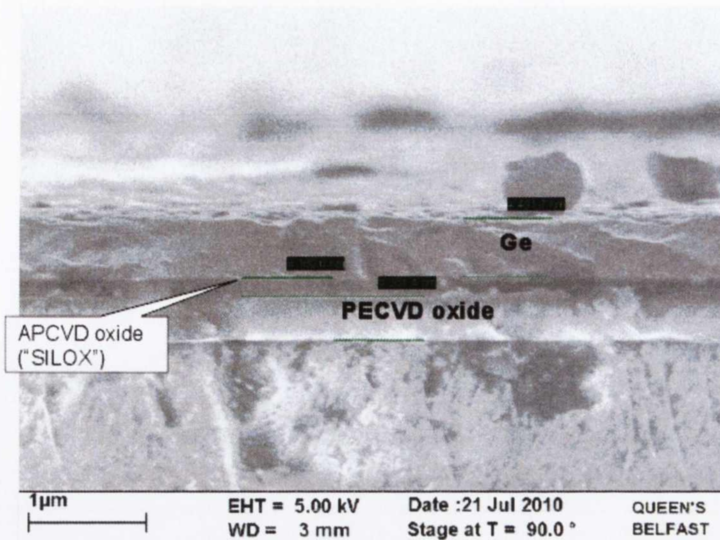

Fig. 4.18. SEM image of cross-section of GeOS device.

Figure 4.19 presents the optical microscopy images of the bevelled regions of the GeOS samples annealed at (a) 600 °C and (b) 800 °C. Single-spot Raman measurements were taken from different spots of bevelled sample Ge600C: a), b), c) correspond to germanium, d) sapphire, e) residue on the sample, and f) the top oxide layer. The strongest Raman signal is observed for the Ge layer with SiO_2 layer on the top which can be caused by interference and multiple reflection of the laser light in the oxide layer (see Fig. 4.20 (f)). Raman spectra *a,b,c* from Fig. 4.21 were taken at different locations on the Ge layer. No Raman feature is observed in the frequency range of the Ge-Ge peak in spectra *d* and *e*. The Raman spectra *d* was taken from sapphire and the spectra *e* was taken from residue left after the bevelling process. The peak position, intensity and linewidth of the Ge-Ge band from spectra *a-f* are presented in Table 4.2.

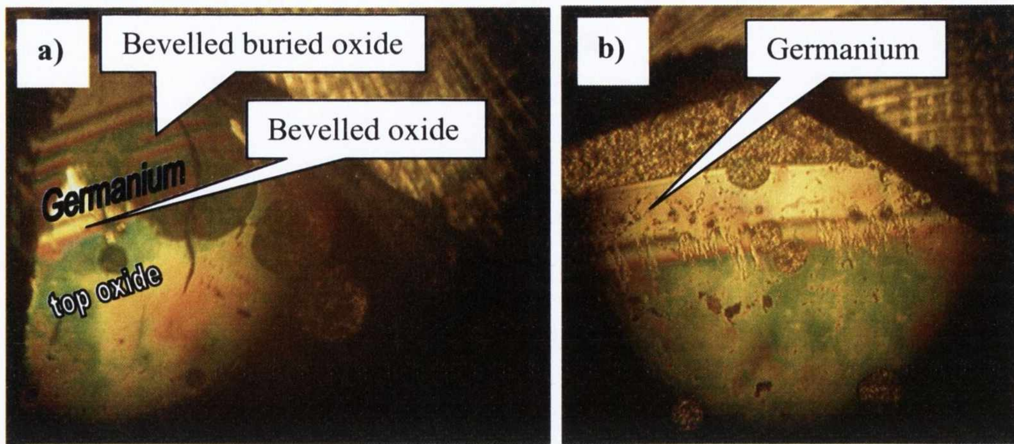

Fig. 4.19. The optical microscopy image of (a) the corner and (b) the edge of the bevelled sample.

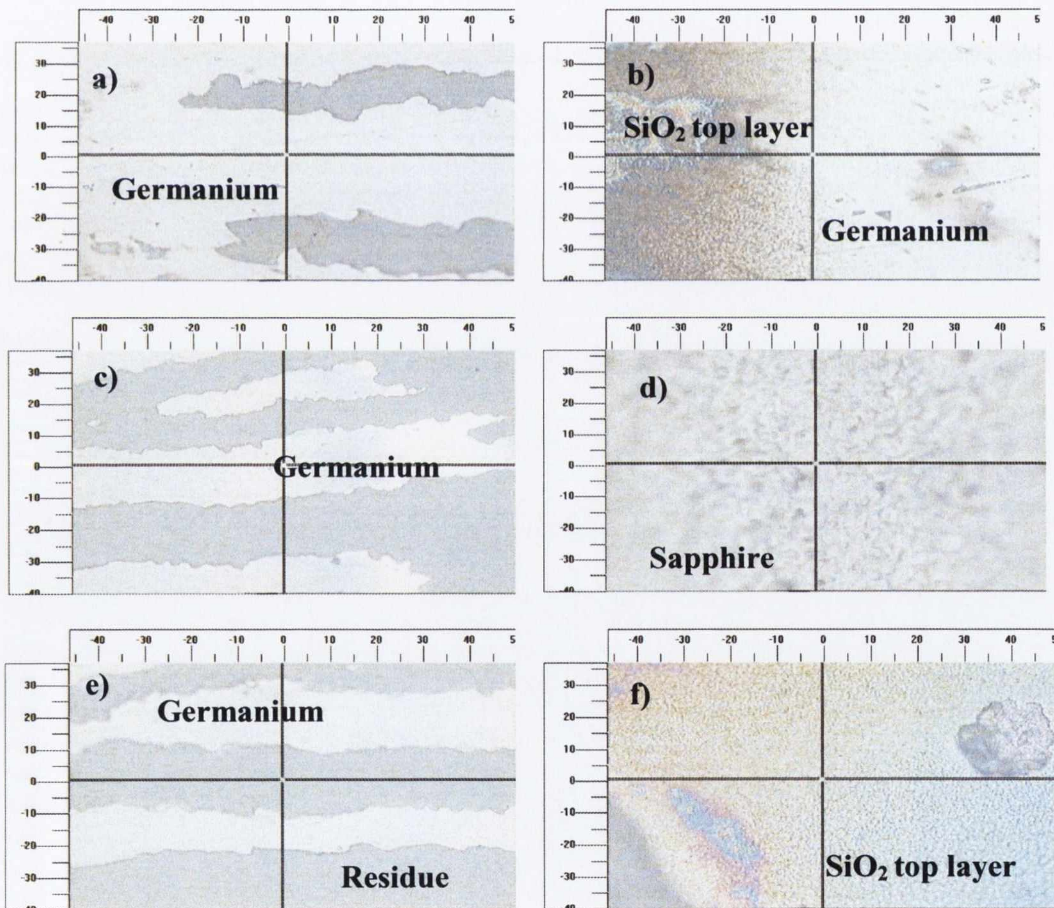

Fig. 4.20. Optical microscopy images of different parts of sample Ge600C.

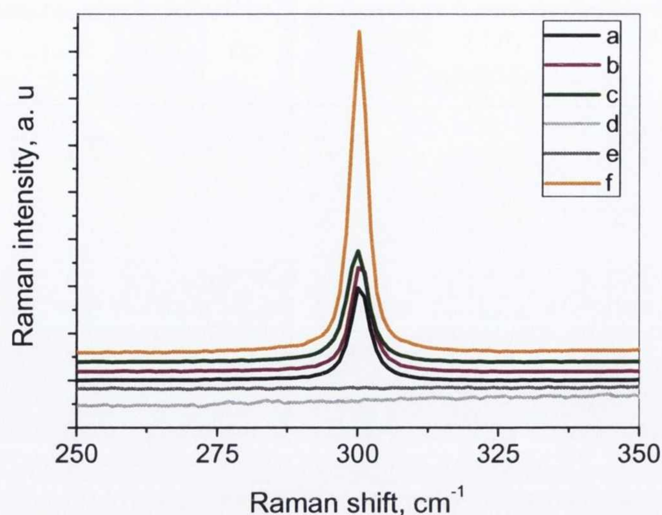

Fig. 4.21. Raman spectra taken from different spot of sample Ge600 (see pictures above).

As can be seen from Table 4.2, the FWHM of the Ge-Ge peak varies from 3.5 cm^{-1} to 4.5 cm^{-1}, which indicates good crystalline quality of the Ge layer. Similar results from single spot measurements were obtained from sample GeOS annealed at 800 ^{o}C (sample Ge800C). Raman spectra from different spots of the sample are presented in Fig. 4.22 (a-d). The most intense Ge-Ge peak is detected for the spectrum *a* due to the enhancement of the Raman signal in the oxide layer. The smallest peak intensity and the largest linewidth of the Ge-Ge band are observed for the spectrum *d*, which correspond to the bottom side of the Ge layer. Tab. 4.3 presents the peak position, intensity and linewidth of the Ge-Ge band for sample Ge800C.

Table 4.2. The peak position, intensity and linewidth of the Ge-Ge band for sample Ge600C.

Measurements	**The Ge-Ge peak**		
	Peak position, cm^{-1}	**Peak intensity, a.u.**	**Linewidth, cm^{-1}**
a	300.4	10106	3.9
b	300.5	11657	4
c	299.9	11882	4.45
d	-	-	-
e	-	-	-
f	300.1	34142	3.43

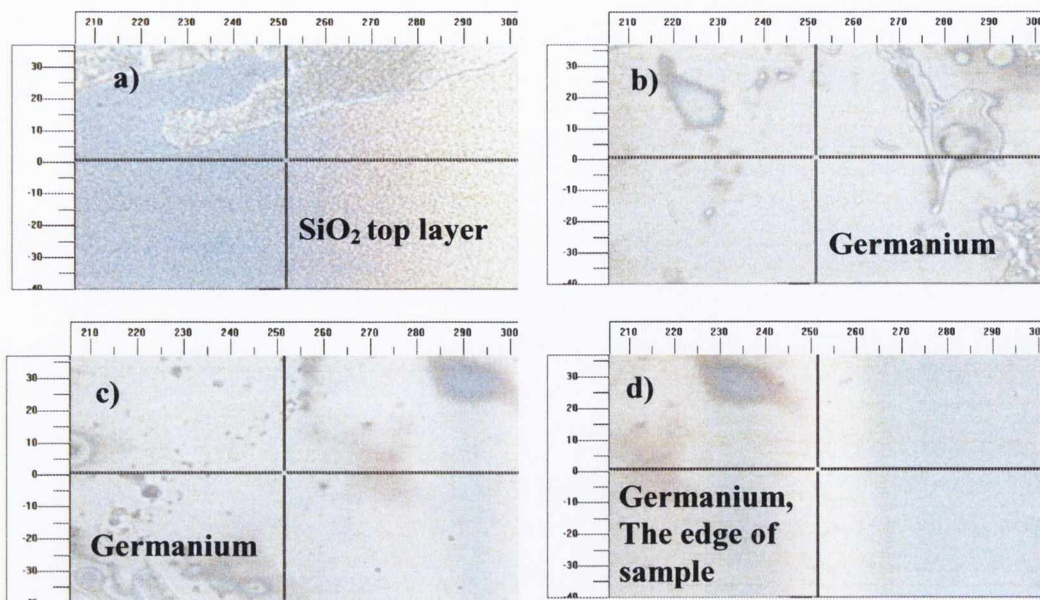

Fig. 4.22. Optical microscopy images of different locations of sample Ge800C.

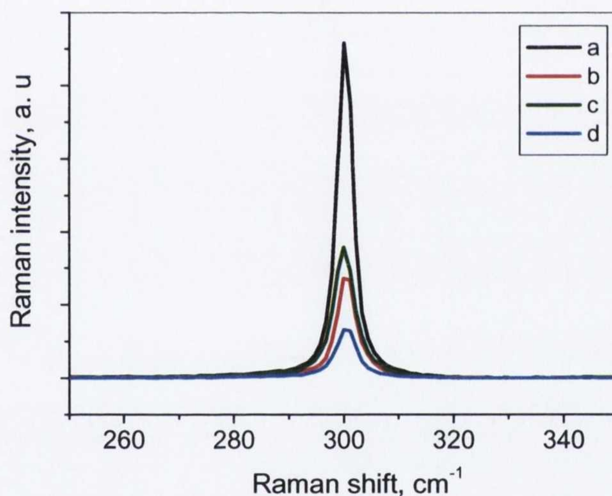

Fig. 4.23. Raman spectra taken from different spot of sample Ge800C (see pictures above).

Table 4.3. The peak position, intensity and linewidth of the Ge-Ge band for the sample Ge800C.

Measurements	The Ge-Ge peak		
	Peak position, cm^{-1}	Peak intensity, a. u.	Linewidth, cm^{-1}
a	300.3	23374	3.3
b	300.6	7204	3.9
c	300.1	8971	4.1
d	300.5	3446	4.2

The aim of this study is to investigate the structural uniformity and quality across the Ge layer after the layer transfer. For this purpose, Raman line mapping measurements were applied. Sample Ge600C was scanned on the bevelled area at a distance from 0 to 400 μm with 5 μm increments, while sample Ge800C was mapped from 0 to 350 μm with a 4 μm step size. The optical microscopy images of both GeOS samples with mapped lines across the Ge layer samples are presented in Figure 4.24.

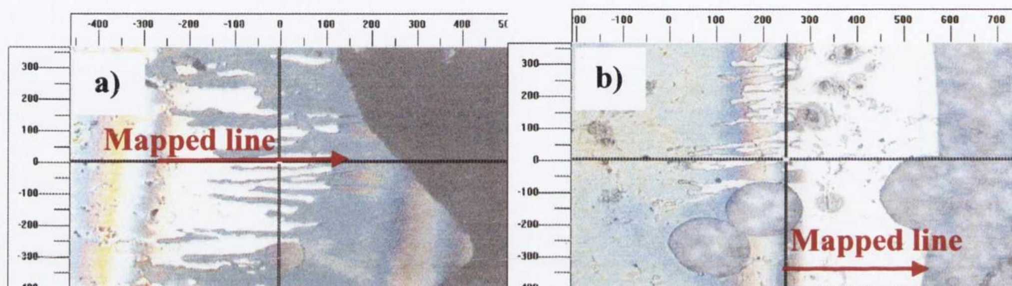

Fig. 4.24. Optical microscopy images of bevelled samples: (a) Ge600C and (b) Ge800C. The red arrows correspond to the lines mapped with a Raman spectroscopy.

Figure 4.25 presents the Raman maps of the Ge-Ge peak position, linewidth and peak intensity of GeOS samples annealed at 600 °C and annealed at 800 °C. Blue and green lines indicate two interfaces SiO_2/Ge and SiO_2/sapphire respectively. Experimental points at the distance range from 20 μm to 320 μm in the maps (a-c) correspond to Ge layer for the sample Ge600C. As one can see from Figs. 4.25 (a-c), in this mapping range the Ge-Ge Raman peak shows a high uniformity in its properties. The linewidth of the Ge-Ge peak is around ~4 cm^{-1} with the peak position at 300.5 cm^{-1}, which indicates good crystalline quality of a relaxed Ge layer after transfer. Different behaviour of the Ge-Ge Raman band is observed at the mapping distance from 320 cm^{-1} to 400 cm^{-1}. This region corresponds to the Ge/buried oxide interface, buried oxide and sapphire. At the distance of 320 cm^{-1} to 375 cm^{-1}, an increase in FWHM and peak position of the Ge-Ge is observed. This indicates that the interface between the Ge layer and the buried SiO_2 is not good quality. In addition, the Raman spectra of amorphous Ge were detected at this region (Fig. 4.26). The Ge samples with SiO_2 capping layer, implanted and annealed were investigated in order to find out what causes the amorphization of Ge. Raman measurements revealed that amorphization of Ge is not

due to implantation itself, or to the annealing process of Ge/SiO_2 sample. We believe that disorder of the Ge lattice can be introduced at the level of layer transfer when implanted Ge is bonded to the substrate. But to prove this assumption, further investigation is needed.

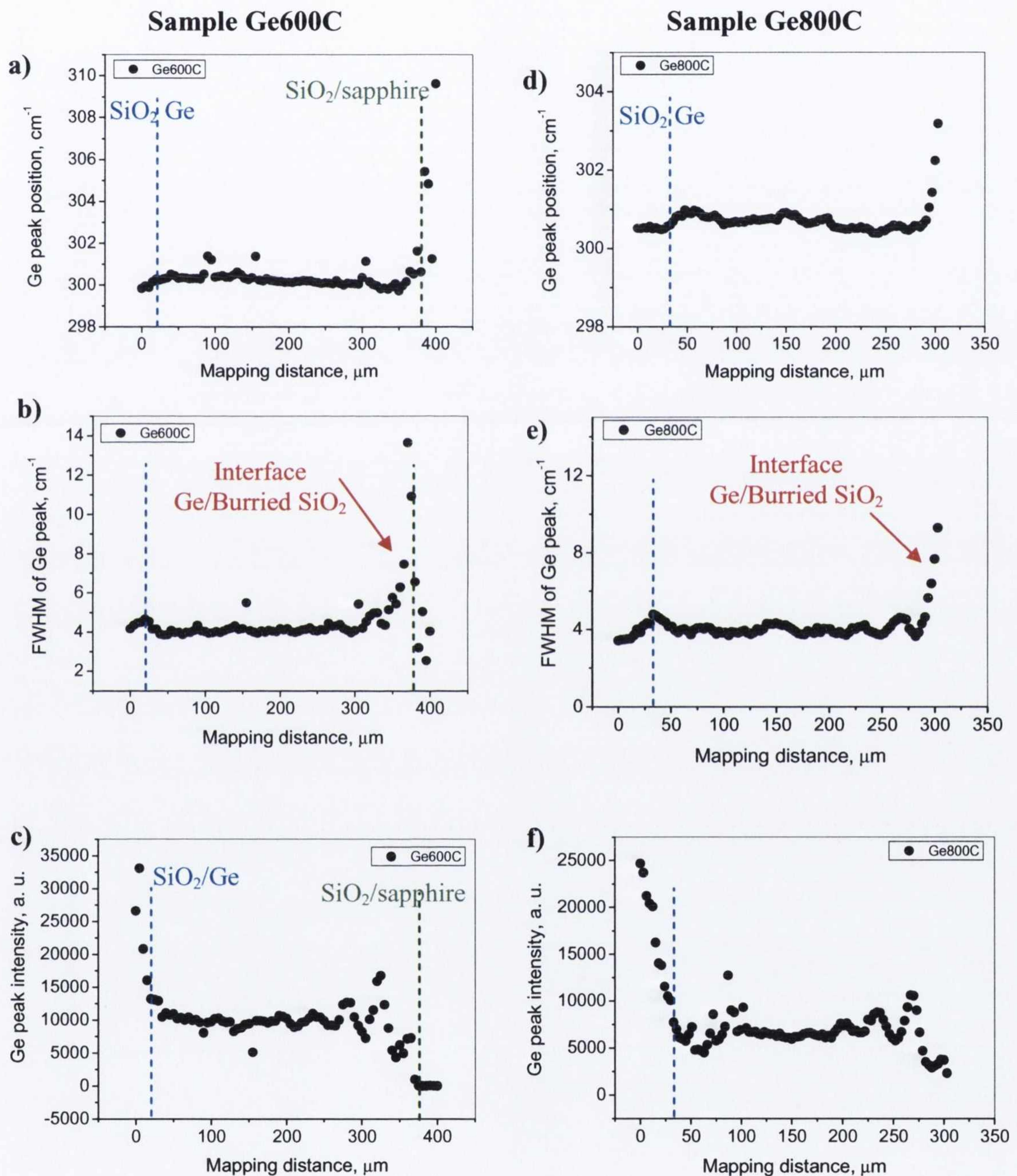

Fig. 4.25. Raman maps of the Ge-Ge peak position, linewidth and peak intensity of sample GeOS annealed at (a-c) 600ºC and (d-f) 800ºC. Blue and green lines indicate two interfaces SiO_2/Ge and SiO_2/sapphire respectively.

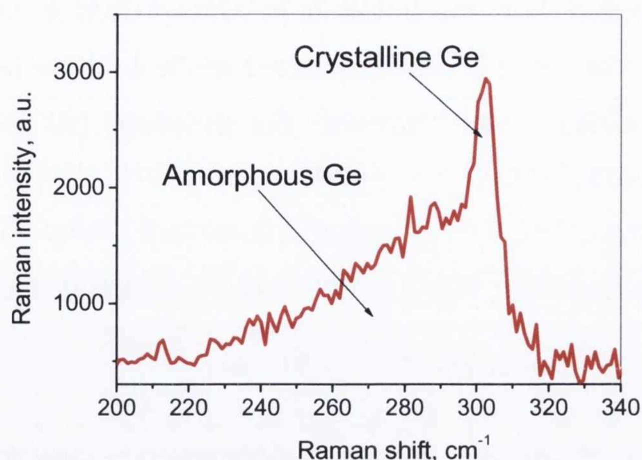

Fig. 4.26. Raman spectrum of Ge structure in both phases: crystalline and amorphous.

4.5. Conclusions

For the first time, Raman analysis on bevelled, H_2 and He implanted germanium samples are presented in this work. It has been shown that the bevelling of a Ge sample allows for Raman probing with nano-scale depth profile. The tensile stress and increase in linewidth (~ 2.4 cm^{-1}) of the Ge-Ge Raman peak is observed at the projected range for the Ge sample implanted with a high hydrogen dose (6×10^{16} molecules/cm^2) without any subsequent anneals. This indicates structural damage at the projected range due to ion implantation, which is also observed in the optical microscopy image. Less structural damage and no stress was detected for a Ge sample implanted with 3×10^{16} atoms/cm^2 after annealing at 450 ºC. In addition to this, the influence of annealing temperature on structural damage is investigated with Raman line mapping technique. It is shown, that annealing at 200 ºC does not introduce any decrease of defects at the projected range in H implanted Ge, while after annealing at 600 ºC, the Ge structure is fully recovered and the Ge-Ge Raman peak shows properties similar to a good quality bulk Ge wafer. An absence of structural defects after annealing at 600 ºC is also observed for Ge implanted with equivalent helium dose. No evidence of amorphization, due to hydrogen and helium implantation is observed. A comparison and correlation of the electrical and structural properties of implant-related defects has been performed for both hydrogen and helium implanted germanium samples. SPR results show that the

maximum of the carrier concentration is at the middle of projected range (~330 nm) for sample 2 and B2 annealed at 450 ^{o}C. The maximum structural damage detected with Raman line mapping corresponds exactly to this maximum carrier concentration, which is in agreement with presented SRIM simulations. Different behaviour is observed for p-type Ge implanted with H_2 without any subsequent anneals. Since the implant was not activated, SRP shows a decrease in mobility in the implanted area. Using SRP, it has been found that, for both ion species, a quantity of 1×10^{16} defects/cm^2 electrically active defects still remain after annealing at 600 ^{o}C. Raman results show that, at 600 ^{o}C, the crystal damage has been repaired, which suggests that these remaining acceptor states are due to the point defects. The Ge layers after smart cut transfer are also investigated in this work. It has been shown that a 500 nm thick Ge layer on Sapphire has a good crystalline quality, except the Ge/buried SiO_2 interface where amorphous Ge has been detected.

References

1. R. Hull, J. C. Bean, Germanium silicon: Physics and materials, Semiconductors and Semimetals, San Diego: academic, 1999
2. M. Bruel, B. Aspar, B. Charlet, C. Maleville, T. Poumeyrol, A. Soubie, A. J. Auberton-Herve, J. M. Lamure, T. Barge, F. Metral, S. Trucchi, IEEE International SOI Conference Proceedings (Cat. No.95CH35763), p 178-9, 1995
3. X.Q Feng, Y. Huang, International Journal of Solids and Structures 41, 4299 (2004)
4. IBM Advances Chip Technology With Breakthrough For Making Faster, More Efficient Semiconductors, Compound Semiconductor Magazine Issue 4 No. 7 (1998)
5. A. Marshall & S. Natarajan, SOI design: analog, memory and digital techniques, Cluwer Academic Publisher, USA, 2002
6. R.E. Hurley, H. Wadsworth, H.S. Gamble, Vacuum 87, 1207 (2007)
7. H. S. Gamble, Materials Science in Semiconductor Proces. 11, 195 (2008)
8. J. C. Tsang, G. S. Oehrlein, I . Haller, J. S. Cluster, Appl. Phys. Lett. 16, 589 (1985)
9. K. Ishioka, K. G. Nakamura, M. Kitajima, Solid St. Commun. 96, 387 (1995)
10. K. Ishioka, K. G. Nakamura, M. Kitajima, J. Materials Science Lett. 16, 281 (1997)
11. K. K. Tiong, P. M. Amirtharaj, F. H. Pollak, D. E. Aspnes, Appl. Phys. Lett. 44, 122 (1984)
12. G. Braunstein, D. Tuschel, S. Chen, S. T. Lee, J. Appl. Phys. 66, 3515 (1989)
13. T. Mitani et al, J.Appl. Phys. 100, 073511 (2006)
14. R. M. B. Agaiby et al, J. Appl. Phys. 104, 013507 (2008)
15. R. Srnanek, A. Vincze, J. Kovac, I. Gregora, D. S. Mc Phail, V. Gottschalch, Mater. Science and Eng. B, Volumes 91-92, 87 (2002)
16. A. Ito, M. Ichimura, A. Usami and T. Wada. J. Appl. Phys. 72, 2531 (1992)
17. M. Xu, X.Q. Feng, Theoretical and Applied Fracture Mechanics 42, 295 (2004)
18. M. K. Weldon, M. Collot, Y. J. Chabal, Appl. Phys. Lett. 73, 3721 (1998)
19. K. Henttinen, T. Suni, A. Nurmela, Nucl. Instrum. Meth. B 190, 761 (2002)
20. A. P. Cracknell, Crystals and Their Structures. Pergamon, Oxford, 1969

21. S.M. Myers, H.J. Stein and D.M. Follstaedt, Phys. Rev. B, 51, 9742 (1995)
22. S.M. Myers, D.M. Follstaedt, H.J. Stein and W.R. Wampler, Phys. Rev. B, 47, 13380 (1993)
23. J. Vanhellemont and E. Simoen, Electrochem. Soc. Trans., 3, 451 (2006)
24. J.M. Zahler, A. Fontcuberta I Morral, M.J. Griggs, Harry A. Atwater and Y.J. Chabal, Phys. Rev. B, 75, 035309 (2007)
25. N. Desrosiers, A. Giguere, B. Terreault, M. Chicoine and F. Schiettekatte, Nucl. Inst. Methods Phys. Res. B, 266, 1971 (2008)
26. M. L. David, J. F. Barbot, S. Rousselet, F. Pailloux, D. Babonneau, MF. Beaufort, L. Pizzagalli, M. Drouet, E. Simoen, C. Claeys, ECS Transactions, 16, 163 (2008)
27. M. Budde, B. Bech Nielsen, P. Leary, J. Goss, R. Jones, P. R. Briddon, and S. J. Breuer, S. Öberg, Phys. Rev. B 57, 4397 (1998)
28. M. Hiller, E. V. Lavrov, and J. Weber, Phys. Rev. B 71, 045208 (2005)
29. S. W. Bedell, W. A. Lanford, J. Appl. Phys. 90, 1138 (2001)
30. T. Akatsu, K. K. Bourdelle, C. Richtarch, B. Faure, and F. Letertre, Appl. Phys. Lett. 86, 181910 (2005)
31. V. V. Kozlovskii, V. A. Kozlov, V. N. Lomasov, Semiconductors 34, 129 (2000)
32. J. Wang, G. H. Xiao, H. L. Tu, Microelectron. Eng. 66, 314 (2003)
33. A. Giguere and B. Terreault, Surf. Coat. Tech., 201, 8205 (2007)
34. M.F. Beaufort, S.E. Donnelly, S. Rousselet, M.L. David, J.F. Barbot, Nucl. Instrum. and Meth. in Phys. Research B 242, 565 (2006)
35. M. Cai, J. Appl. Phys., 92, 3388 (2002)
36. J. K. Lee, J. Appl. Phys., 96, 280 (2004)
37. F. D. Auret, P. Janse van Rensburg, M. Hayes, J. M. Nel, W. E. Meyer, S. Decoster, V. Matias, A. Vantomme, Appl. Phys. Lett. 89, 152123 (2006)
38. M. Stavola, 5th Int. Symp. Adv. Sci. Tech. of Semi. Mat., Koma, Hawaii USA, Nov.10-14 (2008)
39. C.G. Van de Walle, Physica B 170, 21 (1991)
40. C.G. Van de Walle, J.R. Weber, A. Janotti, Thin Solid Films 517, 144 (2008)
41. V. Markevich, L. Dobaczewski, K. Bondenielsen, V. Litvinov, A. Petukh, Y. Pokotilo, N. Abrosimov, A. Peaker, Thin Solid Films 517, 419 (2008)

42. R. Brennan, D. Dickey, Selecon Labs Technical Note, Solecon Laboratories, Inc., San Jose, California
43. C. Su, C. S. Tsai, E. E. Lin, K. H. Chen, J. K. Wang, J. C. Lin, Surf. Science 445, 139 (2000)
44. D. Comedi, F. Dondeo, I. Chambouleyron, Z. L. Peng, and P. Mascher, J. Non-Cryst. Solids 266–269, 713 (2000)
45. M. Cardona, Phys. Status Solidi 118, 463 (1983)
46. M. N. Makadsi, M. F. A. Alias, A. A. Essa, and H. R. Al-Azawi, Renewable Energy 28, 975 (2003)
47. M. Saitou, K. Sakae, and W. Oshikawa, Surf. Coat. Technol. 162, 101 (2003)
48. A. Arras, P. Benzi, E. Bottizzo, C. Demaria, J. Appl. Phys. 102, 104905 (2007)
49. J. M. Zahler, A. Fontcuberta i Morral, M. J. Griggs, H. A. Atwater, Y. J. Chabal, Phys. Rev. B 75, 035309 (2007)
50. G.F. Cerofolini, Materials Science and Engineering: R: Reports, 27, 1 (2000)
51. J. D. Plummer, P. B. Griffin, Proceed. of the IEEE, 89, 240 (2001)
52. D. P. Hickey, Z. L. Bryan, K. S. Jones, R. G. Elliman, and E. E. Haller, Appl. Phys. Lett. 90, 132114 (2007)
53. Y. L. Chao, R. Scholz, M. Reiche, U. Gosele, J. C. S. Woo, Jap. J. Appl. Phys., 45, 8565 (2006)

5. Composition and strain analysis in thin $Si_{1-x}Ge_x$ virtual substrates using micro-Raman spectroscopy and X-ray diffraction

5.1. Introduction

Silicon Germanium (SiGe) offers an alternative to pure silicon technology as a substrate material. However, no suitable bulk SiGe substrates are available, so strain relaxed buffers (SRB) must be grown onto bulk silicon substrate. These are termed virtual substrates as they consist of an epitaxially grown, relaxed SiGe layer on the top of standard Si substrate. The SiGe virtual substrates are applied as global strain platform for n-MOSFETs [1]. In SiGe buffer layers, a high Ge content and a high degree of relaxation are very essential because they provide the required strain in the Si channel as a quantum well for electrons. Strain relaxed buffers are preferred to be thin for improved heat dissipation in MOSFETs, for better compatibility with devices of low dimensions in integrated circuits, as well as for lower time and energy consumption during their production. Also, the quality of virtual substrates is very critical for the performance of the final device. The SRB must have a smooth surface morphology and low defect density. Lattice mismatch between Si and SiGe causes strain relaxation by introduction of misfit dislocations in the interface plane, and especially undesired threading dislocations in the bulk of the layers. The latter can be reduced by special additional measures connected mostly with the growth of much thicker graded or constant composition layers, or with additional ex situ treatment [2–4]. Thus SRB with required low thickness, high Ge content and high degree of relaxation is a rather ambitious aim. As a method to adjust mismatched SiGe buffer layers with the Si substrate, a controlled introduction of point defects during epitaxial growth was proposed in Ref. [5,6]. For thin SiGe SRB growth with high degree of relaxation, the point defect supersaturation was employed at the beginning of the SiGe buffer layer deposition, below the critical thickness [5,6]. This can be realised by extreme reduction of growth temperature or by in situ bombardment with Si^+ ions available in the MBE

chamber during the solid source MBE (first stage of growth) [7]. During the next epitaxy stage at a medium growth temperature (MT) of typically 550 °C, high point defect concentration should lead to the formation of prismatic dislocation loops (instead of dislocation arms threading through the whole layers), and so promote the early relaxation and lower threading dislocation density. The degree of relaxation can be adjusted by the choice of the very low temperature (VLT) step.

The industrial and research developments require metrology solutions for the characterisation and subsequent control of several important parameters in SiGe/Si and s-Si/SiGe/Si structures such as stress and strain in the s-Si layer as well as the Ge content (x) and relaxation factor (R) in the SiGe buffers. Raman spectroscopy and X-ray diffraction (XRD) are the only techniques which facilitate obtaining all the aforementioned parameters simultaneously [8]. Raman spectroscopy was applied widely for investigation of composition and stress in Si/Ge structures such as SiGe epitaxial layers [9-13], Si/Ge supper-lattices [14-17] and Ge/Si quantum wells and quantum dots [18,19]. For these structures the Ge content, x and strain, ε (or relaxation factor, R) can be obtained using three different methods of Raman data analysis. These are:

i) a frequency method, using set of the experimental equations obtained for the peak positions of Si-Si, Si-Ge and Ge-Ge modes,
ii) an intensity method, using the ratio of the integrated intensities of Si-Si, Si-Ge and Ge-Ge modes,
iii) and using thin Si-cap layer (or strained-silicon, s-Si, layer), deposited on the top of SiGe, layer along with coherence conditions for these two layers.

We note, that Raman investigations were applied in the past for the analysis of composition and strain for bulk SiGe [9,10], as well as to samples deposited by different variations of CVD technique (e.g. UVCVD [7]) and liquid-phase epitaxy [11]. Quite recently micro-Raman technique was applied for samples deposited by Reduced Pressure CVD [12] and plasma enhanced CVD (LEPECVD) [13]. However, a very small number of works was devoted to micro-Raman investigation of samples deposited by MBE technique, and most of them were dealing with Si/Ge supperlattices [14-17]. It is worth noting that most of the investigated SiGe samples were with thickness in the range of 300 to 4000 nm, and they were deposited on the top of step-graded or gradually graded $Si_{1-x}Ge_x$ buffer with x varied from 0 to the required value of x.

The main purpose of this work is to investigate the application of micro-Raman spectroscopy to very thin SiGe virtual substrates grown by mentioned above MBE

technique. In this chapter, the validity of the existing equations [8,10-13] obtained for Raman data analysis are tested for thin SiGe virtual substrates using independent evaluation of the Ge content and strain from XRD data. In addition to this, the strain Si layers grown on SiGe buffers were investigated. The strain and composition of s-Si and SiGe layers were calculated based on Raman results.

5.2. Structural properties of SiGe alloys

Silicon and germanium are group IV elements with 4 electrons in the outermost shell. They both crystallise in the cubic diamond lattice with the band gap of the pure elements and their alloys being indirect. A cubic unit cell of crystalline structure of Si and Ge is presented in Fig. 5.1. The parameters of the unit cell include the lattice constant a_{Si} = 0.54309 nm for Si and a_{Ge} = 0.5658 nm for Ge and the angles $\alpha=\beta=\gamma=$ 90°. The Si-Si bond length is 0.2352 nm and for Ge-Ge 0.2449 nm.

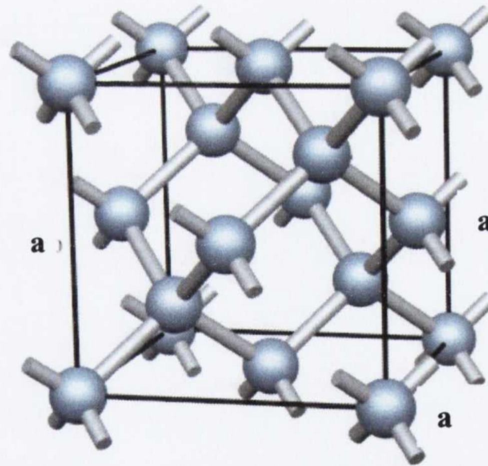

Fig. 5.1. A cubic unit cell of crystal structure of silicon and germanium.

Silicon and germanium are completely miscible forming $Si_{1-x}Ge_x$ solid solutions with x ranging from 0 to 1. The lattice constant of $Si_{1-x}Ge_x$ alloy, a_{SiGe}, can be determined by a linear interpolation of the parameters of the Si and Ge elements which is known as Vegard's law:

$$a_{SiGe}(x) = (1-x) \cdot a_{Si} + x \cdot a_{Ge} \tag{5.1}$$

Although for many applications the use of Vegard's law is practical, frequently, a deviation from Vegard's law has been observed experimentally [20,21]. To date, the most precise and comprehensive determination of bulk lattice parameters across the whole $Si_{1-x}Ge_x$ system has been carried out by Dismukes et al [20] including measurement of the variation of lattice parameters with temperature up to 800ºC for some alloys. Figure 5.2 presents the lattice parameters of $Si_{1-x}Ge_x$ alloys at 25°C for Ge content in the range of 0 to 100% taken from Dismukes [20]. The negative deviation from Vegard's law up to 3% is clearly observed in the range of Ge content from 20 to 80 at. %.

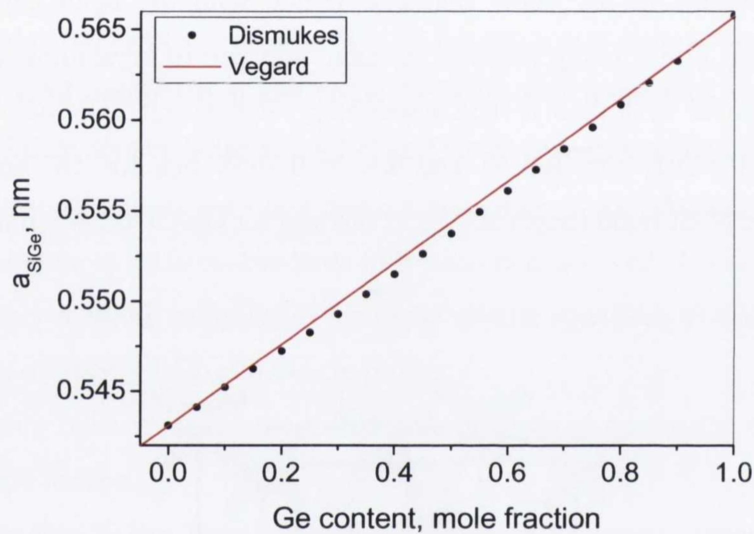

Fig. 5.2. Lattice parameter a_{SiGe} of $Si_{1-x}Ge_x$ alloy calculated using Vegard's and Dismukes law for Ge content varies from 0 to 100%.

By using the values given in [20] for x = 0%, x = 25%, and x = 100% a following parabolic relation for the $Si_{1-x}Ge_x$ lattice parameter as a function of Ge fraction x:

$$a_{SiGe}(x) = 0.5431\,(nm) + 0.01992 \cdot x\,(nm) + 0.002733 \cdot x^2\,(nm) \qquad (5.2)$$

can be delivered which approaches the experimental data with a maximum deviation of about 10^{-4} nm [22]. Differences in lattice parameters and in thermal expansion coefficients between the epitaxial layer and substrate introduced the strain within the

growing layer. If a thin $Si_{1-x}Ge_x$ film is grown on top of a Si film or Si substrate then the top $Si_{1-x}Ge_x$ layer is compressively strained (Fig. 5.3 (b)), while for the Si layer grown on SiGe film, the Si layer is tensile strained (Fig. 5.3 (d)). In both cases the strain is in the plane of the layer $\varepsilon_{||}$ but this strain also produces a perpendicular strain, $\varepsilon_{\perp}$, resulting in a tetragonal distortion to the lattice (Fig. 5.3 (b)) [23]. In isotropic elasticity theory the strains are related by Poisson ratio, ν, through:

$$\varepsilon_{\perp} = \frac{-2\nu}{1-\nu} \cdot \varepsilon_{\|} . \tag{5.3}$$

The biaxial strain in the plane of the interface between the strained layer and substrate is given by the lattice mismatch:

$$\varepsilon = \frac{a_{layer} - a_{sub}}{a_{sub}} \cdot 100\% \tag{5.4}$$

where, a_{layer} and a_{sub} denote the unstrained lattice constants of substrate and growing layer, respectively. Such a strain can only be sustained in thin layers, and relaxation in the form of misfit dislocations will occur for thick layers. An important criterion for growing strained layers without introducing misfit dislocations is that the strained layer should have a thickness below the critical value which can be reduced to [24]:

$$h_c \cong \left(\frac{0.55}{x}\right) \cdot \ln(10h_c) \tag{5.5}$$

$$h_c \cong 1.7793 \cdot x^{-1.237} \; nm . \tag{5.6}$$

As a result of biaxial tensile strain, carriers experience a lower resistance in the strained layer and typically have higher mobility (~50-70% higher for strain Si) in the channel direction [25]. The value of stress σ and ε are related to each other by the following equation:

$$\sigma = \frac{E}{1-\nu} \cdot \varepsilon \tag{5.7}$$

for a biaxial stress, where E is the Young's modulus of the grown film.

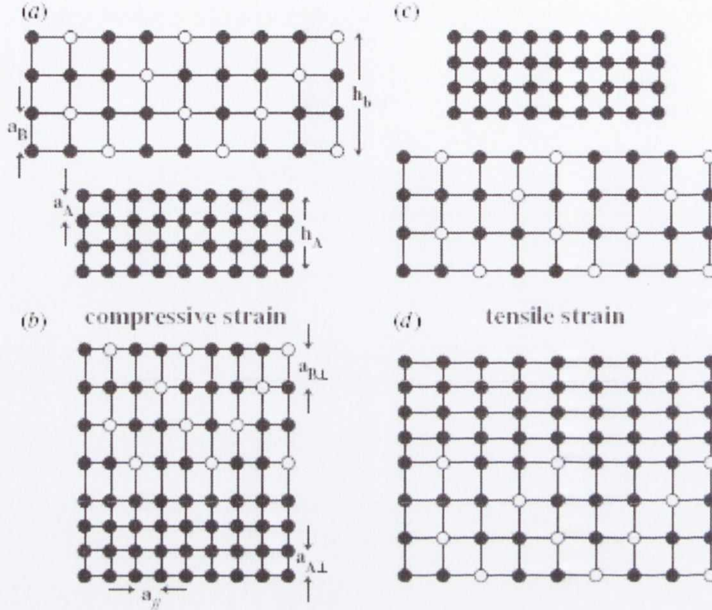

Fig. 5.3. (a) A schematic diagram of a thin $Si_{1-x}Ge_x$ film to be grown on top of a thin bulk silicon layer. (b) A schematic diagram showing the tetragonal lattice distortion when the two films from (a) are placed together with the top $Si_{1-x}Ge_x$ film being compressively strained. (c) A schematic diagram of a Si film to be grown on top of a $Si_{1-x}Ge_x$ film. (d) A schematic diagram of the two films in (c) placed together with the top film being tensile strained [23].

5.3. Experimental

5.3.1. Sample growth

For the growth of virtual substrates with ultra-thin (<100 nm) SiGe buffer layers of high Ge content, a method using point defect supersaturation by a two-step growth procedure in an MBE system is employed [6,7]. First stage at a very-low temperature (130 ºC – 200 ºC) serves for generation of point defects and their supersaturation in the growing layer. During the second stage, growth of an equal composition layer continues at a conventional MBE temperature of 550 ºC. Here, point defects accumulated at VLT

stage may condense and form dislocation loops which support the early relaxation. Interaction of point defects with dislocations introduced during plastic strain-relaxation can also improve the layer quality [26].

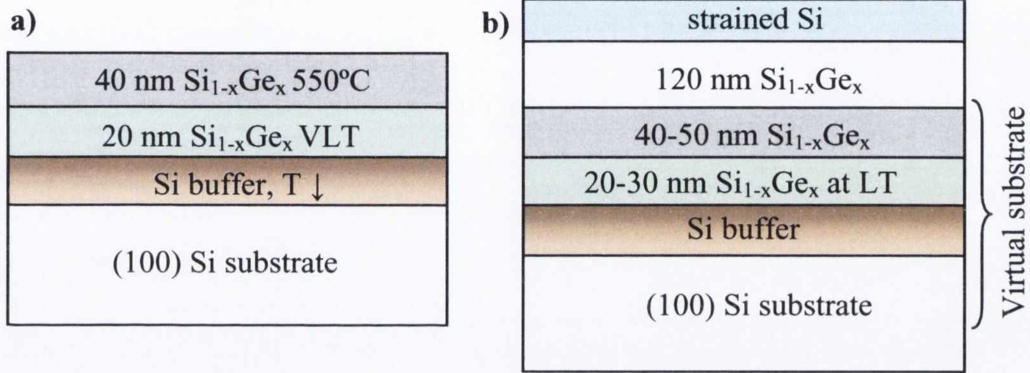

Fig. 5.4. Schematic of (a) SiGe virtual substrate and (b) of a strained-Si layer on an ultra-thin SiGe buffer including a buried part with point defect supersaturation at low temperature initiating the early relaxation.

Numerous samples, schematically shown in Figs. 5.4 (a) and 5.4 (b), are grown for the investigation of thin SiGe virtual substrates with Ge content ranging from 10 to ~ 50% as well as strained-Si grown on top of some of these virtual substrates (Fig. 5.4 (b)). The total thickness of the investigated SiGe buffer layer varies from 60 to 80 nm, including the VLT parts with thickness from 20 to 30 nm, respectively [6]. For s-Si samples, above the SiGe buffer layer, a SiGe intermediate layer is grown which, amongst others things, may serve for well doping and for spacer formation. In these series of samples, Ge content in the intermediate layers is the same as that of the SiGe buffer layer. The total thickness of the buffer layer combined with the intermediate layer does not exceed 200 nm. A 10–20 nm thick strained-Si layer is obtained at 500 °C under conditions providing coherent growth of pseudomorphic layers (sample parameters are given in Table 5.1).

Table 5.1. Thickness and composition for samples with s-Si on SiGe virtual substrate

Sample name	Thickness of s-Si, nm	SiGe layer composition
1797	20	$Si_{0.88}Ge_{0.12}$
1669	15	$Si_{0.8}Ge_{0.2}$
1799	12	$Si_{0.7}Ge_{0.3}$
1800	8	$Si_{0.6}Ge_{0.4}$

5.3.2. Raman measurements and analysis

Unpolarized Raman spectra were registered at room temperature in backscattering geometry using a RENISHAW 1000 micro-Raman system equipped with a Leica microscope. Some additional measurements were also performed on inVia Renishaw MicroRaman System. Data was registered at excitation wavelengths of Ar^+ ion laser at 514.5, 488 and 457 nm and a 325nm HeCd laser with inVia system for investigation of samples with s-Si. Laser light was focused on the sample through the x50 magnification microscope objectives which provide a laser spot size in the range ~1-3 μm. The scattered light from the sample is collected through the same microscope and directed through a spectrometer. It is then detected with a charge-coupled device (CCD). The laser power was kept between 3 and 10 mW to prevent samples heating and as a result an unwanted peak position shift. Before measurements the influence of laser power on the linewidth and the peak position was checked on one of the sample from series and was chosen at the level which did not affect the aforementioned spectra parameters. For the majority of samples the data were collected at 3-5 different locations on the sample, no significant variance was observed, with average values well within experimental error limits.

Raman spectra measured for numerous samples with x varied in the range of 0.1-0.5 and with relaxation factors in the range 20-100% were analysed in order to determine in the most accurate manner the peak position, the peak intensity and the linewidth of phonon modes. Renishaw Wire software allows Raman peaks to be fitted with a variety of inbuilt functions for different peak shapes. To determine the Ge content and strain from the set of equations for Si-Si, Si-Ge and Ge-Ge vibrational modes (as described in the next Section), the position of these peaks must be measured with a high accuracy. Two factors enable us to do so. A position of Si-Si peak from Si

substrate was used as an internal reference for thin SiGe layers for visible excitation and a position of plasma line for UV excitation. All peaks from SiGe layer are fitted with asymmetrical function [22], while Si-Si peaks for s-Si and Si substrate are fitted by Lorentzian function or by mixture of Lorentzian and Gaussian functions.

Determination of peak position from experimental Raman spectrum

The major source of uncertainty in using frequency shifts to determine the composition and strain of a $Si_{1-x}Ge_x$ buffer layers stems from the difficulty of accurately measuring the peak positions for Si-Si, Si-Ge and Ge-Ge phonon modes. This is due to their asymmetry, large linewidth and small intensity, particularly for layers with $x<0.3$. For analysis of all three peaks associated with SiGe layer an asymmetrical function was implemented (see Eqn. (5.8)) into the user defined functions in ORIGIN. This allowed a better estimate of half width at half maximum (HWHM) of the spectrum, the intensity and the wavenumber of an asymmetrical peak from the following equation [27]:

$$I(\omega) = \frac{1}{2}\times\frac{[1-sign(\omega-\omega_0)]\times I_0}{\left(\frac{\omega-\omega_0}{W_1}\right)^2+1} + \frac{1}{2}\times\frac{[1-sign(\omega_0-\omega)]\times I_0}{\left(\frac{\omega_0-\omega}{W_2}\right)^2+1}$$
$$+\frac{1}{2}\times[1-sign(\omega-\omega_0)]\times I_{bkl} + \frac{1}{2}\times[1-sign(\omega_0-\omega)]\times I_{bkr} \quad (5.8)$$

where ω_0 is the peak position, I_0 is the peak intensity, W is the HWHM at the lower frequency side (W_1) and at the higher frequency side (W_2) of the spectrum, I_{bkl} is the background intensity on the lower frequency side of the curve and I_{bkr} is the background intensity on the higher frequency side of the curve. The function $sign(\omega-\omega_0)$ turns to -1 if $(\omega-\omega_0)$ is negative and 1 if $(\omega-\omega_0)$ is positive. Analysis of the peak positions proved to be considerably more accurate after the addition of these two terms. The asymmetrical function was found to fit the data better than the set of standard Lorentzian or Gaussian functions (see Fig. 5.5). This was most notably in particular for the Si-Ge mode at higher Ge concentrations as the asymmetry of this band does increase with increasing Ge content.

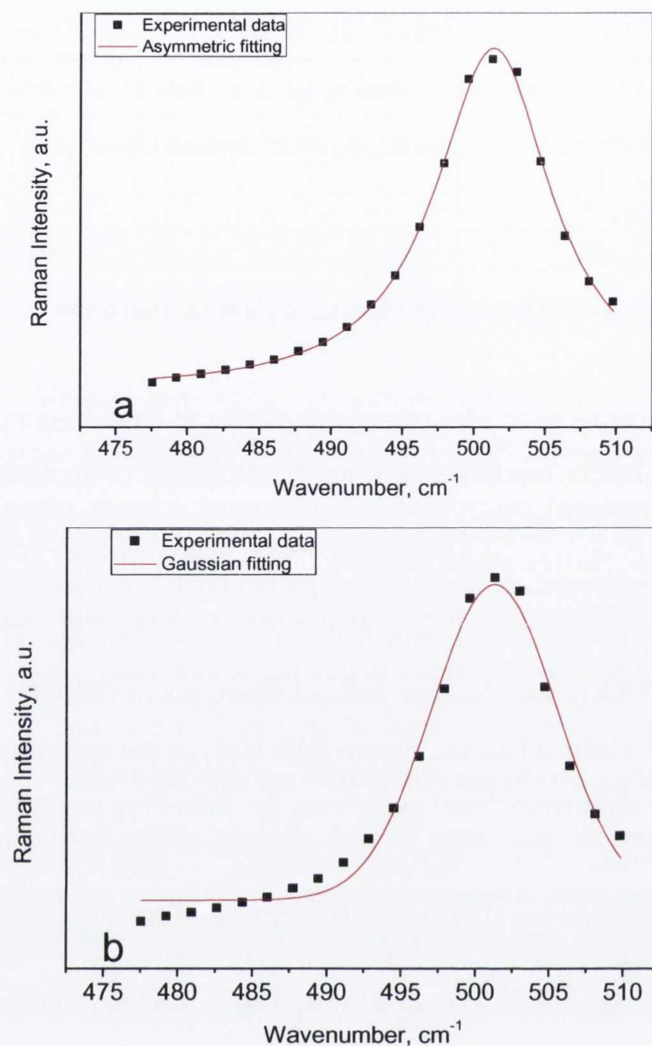

Fig. 5.5. Experimental Si-Si Raman band and the its fitting with (a) an asymmetric function and (b) mixture of Lorentzian and Gaussian functions.

5.3.3. XRD measurements

For high resolution XRD measurements the BRUKER D8 Discovery with a primary beam channel cut Ge (110) crystal monochromator, producing an intense, parallel Cu $K\alpha_1$ monochromatic beam (with wavelength λ=1.5406 Å), was used. The secondary beam is equipped with a LynxEye 1D detector allowing for fast mapping of the reciprocal space. The sample lattice parameters were determined by measuring reciprocal space maps (RSMs) around the Si [113] reflection and estimating the thin film lattice parameters from the relative separation in Ω and 2θ. For sample 940 RSMs

were also registered around Si [224] reflection; the obtained results were similar to Si [113] reflection. We note that XRD of 70 nm thick SiGe layers was also studied at the same (113) glancing incidence in [28]. Strain and Ge concentration were then obtained by assuming the lattice expansion due to the Ge content obeys Dismukes [20] model.

5.4. Results and discussion

The Raman spectrum of a strained SiGe heterostructure alloy consists of three distinct peaks whose energies (and therefore the peak positions) depend on x (Ge content) and strain [9,10,15]. The three strong first-order lines shown in Fig. 5.6 in the Raman spectra of few SiGe virtual substrates are due to the atomic vibrations of Si-Si (at ~ 502 cm^{-1}), Si-Ge (at ~ 405 cm^{-1}) and Ge-Ge (at ~ 290 cm^{-1}) bonds in the SiGe alloy. The Raman spectra for SiGe virtual substrates with different Ge content and with nearly the same relaxation factor (r > 93%), i.e. for fully relaxed samples, are presented in Fig. 5.6 (a). It can be seen from this figure that the position of all three peaks is shifted with respect to each other depending on x. The spectra obtained for samples with different composition and relaxation factor (or strain), shown in Fig. 5.6 (b). As can be seen from Fig. 5.6 (b) the position of all three bands is changed depending on x and ε. The values of x and ε can be estimated from a set of equations suggested in literature for bulk SiGe or relatively thick SiGe layers grown by CVD technique directly on Si or on graded SiGe layer. This includes the bulk materials, obtained by powder compression [10], single crystal SiGe alloy grown by liquid-phase epitaxy [11] as well as SiGe layers deposited by different CVD methods of deposition on graded SiGe layers or directly onto Si substrate.

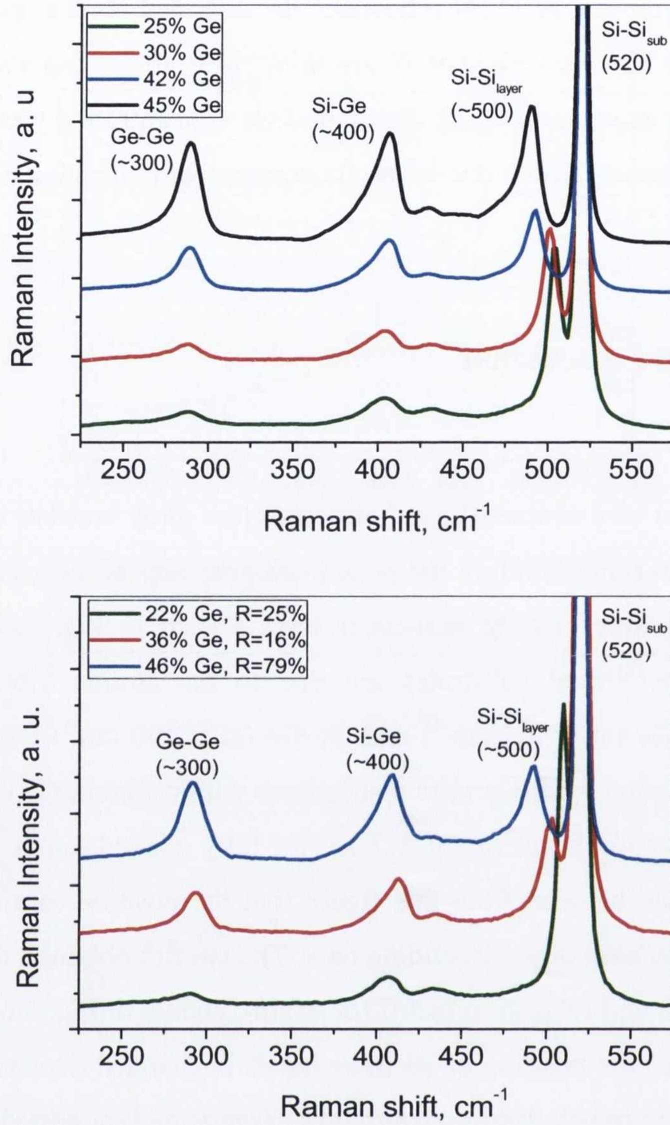

Fig. 5.6. (a) Raman spectra for SiGe/Si sample with R > 90% and different Ge content.

(b) Raman spectra for strained SiGe/Si sample with different Ge content.

For Si-Si peak position, ω_{SS}, of SiGe layer a few different experimental equations are introduced:

$$\omega_{SS}(x) = 520 - 70x \qquad [11] \tag{5.9}$$

$$\omega_{SS}(x) = 520.2 - 62x \qquad [8,10] \tag{5.10}$$

$$\omega_{SS}(x) = 521.2 - 67.9x \qquad [16] \tag{5.11}$$

$$\omega_{SS}(x) = 520.7 - 66.9x \qquad [13] \tag{5.12}$$

The equations (5.9)-(5.11) are valid mainly in the region of Ge content $0<x<0.5$, while Eqn. (5.12) is obtained for the wide range of x. The following equations are used for Si-Ge peak position, ω_{SG}:

$$\omega_{SG} = 400.5 + 14.2x \quad [8] \tag{5.13}$$

$$\omega_{SG} = 400.5 + 12x \quad [11] \tag{5.14}$$

in the range of $0<x<0.5$ and the expressions:

$$\omega_{SG} = 400 + 22.07x - 36.14x^2 + 83.73x^3 - 88.54x^4 \quad [16] \tag{5.15}$$

$$\omega_{SG} = 400.1 + 24.5x - 4.5x^2 - 33.5x^3 \quad [13] \tag{5.16}$$

for $0<x<1$. The experimentally measured dependences of the Ge-Ge phonon frequency, ω_{GG}, on x are described by the equations:

$$\omega_{GG} = 282.5 + 16x \quad [8] \tag{5.17}$$

$$\omega_{GG} = 280.8 + 19.37x \quad [14] \tag{5.18}$$

$$\omega_{GG} = 280.3 + 19.4x \quad [13] \tag{5.19}$$

In order to determine the best set of equations suitable for the set of samples analysed in this work, a number of samples with relaxation factor close to 100% were selected. The Ge content is obtained by XRD and the Raman peak positions are corrected for the small residual strain determined from the relaxation degree:

$$\varepsilon_{SiGe} = f(1-r) \tag{5.20}$$

with ε as a strain, f as a lattice mismatch and r as a strain relaxation.

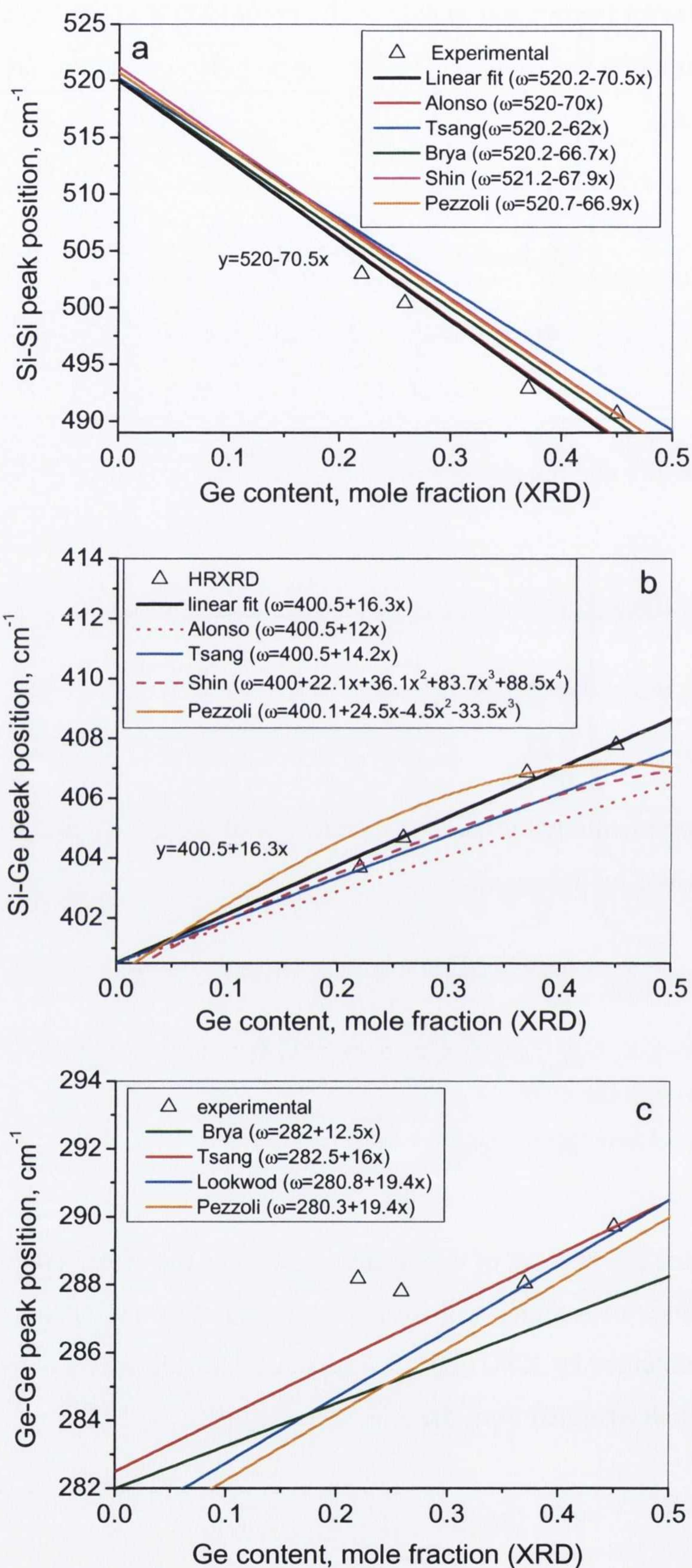

Fig. 5.7. (a) Si-Si, (b) Si-Ge and (c) Ge-Ge Raman peak position versus Ge content determined by HRXRD.

Lattice mismatch f is a parabolic function of Ge content, x, when slight deviation from Vegard's law is taken into account as given by Dismukes [20] for the bulk SiGe. This equation was confirmed later for epitaxial layers [21]:

$$f(SiGe) = \frac{0.02}{0.5431}x + \frac{0.0027}{0.5431}x^2 \tag{5.21}$$

The relaxation degree r of the selected samples varies between 0.92 and 1.05. The values larger than 1 stems from a small tensile strain originating from thermal mismatch of completely relaxed SiGe layers cooled down to room temperature. The correction of Raman peak position for strain is performed using the literature values [8,29-31] of strain phonon coefficients -830 cm^{-1}, -575 cm^{-1}, -384 cm^{-1} for Si-Si, Si-Ge and Ge-Ge bands, respectively. The accurate values of these literature strain-phonon coefficients are not critical, because of the only small correction needed for the selected samples. The results are shown in Fig. 5.7.

5.4.1. Frequency method

Equations for fully relaxed SiGe layers

The peak position obtained for all three Raman modes after the fitting with asymmetrical function are plotted in Fig. 5.7 against of x values, determined from XRD measurements. The linear curves obtained from Eqns. (5.9)-(5.12) on dependence of Si-Si peak position versus Ge content are shown in Fig. 5.7 (a) together with Raman and XRD experimental data. The same set of data and linear dependences are shown in Fig. 5.7 (b) for Si-Ge modes and in Fig. 5.7 (c) for Ge-Ge peaks. As can be seen from Fig. 5.7 (a), the best fit to XRD data results in the linear equation:

$$\omega_{SS} = 520 - 70.5x, \tag{5.22}$$

which is quite close to the equation obtained in Ref. [11], see Eqn. (5.9). Fig. 5.7 (b) shows a similar set of data for peak position of Si-Ge mode versus x obtained from

XRD data. In this case the experimental data obtained for our set of samples significantly deviate from the linear and non-linear dependencies described by Eqns. (5.13), (5.14) and (5.15), (5.16). The best fit to obtained experimental data results in the following linear equation:

$$\omega_{SG} = 400.5 + 16.3x. \tag{5.23}$$

As can be seen from Fig. 5.7 (c) a significant deviation of the experimental data points from all curves is observed for the Ge-Ge peak position versus x. This confirms previously made conclusion [8], that it is more difficult to use Ge-Ge peak for the extraction information on x from Raman data, particularly for thin SiGe layers with $x<0.4$. For consistency we will analyse our experimental results for all three peaks described above, using Eqn. (5.17) obtained in [8] for Ge-Ge peak. However, most of the data analysis was done based on Eqns. (5.22) and (5.23).

Equations for strained SiGe layers

The next step is to determine the set of equations for strained SiGe virtual substrate with relaxation factor < 100%. For this purpose the additional terms accounted for strain in set of Eqns. (5.17), (5.22) and (5.23), introduced in literature earlier (see, for example [8]), were used. This results in the following set of equations describing the peak position of SiGe layer under strain:

$$\omega_{SS} = 520 - 70.5x - 830\varepsilon, \tag{5.24}$$

$$\omega_{SG} = 400.5 + 16.3x - 575\varepsilon, \tag{5.25}$$

$$\omega_{GG} = 282.9 + 16x - 384\varepsilon. \tag{5.26}$$

Then based on the equations (5.25) and (5.26) we can obtain the expressions for x and ε calculations:

$$x = \frac{(\omega_{SG} - 400.5) - 0.6928 \cdot (\omega_{SS} - 520)}{64.84}, \tag{5.27}$$

$$\varepsilon_{SiGe} = \frac{520 - \omega_{SS} - 70.5x}{830}. \tag{5.28}$$

The results of calculations of x and ε using Eqns. (5.27) and (5.28) enable us to processed the Raman data obtained for numerous samples, investigated in this work, with x in the range from 0 to 0.5 and for the relaxation factor varied in the range from 20% to 100%. The following equations, described the shift of the peak position for fully strained layers, were obtained:

$$\Delta\omega_{SS} = 36x, \ \Delta\omega_{SG} = 39x \ \text{ and } \ \Delta\omega_{GG} = 32x \tag{5.29}$$

The degree of relaxation, r in a SiGe layer on Si substrate can be obtained using the experimental Raman shift of the Si-Si peak Δ_{exp} from the unstrained peak position for Si substrate at 520 cm^{-1} from the following expression [32,33]:

$$r_1 = \frac{\Delta_{\exp} - \Delta_s}{\Delta_r - \Delta_s} \cdot 100\% \tag{5.30}$$

where Δ_r = 70.5x and Δ_s = 36x are Raman shifts of the fully relaxed and the fully strained epilayers from the bulk Si, respectively. In addition to the r value can be calculated from the expression:

$$r_2 = 1 + \varepsilon_{SiGe}\left(\frac{a_{SiGe}^{\mathrm{Re}l}}{a_{SiGe}^{\mathrm{Re}l} - a_{Si}}\right). \tag{5.31}$$

The results shown in Figs. 5.8 (a)-(c) demonstrate distribution of the obtained data between two linear dependencies of phonon frequencies on x, obtained for the fully strained and fully relaxed SiGe virtual substrates. It can be seen that the obtained data are within the range of data possible for different values of x for the investigated samples. A small deviation of experimental data from fully strained curve is observed,

which is due to the difficulties of Ge-Ge peak analysis for samples with small Ge content. The results on comparison of the data obtained from XRD and Raman techniques for the relaxation factor and Ge content are summarised in Table 5.2. We can see that the deviation of the r values obtained by Raman spectroscopy for samples 940, 937 and 938 is larger than that obtained for the x value (this will be discussed in the following section). Figure 5.9 demonstrates the difference between x values obtained from Raman (x_{Raman}) and XRD (x_{XRD}) measurements versus Ge content. The maximal deviation of x values estimated from Raman data are within ± 0.04 relatively to XRD data. Bearing in mind the difficulties with analysis of data for very thin layers we believe that the obtained results demonstrate a very good precision of micro-Raman spectroscopy for the determination of Ge content and strain (or degree of relaxation) in thin SiGe layers.

Table 5.2. The calculated Ge concentration and r factor for samples, measured by XRD and Raman techniques, using frequency and intensity methods.

Sample name	Ge content, x at. u.				Relaxation factor r, %		
	HRXRD	Freq. Method Eqn. (5.27)	Intensity method Eqn.(5.32) A=1.7	Intensity method Eqn.(5.33) B=3	HRXRD	Raman, r_1	Raman, r_2
1303	0.36	0.39	0.31	0.37	16	26	19
1308	0.37	0.39	0.37	0.40	104	104	104
753	0.22	0.23	0.22	0.25	81.7	95	95
759	0.22	0.23	0.23	0.22	24.5	28	21
773	0.45	0.42	0.44	0.39	99	98	97
940	0.29	0.31	0.19	0.29	23	33	26
746	0.26	0.27	0.29	0.28	93	97	97
1027	0.46	0.43	0.46	0.44	79	81	80
936	0.35	0.32	0.34	0.42	77	80	78
937	0.32	0.29	0.20	0.35	68	86	85
938	0.37	0.33	0.20	0.33	85	61	58
774	0.44	0.41	0.45	0.44	92	99	98
775	0.43	0.40	0.41	0.41	83	93.5	93
776	0.44	0.40	0.43	0.41	95	93	93

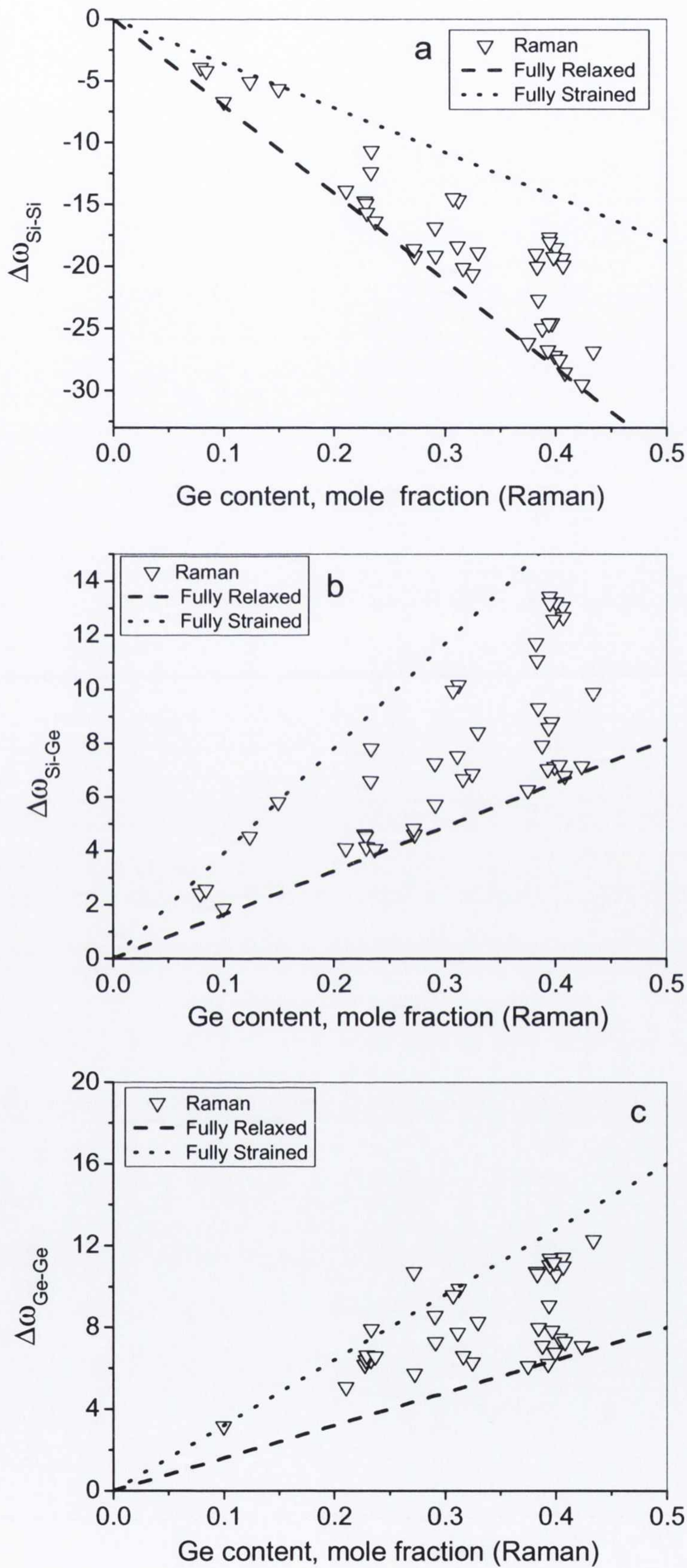

Fig. 5.8. Raman shift of the Si-Si (a), Si-Ge (b) and Ge-Ge (c) peak as a function of Ge content. Dotted lines correspond to the dependence of $\Delta\omega$ vs. Ge content for fully strained samples and dashed line for fully relaxed samples.

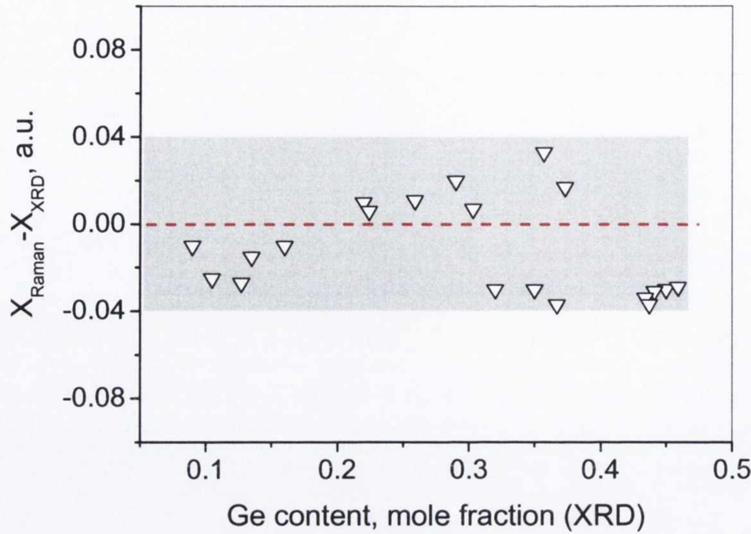

Fig. 5.9. Deviation of Ge content obtained from Raman and XRD data ($x_{Raman}-x_{HRXRD}$) versus Ge content determined by HRXRD measurements.

5.4.2. Intensity method

In this paragraph, the second approach for determination of composition in SiGe alloy using Raman spectroscopy is considered. The methods suggested in Refs. [8,10,34] are based on the comparison of the relative intensities of the first order Si-Si, Si-Ge and Ge-Ge bands. The ratios of the integrated intensities of three main modes can be related in the first order approximation to the number of nearest neighbour bonds and, therefore, are the functions of the Ge content in the alloy. Following to simple statistical model the relative intensities are roughly proportional to the relative numbers of corresponding bonds types, i.e. $(1-x)^2$, x^2 and $2x(1-x)$ for the Si-Si, Ge-Ge and Si-Ge modes, respectively [9]. The major advantage of using the intensity method is that there is no need for highly accurate fitting of the phonon bands, which is extremely important for the frequency method described in the previous Section. The determination of alloy composition using the intensity of the modes is also independent of whether the layer is strained or relaxed. However the intensities of the Si-Ge and Ge-Ge modes depend strongly on the methods used to measure them. In particular there is some uncertainty about the determination of the baseline for each particular band shown in Fig. 5.10. This problem is especially pertinent for the Si-Ge mode as there are significant peaks on

the high energy side of the main Raman mode. These have been attributed to localised Si-Si motion in the neighbourhood of one or more Ge atoms [9,10,15]. As was stated in Ref. [34] the localised Si-Si peaks were included in measurement of integrated intensity of Si-Ge mode. It is shown in Fig. 5.10 how the areas of the SiGe alloy modes were determined for the samples investigated in this work.

Assuming random mixing in the alloy, the relative integrated intensities of the modes are expected to vary with the Ge mole fraction as follows [34]:

$$\frac{I(Si-Si)}{I(Si-Ge)} = \frac{A(1-x)}{2x} \tag{5.32}$$

$$\frac{I(Ge-Ge)}{I(Si-Ge)} = \frac{Bx}{2(1-x)} \tag{5.33}$$

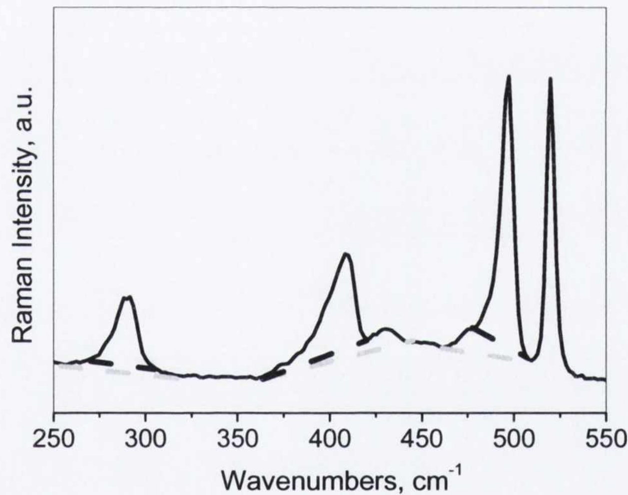

Fig. 5.10. The various different baselines that can be chosen in calculating the intensities of the Si-Si, Si-Ge and Ge-Ge modes. The black dashed line indicates the baselines used in these work.

Because of resonance effects, the intensities of the various modes vary with the wavelength of the exciting light, as does the optical system. Thus, coefficients *A* and *B* must be determined experimentally for each wavelength. *A* and *B* were determined for our experimental set up for 514 nm wavelength using the XRD data available for a number of samples as described above. The integrated intensities of phonon modes were

calculated by using a peak profile analysis inbuilt to Renishaw Wire software. Using x values, measured by XRD, the relative intensities for the investigated samples are plotted versus Ge content in Figs. 5.11 (a) and 5.11 (b). The best fitting of experimental data is obtained at A=1.7 and B=3.0. From comparison of Fig 5.11 (a) and 5.11 (b), it can be concluded that better correlation between Raman and XRD results is achieved with Eqn. (5.32). This is not surprising bearing in mind that Ge-Ge peak for thin SiGe layer is quite weak in particular for small x.

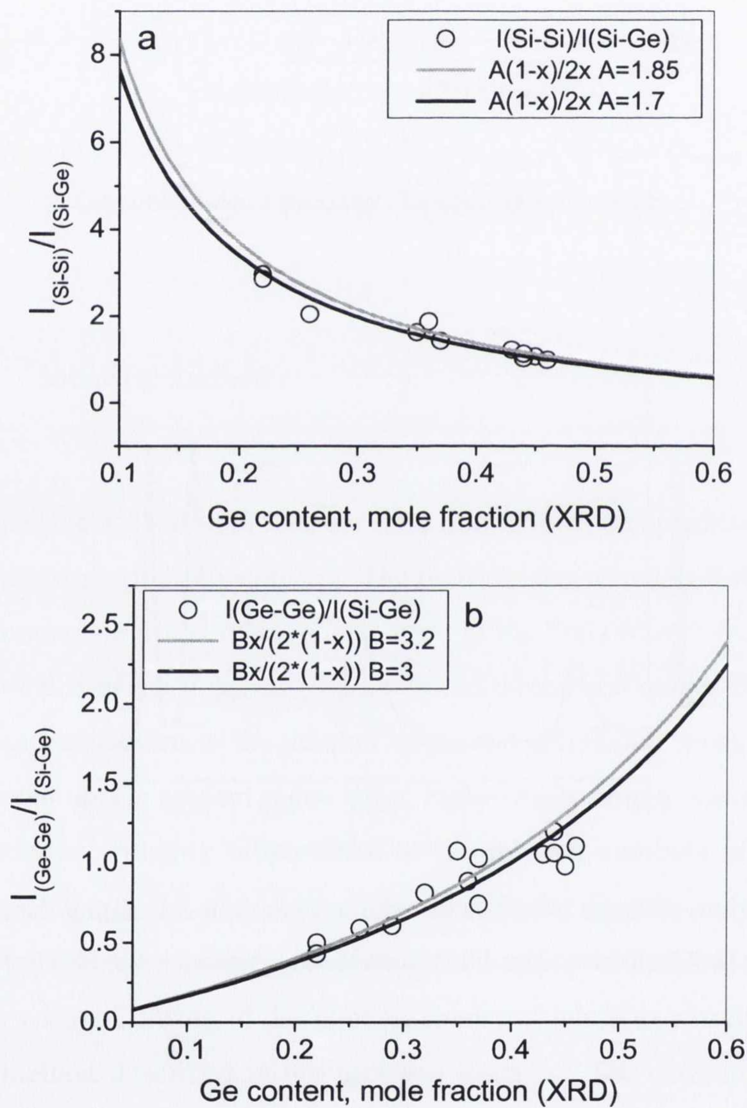

Fig. 5.11. Intensities ratio versus Ge content, x from the experimental data (symbols) and (a) from Eqn. (5.32) at A = 1.85 (grey line) and A = 1.7 (black line) and Eqn. (5.33) at B=3.2 (grey line) and B=3 (black line).

As can be seen from Table 5.2, the intensity method enables the determination of x to an accuracy of ± 0.05 using Eqn. (5.32). It was mentioned above that considerable uncertainty exists as to where the baseline of a peak begins and where it ends. Mooney et al. [34] found the integrated intensities ratios to be in good agreement with Eqns. (4.32) and (4.33) only if the peak at 430 cm^{-1} is included in the intensity of the Si-Ge mode. In this investigation, the intensity of the Si-Ge mode was measured without the peak at 430 cm^{-1}. When this peak was included, the accuracy of this method was reduced to ± 0.08%. Interestingly that for the same samples 940, 937 and 938 described in the previous section a significant deviation between x values obtained by XRD and from Raman intensity method using Eqn. (5.32) was obtained. However, using the Eqn. (5.33) the results obtained for x are quite close to XRD data. This deviation could be due to the larger surface roughness observed for these particular samples.

Strained Si on SiGe virtual substrate

The main feature of the Raman spectra of strained-Si on ultra-thin SiGe substrates obtained with visible excitation light is the presence of three Si–Si peaks in the region ~530-490 cm^{-1} (see Fig. 5.12). These are the peak at 520 cm^{-1} corresponds to the Si substrate, the peak at ~510-518 cm^{-1} which is assigned to strained-Si and the peak in the range ~490-510 cm^{-1} which belongs to the Si–Si mode in the SiGe layer. Depending on the Ge content in the underlying SiGe virtual substrate these three peaks can be either quite well separated or be very close together. This situation is quite different from the case of Raman spectra of strained-Si on thick SiGe substrates where the peak at 520 cm^{-1} is not observed due to the limited depth of laser light penetration into the SiGe layer [32,35]. The Si–Si peak arising from the Si substrate can be used with high accuracy as an internal reference in analyzing the Raman spectrum. The intensity of a peak at 520 cm^{-1} in the case of a thin s-Si layer on an ultra-thin SiGe layer is much larger compared to the two other peaks, and, in particular, in comparison with the peak for s-Si, due to its small thickness. This requires very careful analysis of the Raman spectra, in particular in the range 490-530 cm^{-1} [36]. Raman spectra for the four samples, registered at 514.5 nm excitation, are shown in Fig. 5.12 (a). For the sample 1797 with low Ge content (~10%) there is no visible sign of the Si–Si peak from s-Si, while for the samples with higher Ge content a small shoulder or small bump related to

this peak can be seen in between the two peaks at 520 and at ~490-512 cm^{-1}. By fitting the Raman spectrum with three Lorentzian functions, all three peaks are revealed as shown, for example, in Fig. 5.12 (b). The results obtained for the shift $\Delta\omega$ of Si–Si peak from the unstressed Si–Si peak at 520 cm^{-1} for all analyzed samples are summarized in Table 5.3 together with data obtained using 488 and 325 nm excitations. For UV excitation, a simultaneous recording of the plasma line was used for the internal reference. This is because for the shorter excitation wavelength Si-Si peak from the substrate is not observed in Raman spectrum. As can be seen from Table 5.3, the values of Raman peak shift, $\Delta\omega$ obtained with all three excitation wavelengths are in good agreement. The obtained results demonstrate that visible light Raman spectroscopy can be reliably used for the characterisation of strained Si on ultra-thin SiGe virtual substrates. However, careful fitting of the spectra is required in this case for proper data analysis.

Table 5.3. Comparison of shift of Si-Si peak position in Raman spectra s-Si layer, obtained at different excitation wavelength and stress and strain calculation.

Sample name	**Raman shift of s-Si band, $\Delta\omega$, cm^{-1}**			**σ, GPa** Eqn. (5.34)	**ε_{Si} x100%** (Eqn.(5.35)
	514 nm	**488 nm**	**325 nm**		
1797	2.49	2.66	2.56	0.54	0.3
1669	5.3	-	-	1.13	0.63
1799	7.24	7.3	7.0	1.57	0.87
1800	12.7	12.5	12.4	2.75	1.53

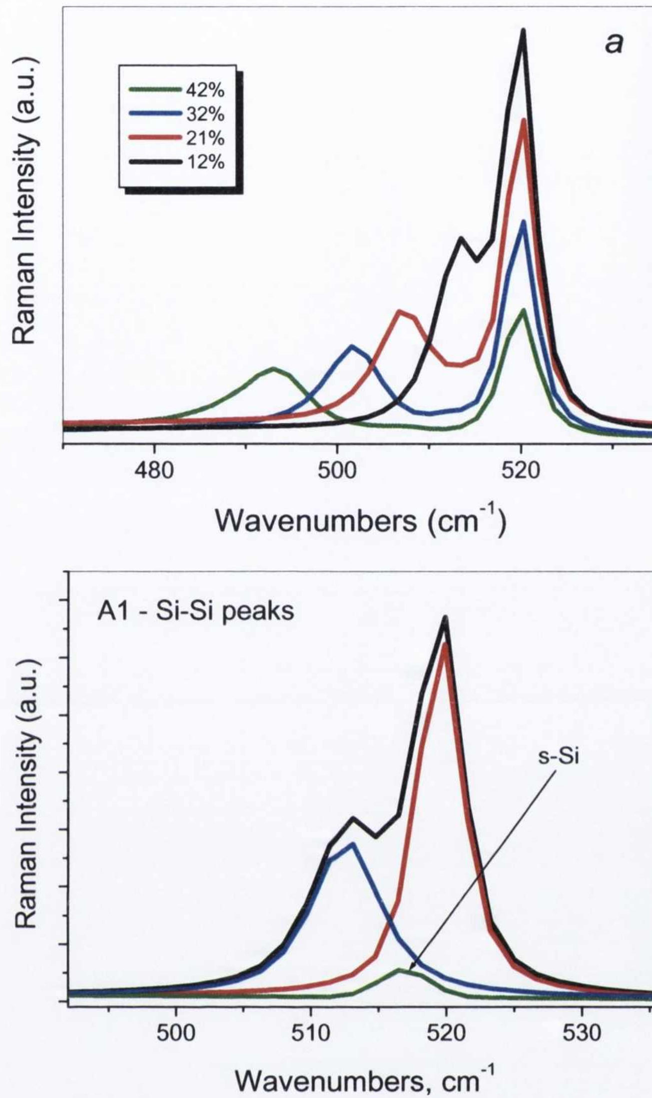

Fig. 5.12. (a) Raman spectra of sample 1797, 1669, 1799 and 1800 with increasing Ge content collected at 514 nm excitation wavelength. The strained-Si peak is observed between the Si substrate peak at 520 cm^{-1} and the Si–Si band from the SiGe layer. (b) Fitting of Raman spectrum for sample 1797 with three Lorentzian functions.

By measuring the shift in the Raman peak position, $\Delta\omega$, obtained for the s-Si layer, the magnitude of stress, σ and strain, ε can be estimated by using a simple equation, describing the biaxial stress in a Si lattice [29,31]:

$$\sigma_{Si} = \Delta\omega / c \tag{5.34}$$

with $c=4.61\cdot10^{-9}$ ($Pa\cdot cm^{-1}$)

$$\varepsilon_{Si}(\%) = (\frac{\Delta\omega}{b}) \cdot 100\% = \frac{a_{Si}^{strain} - a_{Si}}{a_{Si}} \cdot 100\%, \qquad (5.35)$$

where b is the strain-phonon coefficient, which was taken as 830 cm^{-1}, a_{Si} and a_{Si}^{strain} are the lattice constants of relaxed and strained-Si, respectively. The values of σ_{Si} and ε_{Si} are related to the elastic constants as shown in Eqn. (5.7). Taking the values of E and v as 130.2 GPa and 0.28, respectively [37], we conclude that the phonon coefficient ratio b/c should be $b/c = E/(1-v) = 180.5$ GPa. The selected coefficients c and b obtained from the literature fit very well this relationship. The strain values thus obtained were compared with the data estimated for ε_{Si} from analysis of the spectral shifts of the Si–Si phonon band registered from the SiGe layers, taking into account the coherence conditions:

$$a_{SiGe}^{strain} = a_{Si}^{strain}. \qquad (5.36)$$

By analogy with the Eqn. (5.35) and taking into account the Eqn. (5.36) and that:

$$a_{SiGe}^{strain} = a_{SiGe}^{rel}(x)(1 + \varepsilon_{SiGe}) \qquad (5.37)$$

where $a_{SiGe}^{rel}(x)$ can be determined from Dismukes model [20], we can obtain:

$$\varepsilon_{Si}(\%) = \frac{a_{SiGe}^{strain} - a_{Si}}{a_{Si}} \cdot 100\% \qquad (5.38)$$

The results obtained for $\varepsilon_{Si}(\%)$ estimated form Eqns. (5.35) and (5.38) are presented in Table 5.3 and Table 5.4 along with σ values obtained from Eqn. (5.34). Both series of results for $\varepsilon_{Si}(\%)$ show very good agreement. This indicates that the results obtained from the analysis of complicated Raman spectra in Si-Si mode region allow us to obtain reasonably good data on stress in s-Si layers on SiGe virtual substrates. The calculations of Ge content (x) and strain ε_{SiGe} were performed by means of simultaneous measurements of the ω_{SS} and ω_{SG} for the underlying SiGe layer, followed by calculations using the pair of equations (5.27) and (5.28). The relaxation factor for SiGe

layer was also estimated from Eqn. (5.30). Both values (x and r) obtained from analysis of Raman spectra are in good agreement with XRD data.

Table 5.4. Strain in s-Si and in SiGe layers measured by XRD and Raman spectra analysis.

Sample name	SiGe Relaxation factor, r, %		ε_{Si} x100% Eqn.(5.38)	ε_{max}, % Eqn. (5.39)	SiGe Ge content, x	
	XRD	Raman			XRD	Raman
1797	42	58	0.28	71.1	0.13	0.12
1669	-	77	0.61	96.3	-	0.21
1799	67	61	0.75	100	0.30	0.32
1800	89	84	1.42	104	0.40	0.42

Inversely using the coherence conditions, the analysis of the Si-Si peak for s-Si layer enables us to evaluate the value of Ge content and strain in SiGe independently. The obtained results are in very good agreement with Raman analysis of SiGe bands, which supports the use of the altered Eqns. (5.24) and (5.25) for the simultaneous calculation of x and ε_{SiGe} in thin virtual SiGe substrates. It should be note that the estimation of the maximum achieved strain in s-Si layer can be performed using the equation suggested earlier in Ref. [38]:

$$\varepsilon_{\max} = \frac{|\Delta\omega_{Si,\exp}|}{|\Delta\omega_{Si,\max}|} \times 100 \qquad (5.39)$$

Where $\Delta\omega_{Si,exp}$ is experimentally obtained shift of s-Si peak from unstrained Si peak at 520 cm^{-1} and:

$$\Delta\omega_{Si\max} = |b| \cdot \left[a_{Si} - a_{Si}^{strain}\right] / a_{Si}. \qquad (4.40)$$

The calculated values of ε_{max} are also presented in Table 5.4. Table 5.4 shows that the s-Si layer in sample 1797 (with the smallest Ge content) is not fully strained while the s-Si layer can be considered to be fully strained for samples 1669, 1799 and 1800. The higher than 100% value of ε_{max} obtained for sample 1800 can be due to the inaccuracy in measurements and calculations. The good agreement between Raman and

XRD data shows that even results obtained from the analysis of complicated Raman spectra in Si-Si mode region allows us to obtain reasonable data on stress in strained Si layers on SiGe virtual substrates.

5.5. Conclusions

To summarise, there are techniques such as RBS and SIMS, which can be used for Ge content determination in SiGe buffer layers. However, RBS is not very accurate for measurements of thin films in complicated structure, while SIMS is a destructive technique. XRD is quite accurate technique, in particular, using advanced equipment with high resolution, but it requires longer measurements time and more difficult to arrange in-line samples measurements. In this chapter, the applications of micro-Raman spectroscopy for determination of x were presented. It was shown that even for very thin SiGe films micro-Raman spectroscopy is a very valuable and enough accurate characterisation tool.

The Ge content, x, and the relaxation factor, r, were estimated from the set of equations for Si-Si, Si-Ge and Ge-Ge Raman vibrational modes adjusted in this work for thin SiGe layers. The alterations of the equations from previously published works were performed using the independent results on x and r, obtained from XRD and Raman measurements for fully relaxed SiGe virtual substrates. The Ge content in SiGe layers was calculated using both frequency and intensity methods. It was shown that using the ratios of the integrated intensities of Si-Si, Si-Ge and Ge-Ge phonon modes for SiGe virtual substrates provides x values, which are in quite reasonable agreement with XRD and Frequency Raman method. Surprisingly the Intensity Method provide reasonably good results even using Ge-Ge peak for $x<0.3$, while in frequency method only Si-Si and Si-Ge peaks were used at this condition. It should be note that for samples with larger number of defects a significant deviation in x values was obtained from Frequency and Intensity methods. Finally, it was also shown that visible light Raman spectroscopy can be reliably used for the characterisation of strained Si on ultra-thin SiGe virtual substrates. However, careful fitting of the spectra is required in this case.

References

1. K. Lyutovich, M. Bauer, E. Kasper, H.-J. Herzog, T. Perova, R. Maurice, C. Hofer, C. Teichert, Materials Science and Engineering B89, 341 (2002)
2. E.A. Fitzgerald, M.T. Curie, S.B. Samavedam, T.A. Langdo, G. Taraschi, V. Yang, C.W. Leitz, M.T. Bulsara, Phys. Stat. Sol. A 171, 227 (1999)
3. S. Mantl, B. Hollander, R. Liedtke, S. Mesters, H.-J. Herzog, H. Kibbel, T. Hackbarth, Nucl. Instr. Methods Phys. Res. B 148, 200 (1999)
4. Z. Yang, J. Alperin, W.I. Wang, S.S. Lyer, T.S. Kuan, F. Senemdy, J. Vac. Sci. Technol. B 16, 1489 (1998)
5. E. Kasper, K. Lyutovich, M. Bauer, M. Oehme, Thin Solid Films 336, 319 (1998)
6. K. Lyutovich, E. Kasper, F. Ernst, M. Bauer, M. Oehme, Mater. Sci. Eng. B 71, 14 (2000)
7. M. Bauer, M. Oehme, K. Lyutovich, E. Kasper, Thin Solid Films 336, 104 (1998)
8. J.C. Tsang, P.M. Mooney, F. Dacol, J.O. Chu, J. Appl. Phys. 75, 8098 (1994)
9. M. A. Renucci, J. B. Renucci, M. Cardona, M. Balkanski, Light scattering in solids, Paris: Flammarion Sciences; (1971), p. 326
10. W. J. Brya, Solid State Commun 12, 253 (1973)
11. M. I. Alonso, K. Winer, Phys Rev B 39, 10056 (1989)
12. J. M. Hartmann, B. Gallas, J. Zhang, J. J. Harris, Semicond. Sci. Technol. 15, 370 (2000); J. M. Hartmann, Y. Bogumilowicz, P. Holliger, F. Laugier, R. Truche, G. Rolland, Semicond. Sci. Technol. 19, 311 (2004)
13. F. Pezzoli, E. Grilli, M. Guzzi, S. Sanguinetti, D. Chrastina, G. Isella, Mater. Sci. Semicond. Process. 9, 541 (2006); F. Pezzoli, E. Bonera, E. Grilli, M. Guzzi, S. Sanguinetti, D. Chrastina, G. Isella, H. Von Känel, E. Wintersberger, J. Stangl, G. Bauer, Mat. Sci. Semicon. Proces., 11, 279 (2008)
14. J.C. Bean, Science 230, 127 (1985)
15. F. Cerdeira, A. Pinczuk, J. C. Bean, B. Batlogg, B. A. Wilson, Appl. Phys. Lett. 45, 1138 (1984); F. Cerdeira, C. J. Buchenauer, F. H. Pollak, M. Cardona, Phys. Rev. B 5, 580 (1972)
16. H. K. Shin, D. J. Lockwood, J. M. Baribeau, Solid State Commun. 114, 505 (2000)
17. H. Brugger, G. Abstreiter, H. Jorke, H. J. Herzog, E. Kasper, Phys. Rev. B 33, 5928 (1986)

18. P. H. Tan, D. Bougeard, G. Abstreiter, K. Brunner, J. Appl. Phys. 98, 113517 (2005)
19. A. V. Baranov, A. V. Fedorov, T. S. Perova, R. A. Moore, V. Yam, D. Bouchier, V. Le Thanh, K. Berwick, Phys. Rev. B 73, 075322 (2006)
20. J.P. Dismukes, L. Ekstron and R.J. Paff, J. Phys. Chem. 68, 3021 (1964)
21. E. Kasper, A. Schuh, G. Bauer, B. Hollander, H. Kibbel, Journal of Crystal Growth 157, 68 (1995)
22. Silicon Germanium and SiGe:Carbon, E. Kasper, K. Lyutovich, INSPEC, London, UK, (2000)
23. J. P. Douglas, Semicond. Sci. Technol. 19, R75 (2004)
24. J.W. Matthews, and A.E. Blakeslee, J. Cryst. Growth 27, 118 (1974)
25. J. Welser, J.L. Hoyt, J.F. Gibbons, IEEE Electron Device Lett., 15, 100 (1994)
26. K Lyutovich, M Oehme, F. Ernst, Eur Phys J. Appl. Phys. 27, 341 (2004)
27. Raman and Luminescence Spectroscopy for Microelectronics, Catalog of optical and physical parameters "Nostradamus" project SMT4-CT-95-2024, European Communities, (1998)
28. A.P. Powell et al., Appl. Phys. Lett. 64, 1856 (1994)
29. I. DeWolf, Semicond. Sci. Technol. 11, 139 (1996)
30. E. Anastassakis, A. Cantarero, M. Cardona, Phys. Rev. B 41, 7529 (1990)
31. V. Destefanis, D. Rouchon, J.M. Hartmann, A.M. Papon, L. Baud, A. Crisci, and M. Mermoux, J. Appl. Phys. 106, 043508 (2009)
32. B. Dietrich, E. Bugiel, J. Klatt, G. Lippert, T. Morgensten, H.J. Osten, and P. Zaumseil J. Appl. Phys., 74, 3177 (1993)
33. C. H. Perry, F. Lu, and F. Namavar Solid State Commun. 88, 613 (1993)
34. P. M. Mooney, F. H. Dacol, J. C. Tsang, and J. O Chu, Appl.Phys.Lett., 62, 2069 (1993)
35. S. Nakashima, T. Mitani, M. Ninomiya, and K. Matsumoto, J. Appl. Phys. 99, 053512 (2006)
36. T. S. Perova, K. Lyutovich, E. Kasper, A. Waldron, M. Oehme, R.A. Moore, Mat. Sci. Eng. B 135, 192 (2006)
37. J. J. Wortman, R. A. Evans, J. Appl. Phys. 36, 153 (1965)
38. R. Liu, S. Zollinger, M. Liaw, D. O'Meara, N. Cave, Mat. Res. Symp. Proc., 533, 63 (1998)

6. Raman and FTIR study of substitutional carbon incorporation in rapid thermal chemical vapour deposited $Si_{1-x-y}Ge_xC_y$ on Si (1 0 0)

6.1. Introduction

The introduction of C into $Si_{1-x}Ge_x$ layers heteroepitaxially grown on Si has attracted considerable attention as it enables band engineering via strain control in group IV semiconductors [1,2]. It may have application to the fabrication of novel heterostructure devices using Si-based technology. The fundamental properties and possible devices application of SiGe/Si heterostructures have been discussed extensively in the previous chapter. As shown recently, the addition of modest amounts of substitutional carbon into $Si_{1-x}Ge_x$ reduces the strain originating from the lattice mismatch between SiGe and Si and provides an additional design parameter in manipulating electronic properties [3,4]. Carbon is a much smaller atom than those of Si and Ge. The lattice mismatch between Si and diamond is, in fact, 52% compared to only 4% between Si and Ge. This means that only a very small amount of substitutional carbon in Si is necessary to introduce a large average tensile strain in the pseudomorphic epilayers. Assuming a linear dependence of the intrinsic lattice constant $a_0(x,y)$ of $Si_{1-x-y}Ge_xC_y$ on the compositional x and y between Si, Ge and diamond one obtains the following expression:

$$a_0(x,y) = a_{Si} + (a_{Ge} - a_{Si}) \cdot x + (a_C - a_{Si}) \cdot y \quad (6.1)$$

where a_{Si}, a_{Ge} and a_C are the lattice constants of silicon, germanium and diamond, respectively. Based on this linear interpolation it turns out to that the compressive strain of 8.2% Ge can be compensated by 1% of C in a pseudomorphic $Si_{1-x-y}Ge_xC_y$ layer on Si substrate. Osten et al [4] used a linear interpolation between SiC, Si, and Ge. In this case the expression for the lattice constant of $Si_{1-x-y}Ge_xC_y$ is:

$$a_0(x,y) = a_{Si} + (a_{Ge} - a_{Si}) \cdot x + 2(a_{SiC} - a_{Si}) \cdot y, \qquad for \;\; 0 < y < 0.5 \quad (6.2)$$

This equation provides the strain compensation for 9.4% Ge by 1% C. The difference is due to the fact that a_{SiC} is not exactly in the middle between a_{Si} and a_C. Moreover, a_{SiC} is 0.436 nm, whereas $(a_{Si} + a_C)/2$ is 0.461 nm.

In 1992 by Eberl et al [1] reported the first pseudomorphic $Si_{1-x-y}Ge_xC_y$ films directly on Si with reduced compressive strain. Since that time several research groups have prepared SiGe films with substitutional C by molecular beam epitaxy (MBE) [1,4,] and different chemical vapour deposition (CVD) and gas source techniques [2,5,6]. In particular, MBE and CVD grown pseudomorphic SiGeC alloy layers on Si have demonstrated good crystalline quality and are essentially free of extended lattice defects when prepared under appropriate conditions.

The presence of carbon in the SiGeC lattice induces a very large local bond distortion, resulting in a significant change in the phonon frequencies. Determination of the exact amount of substitutional carbon in alloys is not trivial, as the parameters of the vibrational bands: peak position, linewidth and intensity, are strongly dependent on the carbon content. A measurement of the vibrational C local mode at ~ 605 cm^{-1} can be used to quantify the amount of substitutional carbon in $Si_{1-x-y}Ge_xC_y$, since it originates only from substitutional carbon. This measurement can also be used to estimate the amount of ordered carbon pairs versus randomly distributed carbon atoms. A number of recent publications [7-15] were devoted to the study of the mechanism of the carbon distribution and ordering during $Si_{1-x-y}Ge_xC_y$ growth, and the microscopic strains in $Si_{1-x-y}Ge_xC_y$ alloys with respect to the average lattice constant. There are a variety of interpretations in the literature on the origin of the Raman satellite Si-C peak at ~630 cm^{-1}. Rowell et el. [15] assign this peak to presence of carbon on the non-substitutional sites, while Guedj et el. [14] and H. Rücker et el. [16] showed, by combining theoretical and experimental results, that the satellite Si-C peak corresponds to the third-nearest-neighbour (3nn) carbon pairs. To date, no completely satisfactory experimental methods exist for the extraction of information on the fraction of substitutional carbon from the total carbon content in SiGeC films with varying Ge content. A discrepancy exists in the literature regarding the frequency behaviour of Si-Si, and Si-Ge vibrational bands in Raman spectroscopy as a function of C content. This is partly due to the limited number of investigations that have been performed on SiGeC structures. For instance, a decreasing dependence of the Si-Si peak with C content was experimentally observed in Ref. [9,17]. Rücker et al. [18] predicted a negative shift of

the Si-Si peak for SiGeC alloys using theoretical calculations. Rowell et al. [15] did not find any systematic trend in the variation of the frequencies of Si-Si and Si-Ge peaks with changing C content. Measurements by Melendez-Lira et al. [12], showed a positive shift of the Si-Si peak with increasing C concentration. In Ref. [12] an increase of the Si-Ge peak with C content is also observed. However, the opposite trend in the Si-Ge peak frequency versus C content was obtained in this work. Differences in the behaviour of the Si-Si and Si-Ge peak are discussed in this work in the context of sample properties. Contradictions also exist in the literature regarding changes in the frequency and intensity of the Si-C bands resulting from the addition of substitutional carbon. An increase in both intensity and frequency for both satellite and local Si-C modes was observed by Finkman et al. [10]. Whereas, in Ref. [15] it was shown that the frequency of the Si-C local mode at ~ 605 cm^{-1} decreases with C content.

This chapter reports a more detailed study of the carbon concentration dependence of the infrared and Raman modes in Rapid Thermal Chemical Vapour Deposited (RTCVD) $Si_{1-x-y}Ge_xC_y$ samples with different x and y fractions varied over a small range. Also, a new approach is presented to the calibration of optical methods for the extraction of the substitutional carbon concentration in SiGeC layers with carbon concentrations of up to 1.8 %.

6.2. Experimental

6.2.1. Sample growth and description

The samples were grown on (100) n-type Si substrates using a RTCVD deposition reactor. The layers were obtained using silane, germane and methylsilane as precursors in a hydrogen carrier gas. Growth was performed at low temperature and reduced pressure, typically 550ºC and 1 torr, respectively [19]. Four series of samples with different Ge and C content were studied: four samples with a Ge concentration of ~16% and carbon concentrations varying from 0% to 1.8% (first set, SX), three samples with a Ge concentration of ~ 13.5% and carbon concentrations varying from 0% to 1.7% (second set, X09), three samples with Ge concentrations of ~ 9-10% and carbon concentrations varying from 0% to 1.8% (third set, XX05) and five samples with Ge

concentrations of ~ 10% and carbon concentrations varying from 0% to 1.25% (fourth set, 1003/X). The sample thickness varied from 500 to 1100 Å. Table 6.1 presents the structural parameters of these samples. The Ge content was determined by Rutherford Backscattering Spectroscopy (RBS) data and the substitutional C concentration was obtained using X-ray diffraction (XRD) measurements (see Ref. [20] for details).

Table 6.1. Structural parameters of the $Si_{1-x-y}Ge_xC_y$ thin films.

Sample	Ge content, x % (by RBS)	C content, y % (by XRD)	Thickness of SiGeC layer, Å
Set 1 (SX)			
S1	16	0	700
S2	16	0.5	1000
S3	16	1.1	1000
S4	16	1.8	1000
Set 2 (X09)			
309	13.5	0	800
409	13.5	1.1	1000
509	13.5	1.7	800
Set 3 (XX05)			
1105	9	0	500
805	9.5	1.2	570
1005	10	1.8	530
Set 4 (1003/X)			
1003/1	10.5	0	1080
1003/2	9.7	0.35	1550
1003/3	9.6	0.7	1550
1003/4	10.2	1.1	1040
1103	10.2	1.25	1100

Prior to measurements, the SiGeC samples required chemical cleaning. Some samples were covered with photoresist in order to prevent SiGeC layers from the oxidation process. Those samples which were not protected by photoresist, were already oxidised.

In order to strip off the photoresist layer, for a very short time samples were treated with acetone in an ultrasonic bath. Hydrofluoric acid was applied to samples with an oxide layers in order to strip off those layers. FTIR and Raman measurements were performed immediately after cleaning in order to obtain the most accurate measurements. After the measurements, the SiGeC samples were stored in a bottle with ethanol in order to prevent them from the oxidizing.

6.2.2. Infrared and Raman measurements

Fourier Transform Infrared (FTIR) measurements on $Si_{1-x-y}Ge_xC_y$ films were performed using a Digilab FTS 6000 spectrometer with a Globar source, a KBr beam splitter, and a mercury cadmium telluride (MCT) detector. Due to the small size of samples, a microsampling Perkin-Elmer attachment was used for measurements, allowing the infrared beam to be focused to a spot size of ~ 3-5 mm in diameter. The spectra were collected with 0.5, 4 and 8 cm^{-1} resolution and 128 scans were averaged for each spectrum in order to improve the signal-to-noise ratio.
Raman spectra were registered in backscattering geometry using a micro-Raman Renishaw 1000 system equipped with a Leica microscope. An 1800 lines/mm grating was used for all measurements, providing a spectral resolution of ~ 1 cm^{-1}. As an excitation source, the 514 nm line of an Ar^+ laser with a power of 10 mW was used. The laser spot was focused on the sample surface using a 50x magnification objective. The infrared and Raman spectra obtained were analyzed using a mixture of Gaussian and Lorentzian peak fitting functions.

6.3. Results and discussion

6.3.1. FTIR results

The infrared absorption spectra of $Si_{0.887}Ge_{0.095}C_{0.018}$ and $Si_{0.91}Ge_{0.09}$ layers are shown in Fig. 6.1. The Si-C vibrational band at 605 cm^{-1} possesses a very small intensity for the SiGeC layers with a low carbon concentration (~1-2%). Additionally, this band is

overlapped by an intense Si-Si phonon band of Si crystalline lattice at 614 cm^{-1} (see Fig. 6.1). For these reasons, quantitative analysis of the band at 605 cm^{-1} becomes complicated. The spectra of the reference samples, that is, SiGe layers with no carbon, were subtracted from the spectra of samples containing C in order to remove the contribution of vibrational bands other than those attributed to carbon from the spectra corresponding to the $Si_{1-x-y}Ge_xC_y$ film. For this, we obtained a difference spectrum of:

$$A_{dif} = A_{sample} - f \cdot A_{ref} \tag{6.3}$$

for all $Si_{1-x-y}Ge_xC_y$ samples where f is the subtraction factor, A_{sample} is the absorption spectrum of the SiGe sample with C content and A_{ref} is the absorption spectrum of the reference sample. The subtraction factor f was calculated from the following equation:

$$f = \frac{d_{sample}}{d_{ref}} \tag{6.4}$$

where d_{sample} and d_{ref} are the thicknesses of the SiGeC sample and reference sample, respectively. The thickness of both samples was determined using the interference fringes from the Eqn. 5.5, where N is the number of periods, n - refractive index and ν_1, ν_2 –wavenumbers:

$$d = \frac{N}{2n \cdot (\nu_1 - \nu_2)}. \tag{6.5}$$

Fig. 6.2 shows the interference fringes in the spectra of samples 1105 and 805 collected with a resolution of 0.5 cm^{-1} in order to determine the position of the minima (or maxima), ν_1 and ν_2, with high accuracy.

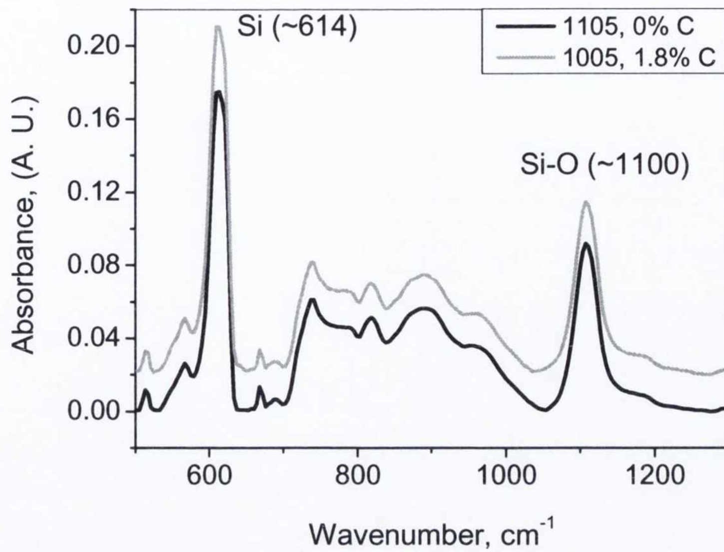

Fig. 6.1. FTIR spectra of samples 1105 and 1005 with $Si_{0.91}Ge_{0.09}$ and $Si_{0.882}Ge_{0.10}C_{0.018}$ thin films, respectively, deposited onto (100) Si substrate.

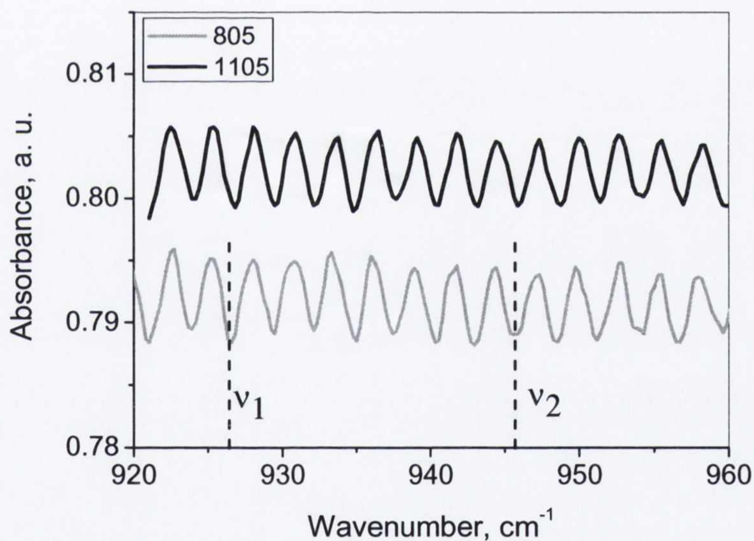

Fig. 6.2. Interference fringes obtained at resolution 0.5 cm^{-1} in FTIR spectra of samples 1105 and 805.

The infrared absorption spectra obtained after subtraction for the first set of samples are shown in Fig. 6.3 as an example. The spectral feature near ~605 cm^{-1} is due to the Si-C local mode stretching vibration of the substitutional carbon. A Full Width at Half Maximum (FWHM) of about 20 cm^{-1} is observed from the SiGeC sample with a low carbon concentration. The linewidth of the Si-C peak increases asymmetrically to higher energies with increasing carbon concentration, due to the presence of a satellite

peak at ~ 625 cm^{-1}. The region between 750 and 800 cm^{-1} was also monitored for a peak assignable to the Si-C stretching vibration. No absorption peak at ~800 cm^{-1} was observed for any of the measured SiGeC samples, indicating the absence of SiC precipitates [21]. The dependence of the integrated intensity (A_{int}) of the Si-C peak on the substitutional C content (y) is shown in Fig. 6.4, allowing comparison with the results obtained by Finkman et al. [17] for a set of samples with a Ge content of 10%. As can be seen from this figure, all four sets of samples investigated here fit the linear function:

$$A_{int}=0.39y, \tag{6.6}$$

which is independent of the Ge content. The linear fit obtained differs only slightly from the linear dependence $A_{int}=0.34y$, obtained by Finkman [17]. Therefore, we conclude that the intensity of the infrared Si-C vibrational band can indeed be used for the determination of the C content in the substitutional sites for SiGeC layers.

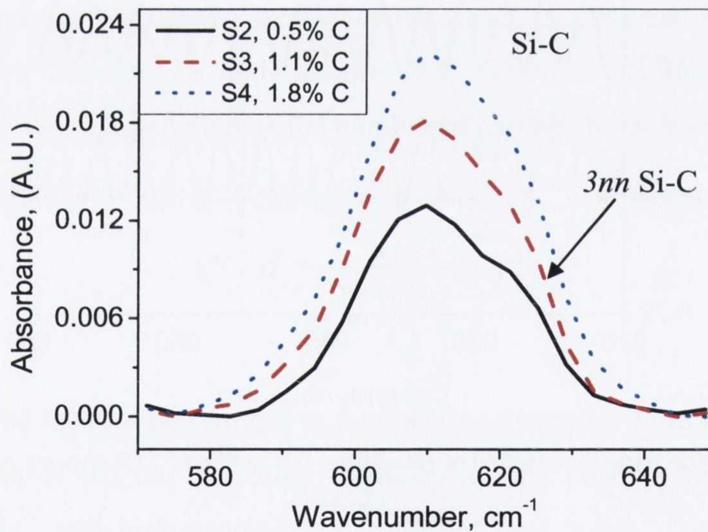

Fig. 6.3. FTIR spectra for the first set of samples (SX) with a Ge content of 16% shown in the region of the Si-C band at ~605 cm^{-1}.

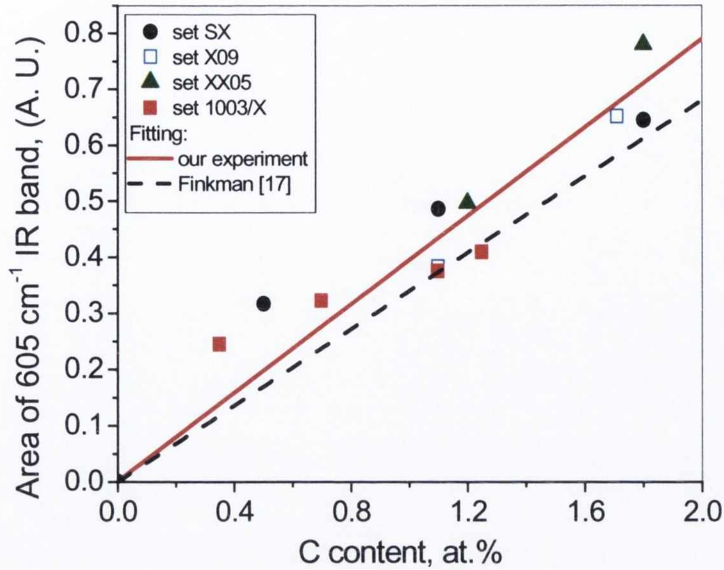

Fig. 6.4. Integrated intensity of the Si-C infrared peak as a function of carbon content for all samples. Solid line is a linear fitting function $A_{int}=0.39y$ to the experimental results obtained in this work. Dashed line is a linear fitting function $A_{int}=0.34y$ obtained by Finkman et al. [17] for one set of samples.

6.3.2. Raman results

Raman scattering offers an advantage over infrared absorption in that no absolute intensity measurements are required. This is because the intensity of the Si-C Raman peak at 605 cm^{-1} can be compared with the intensity of the Si-Si peak near 520 cm^{-1} (the Si-Si mode is infrared forbidden). The Raman spectrum of the $Si_{1-x-y}Ge_xC_y$ layer structure is composed of four distinct features, identified as the Ge-Ge (200-300 cm^{-1}), Si-Ge (350-450 cm^{-1}), Si-Si (~520 cm^{-1}) and Si-C (600-650 cm^{-1}) vibrations (see Fig. 6.5). Due to the small film thickness, the dominant peak in the spectrum is the Si-Si vibrational mode from the substrate. In the same manner used for the infrared data, the spectra of SiGe layers without carbon were used as references for subtraction from the SiGeC sample spectrum.

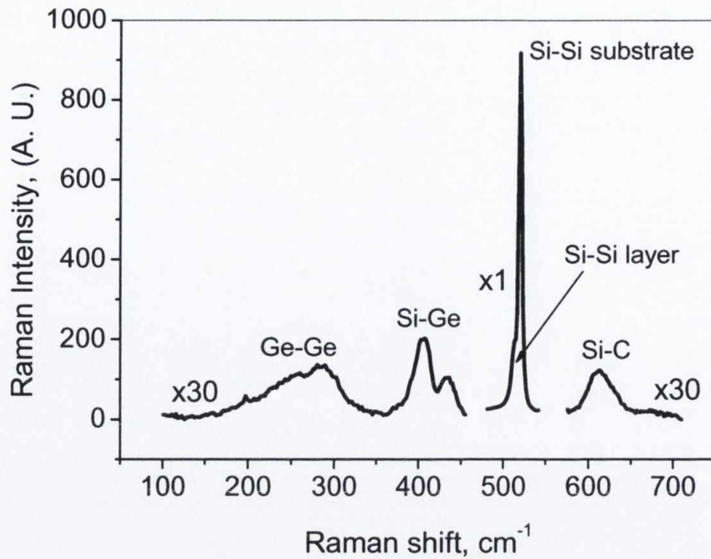

Fig. 6.5. Raman spectrum of sample S4 with $Si_{0.822}Ge_{0.16}C_{0.018}$ thin film deposited on (100) oriented Si substrate.

Figure 6.6 shows the spectra of samples $Si_{0.887}Ge_{0.095}C_{0.018}$ and $Si_{0.893}Ge_{0.095}C_{0.012}$, with the Si-C vibrational mode obtained after subtraction. Two Si-C peaks are seen (Fig. 6.6): the main C local peak at ~605 cm^{-1} corresponds to substitutional carbon, and the satellite peak at ~630 cm^{-1} is assigned to a partial contribution from the third nearest-neighbour configuration (*3nn*) of C atoms [14,16].

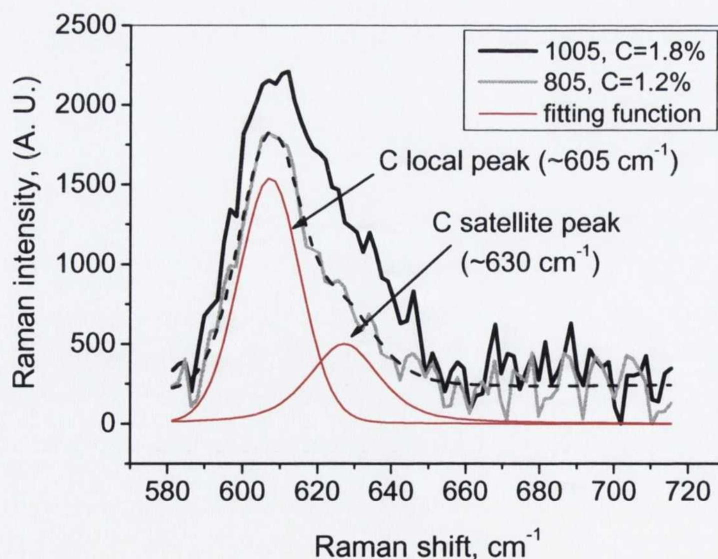

Fig. 6.6. Raman spectra of samples 1005 and 805 shown in the region of the Si-C peaks. The dashed line shows the fitting of the spectrum for sample 805 with two functions (thin lines).

Our results demonstrate that both of the peaks at ~605 and ~630 cm^{-1} change their position and intensity depending on the carbon concentration, y. There is a pronounced linear increase in the peak position of the satellite and local Si-C peak with concentration y (Fig. 6.7), which is in agreement with Refs. [17,24]. Their dependence on the C content is:

$$\omega_{Si\text{-}C} = 623.9 + 364.2y \qquad (6.7)$$

for the satellite peak, and

$$\omega_{Si\text{-}C} = 604.3 + 229.3y \qquad (6.8)$$

for the local peak. These results differ slightly from the linear dependence obtained in Ref. [17], because a larger number of samples with a wider range of Ge and C concentrations is analysed in this present work. The deviation observed could also be due to different fitting procedures. The total intensity of the Si-C peaks increases with carbon content, which is in good agreement with previously published data [17].

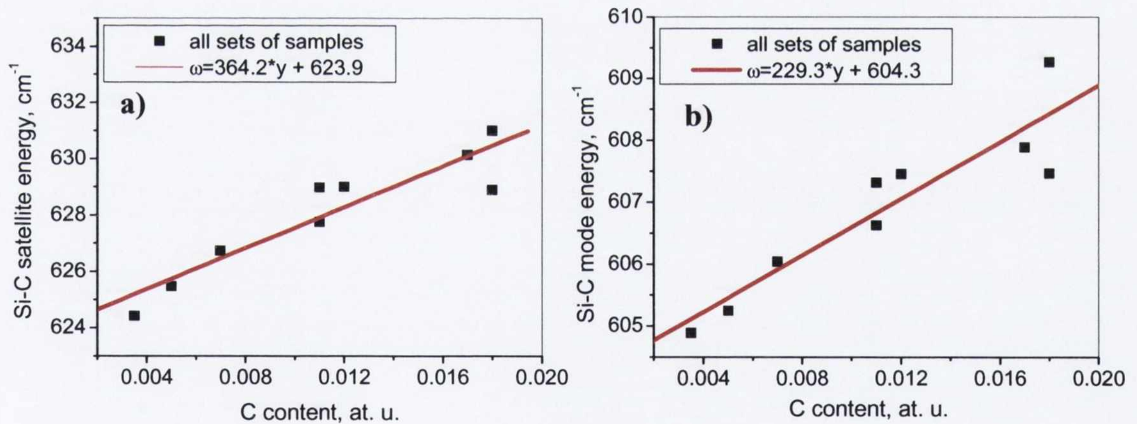

Fig. 6.7. The Raman peak position of the satellite C band (a) and the main C band (b) for the sets of samples studied in this work.

Figure 6.8 shows the ratio of the integrated intensities of the Si-C Raman peak (at ~605 cm^{-1}) to the Si-Si peak for the SiGeC layer, as a function of y. Data points are presented for all four sets of samples studied here and compared with previously

published data on a set of samples with a Ge content of 10% [17]. The ratio of the integrated intensities of the Si-C Raman peak to the Si-Si peak of the $Si_{1-x-y}Ge_xC_y$ layer increases linearly with carbon content. The linear dependence $I(C_{local})/I(Si\text{-}Si_{layer})$ versus C content can be described by the following equation:

$$I(C)/I(Si\text{-}Si) = 0.0303y. \quad (6.9)$$

As can be seen from Fig. 6.8, a linear dependence for all sets of samples with different Ge concentration is in good agreement with previously published data for samples with a Ge concentration of approximately 10% [17], as well as with results obtained in Ref. [22] for SiC alloys with C contents of up to 0.4%. This leads to the conclusion that the dependence of $I(C_{local})/I(Si\text{-}Si_{layer})$ on y (with y in the range of 0 to 1.8%) is unaffected by the Ge content. These results confirm that Raman spectroscopy can be used to determine substitutional carbon concentrations in the SiGeC layer with Ge concentrations of up to 16% and C up to 1.8%.

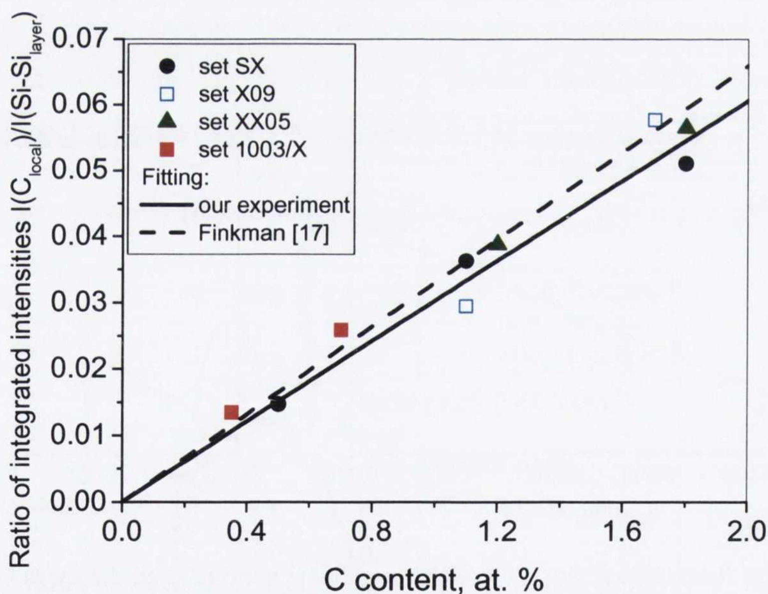

Fig. 6.8. The ratio of the integrated intensities of the Si-C Raman peak to the Si-Si peak of the $Si_{1-x-y}Ge_xC_y$ layer as a function of substitutional carbon content. Solid line is a linear fitting function $I(C)/I(Si\text{-}Si)=0.0303y$ to the results obtained in this work for all sets of samples. Dashed line is a linear fitting function $I(C)/I(Si\text{-}Si)=0.033y$ to the results for one set of samples obtained in Ref. [17].

The dependence of the peak intensity ratio of the Si-C Raman peak to the Si-Si peak of the $Si_{1-x-y}Ge_xC_y$ layer on y was also investigated (see Fig. 6.9). The experimental data are described by the linear function $I(C)/I(Si\text{-}Si)=0.0117y$. It was found that the experimental results obtained for the peak intensities have a better linear fit than the integrated intensities. This could be due to greater inaccuracy in determining the integrated intensity of Raman spectra with two overlapping peaks.

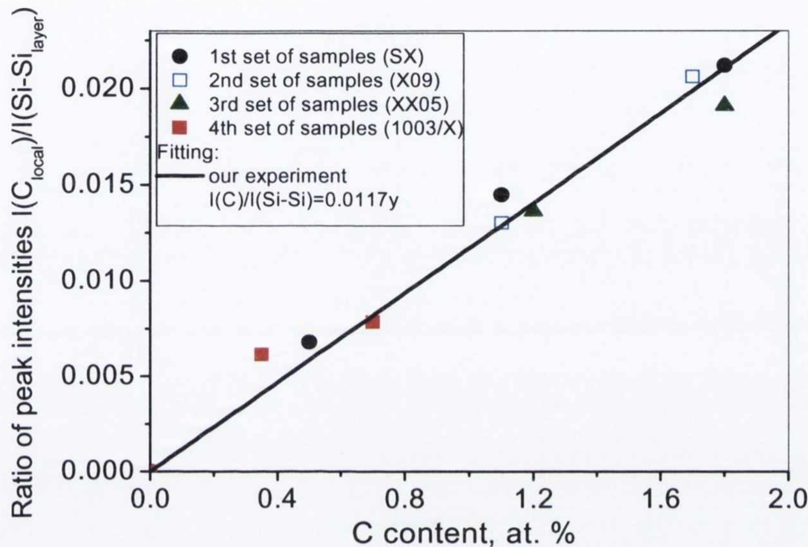

Fig. 6.9. The ratio of the peak intensities of the Si-C Raman peak to the Si-Si peak of the $Si_{1-x-y}Ge_xC_y$ layer as a function of substitutional carbon content. Solid line is a linear fitting function $I(C)/I(Si\text{-}Si)=0.0117y$ to the results obtained in this work for all sets of samples.

As predicted from calculation [18], the presence of a satellite peak in the Raman spectrum is associated with ordered carbon pairs in substitutional sites. The intensity ratio of the carbon *3nn* satellite peak to the total carbon-local-mode as a function of C content up to 1.8 % is shown in Fig. 6.10. The ratio increases with carbon content as the probability of creating *3nn* pairs increases, which is in agreement with the results obtained in Ref. [17]. The carbon pair is most strongly bound at the third-nearest-neighbour coordination. This configuration is the one most preferred by carbon atoms as for this geometry the short Si-C bonds can be accommodated easily without strong bond-bending distortion [16].

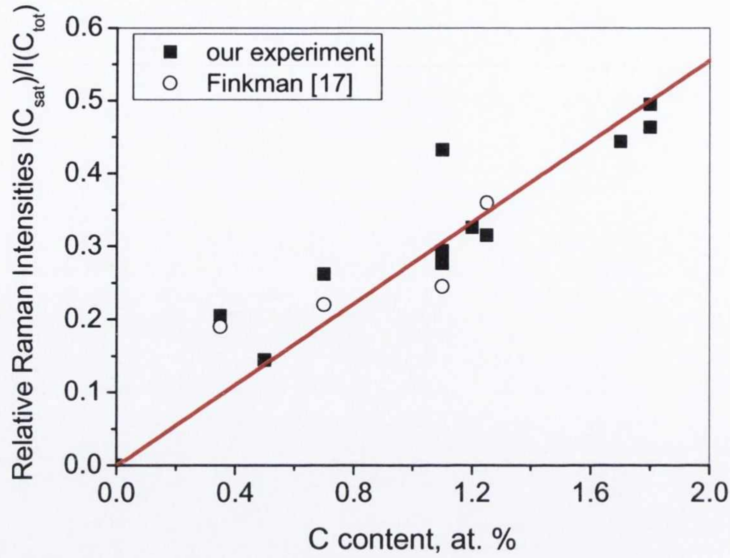

Fig. 6.10. Raman peak intensities ratio of the carbon satellite peak ($I(C_{sat})$) to the total intensity ($I(C_{tot})$) of the carbon local mode as a function of y.

Despite the absence of data points for C concentrations <0.35%, the experimental data were fitted with a linear function based on the fact [23] that for total carbon concentrations of up to 1%, carbon atoms predominantly sit on substitutional sites. This enables us to consider that the ratio of the carbon *3nn* satellite peak to the total carbon-local-mode equals zero in the absence of substitutional carbon in the SiGeC layer. The deviation of the experimental data from the linear function can be due to the fact that fitting the Raman spectra with two curves is not very accurate, particularly at low carbon concentrations.

In this study, a reduction in the frequency of the Si-Si peak with increasing C content was observed for all sample sets. This is in agreement with data obtained in Ref. [9,17] for SiGeC samples as well as in Ref. [25] for SiC layers. Figure 6.11 shows the Raman peak position of the Si-Si mode of the SiGeC layers, for two sets of samples (XX05 and 1003/X) with approximately the same Ge content (~10%), as a function of C content. The Si-Si peak from the SiGeC layer shifts to lower wavenumbers with increasing C concentration. The linear relationship obtained in this work is:

$$\omega_{Si\text{-}Si}=-0.43y+516, \tag{6.10}$$

This is in agreement with results obtained earlier for one set of samples [17]. However, different linear dependencies of ω_{Si-Si} on C content are observed for samples with a different Ge concentration (see Fig. 6.12). For the set of samples with 16% Ge content, the dependence of the Si-Si peak on the C content is described by the function:

$$\omega_{Si-Si}=-0.95y+514.4, \tag{6.11}$$

while for the set of samples with 13.5% Ge content, the experimental data fit the function:

$$\omega_{Si-Si}=-0.75y+514.9. \tag{6.12}$$

As expected, the shift of the Si-Si mode from the SiGeC layer depends on the Ge content. The Si-Si peak positions for samples with different Ge content are presented in Table 6.2. As can be seen from Figs. 6.11 and 6.12, and also from Tab. 6.2, the increase of Ge content in the $Si_{1-x-y}Ge_xC_y$ layer shifts the Si-Si phonon peak to lower frequencies. This is in agreement with theoretical calculations performed in Refs. [9,18].

Table 6.2. The Si-Si peak position of $Si_{1-x}Ge_x$ and $Si_{1-x-0.011}Ge_xC_{0.011}$ thin films with different Ge content.

Ge content, x at %	**Si-Si peak position of $Si_{1-x}Ge_x$, cm^{-1}**	**Si-Si peak position of $Si_{0.989-x}Ge_xC_{0.011}$, cm^{-1}**
~ 10	516.1	515.78
13.5	514.9	514.4
16	514.4	513.35

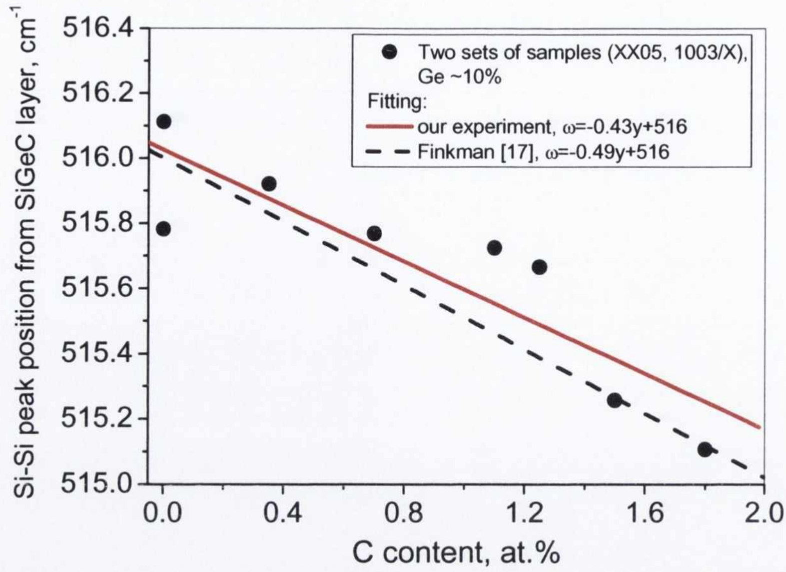

Fig. 6.11. The Raman peak position of the Si-Si mode of the $Si_{0.9-y}Ge_{0.10}C_y$ layer as a function of C content. Solid line is a fitting function to our experiment. Dashed line is a fitting function for the data from Finkman [17].

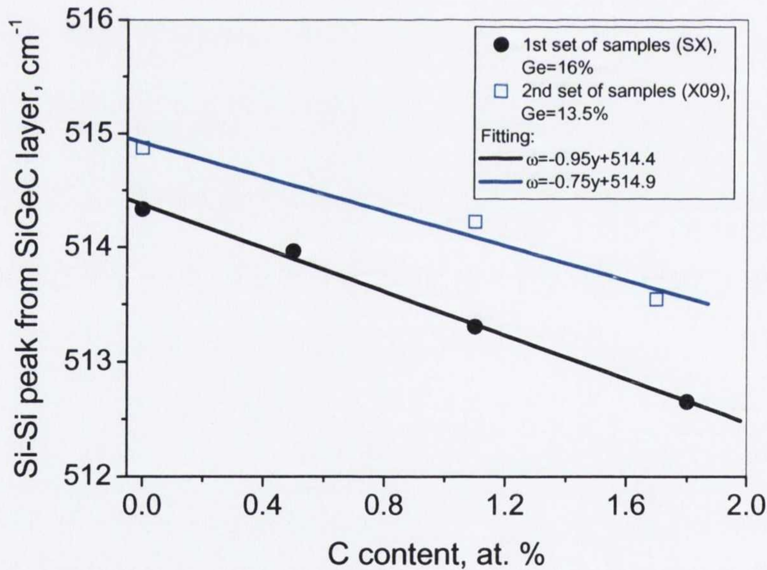

Fig. 6.12. The measured Raman peak position of Si-Si mode of the $Si_{1-x-y}Ge_xC_y$ layer for set SX with 16% of Ge and set X09 with Ge concentration of 13.5% as a function of C content.

The dependencies of the Si-Ge peak shift ($\Delta\omega_{Si-Ge}$) versus carbon content for different sets of SiGeC samples are shown in Fig. 6.13. $\Delta\omega_{Si-Ge}$ is the experimental Raman shift between the position of the Si-Ge peak from the SiGeC layer and the Si-Ge peak for the SiGe layers. Different linear dependencies of the Si-Ge peak versus C content were

obtained from different sets of samples with Ge contents ~10, 13.5 and 16% (see Fig. 6.13). For low Ge content, around ~10%, an increase of the shift, $\Delta\omega_{Si\text{-}Ge}$,with increasing carbon content is observed. For the SiGeC layer with Ge content ~13.5% we observe the opposite behaviour in the Si-Ge peak position. $\Delta\omega_{Si\text{-}Ge}$ only slightly decreases with C content. For higher Ge content, x≈16%, the shift of the Si-Ge peak decreases faster with the addition of carbon than for SiGeC layers with a Ge content around ~13.5%. A similar analysis of the compositional dependence $\Delta\omega_{Si\text{-}Ge}(y)$ with carbon content was performed in Ref. [12] for SiGeC layers with a substitutional carbon content of up to 0.5% and a Ge content of around ~20% and ~50%. As shown in Ref. [12], $\Delta\omega_{Si\text{-}Ge}(y)$ increases with increasing carbon content for a SiGeC layer with Ge content of up to 50%. However, if one considers only the data points for Ge content around 20%, the decrease of $\Delta\omega_{Si\text{-}Ge}(y)$ versus C content is clearly seen from Fig. 3 in Ref. [12]. This agrees with our experimental results obtained for SiGeC layers with Ge content, x≈16%. The behaviour of Ge-Ge peak was not considered in this work due to the low Ge content (up to 16%) in the SiGeC alloys under investigation. It has an effect on the Ge-Ge peak, but the effect is not large enough for reliable analysis.

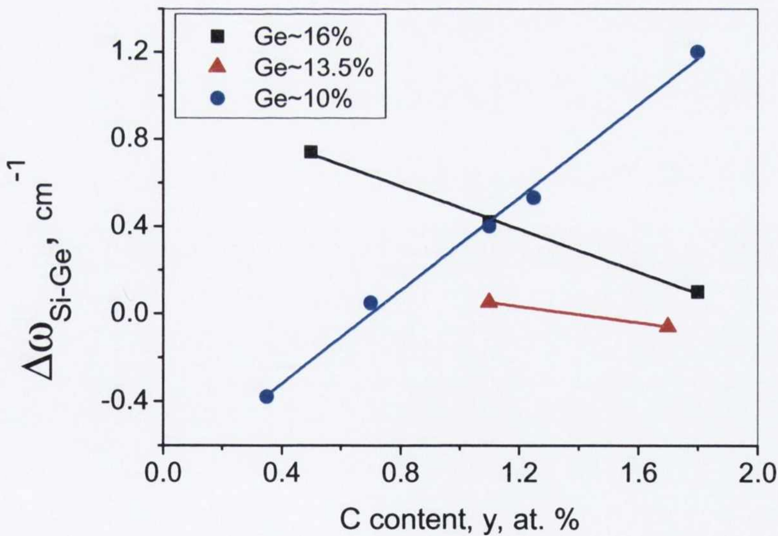

Fig. 6.13. Raman shift of the Si-Ge mode of the SiGeC layers as a function of carbon content. $\Delta\omega_{Si\text{-}Ge}$ is the Raman shift between the peak position of the Si-Ge phonon mode for SiGeC layers and the Si-Ge mode for SiGe layers.

The composition and strain dependence of the Si-Si phonon energies in $Si_{1-x}Ge_x$ layers is also analysed in this work. For small values of strain, the frequency of the Si-Si peak can be described by the expression given by Tsang [25]:

$$\omega_{Si-Si} = 520 - 68x + \Delta\omega_{Si-Si} \tag{6.13}$$

where ω_{Si-Si} is the experimental Si-Si peak position of the $Si_{1-x}Ge_x$ layer and x is the Ge content. The term $68x$ describes the compositional shift of a fully relaxed film and the last term $\Delta\omega_{Si-Si}$ describes the shift of the Si-Si peak due only to strain. $\Delta\omega_{Si-Si}$ is the frequency shift between the Si-Si peak position measured experimentally from the $Si_{1-x}Ge_x$ film and the calculated frequency of the Si-Si peak for a fully relaxed $Si_{1-x}Ge_x$ layer. It is well known that, for small values of strain, the shift in the Si-Si phonon energy is linear with strain, ε:

$$\Delta\omega_{Si-Si} = -p_{Si}\varepsilon(x), \tag{6.14}$$

where p_{Si} is a strain phonon coefficient. $\varepsilon(x)$ is obtained from the lattice mismatch between the SiGe alloy and the Si substrate:

$$\varepsilon(x) = [a(Si) - a_{rel}(Si_{1-x}Ge_x)] / a_{rel}(Si_{1-x}Ge_x). \tag{6.15}$$

$a(Si)$ is the lattice constant of Si (5.43Å) and $a_{rel}(Si_{1-x}Ge_x)$ is the lattice constant of the relaxed $Si_{1-x}Ge_x$ alloy with the appropriate composition. The calculated values of $\varepsilon(x)$, $\Delta\omega_{Si-Si}$ and the constant p_{Si} are presented in Table. 6.3. The value of the constant p_{Si} varies from 720 to 850 cm^{-1} for SiGe layers with Ge content in the range ~10 to 16%. After fitting a linear function to our data, we obtained the average value of the strain phonon coefficient, p_{Si}=790 cm^{-1}. This value is in very good agreement with the calculation performed by Rücker et al. [18] and it does not differ greatly from the value of ~830 cm^{-1} obtained experimentally by Tsang [25] for SiGe layers with Ge content < 50%, and p_{Si} calculated theoretically in Refs. [26,27]. Values of p_{Si} = 730±70 cm^{-1} were most recently obtained by Pezzoli et al. [28] for SiGe alloys with a wide range of Ge content, which is also in good agreement with the value obtained in this work.

Table 6.3. The lattice constant, strain, Si-Si peak position and strain phonon coefficient for $Si_{1-x}Ge_x$ layers.

Samples	**$a_{SiGe}(x)$, Å**	**ε(x)**	**ω_{Si-Si} for relaxed SiGe layer, cm^{-1}**	**ω_{Si-Si} experimental value, cm^{-1}**	**$\Delta\omega_{Si-Si}$, cm^{-1}**	**p_{Si}, cm^{-1}**
$Si_{0.84}Ge_{0.16}$	5.4636	-0.00615	509.12	514.33	-5.21	847
$Si_{0.865}Ge_{0.135}$	5.45835	-0.00519	510.82	514.87	-4.05	781
$Si_{0.903}Ge_{0.097}$	5.45037	-0.00374	513.40	516.11	-2.71	725
$Si_{0.895}Ge_{0.105}$	5.45205	-0.00404	512.86	515.78	-2.92	722

6.4. Conclusions

A detailed study of Raman and infrared spectra of the $Si_{1-x-y}Ge_xC_y$ layers with different Ge and C content was performed in order to gain a better understanding of carbon incorporation and its influence on SiGeC structures. An increase of the linewidth and intensity of the Si-C peaks with the carbon content was observed in both the infrared and Raman spectra, which is in agreement with previously published data, over a limited range of x and y [15,17]. FTIR analysis shows that the integrated intensity of the Si-C peak increases linearly with the C concentration and is independent of the Ge content, at least up to 16%. In all the Raman experiments performed in this study, a linear dependence of the relative Raman intensity $I(C_{local})/I(Si\text{-}Si_{layer})$ versus C content of the SiGeC samples was obtained. The relative Raman intensities increase linearly with C content and are independent of the Ge content up to 16%. We conclude that both FTIR and Raman spectroscopy can be used as non-destructive analytical methods for the determination of the amount of substitutional carbon in SiGeC layers. However, since the Raman approach uses relative intensity measurements, it is far less dependent on the sample condition than traditional infrared methods. A satellite peak at ~630 cm^{-1} has been observed in the Raman spectrum of all samples containing C, confirming the ordering of the C-C pairs during RTCVD layer growth. This is in accordance with both theoretical predictions [16] and some experimental results [10,12,17] obtained for SiGeC films (with lower Ge content) grown by MBE and RTCVD techniques. It was

shown that increasing the C and Ge content in the SiGeC lattice leads to a reduction in the frequency of the Si-Si mode. The frequency of both the satellite and local Si-C modes increases with C content. A Si-C absorption band at ~800 cm^{-1} was not observed from any of samples studied here, indicating that there is no carbon in the SiC precipitate phase.

This is the first investigation on SiGeC layers which was performed for a range of samples with different Ge content and in a wide range for possible for these structures C content. The established relationship of Infrared and Raman intensities of Si-C peak versus C content are important in semiconductor engineering as these spectroscopic methods allows for a non-destructive and relatively fast estimation of the substitutional carbon content in SiGeC layers.

References

1. K. Eberl, S.S. Iyer, S. Zollner, J.C. Tsang and F.K. LeGoues, Appl. Phys. Lett. 60, 3033 (1992)
2. P. Boucaud, C. Francis, F.H. Julien, J.M. Lourtioz, D. Bouchier, S. Bondar, B. Lambert and J.L. Regolini, Appl. Phys. Lett. 64, 875 (1994)
3. A.R. Powel, K. Eberl, F.E. Legues, B.A. Ek and S.S Iyer, J. Vac. Sci. Technol. B 11, 1064 (1993)
4. H. J. Osten, E. Bugiel and P. Zaumseil, Appl. Pys. Lett. 64, 2559 (1994)
5. G. He, M.D. Savellano, H. A. Atwater, appl. Phys. Lett. 65, 1159 (1995)
6. M. Todd, P. matsunaga, J. Kouvetakis, Appl. Phys. Lett. 67, 1247 (1995)
7. J. L. Regolini, S. Bondar, J. C. Oberlin, F. Ferrieu, M. Gauneau, B. Lambert and P. Boucaud, J. Vac. Sci. Technol. A 12, 1015 (1994)
8. J. Boulmer, P. Boucaud, C. Guedj, D. Debarre, D. Bouchier, E. Finkman, S. Prawer, K. Nugent, A. Desmur-Larre, C. Godet, I. Roca and P. Cabarrocas, J. Crystal Growth 157, 436 (1995)
9. J. Menendez, P. Gopalan, G. S. Spencer, N. Cave, and J. W. Strane, Appl.Phys.Lett. 66, 1160 (1995)
10. E. Finkman, H. Rücker, F. Meyer, S.D. Prawer, D. Bouchier, J. Boulmer, S. Bodnar and J.L. Regolini, Thin Solid Films 294, 118 (1997)
11. M. Melendez-Lira, J. Lorentzen et al. Phys. Rev. B 56, 3648 (1997)
12. M. Melendez-Lira, J. Menendez, W. Windl, O.F. Sankey, G.S. Spencer, S. Sego, R.B. Culbertson, A.E. Bair and T.L. Alford, Phys. Rev. B 54, 12866 (1996)
13. H. Nitta, J. Tanable, M. Sakuraba, J. Murota, Thin Solid Films 508, 140 (2006)
14. C. Guedj, X. Portier, A. Hairie, D. Bouchier, G. Calvarin, B. Piriou, Thin Solid Films 294, 129 (1997)
15. N. L. Rowell, D. J. Lockwood, J. M. Baribeau, J. Appl. Phys. 103, 063513 (2008)
16. H. Rücker, M. Methfessel, B. Dietrich, K. Pressel, H. J. Osten, Phys. Rev. B 53, 1302 (1996)
17. F. Finkman, F. Meyer and M. Mamor, J. Appl. Phys. 89, 2580 (2001)
18. H. Rücker and M. Methfessel, Phys. Rev. B 52, 11059 (1995)
19. S. Bodnar and J. L. Regolini. J. Vac. Sci. Technol. A 13, 2336 (1995)
20. M. Mamor, C. Guedj, P. Boucaud, F. Meyer, D. Bouchier, Mater. Res. Soc. Symp. Proc. 379, 137 (1995)

21. J. W. Strane, H. J. Stein, S.R. Lee, B. L. Doyle, S. T. Picraux, J. W. Mayer, Appl. Phys. Lett. 63, 2786 (1993)
22. M. Melendez-Lira, J. Menendez, K. M. Kramer, M. O. Thompson, N. Cave, R. Liu, J. W. Christiansen, N. D.Theodore, and J. J. Candelaria, J. Appl. Phys. 82, 4246 (1997)
23. J.-M. Baribeau, D. J. Lockwood, J. Balle, S. J. Rolfe, G. I. Sproule, Material Sci. Eng. B 89, 296 (2002)
24. D. L. Lockwood, H. X. Xu, J.-M. Baribeau, Phys. Rev. B 68, 115308 (2003)
25. J. C. Tsang, P. M. Mooney, F. Dacol, J. O. Chu, J. Appl. Phys. 75, 8098 (1994)
26. S. de Girencoli, Phys. Rev. B 46, 2412 (1992)
27. J. Zi, K. Zhang, X. Xie, Phys. Rev. B 45, 9447 (1992)
28. F. Pezzoli, E. Bonera, E. Grilli, M. Guzzi, S. Sanguinetti, D. Chrastina, G. Isella H. von Kanel, E. Wintersberger, J. Stangl, G. Bauer, Mater. Sci. in Semic. Materials Science in Semiconductor Processing 11, 279–284 (2008)

7. Micro-Raman investigation of SiC thin films grown by solid-gas phase epitaxy on Si(111)

7.1. Introduction

Silicon carbide (SiC) is a promising indirect wide band gap semiconductor (E_g >3 eV) for high-power, high frequency and high temperature devices and optical sensors in the ultraviolet regions, due to its breakdown field, high electron saturated drift velocity and good thermal conductivity [1]. Furthermore, SiC is also attractive material to be used as a substrate or buffer layer for GaN and AlN blue light-emitting diodes (LEDs) [2]. Therefore, the reproducible growth of SiC polytype on silicon wafer is in these days a very important issue for the semiconductor and MEMS industry. At present mainly two methods exist for deposition of SiC on Si substrate: molecular-beam epitaxy (MBE) [3] and chemical vapour deposition from the gas state [4]. None of these yet provide the possibility of growth of very good quality SiC substrates for use in power electronics or as a buffer layer for high quality GaN growth.

Another aspect that makes SiC material fascinating from a fundamental sciences point of view is that in some sense SiC is not a single semiconductor but a whole class of semiconductors because of its polytypism [5]. As is well known, the term "polytypism" refers to one-dimensional polymorphism, i.e. the existence of different stackings of the basic structural elements: in the present case, the (111) Si-C bilayers of the cubic (zincblende) structure, or (0001) layers of the hexagonal modifications. More than 200 SiC polytypes have been determined to date [6]. Only a few of these have practical importance and are commonly used. These include the cubic form 3C (β-type) and the 6H and 4H (α-type) hexagonal forms. The rhombohedral 15R and 21R polytypes (α-type) are also fairly common and substantial information about their properties is available. The 2H form (also known as wurtzite), although rare in SiC, is of interest as an extreme hexagonal case. All polytypes have a hexagonal frame with a carbon atom situated above the centre of a triangle of Si atoms, and underneath, a Si atom belonging to the next layer (see Fig. 7.1). The distance, a, between neighbouring silicon or carbon atoms is approximately 3.08 Å for all polytypes [7]. The distance between carbon and silicon atoms (very strong sp^3 bonding), C-Si, is $a(3/8)^{1/2}$, which

approximately equals to 1.89 Å. The distance between two silicon planes is, thus, $a(2/3)^{1/2}$ or approximately 2.52 Å. The height of a unit cell, *c*, varies between the different polytypes. The ratio *c/a*, thus, differs from polytype to polytype, but is always close to the ideal for a close-packed structure. This ratio is for instance approximately 1.641, 3.271 and 4.908 for the 2H-, 4H- and 6H-SiC polytypes respectively, whereas the equivalent ideal ratios for these polytypes are $(8/3)^{1/2}$, $2(8/3)^{1/2}$ and $3(8/3)^{1/2}$ respectively. The difference between the polytypes is the stacking order between succeeding double layers of carbon and silicon atoms.

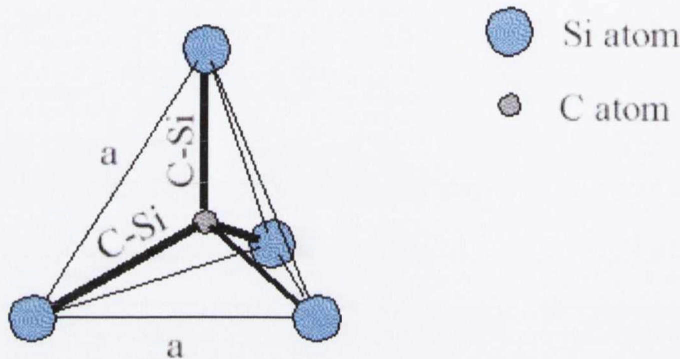

Fig. 7.1. The tetrahedral bonding of a carbon atom with its four nearest silicon neighbours. The distances a and C-Si are approximately 3.08 Å and 1.89 Å respectively.

If we consider the locations of the carbon atoms within a bilayer these form a hexagonal structure, labelled "A" in Fig. 7.2. The next bilayer then has the option of positioning its carbon atom on the "B" or the "C" lattice sites. The different polytypes will be constructed by permutations of these three positions. The 3C-SiC polytype is the only cubic polytype and it has a stacking sequence ABCABC... or ACBACB... . By observing the SiC crystal from the side as previously proposed, the stacking sequence can be projected as in Fig. 7.3, where the 4H, 6H and 3C-SiC polytypes are shown. When the stacking sequence is drawn in this manner, a zig-zag pattern is revealed. The silicon atoms labelled "h" or "k" denote Si-C double layers that reside in quasi-hexagonal or quasi-cubic environments with respect to their neighbouring bilayers above and below. In the 4H stacking sequence of ABCB, all the A sites are the cubic "k" sites and all the B and C sites are the hexagonal "h" sites. Similarly in the 6H stacking sequence of ABCACB, while all the A sites are the hexagonal "h" sites, there are two kinds of inequivalent quasi-cubic sites for B and C, denoted k_1 and k_2, respectively, as shown in Fig. 7.3.

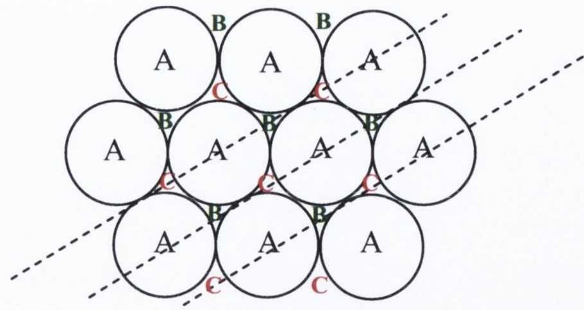

Fig. 7.2. Site locations for C atoms in the (1100) plane.

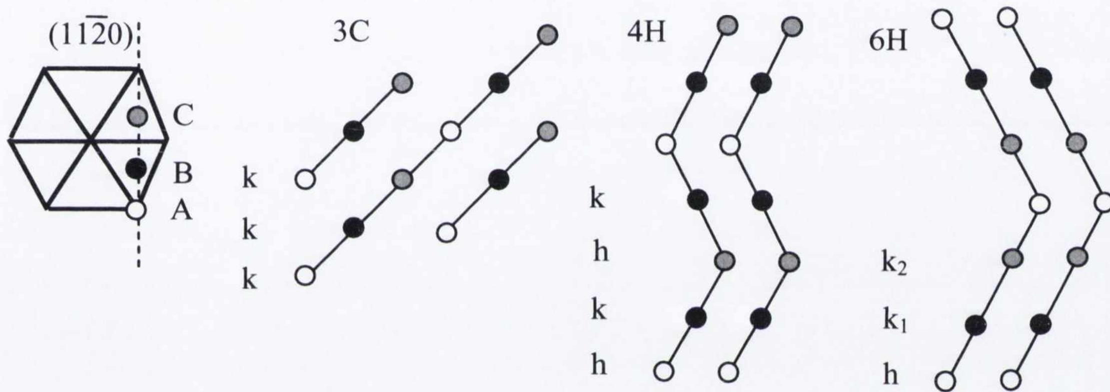

Fig. 7.3. Stacking sequence of 3C-, 4H- and 6H-SiC in (11 2 0) plane.

The different stacking of double layers of Si and C atoms affects all electronic and optical properties of the SiC crystal. The bandgaps at liquid helium temperatures of the different polytypes range between 2.39 eV for 3C-SiC and 3.33 eV for the 2H-SiC polytype. The important polytypes 6H-SiC and 4H-SiC have bandgaps at liquid helium temperatures of 3.02 eV and 3.27 eV, respectively. All polytypes are extremely hard, very inert and have high thermal conductivity. Properties such as the breakdown electric field strength, the saturated drift velocity and the impurity ionization energies are all specific for the different polytypes. In the case of 6H-SiC, the breakdown electric field strength is an order of magnitude higher than Si and the saturated drift velocity of the electrons is even higher than in the case of GaAs.

Although, the potential of SiC has been recognized for a long time, difficulty in the growth of large, high-quality SiC crystals has prevented electronic applications. One innovation has been achieved in bulk crystal growth utilizing a seeded sublimation method by which large α-SiC boule crystals can be grown with controlled polytypes [8]. Using this technique, 6H- and 4H-SiC wafers with 35 mm diameter are commercially available today [9]. For the purpose of device fabrication as well as due to lack of large size of SiC substrates, the heteroepitaxial growth of SiC thin films on Si substrates has been widely used and investigated. However, the growth of monocrystalline and defect-free SiC films on Si is one of the most difficult challenges of heteroepitaxy due to the large lattice mismatch (~20%) and thermal expansion coefficient (~8%) between 3C-SiC and Si. The most popular methods applied to deposit epitaxial SiC layers on Si are chemical vapour deposition (CVD) [4,10] and molecular beam epitaxy (MBE) [11,12,13].

Raman spectroscopy is a powerful and non-destructive technique for characterisation of SiC structures particularly since it allows the identification of its different polytypes. The Raman efficiency of SiC is sufficiently high because of the strong covalency of the Si-C bonding. In addition, the parameters of a Raman spectrum, such as peak position and linewidth, provide useful information on the stress and crystal quality of the SiC layers.

In this chapter, SiC thin layers grown by a new method of solid gas phase epitaxy were investigated using Raman spectroscopy, scanning electron microscopy (SEM), atomic force microscopy (AFM) and energy dispersive X-ray analysis (EDX). It is shown that during the epitaxial growth in an atmosphere of CO, 3C-SiC films of high crystalline quality, with a thickness of $< 1\mu m$ can be formed on a (111) Si wafer, with a simultaneous growth of voids in the silicon substrate under the SiC film. The presence of these voids has been confirmed by SEM and micro-Raman line-mapping experiments. A significant enhancement of the Raman signal was observed in SiC films grown above the voids and the mechanisms responsible for this enhancement are discussed. In addition to this, different polytypes of the SiC were investigated by means of Raman spectroscopy.

7.2. Phonon modes in Raman spectra for different polytypes of SiC

The primitive unit cell of *nH* or *3nR* polytypes contains *n* formula Si-C units. The unit cell length of the polytypes along the c-axis (corresponding to the [111] direction of the zincblende structure) is *n* times larger than that of the basic 3C polytype. Accordingly, the Brillouin zone in the direction of Γ-L is reduced to *1/n* of the basic Brillouin zone, i.e. minizone [14]. The dispersion curves of the phonon modes propagating along the *c*-direction in higher polytypes are approximated by folded dispersion curves in the basic Brillouin zone as shown schematically in Fig. 7.4. This zone folding provides a number of new phonon modes at the Γ point (q = 0), which correspond to the phonon modes inside or at the edge of the basic Brillouin zone. The phonon modes arising from the zone folding are called folded modes. Group theory analysis predicts a number of phonon modes at the Γ point for higher polytypes which correspond to the folded modes, because their unit cell contains a number of atoms. The unit cell of 3C-SiC contains one formula unit and there are both a LO mode and a doubly degenerate TO mode in optical branches.

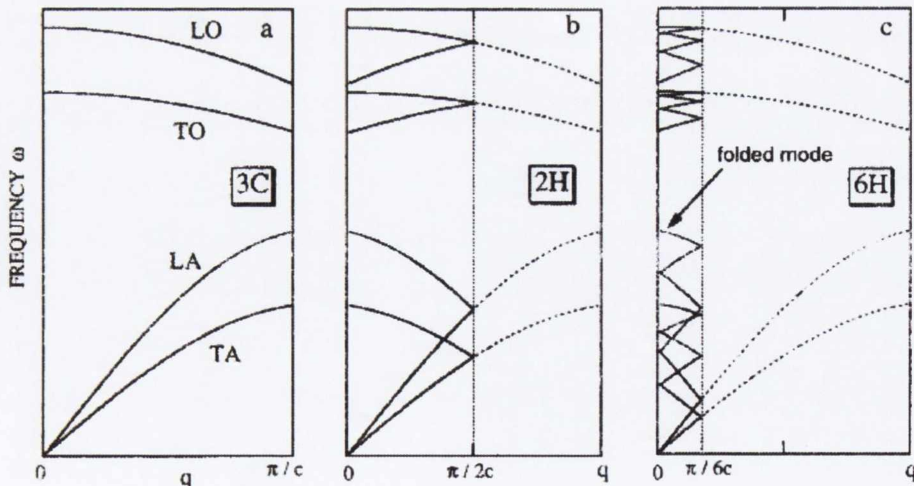

Fig. 7.4. Schematic phonon dispersion curves of 3C, 2H and 4H polytypes. Their dispersion curves are approximated by zone folded dispersion curves of 3C polytype. The zone folded mode at the Γ point can be observed in Raman spectra [1].

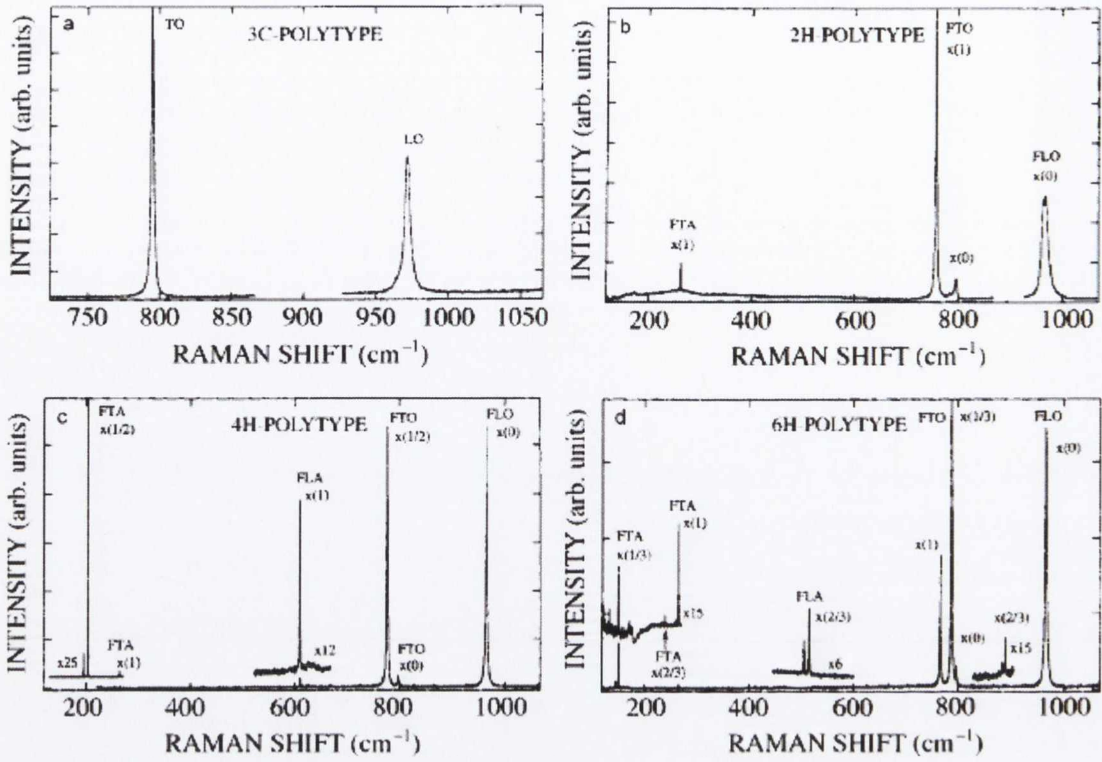

Fig. 7.5. Raman spectra of 3C, 2H, 4H and 6H- SiC measured at backscattering geometry by Nakashima et al [1].

The phonon modes are divided into axial and planar modes for which atoms displace along the directions parallel and perpendicular to the *c*-axis, respectively. A folded mode corresponds to a phonon mode having a reduced wave vector $x = q/q_B = 2m/n$ along the [111] direction in the basic Brillouin zone of the 3C-SiC. *m* is an integer less than or equal to $n/2$ and q_B is a wave vector of the zone edge in the basic Brillouin zone. Fig. 7.5 presents Raman spectra of 3C, 2H, 4H and 6H polytypes obtained by Nakashima et al [1], which are observed with the back scattering geometry. The folded modes of transverse acoustic (FTA) and optic (FTO) branches are clear to observe. As the unit cell length of the polytype is increased, the number of observable folded modes increases. As shown in Fig. 7.5, the Raman intensities of the folded modes are not equal even when these modes belong to the same symmetry. The Raman intensity profiles depend strongly on the stacking arrangement of the polytypes. This fact indicates that the intensity profile as well as frequency of the folded modes enables us to identify the stacking arrangement of the polytypes based on Raman spectra. Table 7.1 lists frequencies of the folded modes of the transverse and longitudinal phonons of main four

SiC polytypes obtained by Nakashima et al [1] and Nienhaus et al [15] based on Raman measurements.

Table 7.1. Raman frequencies of the optical and acoustic phonon modes for bulk 3C, 2H, 4H and 6H polytypes of SiC obtained by different groups.

		Raman frequency, cm^{-1}			
Polytype	**$x=q/q_B$**	**Planar acoustic FTA**	**Axial acoustic FLA**	**Planar optic FTO**	**Axial optic LTO**
3C	0	-	-	796 (794.2)	972 (972.7)
2H	0	-	-	799	968
	1	264	-	764	-
4H	0	-	-	796 (795.6)	964 (867.3)
	2/4	196, 204	-	776 (775.7)	-
	4/4	266	610		838
6H	0	-	-	797	965 (969.5)
	2/6	145, 150	-	789 (787.9)	-
	4/6	236, 241	504, 514		889
	6/6	266	-	767 (765.6)	-

*Data come from the Ref [1], in (bracket) from the Ref [10].

7.3. Experimental

7.3.1. Sample growth and description

A series of SiC films with thickness varying from ~20 nm up to 200 nm and with different polytype structure (3C, 6H, 4H) were grown on Si (111) and 6H-SiC substrates by a new method of solid gas phase epitaxy, resulting in the formation of voids in the Si substrate near the SiC/Si interface. A theoretical and experimental basis for a new method of solid-gas phase epitaxy of different polytypes of SiC on Si has been demonstrated recently in Refs. [16,17]. The deposition of SiC is achieved by means of a chemical interaction between mono-crystalline Si and CO in gas phase:

$$Si(cr) + CO(g) \downarrow = SiC(cr) + SiO(g) \uparrow . \quad (7.1)$$

The principal difference of this method, with respect to other existing methods, is that during Si (solid) and CO (gas) interaction one of the C atoms joins one atom of Si, generating SiC. At the same time, the neighbouring Si atom reacts with an oxygen atom, creating a SiO molecule which diffuses from the surface. The process of film and voids formation is shown schematically in Fig. 7.6. The essence of the suggested approach is that in the moment of SiC seed formation, simultaneous growth of the pores from the vacancies occurs. This leads to the simultaneous relaxation of the elastic strain and therefore improves the quality of the SiC film.

A low-pressure CVD system with a vertical cold-wall reactor made from sapphire, with a diameter of 40 mm and length of 50 mm, in which the central zone was heated, was used for SiC film deposition. The silicon wafer was placed on a graphite holder, with a thermocouple attached to the end. The sapphire tube was connected to a high vacuum system, consisting of diffusion and turbo-molecular pumps. Initially, the system was pumped down to a pressure of 10^{-5} - 10^{-6} Torr. For SiC deposition, a 2' (111)-orientated Si substrate with a thickness of 300 μm and a tilt of 4° was used. CO gas was supplied at a rate of 1-10 ncm^{3}/min and a pressure of 0.1-10 Torr. Growth of SiC layers occurred in the temperature range 1100°C to 1350°C and growth durations of 10-60 min were used. Due to the fabrication procedure, the SiC samples obtained are lightly doped with nitrogen at a level of 10^{14} cm^{-3}.

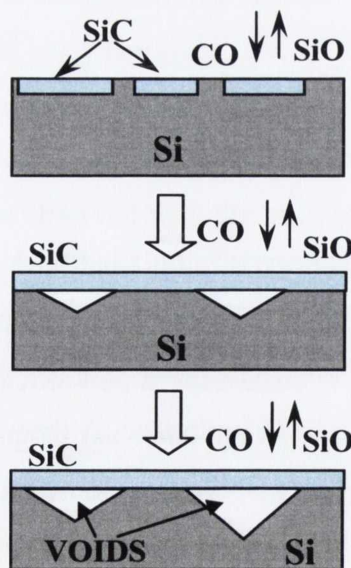

Fig. 7.6. Schematic model of void formation during SiC growth.

The 3C-SiC samples B349, B369, B378, B389, FK 468(2), FK 469(2), FK 452, FK 308, FK 341, FK 439, FK 424, 501 were grown on silicon substrate, while sample AZ consists of cubic SiC deposited on 6H-SiC substrate. Sample description is presented in Table 7.2.

Table 7.2. Description of SiC samples

3C-SiC on Si substrate	
samples	comments
B349, B369, B378, B389, FK 468(2), FK 469(2)	the presence of 6H-SiC is possible
FK 452	bad electronography
FK 308	better electronography
FK 341	much better electronography
FK 226	c-Si (111) substrate heated
c-Si	c-Si (111) substrate
FK 439	-
FK 424	-
501	Improved growth condition, presence of 6H
6H-SiC substrate	
samples	comments
AZ	cubic SiC grown on the 6H-SiC substrate
SiC 6H	bulk 6H-SiC-reference

7.3.2. Characterisation techniques

Raman spectra were registered in a backscattering geometry using a RENISHAW 1000 micro-Raman system equipped with a CCD camera and a Leica microscope. A 1800 lines/mm grating was used for all measurements, providing a spectral resolution of ~1 cm^{-1}. Two types of measurements were performed: single spot measurements both from a void area and outside the void of the SiC layers, and line mapping measurements conducted along the voids. As an excitation source for single measurements an Ar+ laser at 457 nm with a power of 10 mW was used, while for line mapping the excitation wavelength λ was 633 nm using a HeNe laser with a laser power of 10 mW. The line mapping was performed at the distance, x ranging from 0 to 13 μm with a step size of

0.5 μm, where zero corresponds to the starting point of the measurements. The laser radiation was focused onto the sample using a 100x microscope objective with short-focus working distance, providing a spot size of ~ 1 μm. UV Raman spectra were collected using the micro-Raman system HR800 model supplied by Horiba Jobin Yvon. As an excitation source the He-Cd laser at 325 nm with power of 7 mW was used. The laser spot was focused on the sample surface using 40x objectives with short-focus working distance. These measurements were carried out in Dublin City University. The UV measurements have been performed in the extended mode from 400 to 1200cm^{-1} with 60 seconds of registration time.

The cross section and surface morphologies of SiC films were examined using a Tescan Mira Scanning Electron Microscope (SEM) and using NT-MDT Atomic Force Microscopy (AFM) operating in contact mode. The quality of the crystalline structure was investigated using Energy Dispersive X-ray spectroscopy (EDX). The MATLAB program was used to simulate the enhanced behaviour of a Raman signal.

7.4. Results and discussion

7.4.1. Investigation of voids formed at SiC/Si interface and surface morphology

As shown in Fig. 7.6 the suggested growth process is accompanied by the formation of voids in Si substrate [16,17]. The voids typically have an inverted pyramid shape when using (111) Si or (100) Si. The formation of voids at the initial stage of SiC film growth (carbonization process) on Si substrate has already been discussed in the literature for different types of growth processes [18-20]. The voids can also appear in the shape of hollow rectangles or trenches [18,21]. A number of papers have been devoted to the investigation of the mechanism of void formation [18,21,22] and to their experimental verification, using mainly SEM and AFM experimental techniques. The voids formed during the process suggested in [16,17] are often filled with some type of SiC crystallites grown inside the voids and attached to the Si (110) planes (see Fig. 7.7). We assume that those SiC crystallites have orientations different than the SiC material from the top layer. Figure 7.7 presents scanning electron microscopy images of a cross section of the SiC/Si sample with observed triangular voids. In this work, the presence

of the voids is confirmed for the first time by micro-Raman spectroscopy, as reflected by the strong enhancement of Raman signal observed at the voids. The voids were also observed by optical microscopy (see Fig. 7.8). In addition, micro-Raman measurements were applied for investigation of the voids influence on properties of the SiC layer. The results on this matter will be discussed in the next paragraph.

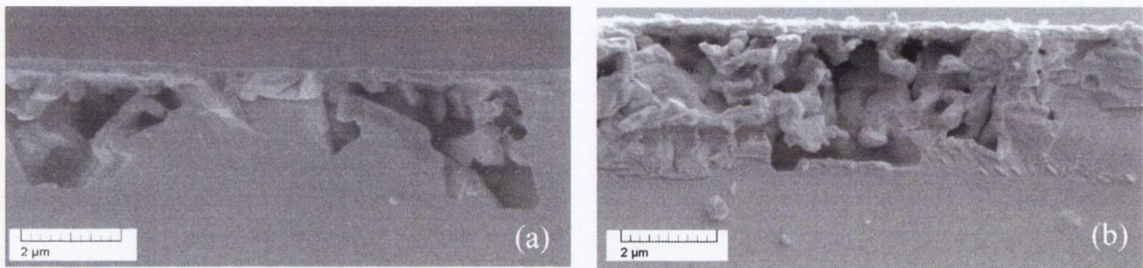

Fig. 7.7. Scanning electron microscopy images of cross section of samples SiC/(111)Si: (a) sample FK 439, (b) sample FK 452.

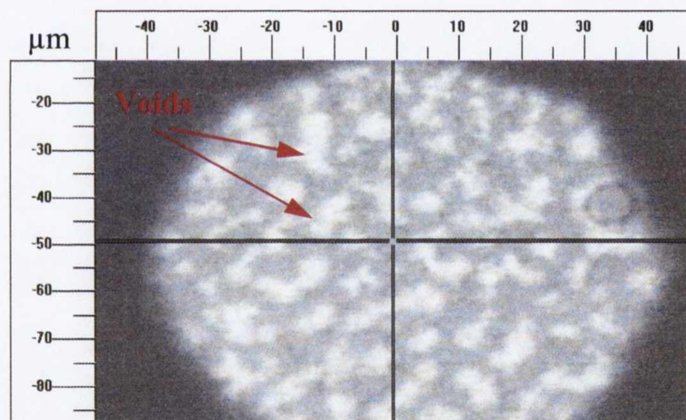

Fig. 7.8. Optical microscopy image of 3C-SiC layer with clearly seen void beneath (Renishaw).

The surface morphology of 3C-SiC layers on Si (111), investigated by SEM and AFM microscopy, is demonstrated in Figs. 7.9 and 7.10. The triangular grain structure characteristic for sample 424 is observed in Fig 7.9, which was also observed in previously published data [23,24]. The triangular shape of the grain is well explained by the strong anisotropic in plane growth rates occurring for fcc(111) films which contributes to reveal crystalline facets oriented perpendicularly to the lowest growth rate direction [24, 25]. The AFM image analysis reveals a surface roughness of about 15 nm rms on the 4x4 μm^2 scan.

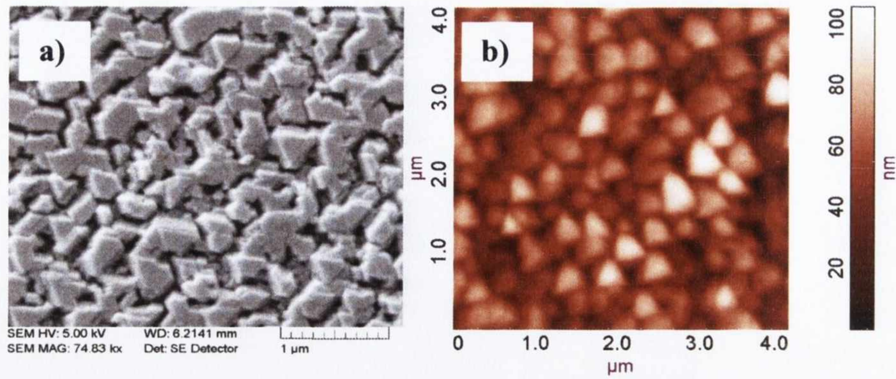

Fig. 7.9. (a) SEM and (b) AFM images of the sample 424 (surface roughness is 15 nm rms).

Figure 7.10 presents the SEM and AFM images for sample 501 which was grown with improved growth conditions. This SiC layer also reveals the mixture of 6H and 3C polytypes, which is discussed in the next paragraph. As one can see, the surface of the SiC layer is smoother than for sample 424, roughness is ~5 nm rms. A SEM image of cubic SiC layer deposited on 6H-SiC substrate is shown in Fig. 7.11. As one can see the surface of the layer grown on SiC is smooth compared to that grown on Si.

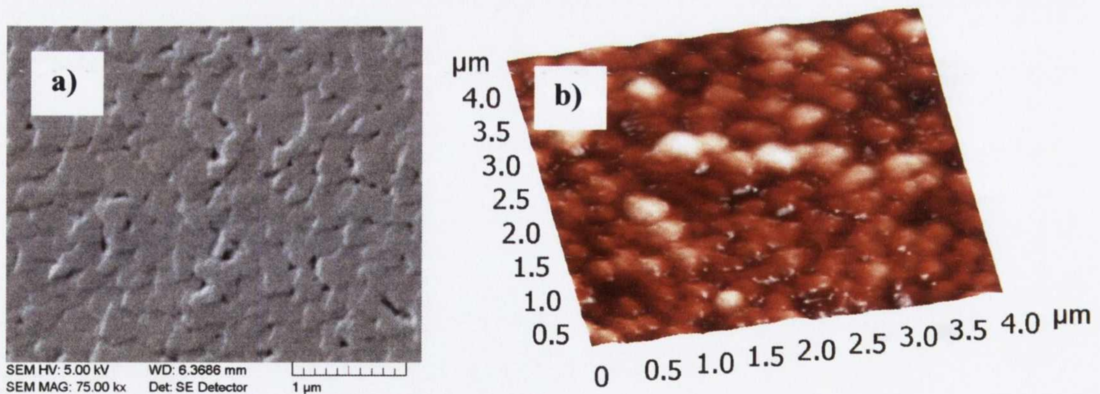

Fig. 7.10. (a) SEM and (b) AFM images of the sample 501 with improved growth condition (surface roughness is 5 nm rms).

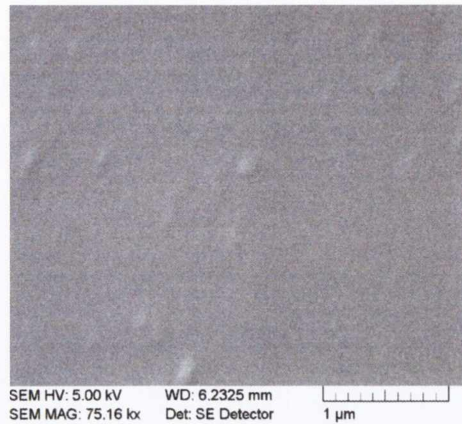

Fig. 7.11. (a) SEM images of the sample AZ (3C-SiC on 6H-SiC substrate).

7.4.2. Investigation of different polytypes of SiC layers

The results of Raman analysis of samples with SiC film grown on Si (111) and 6H-SiC substrates will be discussed in this work. Raman spectra of bulk 6H-SiC substrate and 3C-SiC layer grown on 6H-SiC substrate, measured with 457 nm of excitation wavelength, are shown in Fig. 7.12. For bulk 6H-SiC three characteristic features are observed: the LO phonon mode with A_1 symmetry at 965 cm^{-1} and two TO phonon modes at about 788 and 766 cm^{-1} with E_2 symmetry. This is in agreement with previously published data [1,15,26]. For the sample with a SiC layer grown on 6H-SiC substrate two additional bands, corresponding to 3C-SiC, were observed: TO phonon mode at ~796 cm^{-1} and low intensity LO phonon mode at ~978 cm^{-1} on the left side of LO 6H-SiC peak. Table 7.3 presents the peak position, intensity and linewidth of TO and LO SiC phonon modes for samples AZ and 6H-SiC substrate. The different polytypes of SiC can also be investigated based on the low frequency acoustic phonon modes. Fig 7.13 shows Raman spectra measured at low frequency range for sample 6H-SiC. To detect acoustic phonons a long time of laser exposure is needed. Table 7.4 presents the Raman frequency of the detected acoustic phonons which is in agreement with the previously presented Table 7.1 [1]. Figure 7.14 (a) shows Raman spectra of SiC film, grown on Si substrate, measured with 457 nm of excitation wavelength at the void and outside the void. As seen from Fig. 7.14 (a) the cubic 3C-SiC characteristic modes of TO and LO phonons appear at 794 cm^{-1} and at ~ 968 cm^{-1} respectively. This

confirms that the SiC layers, analyzed in this work, consist mainly of cubic polytype structure [1,26]. We note that the peak at 794 cm^{-1} can also be attributed to TO phonon mode for disordered 6H-SiC structure observed for the back scattering configuration. However, this peak is significantly low intensity compare with another TO peak observed in 6H-SiC at 788 cm^{-1} (see Fig. 7.12). This excludes an assignment of the peak at 794 cm^{-1} to the 6H-SiC polytype. Also, we confirmed the validity of the assignment of the peak at ~794 cm^{-1} to the cubic SiC by measuring the Raman spectra for this sample with a low Numerical Aperture (NA) objective of x10 and x20. The NA of x100 objective gathers signal over a wide angle. The backscattering geometry is distorted determining the presence of 797 cm^{-1} Raman peak in 6H polytype SiC. This peak is forbidden when the low NA objective is used. The peak at 794 cm^{-1} was observed in the Raman spectra taken with different objectives: x100, x50, x20 and x10. This also excludes assignment of the peak at 794 cm^{-1} to 6H polytype of SiC. A low intensity shoulder observed at ~ 764 cm^{-1} near the TO band indicates the presence of a small amount of 6H-SiC polytype in this SiC layer. From Figs. 7.14 (a) and 7.14 (b), the TO peak at 794 cm^{-1} demonstrates asymmetry from the low-frequency side. At the same time, in accordance with Nakashima [1], structural disorder in the SiC leads to a symmetrical widening of all the TO peaks. We conclude that the observed asymmetry of the TO peak is due to the presence of a 6H-SiC peak at ~789 cm^{-1}, clearly demonstrated by the fitting of the TO band in Fig. 7.14 (b). The wide feature seen in the range 900-1010 cm^{-1} is associated with Si second-order Raman scattering [27]. This peak is overlapped with the LO phonon peak of the SiC layer, which complicates the use of LO peak position for drawing the conclusion on SiC structure. From the fit, the full width at half maximum (FWHM) of the band at ~794 cm^{-1} is approximately ~7.7 cm^{-1} (see Tab. 7.5). This is only 2.5 cm^{-1} larger than that for relaxed 3C-SiC on a 6H-SiC substrate presented in Fig. 7.12. This relatively small difference in linewidth leads to the conclusion that the thin SiC layer grown on Si (111) has reasonably good crystalline quality. This was confirmed by energy dispersive X-ray analysis (see Fig. 7.15). Almost no circles characteristic of the polycrystalline phase are seen on Fig. 7.15, but there are well-defined Kikuchi lines, which indicates that the crystal structure of the film is of good quality [17]. It was shown by numerous x-ray diffraction and electron diffraction studies and luminescence analysis that either the hexagonal or cubic polytype structure or a mixture of both can be grown using the growth method presented in this work [17]. It was also experimentally demonstrated that the quality of

GaN layers grown on SiC layers with a mixture of cubic and hexagonal polytypes is better than that grown on single polytype of SiC [28].

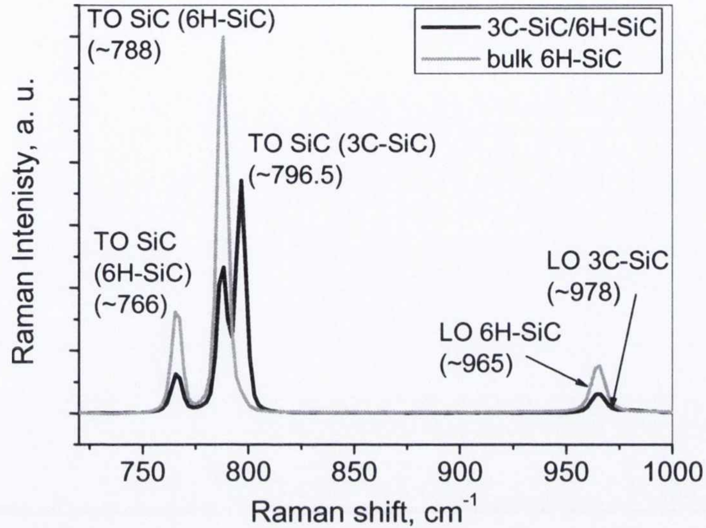

Fig. 7.12. Raman spectra of bulk 6H-SiC and sample AZ (3C-SiC layer on 6H-SiC substrate).

Table 7.3. Peak position, intensity and linewidth of TO and LO SiC phonon modes for samples AZ and 6H-SiC substrate.

Sample name	Phonon mode	Peak position, cm^{-1}	Intensity, a. u.	Linewidth, cm^{-1}
AZ	TO (E_1) SiC (6H-SiC)	766.1	25684.1	5.8
	TO ($2E_2$) SiC (6H-SiC)	787.6	93481.4	5.6
	TO SiC (3C-SiC)	796.5	146079	5.4
	LO (A_1) SiC (6H-SiC)	965	12038.7	7.4
	LO SiC (3C-SiC)	978.6	1640.1	25
	SiC 2nd order	1527.2	3644.4	46.2
Bulk 6H-SiC	TO (E_1) SiC (6H-SiC)	766.1	67651.6	5.7
	TO ($2E_2$) SiC (6H-SiC)	787.7	247188	5.6
	LO (A_1) SiC (6H-SiC)	965	30730.4	7.5
	SiC 2nd order	1525.7	4027.1	50.2

Table 7.4. Raman frequencies of acoustic phonon modes of 6H-SiC.

$X=q/q_B$	Frequency of planar acoustic phonon (FTA), cm^{-1}	Frequency of axial acoustic phonon (FLA), cm^{-1}
2/6	143, 150	-
4/6	236, 240	503.9, 513.2
6/6	265	-

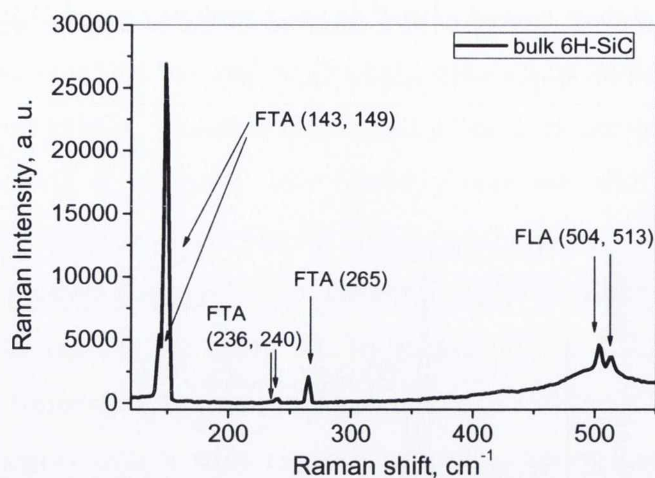

Fig. 7.13. Low frequency acoustic phonon modes of 6H polytype of SiC measured with 514 nm excitation wavelength.

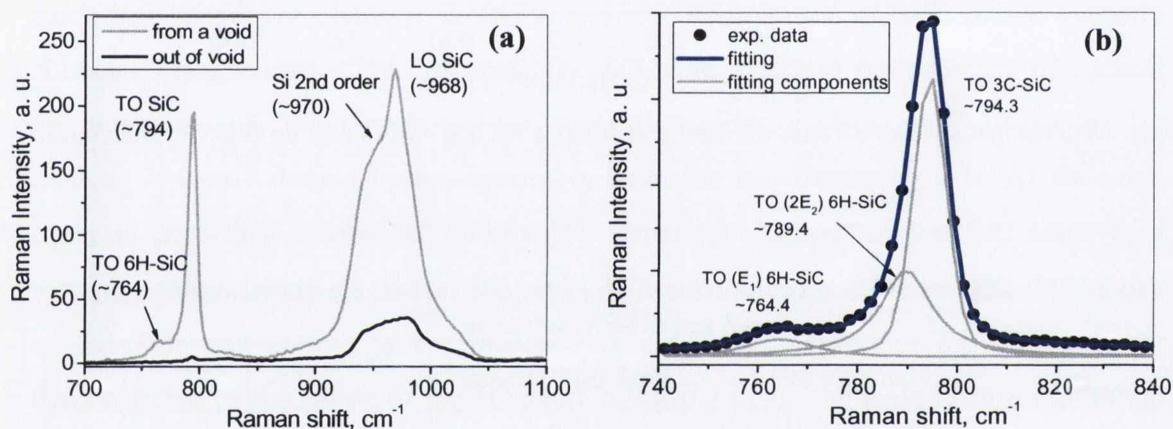

Fig. 7.14. (a) Raman spectra of SiC layer grown on Si substrate (sample FK 452) measured at the void area and from outside the void area. (b) Fitting of TO-band spectrum, detected at the void, with functions (Lorentzian + Gaussian).

Fig. 7.15. Electron diffraction pattern of 3C-SiC layer on Si (111).

Table 7.5. Peak position, intensity and linewidth of TO and LO SiC phonon modes for sample 452.

name of sample	TO SiC				SiC 2nd order		
	mode	peak position, cm^{-1}	intensity, a. u.	linewidth, cm^{-1}	peak position, cm^{-1}	intensity, a. u.	linewidth, cm^{-1}
452	TO SiC (3C-SiC)	794.4	19797.5	7.7	1517.6	1736.2	43.6
	TO ($2E_2$) SiC (6H-SiC)	789.7	5031	12			
	TO (E_1) SiC (6H-SiC)	764.4	1057	16.6			

The UV Raman spectra of representative SiC samples are presented in Fig. 7.16. The UV light has smaller depth of penetration than visible laser light. Due to this fact, LO SiC phonon mode related to cubic SiC structure is more pronounced as can be seen from Fig. 7.16. Weak bands are observed at ~ 765 cm^{-1} and 790 cm^{-1} related to TO 6H-SiC peaks for samples FK 452 and FK 469. This provides evidence of the presence of small amount of 6H- SiC in 3C-SiC layers. The peak position, intensity and linewidth of TO and LO Si-C phonon modes measured for different samples with UV excitation wavelength are presented in Table 7.6.

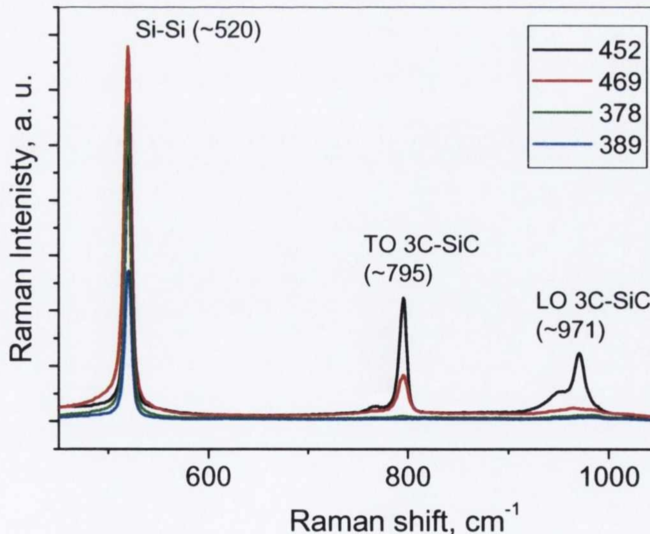

Fig. 7.16. Raman spectra of samples: FK 452, FK 469, FK 378, FK 389 measured with UV excitation wavelength.

Table 7.6. Peak position, intensity and linewidth of TO and LO Si-C phonon modes for different samples measured with UV excitation wavelength.

name of sample	TO SiC			LO SiC
	peak position, cm^{-1}	intensity, a. u.	linewidth, cm^{-1}	peak position, cm^{-1}
452	795.1	691.2	8.3	970.8
469	795.5	3309.7	10.9	-
378	794.9	165.4	16	-
308	794.1	315.5	11.1	-
341	794.4	1490.8	13	-
369	794.9	264.2	17.6	-
468	794.3	3504.9	11.1	969.5
501	794.1	3554.8	10.2	970.9

7.4.3. Raman enhancement and micro-Raman mapping measurements

A large enhancement of the Raman peak intensity, by up to 30 times for some samples, for both TO and LO modes, is observed at the void area in Fig. 7.14. This enhancement enables the acquisition of a reasonably good Raman spectrum from ultra-thin SiC layers, as shown in Fig. 7.14 (a). Three mechanisms may contribute to the observed enhancement of the Raman signal: i) multiple reflection of the incident light at the void, ii) interference and multiple reflection of the Raman signal in the SiC layer above the void and iii) the presence of additional SiC material grown on the (110) Si ribs of the pyramid inside the voids [17,18]. The first mechanism is also responsible for the moderate enhancement of the Si second order peak, by approximately 4 times, from the Si ribs. A somewhat similar effect was discussed for porous Si and SiC in Refs. [29,30]. For the second mechanism mentioned, the enhancement of the Raman signal in thin films, surrounded by media with low refractive indexes, was discussed recently for graphene in Ref. [31]. We use a similar approach in the estimation of the effect of multiple reflections of the Raman signal on the peak intensity from the thin film. This is done by using a three-layer model consisting of SiC-Air-Silicon. This model compared with the line-mapping results will be discussed further in this paragraph. Fig. 7.17 (a) presents an optical microscopy image of a 3C-SiC/Si sample, where the brighter dots correspond to the voids seen under thin SiC layers. The arrow on Fig. 7.17 (a) shows the route of the line-mapping measurements. Figures 7.17 (b), (c) and (d) show Raman line-maps for the peak position, peak intensity and linewidth of the SiC TO-peak along the

voids for the 3C-SiC/Si sample. Since the TO peak position is more sensitive to the stress relaxation effect [29], the TO SiC peak was used to study the relaxation level in 3C-SiC films with different thicknesses and void size. The Raman position of the SiC TO-band in a relaxed 3C-SiC structure is typically located at 796 cm^{-1}, but for SiC layers grown on Si, the TO band shifts to the low frequency side [32]. We observed the TO-SiC peak position at around 794 cm^{-1}, indicating that the SiC layer is under stress. Tensile stress in the SiC layer is observed since the lattice constant for SiC (a_{SiC}=4.3Å) is less than that for Si (a_{Si} = 5.38Å). Fig. 7.17 (b) presents the peak position of the TO-SiC peak as a function of distance, *x*. From this figure, the peak position varies from 794.5 cm^{-1} at the middle of the void to 793.5 cm^{-1} outside the voids. A larger tensile stress is observed outside the voids than at the voids, confirming that partial stress relief is occurring at the cavities.

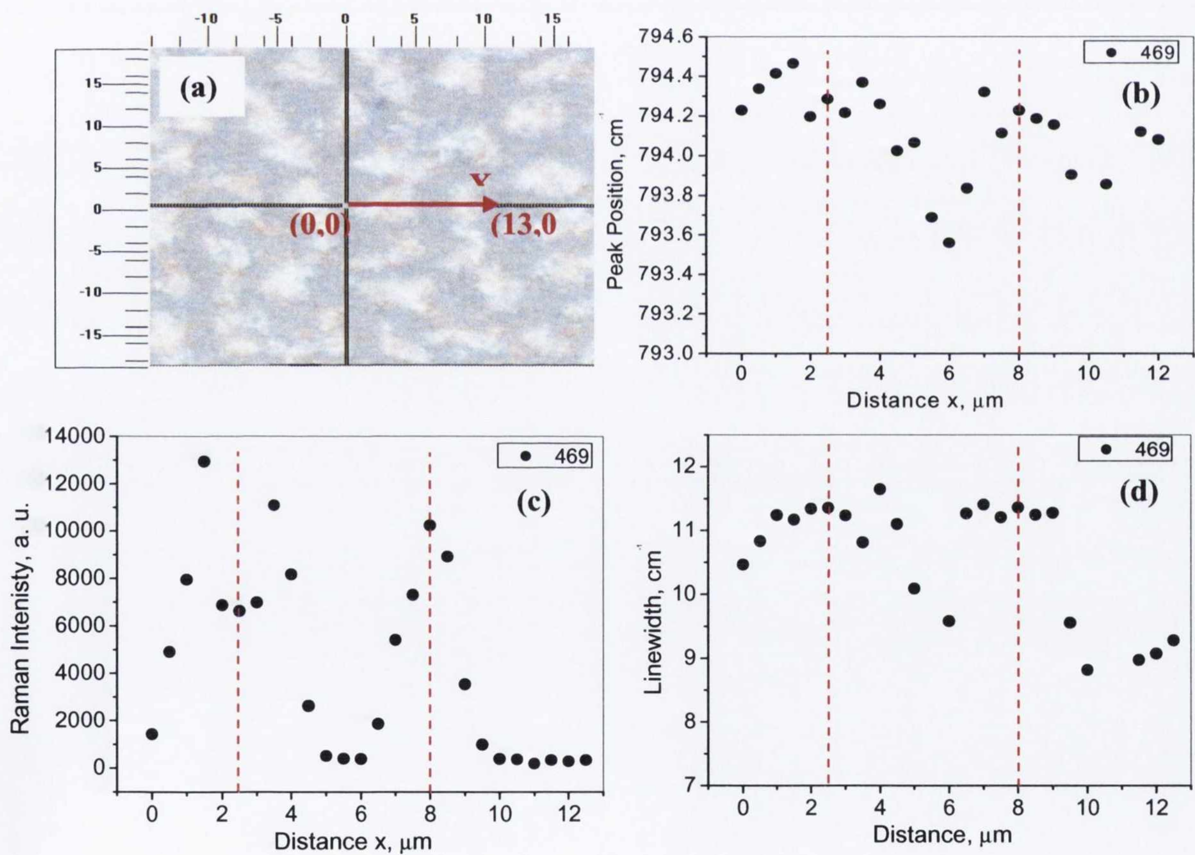

Fig. 7.17. (a) Top view of the sample of 3C-SiC obtained by optical microscopy (scale in μm), the red arrow shows the mapping line. Results of Raman line-mapping for (b) peak position, (c) linewidth, and (d) peak intensity of the TO phonon mode for the 3C-SiC/Si sample (dashed lines correspond to the centres of the voids).

Fig. 7.17 (d) shows the full width at half maximum (FWHM) of the SiC TO-mode as a function of mapping distance. The linewidth of the TO peak significantly increases at the cavities (by ~ 3 cm^{-1}), as a result of the contribution of differently oriented SiC materials inside the void as mentioned earlier. The strong enhancement of the Raman peak intensity of the SiC TO-mode, by a factor of 15, inside the cavities is confirmed by the line mapping measurements presented in Fig. 7.17 (c). It can be seen that the enhancement is significantly larger at the centre of the voids, corresponding to a larger cavity depth or a thicker Air layer. The enhanced behaviour of the Raman signal was calculated considering both the multilayer interference of incident light and the multi-reflection of the Raman signal based on Fresnel's equation [33]. The MATLAB program was used for this purpose. We consider the incident light from air ($n_0=1$) onto a SiC layer (n_1), Air(n_2)/Si(n_3) double-layer system, where $n_1=2.65-0.2i$, $n_2=1.5$, and $n_3=4.15-0.044i$ are refractive indices of SiC, Air, and Si at 633 nm, respectively. The extinction coefficient, $k_1=0.2$, was introduced to the complex refractive index of SiC layer due to the observed surface roughness of SiC film. The refractive index of air in the void was taken ~1.5 due to parts of Si and SiC present in the void. d_1 is the thickness of SiC layer which is considered as a sum of 1 nm thick SiC monolayers. Therefore the thickness d_1 can be estimated as $d_1=N\Delta d$ and $\Delta d=1\ nm$, where N is the number of mono-layers. d_2 is the depth of the void filled with Air and the Si substrate is considered as semi-infinite. The TO-SiC Raman intensity of SiC layer depends on the electric field distribution, which is a result of interference between all transmitted optical paths in SiC layer. The total amplitude of the electric field at certain depth y in SiC layer is viewed as a sum of the infinite transmitted laser, whose amplitudes are:

$$
\begin{aligned}
& t_1 e^{\beta y} e^{-i(2\pi\tilde{n}_1 y/\lambda)}, \\
& t_1 r' e^{\beta(2d_1-y)} e^{-i(2\pi\tilde{n}_1(2d_1-y)/\lambda)}, \\
& -t_1 e^{\beta y} e^{-i(2\pi\tilde{n}_1 y/\lambda)} r_1 r' e^{-2if_{i1}} e^{2\beta d_1}, \\
& -t_1 r' e^{\beta(2d_1-y)} e^{-i(2\pi\tilde{n}_1(2d_1-y)/\lambda)} r_1 r' e^{-2if_{i1}} e^{2\beta d_1}, \ldots,
\end{aligned}
\tag{7.2}
$$

where $\beta=-2\pi k_1/\lambda$ (λ is the excitation wavelength) emerges as a measure of the absorption in the SiC layer, $t_1=2n_0/(n_0+\tilde{n}_1)$ is transmission coefficients at the interface of air/SiC, $r_1=(n_0-\tilde{n}_1)/(n_0+\tilde{n}_1)$ is reflection coefficient at the interface of

air/SiC, $f_{i1,2} = -2\pi\tilde{n}_{1,2}d_{1,2}/\lambda$ are the phase differences when light passes through SiC monolayers and Air layers in the void, respectively. Here, $r' = \left(r_2 + r_3 e^{-2if_{i2}}\right)/\left(1 + r_2 r_3 e^{-2if_{i2}}\right)$ is the effective reflection coefficient of SiC/(Air void in Si) interface, where $r_2 = (\tilde{n}_1 - n_2)/(\tilde{n}_1 + n_2)$ and $r_3 = (n_2 - \tilde{n}_3)/(n_2 + \tilde{n}_3)$ are individual reflection coefficients at the interface of SiC/Air void and Air void/Si. Thus, the total amplitude of the electric field at the depth y is:

$$t = \frac{t_1 e^{\beta y} e^{-i(2\pi\tilde{n}_1 y/\lambda)} t_1 r' e^{\beta(2d_1 - y)} e^{-i(2\pi\tilde{n}_1(2d_1 - y)/\lambda)}}{1 + r_1 r' e^{-2if_{i1}} e^{2\beta d_1}} \tag{7.3}$$

In addition, further consideration should be applied to the multireflection of scattering Raman light in SiC at the interface of SiC/Air and SiC/Air void in Si, which contribute to the detected Raman signal. Thus, the detected signal is a result of summation of infinite transmitted light from the interface of SiC/Air, which makes the amplitude multiplied by:

$$\gamma = \frac{\left(e^{\beta y} + r' e^{\beta(2d_1 - y)}\right) t_1'}{1 + r_1 r' e^{2\beta d_1}} \tag{7.4}$$

where $t_1' = \left(1 - r_1^2\right)/t_1$ represents the transmission coefficients at the interface of SiC/Air. In the equation above, the interference of Raman scattering light is not considered as the phase of spontaneous random Raman lights. Thus, the total Raman signal can be expressed as:

$$I = \int_0^{d_1} |t\gamma|^2 \Delta y \tag{7.5}$$

Figure 7.18 shows the calculation results of Raman intensity of TO Si-C band as a function of thickness of SiC layer. The black curve shows the calculation result for SiC layer directly on Si without the Air void. It can be seen that the Raman intensity of the Si-C peak increases as the thickness of the layer increases, which is in agreement with

experimental results. The red curve gives the calculated results for SiC layer grown on Air void.

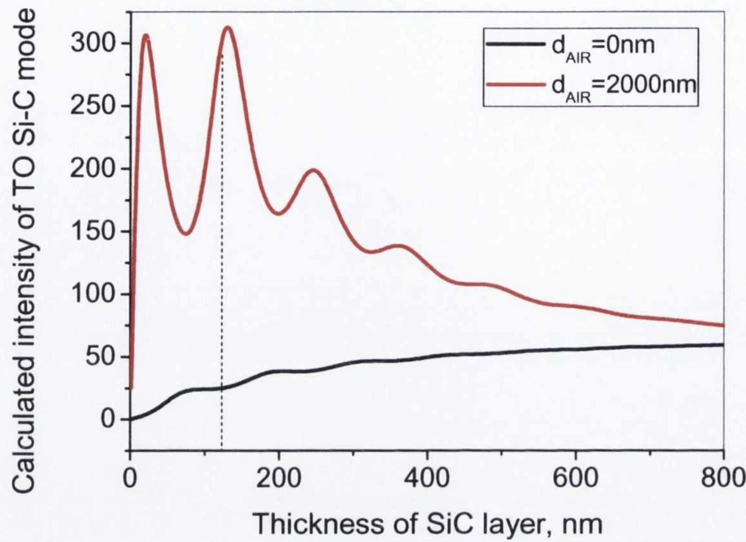

Fig. 7.18. The calculation results of the Raman intensity of the TO Si-C phonon mode versus the thickness of SiC layer with (red) and without (black) air void beneath.

With varying the thickness of the Air layer (cavity depth) from 0 to 2000 nm, and the thickness of the SiC layer between 0 and 800 nm, the Raman enhancement at the centre of the void was estimated to be approximately 12 times larger than that at the edge of the void for a SiC layer with a thickness of about 120 nm. An increase in the layer thickness to 800 nm reduces the Raman signal enhancement by a factor of ~ 8. This was confirmed experimentally by Raman line-mapping measurements for the sample with an ~800 nm thick SiC layer, where enhancement of the Raman signal by a factor of 1.5 was detected at the void centre. These results were also confirmed by the Transfer Matrix Method calculations [34]. Figure 7.19 presents the evolution of experimental Raman spectra in the range of TO SiC peak with mapping distance along 4 voids for sample FK 452. As one can see, the significant increase of the phonon mode at ~794 cm^{-1} is observed at the centre of each of the voids. Raman area maps were also performed at the voids (see Fig. 7.20). The maximum intensity of the TO Si-C mode in Fig. 7.20 (a) corresponds exactly to the voids observed in the microscopy image in Fig. 7.20 (b). Peak intensity increases as the depth of the void increases.

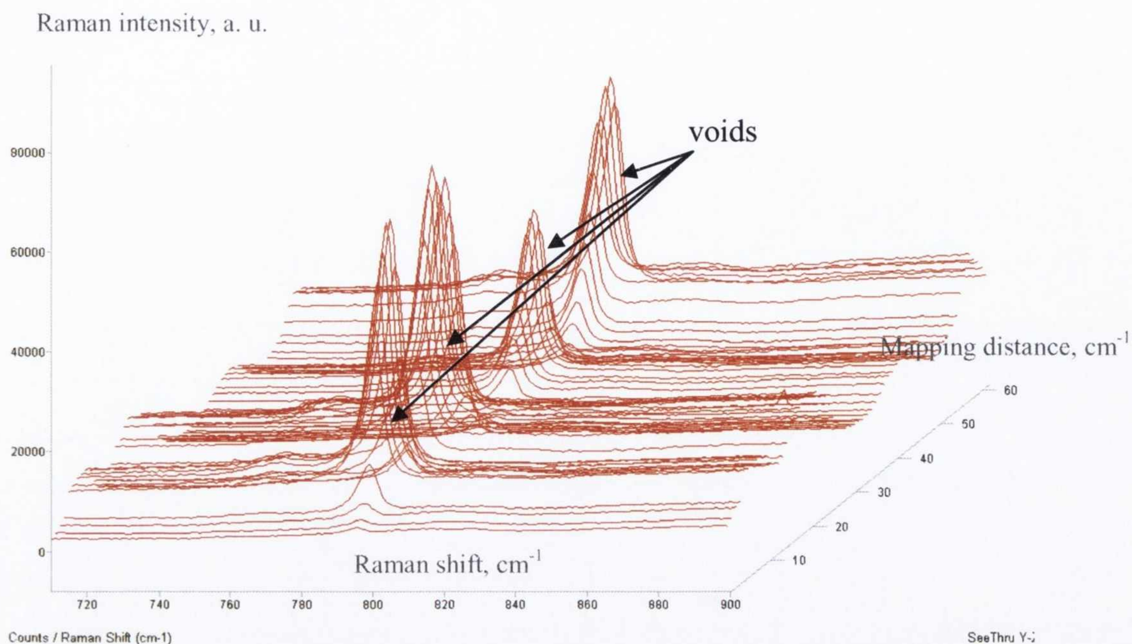

Fig. 7.19. Evolution of Si-C peak along four voids for sample FK 452.

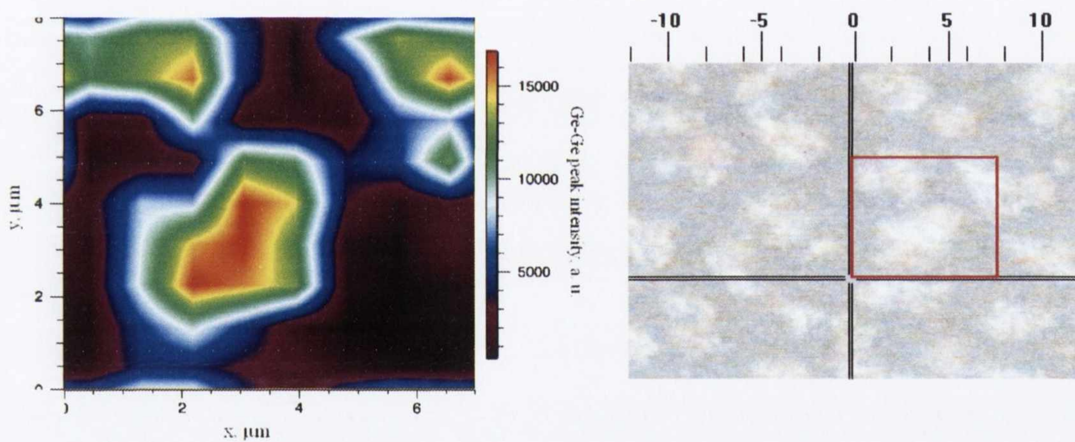

Fig. 7.20. (a) Raman area map of the Si-C peak intensity corresponding to (b) the optical microscopy image of mapped area.

7.5. Conclusions

The thin SiC layers grown by a new method of solid-gas phase epitaxy were investigated using Raman spectroscopy, SEM, AFM and EDX techniques. It is shown that the SiC layer on Si (111) investigated here is composed of a cubic polytype of SiC with a small amount of 6H-SiC. The presence of the voids has been experimentally confirmed by micro-Raman spectroscopy and scanning electron microscopy. Line and area Raman maps were performed at the voids area. The strong enhancement in the peak intensity of the TO and LO modes is observed for the Raman signal measured in the void area. The intensity of TO Si-C peak increases with void depth. The enhancement of the electromagnetic field at the voids was also confirmed by theoretical calculation based on Fresnel's equation. The Raman line mapping experiments presented in this work confirm that the presence of the voids formed in the Si substrate under the SiC layer causes relaxation of the elastic stress in the SiC layer. This enhancement of the Raman signal is advantageous as it allows micro-Raman measurements to be used for the detection of different polytypes in ultra thin SiC layers. It was demonstrated that the quality of GaN layers grown on SiC layers consisting of a mixture of the cubic and hexagonal polytypes is better than that of GaN layers grown on a single SiC polytype [28].

References

1. S. Nakashima, H. Harima, Phys. Stat. Sol. A 162, 39 (1997)
2. A. Wakahara, H. Oishi, H. Okada, A. Yoshida, Y. Koji, M. Ishida., J. Cryst. Growth 236, 21 (2002)
3. K. Zekentes, V. Papaioannou, B. Pecz and J. Stoemenos, J. Cryst. Growth, Vol. 157, 392 (1995)
4. A. J. Steckl, C. Yuan, and J. P. Li, M. J. Loboda, Appl. Phys. Lett. 63, 3347 (1993)
5. A. P. Verma, P. Krishna, Polymorphism and Polytypism in Crystals, Wiley, New York, 1996
6. N. W. Jeeps, T. F. Page, Prog. Cryst. Growth Charact. 7, 259 (1983)
7. W.F. Knippenberg, Philips Research Reports, 18, 161 (1963)
8. Yu.M. Tairo, V.F. Tsvetkov, J. Cryst. Growth, 52, 146 (1981)
9. Cree Research Inc., Durham, NC, USA
10. J. A. Powel, L. G. Matus, M. A. Kuzmarski, J. Elektrochem. Soc., 134, 1558 (1987)
11. S. Motoyama, N. Morikawa, M. Nasu and S. Kaneda, J. Appl. Phys., 68,101 (1990)
12. T. Sugii, T. Aoyama and T. Ito, J. Electrochem. Soc., 137, 989 (1990)
13. K. Zekentes, V. Papaioannou, B. Pecz and J. Stoemenos, J. Cryst. Growth, Vol. 157, 392 (1995)
14. D. W. Feldman, J. H. Parker, Jr., W. J. Choyke, and L. Patrick, Phys. Rev. 170, 698 (1968)
15. H. Nienhaus, T.U. Kampen, W. Monch, Surf. Sci. 324, L328 (1995)
16. S.A. Kukushkin, A.V. Osipov and N.A. Feoktistov, Patent RF No 2008102398, filed on 22 January 2008
17. S.A. Kukushkin and A.V. Osipov, Rus. Solid State Phys. 50, 1188 (2008)
18. R. Scholz, U. Gösele, E. Niemann, F. Wischmeyer, Appl. Phys. A 64, 115.125 (1997)
19. A. Severino, G. D'Arrigo, C. Bongiorno, S. Scalese, and F. La Via, G. Foti, J.Appl. Phys. 102, 023518 (2007)
20. M. Kitabatake, Phys. Stat. Sol. B 202, 405 (1997)
21. J. P. Li, A. J. Steckl, J. Electrochem. Soc. 142, 2 (1995)
22. W. Attenberger, J. Lindner, V. Cimalla, J. Pezoldt, Materials Science and Engineering B 61/62, 544 (1999)

23. R. Anzalone, A. Severino, G. D'Arrigo, C. Bongiorno, G. Abbondanza, G. Foti, S. Saddow, F. La Via, J. Appl. Phys. 105, 084910 (2009)
24. M. Portail, T. Chassagne, S. Roy, C. Moisson, M. Zielinski, Mat. Science Forum 645, 155 (2010)
25. J. Nishizawa, M. Kimura, J. Crst. Growth 74, 331 (1986)
26. Z. C. Feng, C. C. Tin, R. Hu, K. T. Yue, Semicond. Sci. Technol. 10, 1418 (2005)
27. P.A. Temple, C.E. Hathaway, Phys. Rev. B 7, 3685 (1973)
28. I.G.Aksyanov, V.N.Bessolov, Yu.V.Zhilyaev, M.E.Kompan, E.V.Konenkova, S.A.Kukushkin, A.V.Osipov, N.A.Feoktistov, Sh.Sharofidinov, M.P.Shcheglov, submitted for publication
29. V. Lysenko, D. Barbier, B. Champagnon, Appl. Phys.Lett. 79, 2366 (2001)
30. I. Gregora, B. Champagnon, L. Saviot, and Y. Monin, Thin Solid Film 255, 139 (1995)
31. Y.Y. Wang, Z.H. Ni, Z.X. Shen, H.M. Wang and Y.H. Wu, Appl.Phys.Lett. 92, 043121 (2008)
32. Z.C. Feng, W.J. Choyke and J.A. Powell, J. Appl. Phys. 64, 6827 (1988)
33. Y.Y. Wang, Z.H. Ni, Z.X. Shen, H.M. Wang and Y.H. Wu, Appl.Phys.Lett. 92, 043121 (2008)
34. S. Dyakov, J. Wasyluk and T.S. Perova, in preparation

8. Ultraviolet and visible Raman analysis of thin a-C films grown by filtered cathodic arc deposition

8.1. Introduction

Amorphous carbon, or free, reactive carbon, is an allotrope of carbon that does not have any crystalline structure (see Fig. 8.1). As with all glassy materials, some short-range order can be observed. Amorphous carbon is often abbreviated to a-C for general amorphous carbon, a-C:H for hydrogenated amorphous carbon, or to DLC for diamond-like carbon (includes also tetrahedral amorphous carbon (ta-C)).

The sheer versatility of the carbon material system is based on the different bond hybridisation available to carbon, as shown in Fig. 8.2. Carbon atoms have a valence of four, and this gives rise to many different bonding configurations. Diamond is composed of a fully tetrahedral sp^3-hybridised C-C bonding configuration. Four bonds at 109.5° to each other give it the largest bulk modulus of any material and an optical bandgap of 5.5 eV. Graphite is a fully trigonal sp^2 network that forms planar six-fold rings of single and double bonds, with weak Van der Waals π bonding between planes. The in-plane σ- bonded C atoms are spatially closer to each other than the isotropic diamond lattice and this gives higher in-plane strength to graphite than diamond. The bandgap of graphite is zero due to the highly delocalised π electrons between the planes along the '*c*' axis. The sp^1 bond is composed of two strong σ orbitals, directed along the *x*-axis, and a further two π orbitals in the *y* and *z* directions.

Amorphous carbon can have any mixture of sp^3 and sp^2 sites, with the possible presence of hydrogen up to 60 %. The compositions of the various forms of amorphous C-H alloys are conveniently shown on the ternary phase diagram in Fig. 8.3, first introduced by Jacob and Moller [1]. Diamond-like carbon is defined as a-C or a hydrogenated amorphous carbon (a-C:H) with a significant fraction of sp^3 bonds (from 40 to 60%), while the DLC films with highest sp^3 content are called tetrahedral amorphous carbon (ta-C). The fraction of sp^3 bonded carbon sites and hydrogen content are key parameters, which determine some of the advantageous and variable material properties of a-C, shown in Table 8.1.

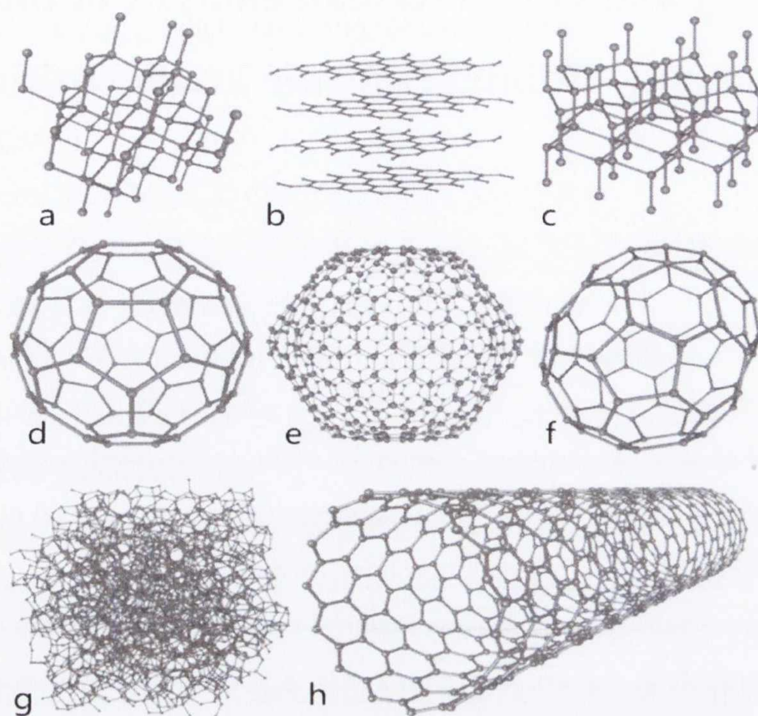

Fig. 8.1. Some allotropes of carbon: a) diamond, b) graphite, c) lonsdaleite, d–f) fullerenes (C60, C540, C70), g) amorphous carbon, and h) carbon nanotube.

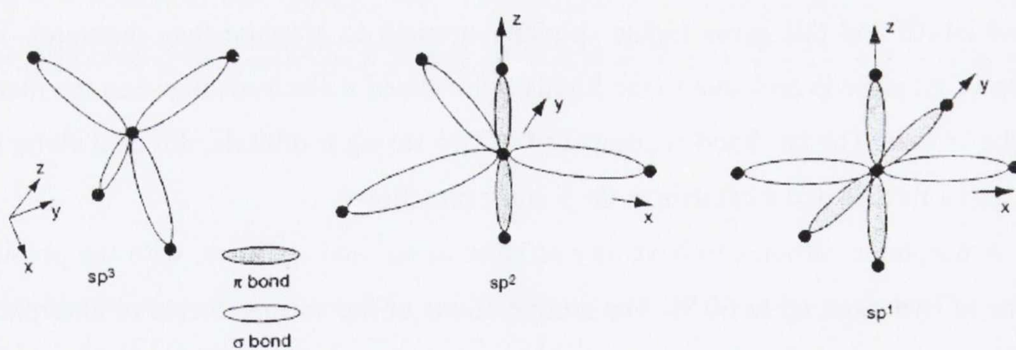

Fig. 8.2. The three bond hybridisations found in carbon: sp^3, sp^2 and sp^1 [2].

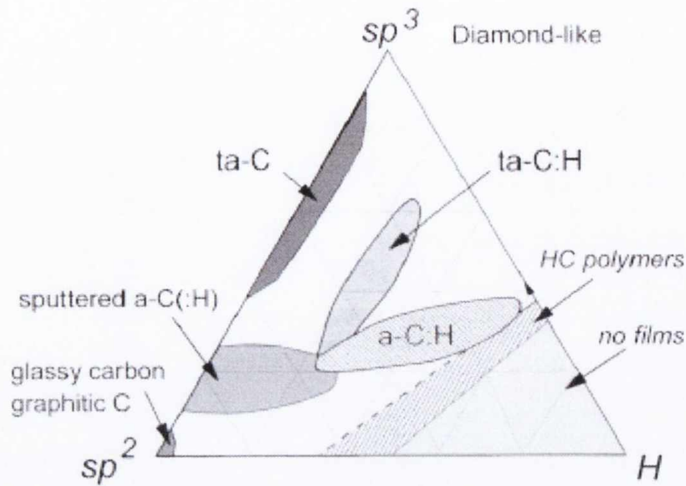

Fig. 8.3. Ternary phase diagram of bonding in amorphous carbon-hydrogen alloys [3].

Another crucial parameter is the degree of clustering of the sp^2 phase, which should be added as a fourth dimension in the ternary phase diagram [3]. Amorphous carbons with the same sp^3 and H content show different optical, electronic, and mechanical properties according to the clustering of the sp^2 phase. Diamond-like carbon has some extreme properties similar to diamond, such as the hardness, elastic modulus and chemical inertness, but these are achieved in an isotropic disordered thin film with no grain boundaries [4]. DLC is also much cheaper in production than diamond itself. This has great advantages for many applications. The DLC-based products are in commercial use and they contribute immensely especially in the area of scratch-resistant coatings and in many other passive applications. The DLC films have widespread applications in magnetic storage disk coatings, biomedical coatings, and as microelectromechanical devices (MEMs).

There are many different methods that are applied to grow amorphous carbon films, such as ion beam deposition [12,13], sputtering [14,15], cathodic arc deposition [7,8], pulsed laser deposition [16,17] and plasma-enhanced chemical vapor deposition [10,18]. The first DLCs were prepared as thin films by Aisenberg and Chabot [12] using ion beam deposition. Deposition methods have been developed to produce a-Cs with increasing degrees of sp^3 bonding. Sputtering can extend from sp^2 bonding some way towards sp^3 bonding and it is preferred for industrial applications because of its versatility and its widespread use to sputter many materials [4]. A range of deposition methods, such as plasma enhanced chemical vapour deposition (PECVD), is able to

reach into the interior of the phase diagram. This produces a-C:H. Although this is diamond-like, it is seen from Fig. 8.3 that the content of sp^3 bonding is actually not so large, but its hydrogen content is rather large. A more sp^3 bonded material with less hydrogen is called ta-C:H by Weiler et al. [11].

Table 8.1. Typical physical properties for different forms of amorphous carbon thin films, diamond and graphite.

Form of carbon	**sp^3, %**	**H, %**	**Density, g/cm^3**	**Optical Bandgap, eV**	**Hardness, GPa**	**References**
Diamond	100	0	3.515	5.5	100	[5]
Graphite	0	0	2.267	0	-	[6]
DLC	40-60	0	2.5-3.5	0.8-4	20-40	[2]
ta-C	80-88	0	3.1	2.5	80	[7,8,9]
a-C:H hard	40	30-40	1.6-2.2	1.1-1.7	10-20	[10]
a-C:H soft	60	40-50	1.2-1.6	1.7-4	<10	[10]
ta-C:H	70	30	2.4	2-2.5	50	[11]

Different characterisation methods are used to determine the structural parameters of a-C films. For instance, the sp^3 content is usually measured by nuclear magnetic resonance (NMR) or electron-energy-loss spectroscopy (EELS), but these are time consuming and destructive methods. Raman spectroscopy is a very popular, non-destructive tool for the structural characterisation of a-C films. It is traditionally carried out at wavelengths in the blue-green spectral region ~ 488 - 514.5 nm, but multi-wavelength Raman studies are becoming increasingly used. Indeed, Raman scattering from a-C is always a resonant process, in which configurations whose band gaps match the excitation energy are preferentially excited. Any mixture of sp^3, sp^2, and sp^1 carbon atoms always has a gap between 0 and 5.5 eV, and this energy range matches that of VIS-UV Raman systems. This implies that understanding the resonant Raman process in carbon systems will give a powerful, fast means for their structural and electronic characterization. It has to be noted that visible Raman spectroscopy is 50-230 times more sensitive to sp^2 sites, as photons with wavelength in the visible range

preferentially excite π-states. UV Raman, with its higher photon energy, excites both the π and the σ states and so it is able to probe both the sp^2 and sp^3 sites [19].

This chapter reports on the application of multi-wavelength micro-Raman spectroscopy to distinguish between the a-C and ta-C films grown by filtered cathodic arc deposition and to assess their structural properties. The intrinsic stress of a-C thin films was investigated as a function of substrate bias and hence ion energy. The microstructure of the films was also analysed using transmission electron microscopy and electron energy loss spectroscopy.

8.2. Experimental

8.2.1. Sample growth and description

Carbon thin films with sp^2 content between ~20% to ~90% were deposited onto silicon wafers using a dual bend filtered cathodic arc deposition (FVCA) system operating with a 99.9 % pure graphite target, an arc current of 56 A and a base pressure of better than 10^{-5} Torr. Three different flow rates of Ar (0, 7, and 15 ml/min) were used with the different deposition parameters provided in Table 8.2. Silicon (100) substrates were cleaned prior to deposition in an ultrasonic bath with acetone, ethanol and distilled water before being air dried. The substrate holder was connected to a regulated DC power supply, allowing films to be deposited over a range of bias voltages from -25 V to -1000 V. The average energy of the depositing species was calculated from the applied substrate bias by adding the plasma potential measured using a Langmuir probe for each of the Ar flow rates of Table 8.2. The stress was determined from substrate curvature using Stoney's equation [20] and the film thickness (from 20 to 80 nm) was determined by step height measurements obtained using a Tencor P-16 profilometer. To obtain accurate stress values, two curvature measurements were performed in orthogonal directions on each substrate both before and after deposition. Samples were also prepared with a thin Cu under layer approximately 2 nm thick sputter deposited onto the substrate prior to the carbon deposition.

Two sets of a-C films on Si(100) were analysed using micro-Raman spectroscopy. The sample description is presented in Tab. 8.3. The first set consists of

four samples with high sp^2 content from 60 to 88% with thickness of amorphous carbon layer varied from 14 to 22 nm. The second set consists of ten samples of ta-C with smaller sp^2 content varied from 27 to 47% and with thickness in the range of 60 to 85nm.

Table 8.2. The operating parameters of the cathodic arc deposition system used to produce the three sets of samples. E_0 is the plasma potential measured using a Langmuir probe.

Deposition Parameter	Series 1	Series 2	Series 3
Ar (ml/min)	0	7	15
Deposition Pressure (Torr)	6×10^{-6}	2×10^{-4}	6×10^{-4}
E_0(eV)	20	13	9
Deposition rate at 75 V (nm/min)	0.4	0.2	0.06

Table 8.3. Sample description of a-C films.

Sample	Stress (GPa)	Density (g/cc)	sp^2 (%)	Thickness (nm)
E40	4.36	1.81	-	21.40
E67	5.73	1.79	82.85	19.30
E77	6.82	2.41	60.77	20.3
E81	1.36	1.79	88.24	14.00
E89	18.75	3.18	29.42	-
E90	13.30	3.34	27.89	80.60
E91	9.55	3.22	28.21	66.40
E92	6.63	2.95	47.28	74.00
E93	9.76	3.35	38.87	80.00
E94	10.46	3.22	35.71	59.50
E95	7.41	3.23	31.71	70.30
E96	9.35	-	-	84.50
E97	6.27	2.86	39.87	71.90
E98	6.37	2.23	46.29	78.20

8.2.2. Characterisation techniques

The a-C films were mainly investigated using micro-Raman spectroscopy with visible and UV excitations. Unpolarized visible Raman spectra were excited at the backscattering geometry using 457 and 514 nm line of an Ar^+ laser as well as 633 nm line of a HeNe laser. Spectra were collected using RENISHAW 1000 micro-Raman system equipped with a CCD camera and a Leica microscope. An 1800 lines/mm grating was used for all measurements, providing a spectral resolution of ~ 1 cm^{-1}. A laser output of 10 mW was used and the laser spot was focused on the sample surface using 50x objectives with short-focus working distance. UV Raman spectra were collected using the micro-Raman system HR800 model supplied by Horiba Jobin Yvon. As an excitation source a He-Cd laser at 325 nm with power of 22 mW was used. The laser spot was focused on the sample surface using 40x objectives with short-focus working distance. The Raman spectra were fitted with mixture of Gaussian and Lorentzian functions to obtain the position, intensity, and linewidth of the detected peaks.

The microstructure of the films was investigated using a JEOL 2010 transmission electron microscope (TEM) operating at 200 kV. Plan view samples were prepared by acid etching (48 % concentrated HF) of the silicon wafers. A selection of samples was also prepared in cross-section by a combination of mechanical tripod polishing and Ar ion beam thinning. The film density and fraction of sp^2 bonded carbon atoms was estimated from EELS measurements. EELS analysis was performed using a Gatan Imaging Filter (GIF2000). An EELS spectrum was collected in the low loss region in order to determine the plasmon peak position which was used to calculate the film density, assuming carbon has four valence electrons with an effective mass of $0.88m_e$ taking part in plasmon oscillations [21,22]. EELS spectra were also collected in the region of the carbon K-shell ionisation edge so that the fraction of sp^2 bonded carbon atoms could be estimated [23]. Energy filtered electron diffraction patterns were collected using the GIF2000 with procedures outlined elsewhere [24]. A VG310F scanning auger nanoprobe was utilised to measure the Ar content of the films by performing elemental depth profiles in which Xe was used as the sputtering gas.

8.3. Results and discussion

Figure 8.4 shows the effect of increasing Ar flow rates on the intrinsic stress of carbon films deposited at a range of ion energies. Figure 8.4 (a) shows the films prepared in the absence of Ar. In the absence of Ar gas, the intrinsic stress of the carbon films increases with ion energy up to a maximum of ~ 12 GPa at 95 eV before decreasing at higher energies. This behaviour has been observed previously for FCVA deposited films [25,26] and has been interpreted as a competition between stress generation (when ions impact with energies 10-100 eV) and stress relief processes (when ions impact at ion energies > 100 eV) [27,28]. Adding 7 ml/min of Ar (results shown in Figure 8.4 (b)) extends the stress peak to lower energies and reduces the maximum stress to approximately 10 GPa. Ar at this flow rate also halved the deposition rate at 95 eV (see Table I). There is no net film growth at energies above 600 eV. Increasing the Ar flow rate to 15 mL/min reduces the peak stress to approximately 6 GPa, further reduces the deposition rate, and prevents film growth for energies above 200 eV.

Measurements of the energy distribution of C ions ejected from a cathodic arc source operating in a vacuum show a relatively narrow distribution around the mean energy [29]. When Ar is introduced as a background gas, two main effects occur. The first is an asymmetric broadening to lower energies of the energy distribution of the incident C ions as a result of collisions with Ar. As a result, fewer ions have the optimal energy for stress generation, and the stress maximum at 95 eV is lowered to approximately 10 GPa in the case of 7 ml/min of Ar flow rate. These results are consistent with previous findings [30] in which a lowering of stress was observed in the presence of Ar for samples prepared at earth potential. The second effect of introducing Ar into the deposition process is bombardment of the substrate by Ar ions. At lower energies, these ions can generate compressive stress, a process that is exploited in ion assisted deposition [31]. The result is increased stress in films grown with biases below 75 V. As the bias is increased, the sputter yield increases and no net film growth occurs. For the higher Ar flow rate of 15 ml/min, the mean free path is very short so that the average C ion energy is low. In this case, the stress generation mechanism is likely to be dominated by Ar bombardment. The higher mass of the Ar ions relative to C ions results in a stress maximum at a lower bias value. The effect of a Cu under layer is to

reduce the stress induced in the film by ions with energies up to approximately 200 eV, which is clearly seen on Figs. 8.4 (a), (b) and (c).

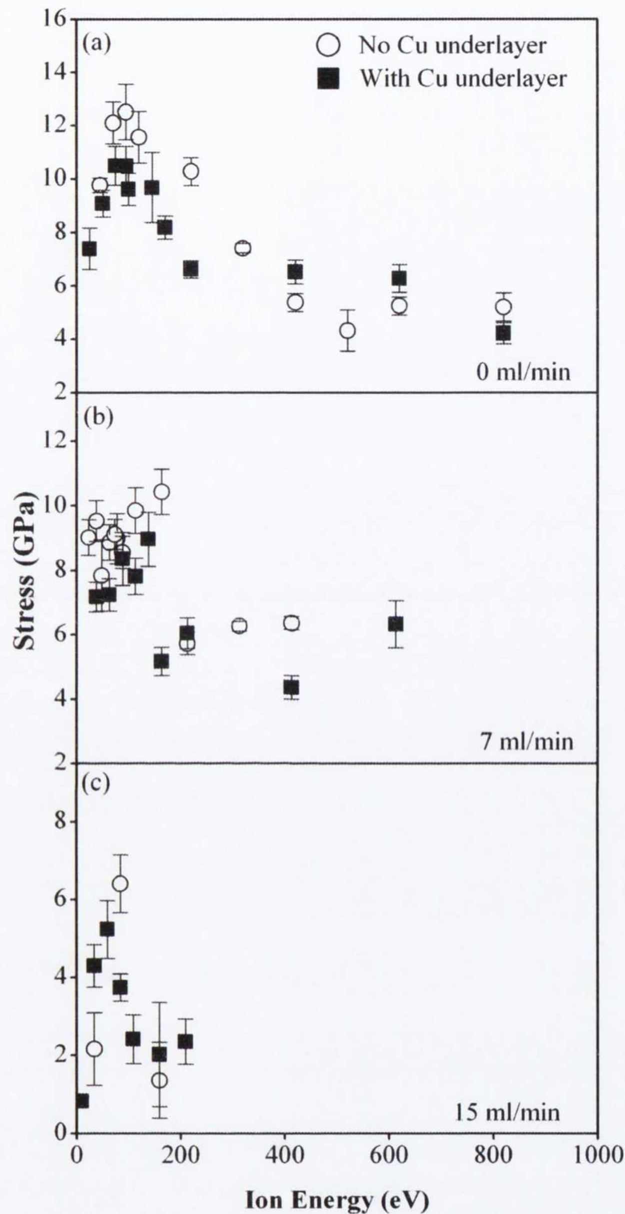

Fig. 8.4. The intrinsic stress measured as a function of ion energy for carbon thin films deposited with various Ar flow rates of (a) 0 ml/min, (b) 7 ml/min and (c) 15 ml/min, both with and without a Cu under layer.

Figure 8.5 shows AES depth profiles that confirm no Ar was incorporated into the films at either 7 ml/min or 15 ml/min flow rate. Ar was detected at the film/substrate interface (indicated by an arrow), possibly as a result of ion implantation during the initial stages of film growth.

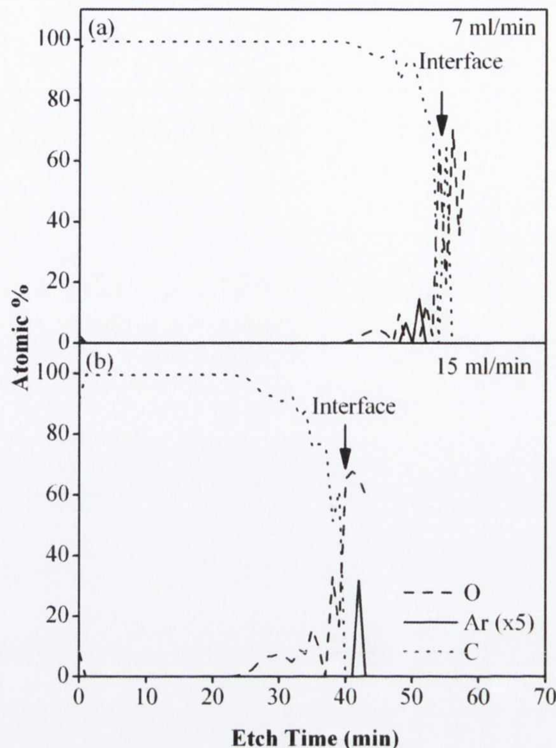

Fig. 8.5. AES depth profiles for films grown using Ar flow rates of (a) 7 ml/min at 88 eV and (b) 15 ml/min at 159 eV. The arrow indicates the film/substrate interface.

Figure 8.6 shows a cross sectional TEM image of a film prepared using an ion energy of 60 eV, with 15 mL/min of Ar background gas and with a 2 nm thick Cu under layer. There is no evidence of voids or bubbles that could be associated with Ar incorporation into the films. Note that the silicon substrate has an approximately 6 nm thick surface oxide. Figure 8.7 (a) shows the relationship between stress and density calculated from the plasmon peak position for samples prepared with and without a Cu under layer using a range of Ar flow rates. A point is included for a film of low stress prepared using sputtering. All the films fall on the same curve with a transition from a low to a high density phase occurring at a stress of 6.5 ± 1.5 GPa. The region of stress is termed the "transition region". The value of the transition stress is not affected by Ar flow rate or the presence or absence of a Cu under layer. This proves that the transition is induced at a fixed value of stress, and not by the conditions that give rise to the stress. For the same samples, the relation between density and sp^2 fraction is given in Figure 8.7 (b) and shows a linear relation.

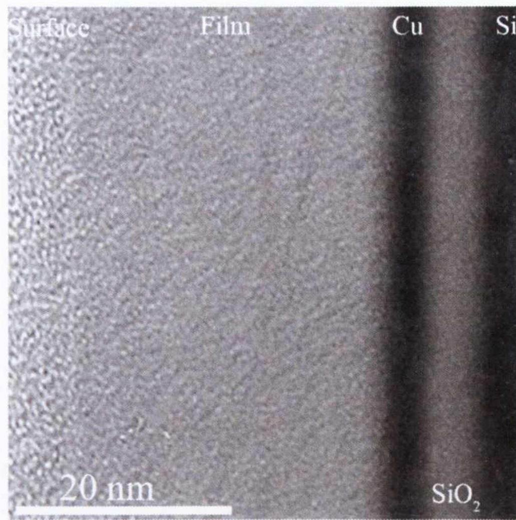

Fig. 8.6. Cross-sectional TEM image of an a-C film deposited onto a Cu under layer at an ion energy of 60 eV and 15 ml/min Ar flow rate showing the Cu under layer and Si substrate as dark regions.

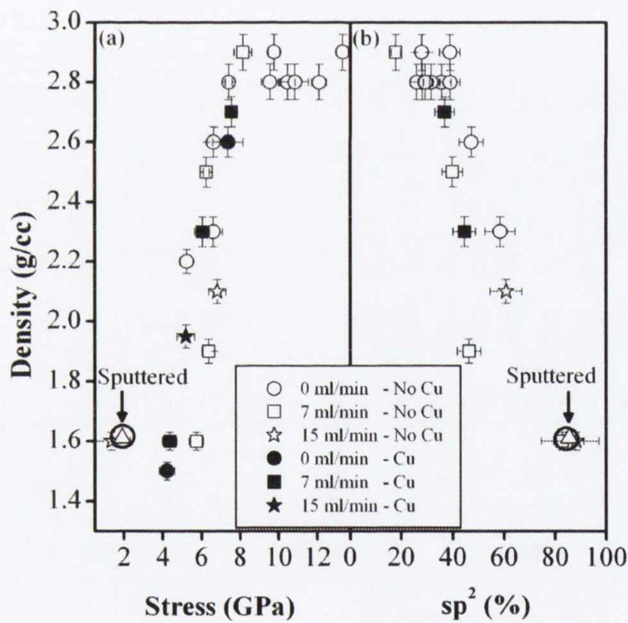

Fig. 8.7. The density of carbon films as a function of (a) stress and (b) sp^2 content. The films were deposited under the indicated flow rates of Ar, in the presence or absence of a Cu under layer.

Within the transition region, diffraction analysis shows evidence for a material which contains more than one type of microstructure. Figure 8.8 shows radially averaged energy filtered diffraction patterns for selected carbon films. Also shown is the

diffraction pattern for glassy carbon, which is a fully sp^2 bonded structure with well formed graphitic sheets. The diffraction pattern for the film prepared at low energy and at a relatively low stress of approximately 5 GPa shows diffuse rings typical of a sp^2 rich amorphous network. This diffraction pattern also shows strong scattering at small angles indicative of the presence of mesoscale inhomogeneities such as voids. The film prepared using 84 eV at a stress of 6.9 GPa develops a graphitic {002} peak at k= 1.77 $Å^{-1}$ as a shoulder corresponding to the material with sp^2 bonding. The peak at k= 2.8 $Å^{-1}$ in the same diffraction pattern indicates the presence of ta-C. This film is in the transition region and shows features characteristic of both partially ordered graphite and an amorphous carbon. An almost identical diffraction pattern has been observed previously in ion implanted ta-C in which the microstructure was found to be a mixture of ta-C and sp^2-rich a-C clusters created by ion beam damage [32,33]. Films in the transition region prepared at energies above 300 eV (as shown in Fig. 8.8 for the case of 6.6 GPa and 420 eV) also show evidence for more than one type of microstructure. However, in this case, a well formed {002} peak indicating well ordered graphitic planes is observed. As described elsewhere [32], films prepared under these conditions develop preferred orientation and contain graphitic planes aligned normal to the sample surface. The diffraction pattern for the film grown with a high stress of 9.7 GPa shown in Figure 8.8 is typical of ta-C [33] and contains very little intensity near the undiffracted beam, indicating a dense homogeneous network. It is conceivable that this type of microstructure may be present in the films of this study in the transition region.

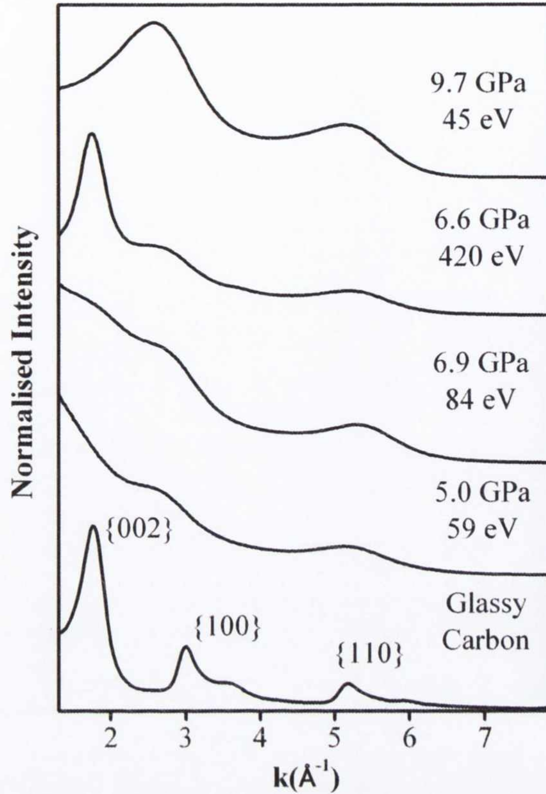

Fig. 8.8. Radially averaged energy filtered diffraction patterns for a range of carbon films prepared at the energy and stress conditions indicated. Also shown for comparison is the diffraction pattern for glassy carbon which has been indexed to graphite.

The shape of Raman spectra of a-C films depends on a number of different factors. These factors are: a clustering of the sp^2 sites, bond disorder, presence of sp^2 rings or chains and the sp^2/sp^3 ratio [19]. Figs. 8.9 (a) and 8.9 (b) show Raman spectra acquired at wavelengths 457 nm and 325 nm, respectively. The following Raman features are observed for both excitation wavelength: a TO Si phonon at ~ 970 cm^{-1} due to the second order phonon scattering from the silicon substrate, and the carbon D and G bands at about 1400 and ~1570 cm^{-1} respectively. The G and D peaks are due to sp^2 sites only [19]. The G peak is due to the bond stretching of all pairs of sp^2 atoms in both rings and chains, and the D peak is due to the breathing modes of sp^2 rings [19]. The TO Si phonon mode is more pronounced for visible excitation (457 nm) due to a larger depth of laser light penetration than in case of UV excitation (325 nm). In addition to that, a weak T band at ~1100 cm^{-1} is observed for UV excitation (see Fig. 8.9 (b)). The T peak contributes to the C-C sp^3 vibrations [19,34]. For visible excitation, the sp^2 sites have a high cross section and they dominate the spectra. At the same time, the sp^3 sites

cannot be detected and the spectrum corresponds only to the configuration or order of the sp^2 sites. At the higher excitation energy (in the UV range), the sp^3 sites are clearly shown in Raman spectra, due to resonant enhancement of the σ states of C-C bonds [34], (see Fig. 8.9 (b)).

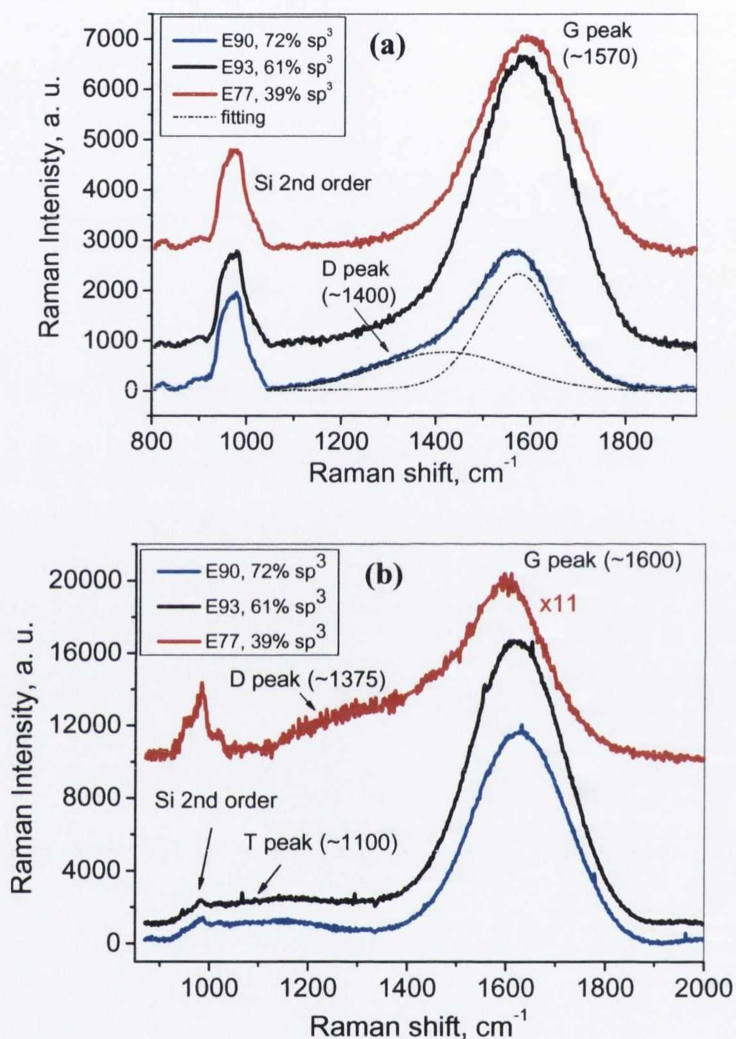

Fig. 8.9. Visible Raman spectra (457 nm) (a) and UV Raman spectra of the a-C films (b) with different sp^3 content.

Figure 8.10 presents the dependence of Raman frequency of the G band versus the sp^3 content for visible and UV excitations. As can be seen from this figure, the G peak behaves differently for a-C films with low sp^3 content (up to 20%) in comparison with that for ta-C films with higher sp^3 fraction. For both excitation wavelengths, the G peak position decreases as sp^3 increases up to 20%. For the sp^3 content in the range from 20%

to 80%, the position of G peak significantly shifts to the higher Raman frequencies. This is in agreement with previously published papers on a-C films [19,35]. The large shift of the G peak position (~ 30 cm^{-1}) to the higher frequencies is observed for UV excitation wavelength (see Fig. 8.10 (b)). The range of behaviour of the G peak can be understood within the three-stage model for different wavelengths introduced by Ferrari [19]. In passing from a-C to ta-C, the sp^3 content rises from 20% to 85%, while the sp^2 sites change gradually from rings to chains. The π states become increasingly localized on olefinic sp^2 chains and, eventually, sp^2 pairs embedded in the sp^3 matrix. Olefinic C=C bonds are shorter than aromatic bonds, so they have higher vibration frequencies and consequently they have a larger contribution at UV excitation wavelength [19,36,37]. There are reasonable arguments in the literature about the origin of an upwards shift of the G peak with sp^3 content. Some conjectures indicate this shift can be due to compressive stress in ta-C films [35], while other investigators show that the G peak position does not decrease when the stress is removed by annealing [38]. In this work, the definite conclusion on the influence of stress on the G peak position cannot be made based on the obtained results. Further research has to be carried out.

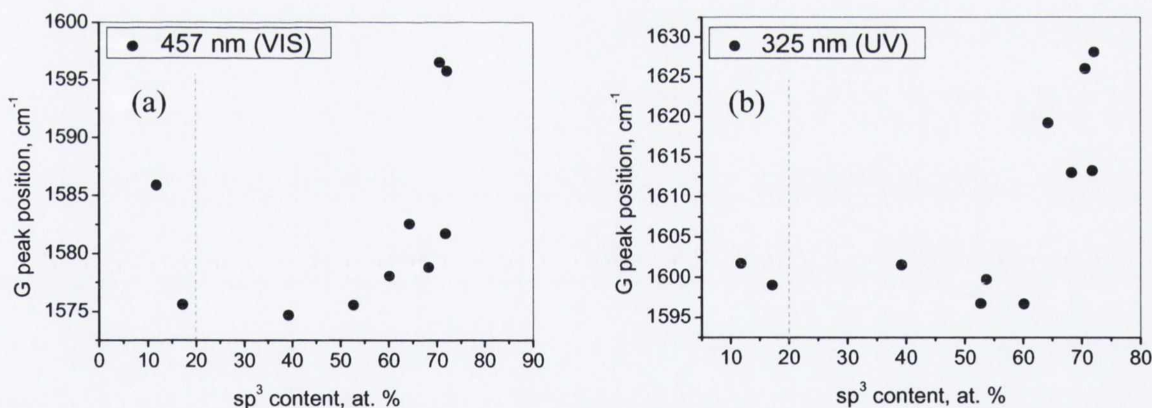

Fig. 8.10. The G peak position as a function of sp^3 content measured by 457 nm (a) and 325 nm of excitation wavelength (b).

Fig. 8.11 shows the full width at half maximum (FWHM) of the G peak as a function of sp^2 content for 457 nm and 325 nm excitation energy. The FWHM of the G peak decreases linearly with sp^2 fraction for both excitation wavelengths. The a-C films with lower sp^2 content have larger G linewidth as they are more disordered. This is in agreement with the fact that the linewidth of the G peak at any excitation increases as

the disorder increases [35,38]. The linewidth of the G band is around 180 cm^{-1} for a-C films and approximately 230 cm^{-1} for ta-C, which is in agreement with Ref. [19]. We did not observe any significant changes in the linewidth of G peak between 457 nm and 325 nm excitation wavelengths. This can be due to the reason that excitation wavelengths used in this work are quite close to each other.

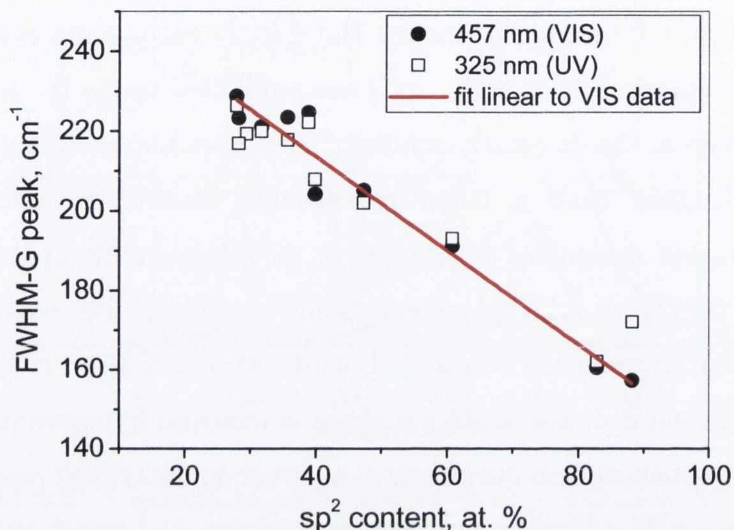

Fig. 8.11. The full width at half maximum (FWHM) of the G peak as a function of sp^2 content measured by excitation with 457 nm and 325 nm.

Fig. 8.12 presents the variation of the G peak position with excitation wavelength for ta-C and a-C samples. The G-peak dispersion occurs only in disordered carbon and it is proportional to the degree of disorder of the sp^2 clustering [34,19,39]. As can be seen from Fig. 8.13, the G peak position decreases with excitation wavelength for both a-C and ta-C films. For ta-C films the G peak position decreases from 1615 cm^{-1} at 325 nm excitation wavelength to 1529 cm^{-1} at 633 nm excitation wavelength. A smaller dispersion is observed for a-C films with high sp^2 content when the G peak position shifts from 1600 cm^{-1} to 1556 cm^{-1} at 325 nm and 633 nm excitations, correspondingly. This is consistent with results obtained in Ref. [34]. The D peak position also decreases with excitation energy (see Fig. 8.13). For ta-C sample with ~ 70% of sp^3 sites, it shifts from 1394.6 cm^{-1} at 457 nm excitation wavelength to 1340 cm^{-1} at 633 nm of excitation wavelength. For UV excitation, the D band is difficult to detect (the G band is symmetrical). Fig. 8.14 presents the intensity ratio of the D and G peaks as a function of sp^3 content. The ratio of I(D)/I(G) decreases with an increase of sp^3 fraction. This

confirms the three stage model introduced by Ferrari [19], which shows that I(D)/I(G) ratio decreases with sp^3 content for a-C films and for ta-C films with high sp^3 content the I(D)/I(G) tends to zero. As the sp^3 content increases, the sp^2 content decreases and sp^2 bonded clusters become smaller. The carbon rings are more distorted, and open up and break into segments with chains of C=C groups. The D band, which is due to the breathing mode of aromatic sp^2 rings, vanishes, and for very high sp^3 values the G band is nearly symmetrical, which is in agreement with spectra presented in Fig. 8.9.

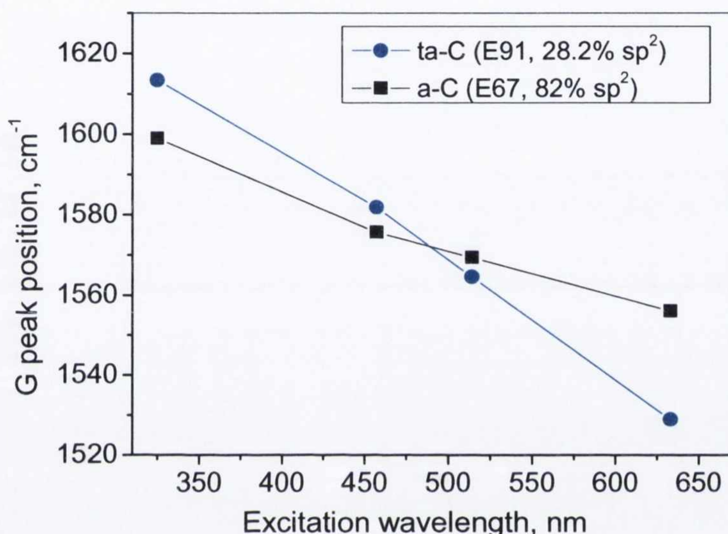

Fig. 8.12. Dispersion of G peak position vs. excitation wavelength for selected ta-C and a-C samples (note that the connecting lines are used as a guide to the eye).

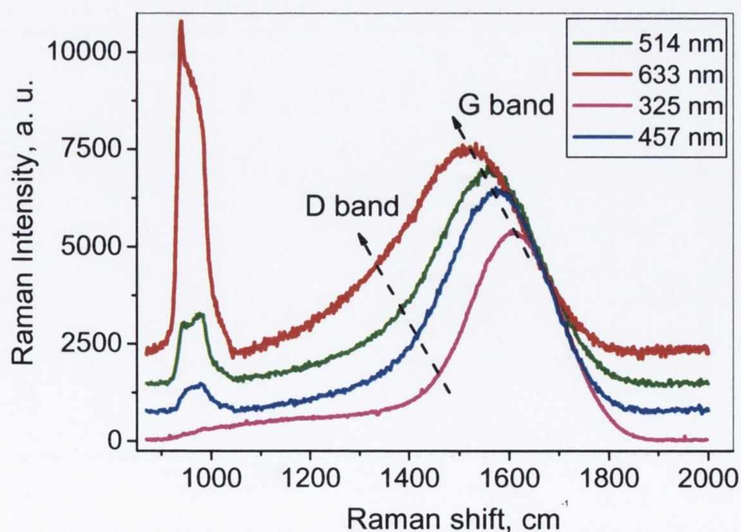

Fig. 8.13. Multi-wavelengths Raman spectra of a ta-C sample with ~70% sp^3. The G and D peaks' dispersions are indicated.

Fig. 8.15 shows that the intensity of T peak at 1060 cm^{-1} increases with an increase of sp^3 fraction, which is in agreement with published data [29,40,41]. This confirms a statement that the T peak is identified with sp^3-bonded carbon. The T peak is sensitive to small changes in sp^3 content, in particular at high sp^3 fractions.

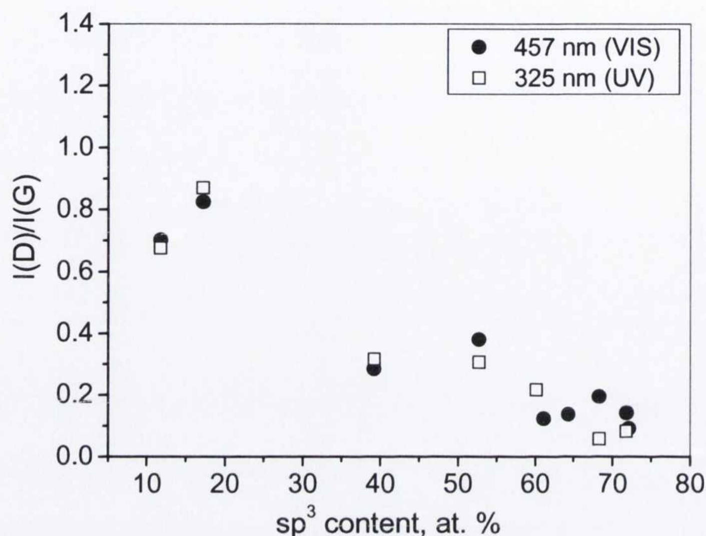

Fig. 8.14. The intensity ratio of the D to G peak as a function of the sp^3 content for visible (457 nm) excitation.

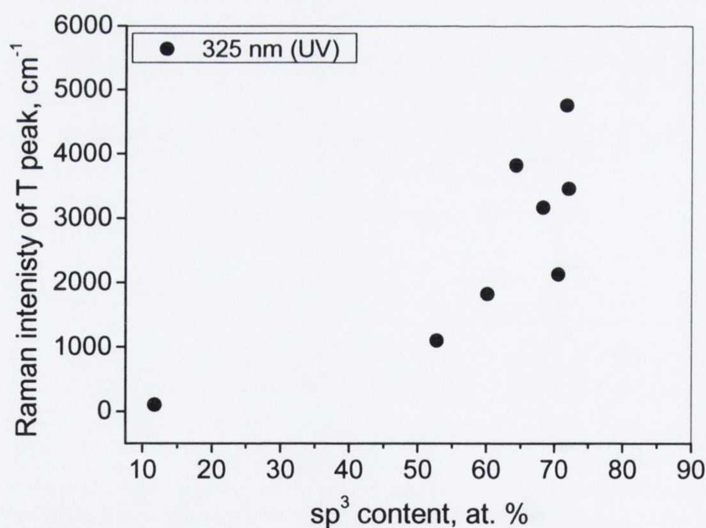

Fig. 8.15. Raman peak intensity of the T band as a function of the sp^3 content.

Figure 8.16 (a) shows the G-peak position as a function of stress. A linear relationship is observed for stresses above 4 GPa. As the stress increases, the G-peak shifts to higher wave numbers. This is expected on the basis of an increase in lattice vibration

frequencies when the amorphous network is compressed. The relationship between stress and G-peak FWHM is shown in Figure 8.16 (b). A transition is observed at ~6.5 GPa between high sp^2 content films to low sp^2 content films. The Raman analysis confirms results from the EELS studies which show a sharp transition from a low density a-C to a high density ta-C structural phase at a stress of approximately 6.5 GPa (see Fig. 8.4 (a)).

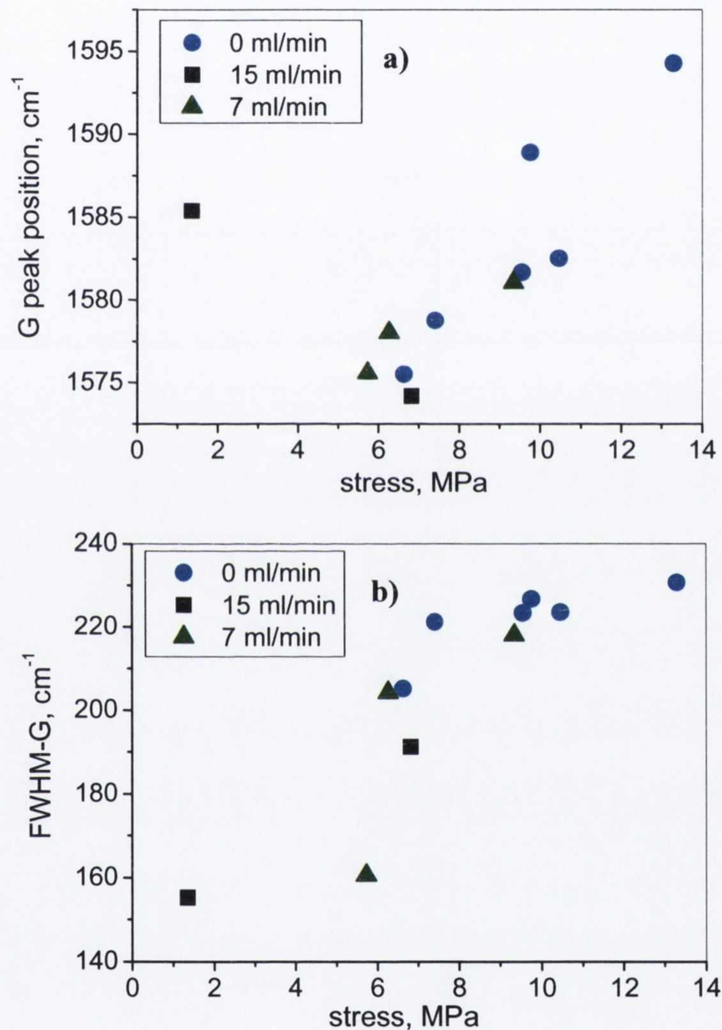

Fig. 8.16. The G-peak position (a) and G-peak FWHM (b) in the Raman spectra of films deposited under the indicated flow rates of Ar.

Figure 8.17 shows the sp^3 fraction (measured using EELS) as a function of stress for films analysed in this chapter, compared with values obtained for pure carbon taken from the literature. Only the films synthesised at room temperature without intentional

doping have been considered, since the presence of dopant atoms [42,43] is known to influence bonding and hence is likely to modify the transition stress. The scatter in the data at high sp^3 content is due to the difficulty in measuring the decreasing levels of π-bonding using EELS [44]. There are three outlier points, circled in Figure 8.17 that contradict the general trend. This trend is suggested by the majority of the data, which is consistent with the proposition that there is a transition region between 5 and 8 GPa (shown as a shaded band) separating low and high density forms of a-C. The value of 6.5 GPa is close to the biaxial stress expected to mark the boundary between graphite and diamond at room temperature, which has been calculated to be 4.5 GPa [45].

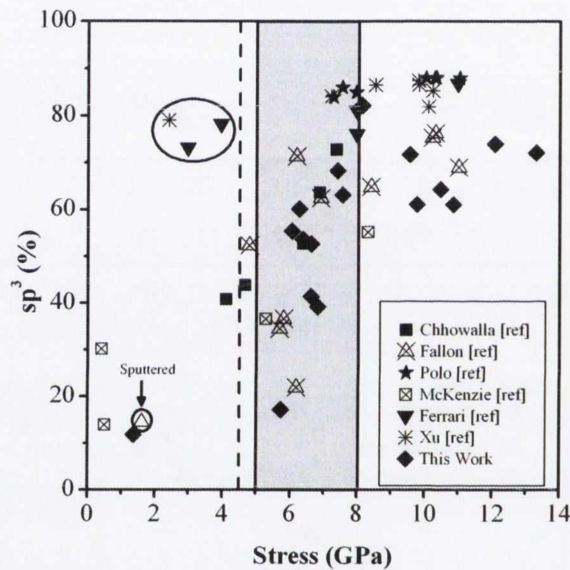

Fig. 8.17. The sp^3 fraction as measured by EELS of a-C films prepared at room temperature as a function of stress, as measured by different groups [8,25,46-49]. The majority of points show the differentiation between the phases of low and high sp^3 fraction, separated by a transition region at 6.5 ± 1.5 GPa shown as the shaded band. The outlying points (circled) at low stress and high sp3 content may be the result of substrate heating during deposition, giving rise to a reduction in stress by annealing. The vertical dotted line indicates the biaxial stress expected to mark the boundary between graphite and diamond at room temperature [25].

8.4. Conclusions

In this chapter, it was shown that introduction of Ar background gas during deposition of a-C films reduces the intrinsic stress at a given substrate bias. The presence of a Cu under layer also has a stress reducing effect. The effect of Ar was to reduce the kinetic energy of incident carbon ions by ion-atom collisions and to increase sputtering. A sharp transition between sp^2-rich and sp^3-rich forms of a-C was observed at a stress of 6.5 GPa, independent of the deposition conditions. This observation provides strong evidence that stress is the driving force behind the formation of the sp^3-rich ta-C phase. A compilation of available data from the literature supports the proposition of a stress induced transition at 6.5 GPa.

A systematic analysis of the Raman spectra measured at 325, 457, 514 and 633 nm excitations for a-C films with sp^2 content varying from ~20% to ~90% was also presented. It was shown that the UV Raman spectra can provide direct evidence for the presence of sp^3 bonds based on the T peak, while visible Raman spectra present a powerful way to follow the evolution and ordering of the sp^2 sites based on the G and D peaks. Within the three-stage model [19], in passing from a-C to ta-C, the sp^2 sites change gradually from rings to chains and the G peak shifts upwards from 1575 to 1598 cm^{-1} for visible excitation and from 1595 to 1630 cm^{-1} for UV excitation. With increase of sp^3 content the I(D)/I(G) ratio shifts to low values and for high sp^3 content tends to zero. The dispersion of the G peak is a crucial parameter to distinguish between different structures of amorphous carbon. It was confirmed that the bigger dispersion of G peak observed for ta-C films with high sp^3 content indicates the larger disorder in these films. Diffraction and Raman analyses of the microstructure of films with stresses in the transition region are consistent with the presence of two phases, rather than a single homogeneous phase with an intermediate sp^3 fraction.

References

1. W. Jacob, W. Moller. Appl. Phys. Lett. 63, 1771 (1993)
2. Properties of Amorphous Carbon, Edited by: S. Silva, P. Ravi, Institution of Engineering and Technology, 2003
3. J. Robertson, Prog. Solid State Chem. 21, 199 (1991); Pure Appl. Chem., 66, 1789 (1994)
4. J. Robertson, Mater. Sci. Eng. R 37, 129 (2002)
5. J.E. Field, Properties of Diamond, Academic Press, London, 1993.
6. B.T. Kelly, Physics of Graphite, Applied Science Publishers, London, 1981.
7. D.R. McKenzie. Rep. Prog. Phys. 59, 1611 (1996)
8. P.J. Fallon, V.S. Veerasamy, C.A. Davis, J. Robertson, G.A.J. Amaratunga, W.I. Milne and J. Koskinen. Phys. Rev. B 48, 4777 (1993)
9. G.M. Pharr, D.L. Callahan, S.D. McAdams, T.Y. Tsui, S. Anders, A. Anders, J.W. Ager, I.G. Brown, C.S. Bhatia, S.R.P. Silva and J. Robertson. Appl. Phys. Lett. 68, 779 (1996)
10. P. Koidl, C. Wagner, B. Dischler, J. Wagner and M. Ramsteiner. Mater. Sci. Forum 52, 41 (1990)
11. M. Weiler, S. Sattel, K. Jung, H. Ehrhardt, V.S. Veerasamy and J. Robertson. Appl. Phys. Lett. 64, 2797 (1994)
12. S. Aisenberg and R. Chabot. J. Appl. Phys. 42, 2953 (1971)
13. B. Druz, R. Ostan, S. Distefano, A. Hayes, V. Kanarov and V. Polyakov. Diamond Rel. Mater. 7, 965 (1998)
14. F. Jansen, M. Mackonkin, S. Kaplan and S. Hark. J. Vac. Sci. Technol. A 3, 605 (1985)
15. W. Gissler, P. Hammer and J. Haupt. Diamond Rel. Mater. 3, 770 (1994)
16. A.A. Voevodin and M.S. Donley. Surf. Coatings Technol. 82, 199 (1996)
17. F. Davanloo, E.M. Juengerman, D.R. Jander, T.J. Lee and C.B. Collins. J. Appl. Phys. 67, 2081 (1990)
18. J.W. Zou, K. Schmidt, K. Reichelt and D. Dischler. J. Appl. Phys. 67, 487 (1989)
19. A. C. Ferrari, J. Robertson, Phys. Rev. B 61, 14095(2000)
20. G. G. Stoney, Proc. R. Soc. London, Ser. A 82, 172 (1909)
21. L. Calliari, S. Fanchenko, and M. Filippi, Diamond Relat. Mater. 16, 1316 (2007)

22. R. F. Egerton, Electron Energy-Loss Spectroscopy in the Electron Microscope, 2nd ed. Plenum, New York, 1996
23. S. D. Berger, D. R. McKenzie, and P. J. Martin, Philos. Mag. Lett. 57, 285 (1988)
24. T. C. Petersen, W. McBride, D. G. McCulloch, I. K. Snook, and I. Yarovsky, Ultramicroscopy 103, 275 (2005)
25. D. R. McKenzie, D. Muller, and B. A. Pailthorpe, Phys. Rev. Lett. 67, 773 (1991).
26. B. K. Tay, X. Shi, L. K. Cheah, and D. I. Flynn, Thin Solid Films 308, 199 (1997)
27. C. A. Davis, Thin Solid Films 226, 30 (1993)
28. M. M. M. Bilek and D. R. McKenzie, Surf. Coat. Technol. 200, 4345 (2006)
29. E. Byon and A. Anders, J. Appl. Phys. 93, 1899 (2003)
30. T.-Y. Kim, C. S. Lee, Y. J. Lee, K.-R. Lee, K.-H. Chae, and K. H. Oh, J. Appl. Phys. 101, 023504 (2007)
31. 28L. K. Cheah, X. Shi, B. K. Tay, and E. Liu, Surf. Coat. Technol. 105, 91 (1998)
32. D. W. M. Lau, D. G. McCulloch, M. B. Taylor, J. G. Partridge, D. R. McKenzie, N. A. Marks, E. H. T. Teo, and B. K. Tay, Phys. Rev. Lett. 100, 176101 (2008)
33. D. G. McCulloch, E. G. Gerstner, D. R. McKenzie, S. Prawer, and R. Kalish, Phys. Rev. B 52, 850 (1995)
34. A. C. Ferrari, J. Robertson, Phys. Rev. B 64, 075414(2001)
35. J. W. Ager, S. Anders, A. Andres, I. G. Brown, Appl. Phys. Lett. 66, 3444(1995)
36. K. W. R. Gilkes, H. S. Sands, D. N. Batchelder, J. Robertson, and W. I. Milne, Appl. Phys. Lett. 70, 1980 (1997)
37. G. Irmer, A. Dorner-Reisel, Advance Engineering Materials 7, 8(2005)
38. A. C. Ferrari, B. Kleinsorge, N. A. Morrison, A. Hart, V. Stolojan, J. Roberston, J. Appl. Phys. 85, 7191 (1999)
39. C. Casiraghi, A. C. Ferrari, J. Robertson, R. Ohr, M.V. Gradowski D. Schneider, Diamond Relat. Mater. 13, 1480 (2004)
40. K. W. R. Glikes, S. Prawer, K. W. Nuget, J. Robertson, H. S. Sands, Y. Lifshitz, X. Shi, J. Appl. Phys. 87, 7283 (2000)
41. G. Adamopoulos, K. W. R. Gilkes, J. Robertson, N. M. J. Conway, B. Y. Kleinsorge, A. Buckley, D. N. Batchelder, Diamond and Related Materials 8, 541 (1999)
42. S. Bhattacharyya, M. Hietschold, and F. Richter, Diamond Relat. Mater. 9, 544 (2000)
43. M. Tan, J. Zhu, J. Han, X. Han, L. Niu, and W. Chen, Scr. Mater. 57, 141 (2007)

44. Y. Lifshitz, Diamond Relat. Mater. 12, 130 (2003)
45. M. Chhowalla, J. Robertson, C. W. Chen, S. R. P. Silva, C. A. Davis, G. A. J. Amaratunga, and W. I. Milne, J. Appl. Phys. 81, 139 (1997)
46. M. Chhowalla, Y. Yin, G. A. J. Amaratunga, D. R. McKenzie, and T. Frauenheim, Appl. Phys. Lett. 69, 2344 (1996)
47. M. C. Polo, J. L. Andujar, A. Hart, J. Robertson, and W. I. Milne, Diamond Relat. Mater. 9, 663 (2000)
48. A. C. Ferrari, S. E. Rodil, J. Robertson, and W. I. Milne, Diamond Relat. Mater. 11, 994 (2002)
49. S. Xu, B. K. Tay, H. S. Tan, L. Zhong, Y. Q. Tu, S. R. P. Silva, and W. I. Milne, J. Appl. Phys. 79, 7234 (1996)

9. Raman and Rutherford back-scattering study of a-C:Pt films

9.1. Introduction

Amorphous carbon (a-C) attracts the attention of researchers by its interesting physical properties and possible applications in photonics and electronics (see Chapter 8). In recent years, steadily increasing attention has been drawn to the composite amorphous carbon containing metallic additives: gold [1], titanium [2, 3], chromium [4], iron [5], cobalt [6], copper [7], and a number of other metals. A metal modifies the amorphous carbon matrix by creating metal nano-clusters, rather than becoming a substitutional impurity. The properties of these nano-clusters and their effect on the manner in which the matrix is modified depend on the nature of the incorporated metal and on the chemical interaction of the metal with carbon atoms. It has been shown by Transmission Electron and Atomic Force Microscopy that, at comparable amounts of the metal and carbon, the typical sizes of metallic clusters are within 1-5 nm for gold [1], 0.6–0.8 nm for copper [7], and 2-15 nm for cobalt, with the distribution of the cluster size having a maximum at ~7 nm [7]. Platinum attracts the particular interest as a modifying metal because of its role as a catalyst for numerous chemical processes [8]. In conjunction with a solid support (e.g. carbon films) they are applicable for technical processes, for example, fuel cell applications. Another important specific feature of platinum is its full chemical neutrality toward the material of the carbon matrix. The a-C and the Pt embedded a-C films were analysed in Ref. [9] by means of ellipsometry, infrared absorption spectroscopy, and Raman spectroscopy. It was demonstrated that platinum clusters are incorporated into the system of graphene planes of amorphous carbon. Similar to the modification of a-C films with cobalt and copper [10,11], modification with Pt changes the size of chain-like and ring graphite structures. In Ref. [9], the calculations of the size of graphene clusters for un-modified amorphous carbon and that containing platinum in amounts comparable with that of carbon were performed. It was demonstrated that, with the introduction of Pt, the structure of the carbon matrix slightly

changes. As the content of platinum increases, this size of carbon clusters decreases from 1.6 to 1 nm and approaches the value characteristic of pure amorphous carbon.
The purpose of this study was to analyse a-C:Pt layers deposited by magnetron sputtering using Raman spectroscopy and Rutherford backscattering of protons. The obtained results were compared with literature on the interaction of metallic inclusions within the amorphous carbon matrix [9–12].

9.2. Experimental

9.2.1. Sample growth and description

Amorphous carbon layers have the form of thin films transparent in the visible spectral range. The a-C films were deposited on single crystal silicon substrates by dc magnetron sputtering of a graphite target in the atmosphere of argon. The deposition was performed using an O1NI-7-006 Oratoriya 5 industrial installation. The procedure used for sample fabrication was described in details in Ref. [13]. The a-C:Pt films were deposited on Si (111) substrates using co-sputtering of graphite and platinum. The concentration of platinum introduced into carbon films was varied by changing the area of the platinum target. The sputtering duration also affects the Pt content in the films because of the different sputtering rates of carbon and platinum [14]. The film thickness was measured using an MII-4 interference microscope. The results of these measurements are listed in Table 9.1.

Table 9.1. Parameters of the studied samples.

Sample no.	Thickness, nm	Volume concentration of platinum, 10^{22} at cm^{-3}
1	40	0
2	130	1.09
3	90	0.47
4	110	0.97
5	60	1.2
6	70	2.06
7	20	2.0

9.2.2. Determination of the Platinum content

The Pt content was determined using the Medium Energy Ion Scattering (MEIS) method, which is a variety of the widely known Rutherford back-scattering technique. Energy spectra of H^+ ions were measured with an initial energy of 242 keV scattered to an angle of 120°. Un-oriented ("random") mode was used with the direction of the primary beam of H^+ ions constituting an angle of 7° with the (111) direction of the single crystal silicon of the substrate. In some cases, mostly for a-C films with a low Pt content, spectra were also measured in the oriented (channelled) mode, in which the direction of the primary H^+ beam was aligned with the (111) direction of the substrate. In this case, the suppression of the flux of ions, scattered from the substrate, enables us to separate more precisely the signals determined by the scattering of H^+ ions at "light" atoms of the film: C, N, and O. According to estimation based on the experimental conditions, the fraction of carbon matrix atoms, displaced from the equilibrium position upon collisions with protons, is less than 0.3%. Information on the film composition was obtained by fitting the experimental MEIS spectrum with theoretical model using the composition and thickness of film as fitting parameters [15].

9.2.3. Analysis of Raman spectra

Raman spectra of a-C:Pt films were registered at room temperature in a backscattering geometry using a RENISHAW 1000 micro-Raman system. A 1800 lines/mm grating was used for all measurements, providing a spectral resolution of ~1 cm^{-1}. As an excitation source a HeNe laser at 633 nm with a power of 10 mW was used. The measurements were carried out with 30s exposure time and 5 accumulations in the frequency range from 450 to 1900 cm^{-1}. The laser beam was focused on the sample surface using a 50x magnification objective with short-focus working distance.

9.3. Results

9.3.1. Rutherford backscattering

Figure 9.1 shows an energy spectrum of back-scattered H^+ ions, measured for sample 3 with a spherical Electrostatic Analyzer (ESA) which gives a high energy and high depth resolutions. Under the conditions the depth resolution for surface layers of the film is ~2 nm. Parameters of the film were obtained using a comparison between experimental and simulated spectrum (see Fig. 9.1). The part of the spectrum in the range of the energy from 210 to 240 keV corresponds to H^+ ions scattered by platinum atoms, while for energies of 200 keV and lower, spectrum corresponds to the Si substrate. In the range from 170 to 200 keV, the signal from the light components of the film such as C, N, and O is superimposed with the signal from the substrate. The Pt concentration of 4.2×10^{16} at/cm^2 was estimated from the simulation. Concentration of C and total amount of O and N were estimated to be 2.5×10^{17} at/cm^2 and 1.7×10^{17} at/cm^2, respectively. The Pt content is determined with the accuracy not exceeding 5%. The "flat top" of the Pt peak indicates a constant concentration of platinum across the film thickness. Knowing the thickness of the a-C:Pt film from interference measurements, the concentration of Pt in units of atoms/cm^3 within the film can be determined (see Tab. 9.1). Some of the samples contain impurities such as hydrogen, oxygen, and nitrogen introduced into the films during the magnetron sputtering due to ionization of gas molecules in the vacuum chamber.

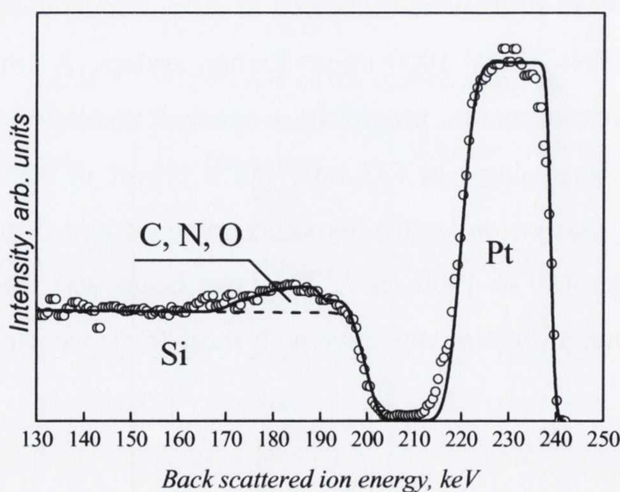

Fig. 9.1. Experimental (circles) and simulated (solid curve) spectra of H^+ ions with an initial energy of 242 keV scattered to an angle of 120° for sample 3.

9.3.2. Raman scattering

Figure 9.2 (a) shows a representative Raman spectra of a-C film without Pt (sample 1), and a-C:Pt (sample 4). Figure 9.2 (b) presents a Raman spectrum and its deconvolution into two peaks by using a mixture of Gaussian and Lorentzian functions for the a-C:Pt sample 3. The spectra are typical of a-C [16] and contain two known bands: the G band (graphitic) at 1560–1600 cm^{-1}, and D band (disordered) at 1350–1420 cm^{-1}, which are related to sp^2 carbon bonds. The G band is due to stretching vibrations of the sp^2 bonds in carbon rings and chains, and the D band is associated with breathing modes in carbon rings [16]. The presence of the D band results from violation of the wave-vector selection rule in phonon transitions for the case of small crystallites in the presence of structure-disturbing factors, e.g., foreign inclusions. The intensity of the D band can to certain extent serve as a measure of the structural disorder. For the Pt-free sample, the D band is noticeably weaker than the G band, while for a-C:Pt samples, the D peak is more pronounce and separate from the G peak. Table 9.2 summarizes the peak positions and FWHM for the D and G bands and the ratio of the peak intensities I_D/I_G. As can be seen from Table 9.2 and Fig. 9.3, the peak position of the D band increases with Pt concentration up to 0.5×10^{22} at/cm^3 and is almost constant for the Pt content from 0.5×10^{22} at/cm^3 to 2×10^{22} at/cm^3. The peak frequency of the G band decreases for Pt concentration up to 0.5×10^{22} at/cm^3 and became stable or slightly increases for the further increase of the Pt content (see Fig. 9.3). The FWHM of the D and G bands also decreases with increasing Pt content (Fig. 9.4), which indicates the higher degree of graphitization of the a-C:Pt films in comparison with those composed of pure a-C [17]. The weak dependence of the peak positions of the D and G bands on the Pt content confirms the opinion that Pt does not give rise to new chemical bonds in the a-C matrix and weakly affects its structure with only a charge redistribution caused in graphene clusters. Similar behaviour was observed for copper and other metals [3,5,6,10,18].

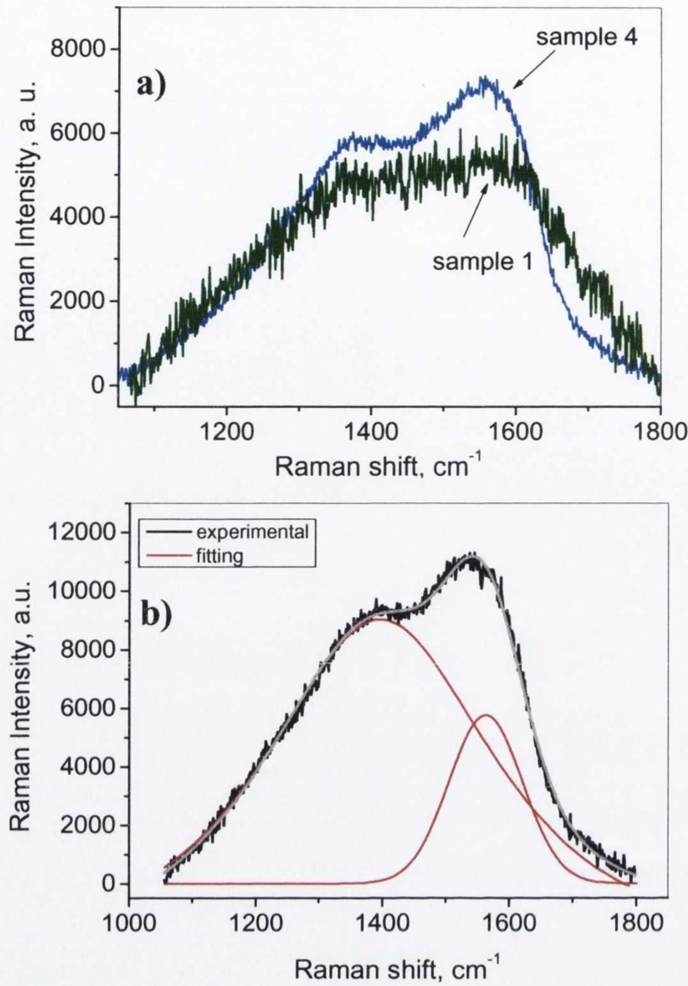

Fig. 9.2. (a) Raman spectrum of a-C films (sample 1) and of sample 4 with a Pt concentration of 0.97×10^{22} at/cm^3. (b) Raman spectrum of sample 3 with a Pt concentration of 0.47×10^{22} at/cm^3. Black line corresponds to the experimental spectrum, while red lines present the peak fitting.

Table 9.2. Pt concentration N, peak positions of D and G (Ω_D and Ω_G), FWHM of D and G bands (W_D and W_G), intensity ratio of D and G bands (I_D/I_G), and average size of graphene clusters (L_a) for the studied samples.

Sample no.	N, 10^{22} at cm^{-3}	Ω_D, cm^{-1}	W_D, cm^{-1}	Ω_G, cm^{-1}	W_G, cm^{-1}	I_D/I_G	L_a, Å
1	0	1350	425	1605	319	0.98	13.3
2	1.09	1412.5	350	1574.4	124	1.47	16.3
3	0.47	1402	387	1564	133	1.84	18.2
4	0.97	1400	349	1572	128	1.46	16.2
5	1.2	1416	346	1568	136	1.63	17.2
6	2.06	1420	302	1588	151	1.37	15.8
7	2.0	1399	277	1574	159	1.14	14.3

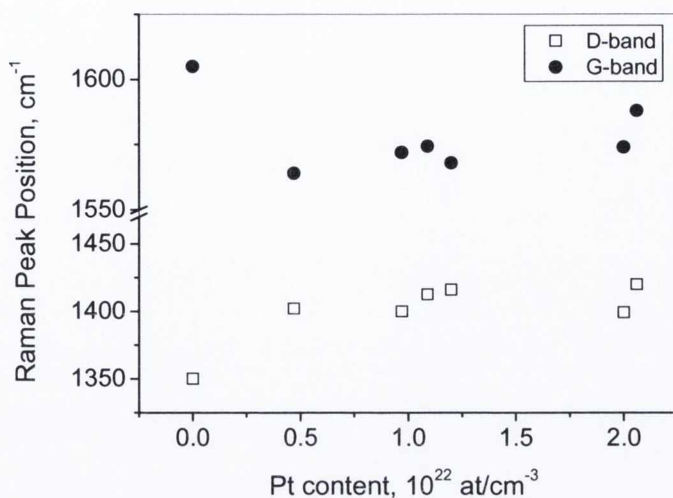

Fig. 9.3. Peak positions of D and G bands versus Pt content.

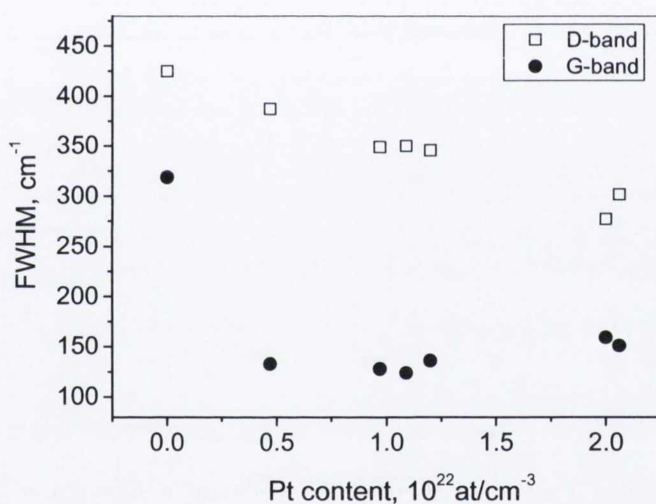

Fig. 9.4. FWHM of D and G bands versus Pt content.

The peak intensity ratio of the D and G bands, I_D/I_G, shows a complex dependence on the Pt content. The I_D/I_G sharply increases for low Pt concentrations up to 0.5×10^{22} at/cm^3, and as the Pt concentration increases further, the peak ratio decreases (see Fig. 9.5). For the Pt content corresponding to the maximum of I_D/I_G ratio, the nature of interaction between platinum atoms and graphene clusters changes and platinum clusters start to be formed in the graphene matrix. Table 9.2 also lists sizes of graphene clusters calculated in accordance with [9,16]. On the assumption that graphene clusters have small sizes, the ratio I_D/I_G can be described as follow:

$$I_D / I_G = \gamma \cdot L_a^2 \quad (9.1)$$

where, L_a is the cluster size and $\gamma = 5.5 \times 10^{-3}$ Å^2 at the excitation wavelength of 515.5 nm, the value obtained at 20 Å equation (9.1) with empirical function:

$$I_D / I_G = 44 / L_a . \quad (9.2)$$

The Eqn. (9.2) is valid when a-C structure changes from nano-graphites to a disordered system. It should be noted that, a wide scatter of points of the I_D/I_G ratio, peak position and FWHM observed in Figs. 9.3–9.5 reflects the diversity of sample properties, despite the measures taken to well reproduce the film deposition conditions. In particular, a specific property of a-C is ambivalence allowing simultaneous existence of phases with sp^3 and sp^2 hybridizations, which correspond to diamond or graphite crystalline allotropic modifications. Therefore, minor differences between the samples are due to not only different Pt content, but also different amounts of sp^3 and sp^2 bonds. In addition, the results of previous IR absorption studies [9] demonstrate that spectra of amorphous carbon films contain bands associated with C–O, C=O, O–H, C–H, and, possibly, single, double, and triple C–N bonds. According to Rutherford back-scattering data, the studied films also contain nitrogen inclusions. It has been reported previously [20] that presence of nitrogen in an amorphous carbon films hardly affects the Raman spectrum, but gives rise to new active absorption bands in the same spectral range. However, subsequent studies demonstrated [21] that presence of nitrogen rather strongly affects the Raman spectrum of amorphous carbon and the I_D/I_G ratio increases with the Pt content. Therefore, for the I_D/I_G ratio for some samples, in particular for samples 1 and 3, a contribution associated with the presence of nitrogen may be somewhat overstated. Samples 1 and 7 also contain hydrogen, which leads, according to Refs. [18,22], to an increase in the fraction of sp^2 bonds in a-C films. However, the general tendency of variation of the Raman peak position, FWHM and I_D/I_G ratio of the D and G bands with the Pt content is not affected by these differences. The question of how the simultaneous presence of various metallic and other incorporated elements affects the Raman spectrum of amorphous carbon requires further, more detailed analysis.

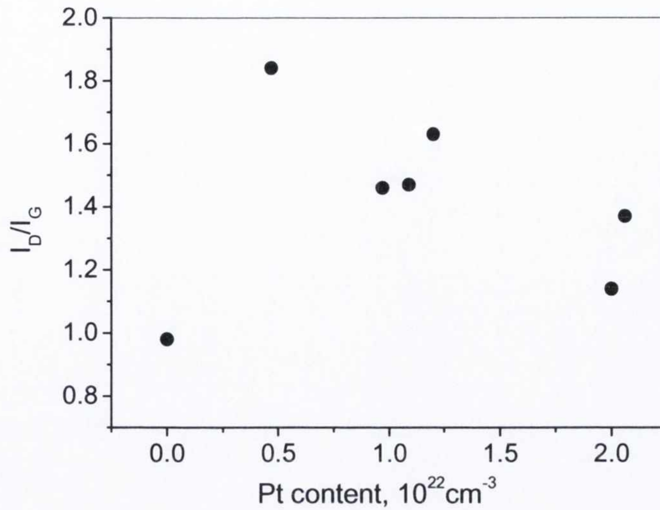

Fig. 9.5. The peak intensity ratio of the D and G bands versus the Pt content.

9.4. Conclusions

Raman spectra of a-C:Pt films with Pt content from zero to 2×10^{22} at/cm^3 comparable with the C content were studied. The platinum content of the films was determined by the Rutherford backscattering method. It was found that the I_D/I_G ratio increases with increasing Pt content at low Pt concentrations while the FWHM of the G band decreases at the same time. Thus, it leads to conclusion that the graphene clusters increase in size as the Pt concentration increases to ~0.5×10^{22} at/cm^{-3}. As the platinum concentration increases further, the size of graphene clusters decreases. A comparison between the Raman spectra for Pt-free a-C and a-C:Pt films confirms that the presence of Pt in the a-C matrix leads to an increase in the fraction of the sp^2 phase within the matrix. This is in agreement with the previously published results [18, 22].

References

1. E. Thune, E. Carpene, K. Sauthoff, M. Seibt, P. Reinke, J. Appl. Phys. 98, 034304 (2005)
2. B. Shi, W. J. Meng, T. L. Daulton, Appl. Phys. Lett. 85, 4352 (2004)
3. P. Wang, X. Wang, Y. Chen, G. Zhang, W. Liu, J. Zhang, Appl. Surf. Sci. 253, 3722 (2007)
4. X. Fan, E. C. Dickey, S. J. Pennicook, M. K. Sunkara, Appl. Phys. Lett. 75, 2740 (1999)
5. S. G. Yastrebov, V. I. Ivanov-Omskii, V. A. Kosobukin, F. Dumitrache, K. Moroshanu, Tech. Phys. Lett. 30, 995 (2004)
6. E. A. Smorgonskaya, T. K. Zvonareva, E. I. Ivanova, I. I. Novak, V. I. Ivanov-Omskii, Phys. Solid State 45, 1658 (2003)
7. V. I. Ivanov-Omskii, T. K. Zvonareva, and G. S. Frolova, Semiconductors 34, 1391 (2000)
8. Yu. V. Pleskov, Yu. E. Evstigneeva, and A. M. Baranov, Russ. J. Electrochem. 37, 644 (2001)
9. D. Remenyuk, T. K. Zvonareva, I. B. Zakharova, V. A. Tolmachev, L. V. Belyakov, and T. S. Perova, Semiconductors 43, 915 (2009)
10. V. I. Ivanov-Omskii, E. A. Smorgonskaya, Semiconductors 32, 831 (1998)
11. V. I. Ivanov-Omskii, E. A. Smorgonskaya, Semiconductors 39, 934 (2005)
12. T. K. Zvonareva, V. I. Ivanov-Omskii, A. V. Nashchekin, L. V. Sharonova, Semiconductors 34, 98 (2000)
13. A. A. Nechitailov, T. K. Zvonareva, A. D. Remenyuk, V.A. Tolmachev, D. N. Goryachev, O. S. El'tsina, L. V. Belyakov, O. M. Sreseli, Semiconductors 42, 1249 (2008)
14. Sputtering by Particle Bombardment I, Ed. by R. Behrisch, Springer, Berlin, 1981; Moscow, Mir, 1984
15. V. V. Afrosimov, R. N. Il'in, S. F. Karmanenko, A. A. Melkov, V. I. Sakharov, I. T. Serenkov, Thin Sol. Films 492, 146 (2005)
16. A. C. Ferrari, J. Robertson, Phys. Rev. B 61, 14095 (2000)
17. V. I. Ivanov-Omskii, T. K. Zvonareva, G. S. Frolova, Semiconductors 42, 1113 (2008)
18. V. I. Ivanov-Omskii and E. A. Smorgonskaya, Phys. Solid State 41, 786 (1999)

19. F. Tuinstra, J. L. Koenig, J. Chem. Phys. 53, 1126 (1970)
20. J. N. Kaufman, S. Metin, D. D. Saperstein, Phys. Rev. 39, 1353 (1989)
21. R. McCann, S. S. Roy, P. Papacostantinou, J. A. McLaughin, S. C. Ray, J. Appl. Phys. 97, 073522 (2005)
22. J. Budai, Z. Toth, A. Juhasz, G. Szakacs, E. Szilagyi, M. Veres, M. Koos, J. Appl. Phys. 100, 043501 (2006)

10. Raman investigation of crystalline uniformity of graphene

10.1. Introduction

There are current industry predictions that, by the year of 2020, silicon devices will have shrunk to about 20 nanometres in size and will have reached their limit in both size and performance [1,2]. Graphene is currently considered as a promising electronic material for "post-silicon electronics" [3]. Graphene is a two dimensional monolayer of sp^2-bonded carbon atoms which are densely packed in a honeycomb crystal lattice (see Fig. 10.1). Single-layered graphene (SLG) is a basic building block for graphitic materials of all other dimensionalities: it can be wrapped up into spherical fullerenes, rolled into cylindrical nanotubes, or stacked into 3D graphite (see Fig. 7.1 in chapter 7).

More than 70 years ago, Landau and Peierls argued that strictly 2D crystals were thermodynamically unstable and therefore could not exist [4,5]. They claimed that a divergent contribution of thermal fluctuations in low-dimensional crystal lattices should lead to such displacements of atoms that they become comparable to inter-atomic distances at any finite temperature [6]. Indeed, the melting temperature of thin films rapidly decreases with decreasing thickness, and the films become unstable (segregate into islands or decompose) at a thickness of, typically, dozens of atomic layers [7,8]. For this reason, atomic monolayers have so far been known only to exist as an integral part of a larger 3D structure, usually grown epitaxially on top of monocrystals with matching crystal lattices [7,8]. Graphene was experimentally discovered for the first time in 2004 by A. K. Geim and K. S. Novoselov [9] from the University of Manchester. The free standing graphene that they created can exist due to the presence of interactions between bending and stretching long-wavelength phonons, which lead to a stabilization of atomically 2D layers through their elastic deformation in all three dimensions [10].

Graphene has attracted substantial research interest of the scientific community because of its remarkable physical properties. Part of the interest lies in the nature of the electronic band structure, which permits carriers to behave as massless Dirac fermions with a vanishing density of states at the Fermi level [3]. This allows electrons to behave

like photons, in that they can zip across the graphene layer without scattering. Experimental results from transport measurements show that graphene has a remarkably high electron mobility at room temperature, with reported values of over 15.000 cm^2/Vs [3]. It is worth noting that freely suspended graphene tends to have a higher carrier mobility than graphene created on substrates. Also, graphene is a promising material for nano-devices [11-14], due to its exhibition of ballistic transport at room temperature as well as its chemical and mechanical stability. There exist a variety of potential applications for graphene. Graphene has attracted the interest of technologists who see it as a way of constructing ballistic transistors. Graphene exhibits a pronounced response to externally applied electric fields in the perpendicular direction, allowing one to build field-effect transistors (FETs) [9]. In 2004, the Manchester group demonstrated the operation of the world's first ever graphene FET with a "rather modest" on-off ratio of ~30 at room temperature [9]. In February 2010, researchers at IBM reported that they have been able to create graphene transistors with an on-and-off rate of 100 GHz, which is above the speed limit of silicon [15]. The graphene transistors from IBM were created using extant silicon-manufacturing equipment, suggesting for the first time that graphene transistors are a conceivable though still fanciful replacement for silicon [15]. The relatively high electrical conductivity and optical transparency of graphene make it an ideal candidate for transparent conducting electrodes, required for such applications as touch-screens, liquid crystal displays, organic photovoltaic cells, and organic light-emitting diodes [16-18]. As such, researchers at Stanford University have successfully developed a brand new concept of organic light-emitting diodes (OLEDs) using graphene of a few nanometres as transparent conductors [19].

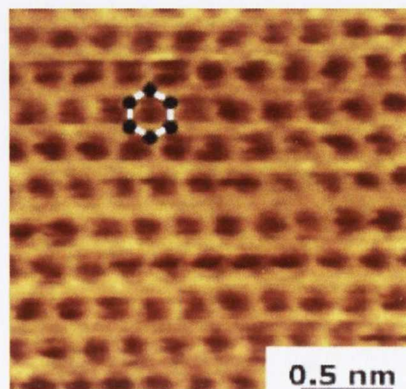

Fig. 10.1. Scanning electron microscopy (STM) image of the atomic structure of a single layer of exfoliated graphene [20].

Graphene can be obtained in many different ways. Existing methods for graphene synthesis include mechanical exfoliation of highly ordered pyrolytic graphite (HOPG) [4,9,21], elimination of Si from the surface of a single crystal SiC by ultrahigh vacuum (UHV) annealing [22,23], deposition of graphene at the surface of a single crystal [24] or polycrystalline metal [25], and various types of wet-chemistry based approaches [26,27]. However, up to now none of these methods have led to the delivery of good quality and uniform graphene with a sufficiently large area for application as a practical electronic material. Mechanical exfoliation is a convenient and inexpensive way of producing graphene but has the main drawback of having huge amounts of multi-layered graphitic pieces as side products. Graphene created on SiC substrates has relatively good carrier mobility, but it may be applicable to SiC-based devices only, since transfer to other types of substrates such as SiO_2/Si has not yet been proved feasible. There have been a number of reports on the growth of graphene on various types of metal substrates such as Ni, Co, Ru, Ir, Cu, etc., by chemical vapor deposition (CVD) [28-31] or UHV-CVD [30-32]. Because of their relatively low cost, grain size, good etch-ability, and their wide applicability in the semiconductor industry, Ni and Cu have received the most attention as a graphene substrate material [28-31]. Single- and multi-layered graphene have successfully been grown on polycrystalline Ni [28,29,31], while large-area graphene has successfully been grown on Cu [30] substrates by CVD.

Raman spectroscopy has historically played an important role in the structural characterisation of graphitic materials, and has also become the prevailing technique for structural studies of graphene. Results of a systematic Raman study of single- and multi-layered graphene at different excitation wavelengths are presented in this chapter. Raman area mapping technique was applied to study the uniformity and structural properties of CVD deposited graphene on Ni/SiO_2/Si and Cu substrates and after transfer onto SiO_2/Si. The Raman peak profiles of the 2D and G peak are also discussed in this chapter.

10.2. Atomic structures of single layer- , few layers- graphene and graphite

Graphene consists of sp^2 carbon hexagonal networks, in which strong covalent bonds are formed between carbon atoms. The unit cell of mono-layer graphene (1-LG) contains two carbon atoms, A and B, each alone forming a two-dimensional triangular network, but displaced from each other by the carbon-carbon distance $a_{C\text{-}C} = 0.142$ nm, as illustrated in Fig 10.2 (a). The 3D graphite structure corresponds to a stacking of the hexagonal networks of individual graphene layers in the direction perpendicular to the layer plane (c-axis) with an AB (Bernal) stacking arrangement and with a weak van der Waals interaction between planes of layers. The two equivalent carbon networks, denoted by A and B in Fig. 10.2 (a), produce the two bands – π and π^*, which intersect in two in-equivalent points in the First Brillouin zone, K and K', justifying the name of graphene as "gapless semi-metal". The term “Bernal stacking” refers to an arrangement in which the vacant centres of the hexagons on one layer have carbon atoms on hexagonal corner sites on the two adjacent graphene layers, as shown in Fig. 10.2 (b). In graphite with AB stacking, the unit cell consists of four carbon atoms A_1, A_2, B_1, and B_2 on the two layer planes shown in Fig. 10.2 (b). The in-plane and *c*-axis lattice constants for graphite are a = 0.246 nm and c = 0.670 nm, respectively. Under normal circumstances, bilayer of graphene obtained from mechanical exfoliation of graphite exhibits AB stacking arrangement, and therefore the number of atoms in the unit cell of bilayer graphene (2-LG) is the same as that for graphite, with four atoms per unit cell, as shown in Fig. 10.2 (b). In turbostratic graphite, denoted by 2D graphite, there is no stacking order between adjacent graphene layers and the interlayer spacing (>0.342 nm) is larger than that for crystalline graphite ($c/2$ = 0.335 nm) [32]. Another common form of crystalline graphite is the highly oriented pyrolytic graphite (HOPG), which is a synthetic AB stacked graphite obtained from carbon-based precursors, and annealed at high temperatures (typically over 3200 °C under pressure) [33]. Tri-layer graphene (3-LG) in turn contains three layers, two of which are like bilayer graphene and the third layer has atom A_3 over A_1 and atom B_3 over B_1 as shown in Fig. 10.2 (d).

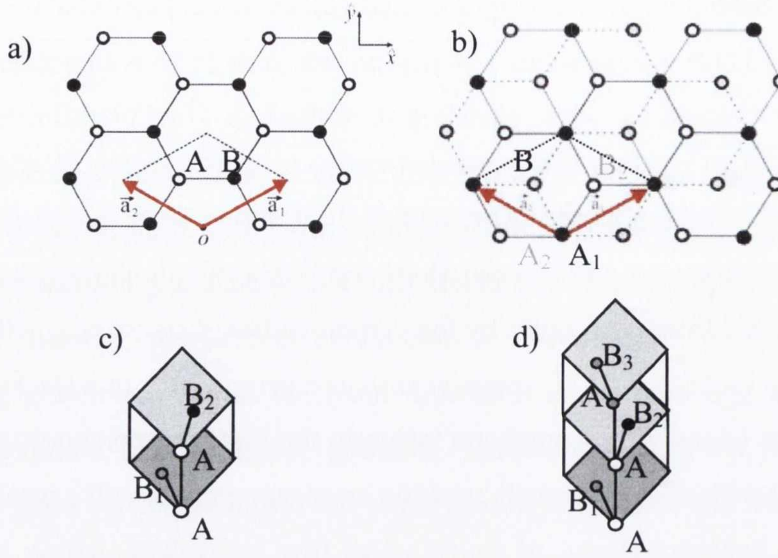

Fig. 10.2. (a) A top view of the real space unit cell of monolayer graphene showing the inequivalent atoms A and B and unit vectors a_1 and a_2. (b) A top view of the real space of bilayer graphene (2-LG). (c) and (d) The unit cell and the x and y unit vectors of bilayer graphene and of trilayer graphene (3-LG).

10.3. Experimental

10.3.1. Sample growth

The substrate (111)Ni/SiO_2/Si is composed of a 500 nm thick nickel film deposited on SiO_2/Si substrates in an electron-beam evaporator. All samples undergo a process of post-deposition annealing for the purpose of promoting grain growths. The annealing was carried out at a temperature of 1000°C in a quartz tube furnace under a total pressure of 200 Torr and a flow of 200 sccm H_2 and 400 sccm Ar. Figure 10.3 shows snapshots of the morphology of the nickel film at 30 min and 60 min of annealing time with the corresponding average grain sizes being 20 μm and 50 μm, respectively [31].

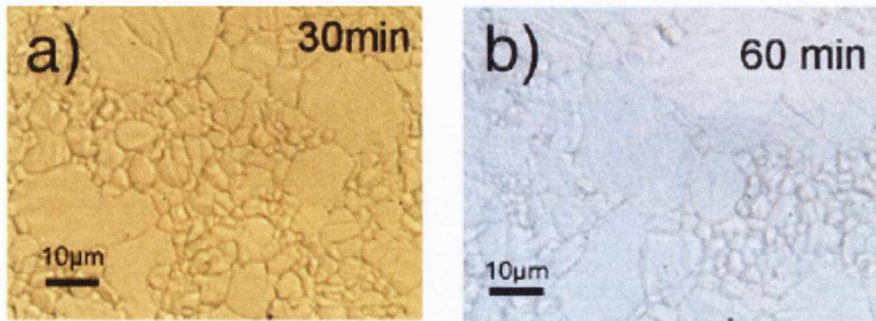

Fig. 10.3. Optical micrographs of the nickel film surface after (a) 30 min and (b) 60 min of annealing [31].

Large nickel grain size and thus a minimum density of grain boundaries are preferable due to the well-known negative impact of grain boundaries on the control of the number of layers of graphene. CVD growth of graphene was carried out at a pressure of 200 Torr under the flow of 50 sccm of 5% diluted methane (CH_4) in argon (Ar) together with 500 sccm of H_2. The growth temperature was varied from 900°C to 1000°C, and the growth time varies from 50s to 120s. Post-growth cooling was carried out under a flow of 2000 sccm Ar and 500 sccm H_2. The cooling rate spanned from 7°C/min to 25°C/min. Graphene also was grown on cupper foil. Cu foil was annealed at 1000°C for 30 minutes under hydrogen environment. CVD growth of graphene on Cu was carried out at a pressure of 30 Torr under the flow of methane and hydrogen. The growth temperature was 1000°C, and the growth time 30 min. Next the samples were cooled down to the room temperature in hydrogen environment (the total hydrogen pressure was 1 Torr). Then, graphene layers were transferred onto SiO_2/Si surface using the polydimethylsiloxane (PDMS) wet-etching method. Figures 10.4 and 10.5 present schematic diagrams of two sets of samples investigated in this research. One of them consists of sample 1 with graphene deposited on Ni/SiO_2/Si and sample 2 with graphene transferred onto SiO_2/Si. The second set involves graphene deposited on cupper foil (sample 3) and graphene transferred onto SiO_2/Si (sample 4).

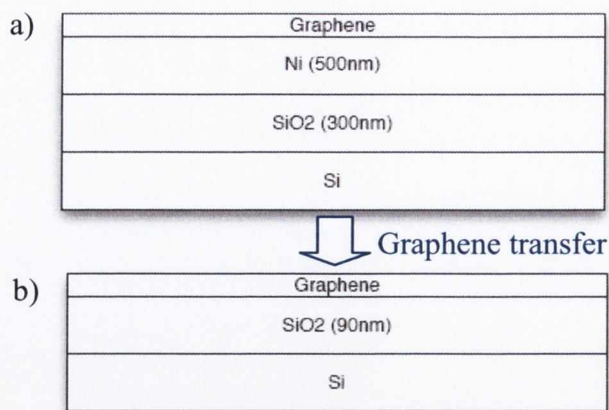

Fig. 10.4. Schematic cross-section view of sample 1: graphene on Ni/SiO_2/Si, and sample 2: transferred graphene on SiO_2/Si.

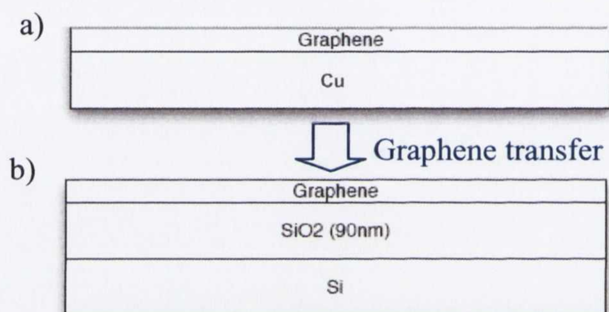

Fig. 10.5. Schematic cross-section view of sample 3: graphene on Cu, and sample 4: transferred graphene on SiO_2/Si.

10.3.2. Characterisation techniques

Optical microscopy in combination with micro-Raman spectroscopy were used as the main characterization methods. Raman measurements were carried out at room temperature in the backscattering geometry using RENISHAW 1000 micro-Raman system. An Ar^+ laser at 457, 488, 514 and HeNe laser at 633 nm with power of 10-40 mW were used as the excitation sources (high power of laser was applied for measurements of graphene on metals). But most of the study was done with an excitation wavelength of 488 nm as it was found that graphene has the highest Raman efficiently for this particular wavelength. Single spot Raman measurements and Raman area mapping were done for graphene on different substrates. The Raman spectra were

taken in an extended mode. The laser spot was focused on the sample surface using a 50x and 100x magnification objectives with short-focus working distance. The Raman spectra were taken with 5s exposure for graphene on SiO_2/Si and 40s exposure time for graphene on Ni. For graphene deposited on Cu and after transfer onto SiO_2/Si measurements were done for 10s at an excitation wavelength of 514 nm. The Raman spectra were fitted with a mixture of Gaussian and Lorentzian function for evaluating the position, intensity, and linewidth of the detected 2D, D and G peaks.

10.4. Results and discussion

10.4.1. Raman spectra of SLG, FLG and graphite

Figure 10.6 shows representative Raman spectra of graphene on SiO_2/Si measured with an excitation wavelength of 488 nm. The most prominent features corresponding to graphene are the so-called G band at ~ 1582 cm^{-1} and the 2D band (also called G' band) at about 2660 cm^{-1}. The defect-induced D band observed at about half of the frequency of the 2D peak (around 1330 cm^{-1}) indicates the presence of disorder in the measured graphene layer [34]. The G peak originates from in-plan vibrational E_{2g} phonon mode at the Brillouin zone centre [34], and it is coming from the first order Raman scattering. The 2D band originates from the second order Raman scattering. The presence of the D peak is due to the breathing modes of sp^2 atoms and requires a defect for its activation. If the peak intensity ratio of the D band to the G band I(D)/I(G) is <0.1, it indicates that the amount of disorder within the graphene sample is negligible [35]. From the shape, intensity, linewidth, and position of the 2D peak, one could distinguish between various numbers of graphene layers and bulk graphite [32]. For mono-layer of graphene (1-LG), the 2D band is a single sharp Lorentzian peak, while in graphite it consists of two components $2D_1$ and $2D_2$, roughly ¼ and ½ the height of the G peak, respectively (see Fig. 10.8 (a)). For multi-layer of graphene layers (2-, 3-, 5-LG) deconvolution of 2D peak is more complicated and is presented in Fig. 10.9 [32]. As one can see from Fig. 10.9 (b), the 2D band for a bilayer of graphene is much broader and up-shifted with respect to the graphene. It has four components, two of which have higher relative intensities than the other two. Figures 10.9 (c) and 10.9 (d) presents the 2D band

evaluation with a further increase in the number of graphene layers. For more than 5 layers of graphene the Raman spectrum is no longer distinguishable from those of bulk graphite.

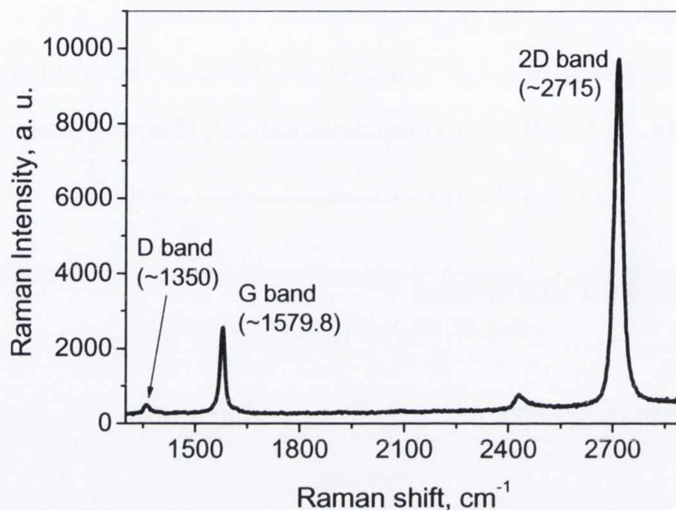

Fig. 10.6. Raman spectra of monolayer of graphene measured with an excitation wavelength of 488 nm.

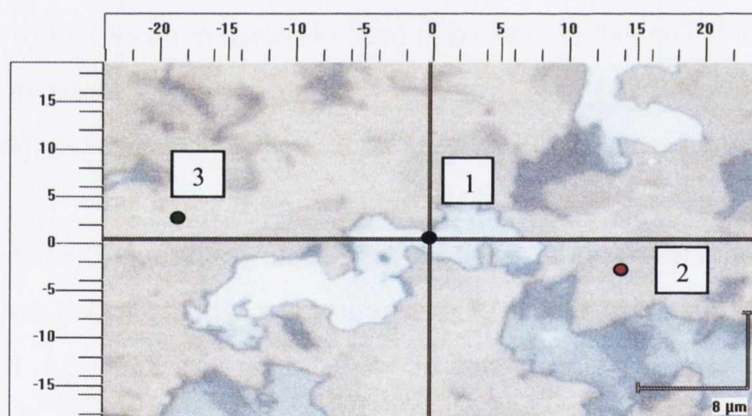

Fig. 10.7. Optical microscopy image of graphene on SiO_2/Si. Points 1, 2 and 3 correspond to Raman spectra presented in Fig. 10.8 (a) and (b).

Figure 10.7 presents an optical microscopy image of graphene grown by CVD on Ni SiO_2/Si and then transferred onto SiO_2/Si substrate. The graphene sheets exhibit different contrast regions, which correspond to different thicknesses of graphene. The origin of such a contrast can be understood from the set of Fresnel's equations based on the refraction and reflection of light from the Air/Graphene, Graphene/SiO_2 and SiO_2/Si interfaces [36]. The silver/grey colour spots correspond to multi-layered graphene with

more than 5 layers of graphene or even graphite (see point 1 in Fig 10.7). The region of mono-layer of graphene is almost transparent and can hardly be identified due to the thickness of the silicon oxide layer of ~90 nm (see point 2). The highest contrast between single-layer of graphene and silicon oxide was obtained for a thickness of SiO_2 around 300 nm, and this chosen thickness of SiO_2 has been widely reported in the literature [36,37].

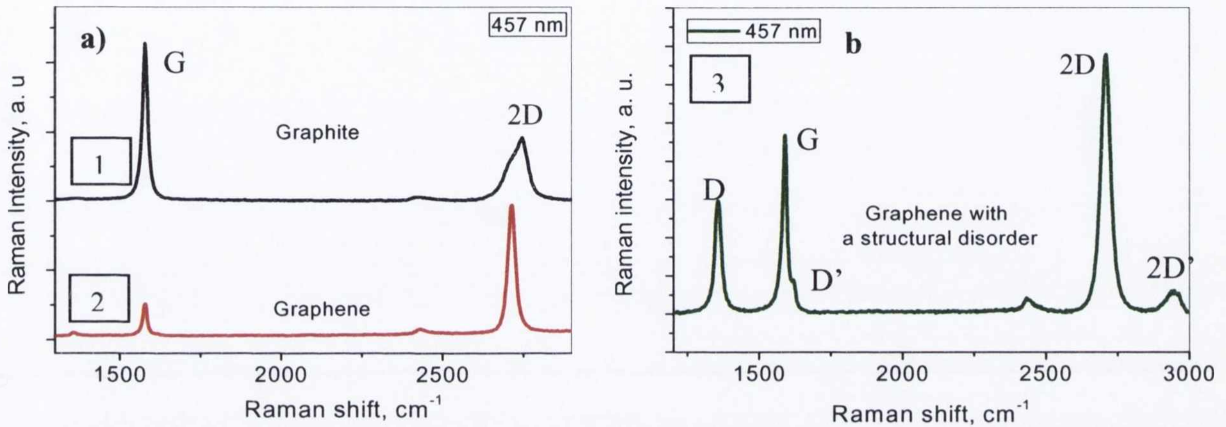

Fig. 10.8. (a) Comparison of Raman spectra at 457 nm for bulk graphite (black line) and graphene (red line). (b) Raman spectrum of disordered graphene.

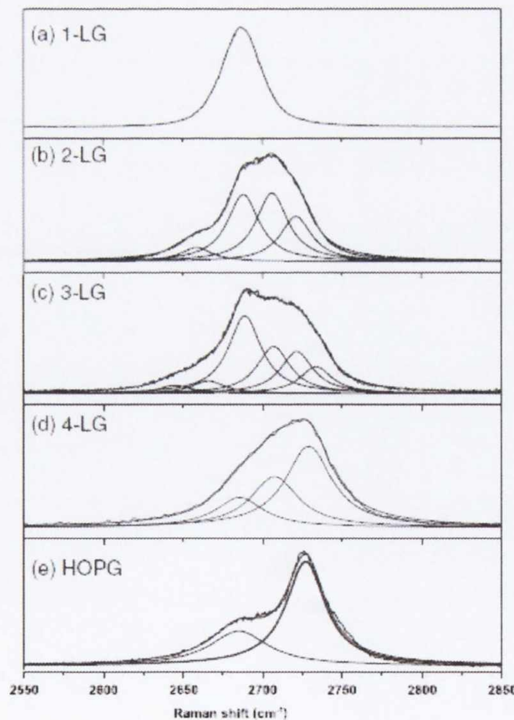

Fig. 10.9. Evaluation of 2D Raman band measured with 514 nm excitation wavelength for (a) 1-LG, (b) 2-LG, (c) 3-LG, (d) 4-LG and (e) HOPG [32].

Point 3 in Fig. 10.7 corresponds to a region of disordered single- or bi-layer of graphene. Figure 10.8 (b) presents Raman spectra of graphene measured for point 3 in Fig. 10.7. A strong D peak at ~1360 cm^{-1} was observed indicating the presence of strong structural defects in graphene or defect-like graphene edges. The D' peak was observed at ~1600 cm^{-1}, which was also observed for defected graphite. The 2D' peak at ~2950 cm^{-1} is associated with a D + 2D combination mode and also is induced by disorder. Data of the peak position, linewidth and peak intensity of the G and 2D bands from the Raman spectra in Fig 10.8 (a) and (b) are shown in Table 10.1.

Table 10.1. The data of the peak position, intensity, and linewidth of the G and 2D bands for mono-layer of graphene measured with an excitation wavelength of 457 nm.

Spectra	G peak			2D peak		
	Position, cm^{-1}	Intensity, a. u.	Linewidth, cm^{-1}	Position, cm^{-1}	Intensity, a. u.	Linewidth, cm^{-1}
1	1577.8	11352	19	($2D_1$) 2710 ($2D_2$) 2747.5	2454 3524	60.5 40.7
2 (1-LG)	1579.8	2302	15.8	2715	9377	28.3
3	1590	4545	19.4	2709.3	6853	40.6

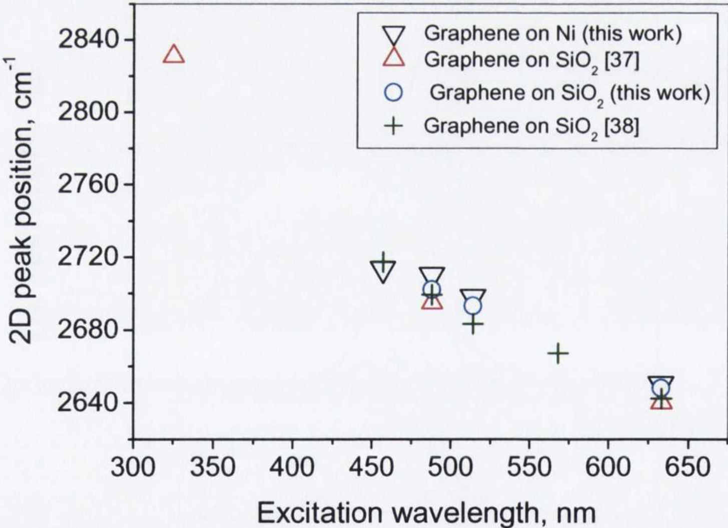

Fig. 10.10. Dispersion of the 2D peak for graphene on Ni/SiO_2/Si and SiO_2/Si compared with the results published elsewhere [37, 38].

Figure 10.10 presents a plot of the frequency of the 2D band against the excitation wavelength. The results obtained were compared with those published in the literature

[37,38]. Graphene samples reported in Refs [37,38] were obtained by a mechanical cleavage of graphite and then transferred onto a SiO_2/Si wafer. As shown in Fig. 10.10, the 2D peak shifts to lower frequency for increasing excitation wavelength. A linear dispersion of the 2D band was observed in this work for the visible range of the excitation light, which is also confirmed by others groups [37,38]. However a different behaviour of the peak shift was observed in the UV range by Calizo group [37]. In this region, the observed dispersion of the 2D peak is nonlinear. Calizo attributes this feature to contributions from the optical transitions involving electrons with the momentum away from the K point when the excitation wavelength is smaller than 400 nm [37]. The 2D band exhibits a strong dispersive behaviour: for visible excitation light the peak position change from ~2640 cm^{-1} at 633 nm excitation wavelength to ~2715 cm^{-1} at 457 nm. For the first time, dispersion of 2D band for graphene on Ni/SiO_2/Si is presented. The results for graphene on Ni are in good agreement with those obtained after a transfer of the graphene sample onto a SiO_2/Si substrate. The origin and the dispersive behaviour in the frequency of the 2D band as well as D band can be explained in term of a double resonance (DR) Raman process [39,40]. In this process, the wave-vector q of the phonon associated with 2D and D bands (measured from the Dirac point K) would couple preferentially to the electronic states with wave-vectors k, such that $q \approx 2k$. The double-resonance (DR) process is presented in Fig. 10.11 (b,d,e) and it begins with an electron of wave-vector k around K point absorbing a photon of energy E_{laser} (with wave-vector q). The electron is inelastically scattered by a phonon or defect of wave-vector q and energy E_{phonon} to a circle around K' point with wave-vector $k+q$. The K' point is related to K by time reversal symmetry. Next, the electron is scattered back to a k state and emits a photon by recombining with a hole at a k state. In the case of the D band, the two scattering processes consist of one elastic scattering by defects of the crystal and one inelastic scattering by emitting or absorbing a phonon, as shown in Fig. 10.11 (b). In the case of the 2D-band, both scattering processes are inelastic and only two phonons are involved. This double resonance mechanism is called an inter-valley process because it connects two high symmetry points K and K' of the first Brillouin zone of graphene. When the double resonance process connects two points belonging to the same circle around the K point (or the K' point), as it is in the case of the D' band (~1600 cm^{-1}), the process is called an intra-valley process [40]. When E_{laser} is increased relative to the Dirac point, the resonance k vector for the electron moves away from the K point. In the DR process, the corresponding q vector for the phonon increases with

increasing k, as measured from the K point. Thus by changing the laser energy, we can observe a dispersion of the phonon energy as a function of E_{laser} [32]. Sometimes, the Raman process can also occur by scattering of holes. In the special case of graphene, where the valence and conduction bands are almost mirror bands of one another relative to the Fermi energy, this can lead to an important effect called the triple resonance (TR) Raman process [41]. As one can see in Fig. 10.11 (e), instead of the electron being scattered back by a phonon with wave-vector $-q$, the hole is scattered by a wave-vector $+q$. In this case, the electron-hole generation is a resonant process, in which both the electron and hole scattering processes are resonant, and finally the electron-hole recombination at the opposite side with respect to the K point also occurs near the K' point between an electron and a hole in resonance states. Therefore, for the triple resonance process all steps in the usual double resonance process now become resonant. This triple-resonance condition might explain why the 2D band is much more intense than the G-band in mono-layer graphene [32].

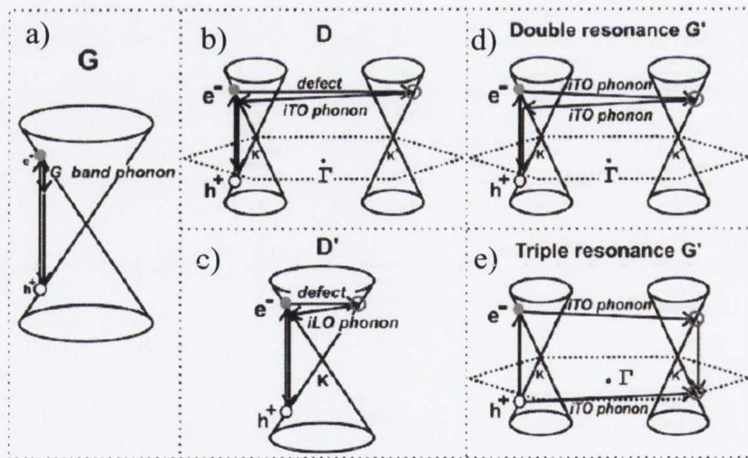

Fig. 10.11. (a) First-order G-band process and one-phonon second-order DR process (b) for the D-band (inter-valley process) and (c) for the D'-band (intra-valley process) and two-phonon second-order resonance Raman spectral processes (d) for the double resonance 2D (G') process, and (e) for the triple resonance 2D (G') band process (TR) for monolayer graphene [32]. Resonance points are shown as open circles near the K point (left) and the K' point (right).

10.4.2. Investigation of structural uniformity of graphene using Raman area mapping technique

The main challenge of graphene technology is to fabricate a large and uniform monolayer of graphene. Raman area mapping is only one easy and precise technique for investigating the uniformity of graphene, as it allows for the mapping all peaks in the same time. From this we can interpret the differences in the Raman maps for the intensity of the G and 2D peaks and the full width a half maximum (FWHM) of the 2D peak. In this work the peak profiles of the 2D and G peak are discussed for graphene samples grown on Ni and Cu and transferred onto SiO_2/Si.

Figures 10.12 (a) and (b) show the optical microscopy images of the scanned areas of the samples. Graphene on Ni was scanned in the area of 5 μm^2 and graphene after transfer was mapped in the region of 6 μm x 7 μm. The Raman mapping results for these samples are presented in Figs. 10.13 and 10.14, respectively.

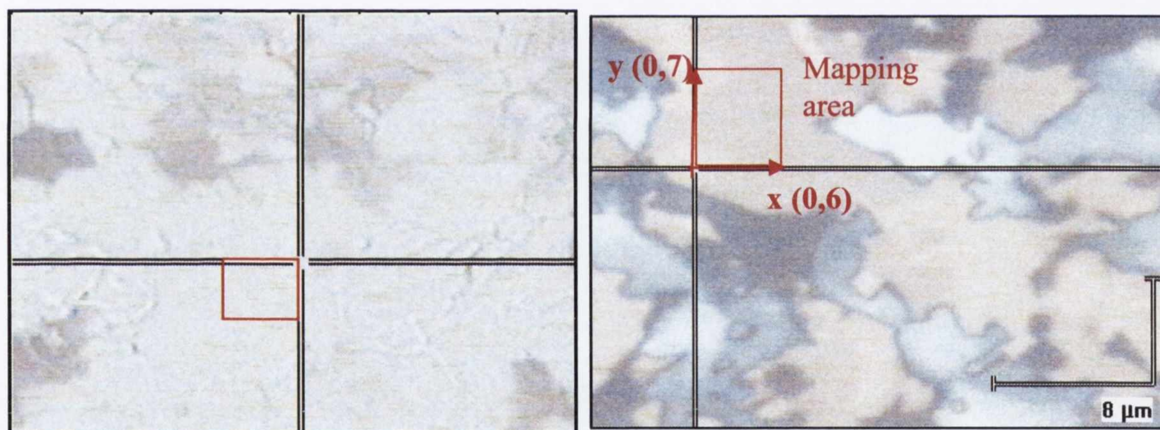

Fig. 10.12. Optical microscopy image of (a) graphene on Ni (red square shows mapped region of 5μm x 5μm) and (b) graphene on SiO_2/Si (6μm x 7μm).

Figures 10.13 (a) – (f) show Raman maps of the intensity, linewidth and peak position of the G and 2D peak for graphene on Ni measured at 488 nm of excitation wavelength and high laser power of 50 mW. The high level of structural non-uniformity was observed for graphene on Ni due to the Ni substrate itself being a metal surface that reflects light strongly and leads to a strong background signal in the Raman spectra. There is also interaction between graphene and Ni atoms, which influences on weak Raman signal. That is why a high laser power is required to detect signal from graphene

deposited on metal. The regions of single-layer of graphene are marked with red circles. We regard a graphene sample to be mono-layer if the intensity ratio of the 2D peak to the G peak is $I_{2D}/I_G \approx 3$ or 4, and if the linewidth of the 2D peak is around ~30 cm^{-1}. In our case the linewidth of the 2D peak from the map in Fig 10.13 (d) is much larger, i.e. ~40-50 cm^{-1} for single-layer of graphene. This increase in linewidth can be explained by a metal-graphene interaction which affects graphene properties. Based on results described above, it can be concluded that flakes with an area of ~1 μm^2 of mono-layer were observed for graphene deposited on Ni. Figure 10.14 shows representative Raman spectra taken from the point 1, 2 and 3 in Fig. 10.13 (b). As can be seen from Fig. 10.14, a strong D peak at ~1270 cm^{-1} was observed which indicates the presence of large structural disorder in graphene or corresponds to the edge of a graphene flake.

Figures 10.16 (a) to 10.16 (f) present the Raman maps for the same graphene but after transfer onto SiO_2/Si wafer. Based on the intensity ratio of 2D peak to the G peak (I_{2D}/I_G), we can regard the green and red region in Fig. 10.16 (b) as a monolayer of graphene. The intensity of the 2D peak in this area is three, four times higher than intensity of the G peak. The linewidth of the 2D peak in this region varies from 28 to 35 cm^{-1}, while the peak position of 2D band varies from 2706 cm^{-1} to 2716 cm^{-1} in this region. After graphene transfer we observed larger graphene uniformity. Single-layer of graphene was detected in the area of 2 μm x 6 μm for this map. This leads to the conclusion that graphene of the same good quality can be obtained after CVD deposition on Ni. However, in this case, the detected Raman signal is much weaker compare to graphene on SiO_2/Si due to due to interaction of Ni with C atoms and the absence of Raman enhancement effect described in the following paragraph.

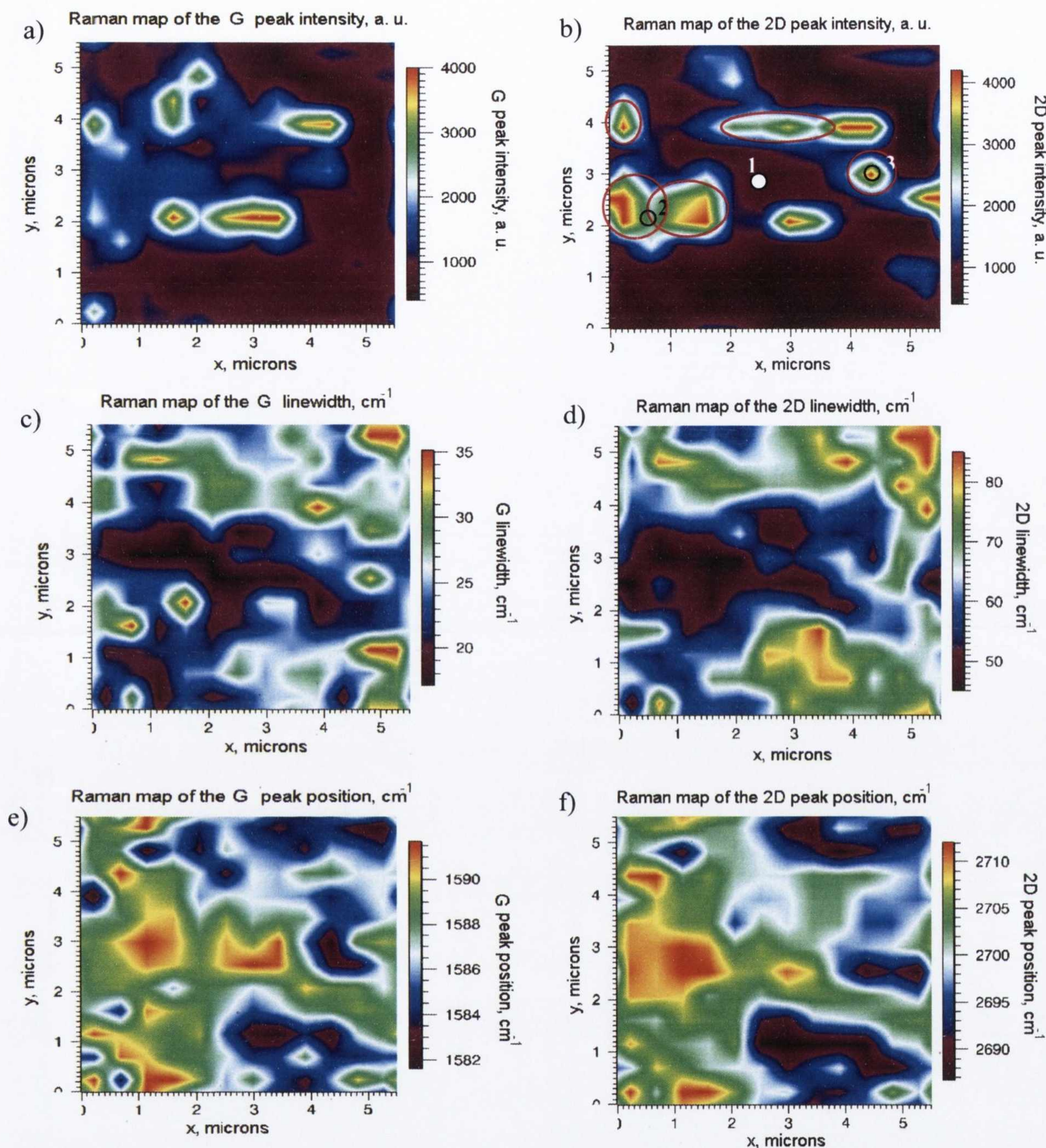

Fig. 10.13. Raman area maps of graphene grown Ni/SiO_2/Si. (a), (c), (e) Raman maps of the intensity, linewidth and peak position of the G peak, respectively. (b), (d), (f) Raman maps of the intensity, linewidth and peak position of the 2D peak, respectively.

Figures 10.14 and 10.15 show Raman spectra from the marked points in the map images of graphene on Ni and on SiO_2/Si, respectively. As one can see, the signal from graphene on SiO_2/Si is much stronger than for graphene on Ni, even if a much shorter time of accumulation and a four times lower power were applied. Raman signal of

graphene was significantly enhanced for measurements on SiO_2/Si substrate. This can be attributed to the lack of the interactive metal background and to the presence of multi-reflection and multi-interference in graphene as described by the Fresnel equations [42]. This enhancement of electric field depends also on the thickness of the silicon oxide beneath the graphene layer as it was demonstrated in Ref [42] (see section 7.4.3 for more details).

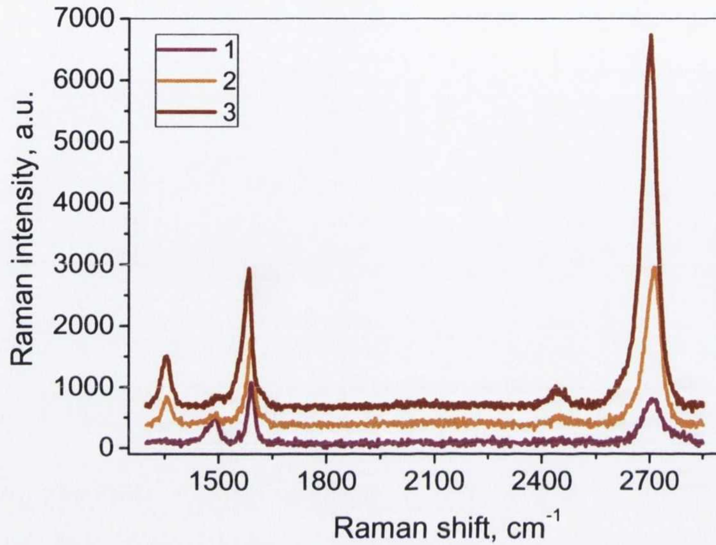

Fig. 10.14. Raman spectra from different spots of graphene on Ni measured at 488 nm of excitation wavelength. The spectra 1-3 correspond to spots of the sample presented in Fig. 10.13 (b).

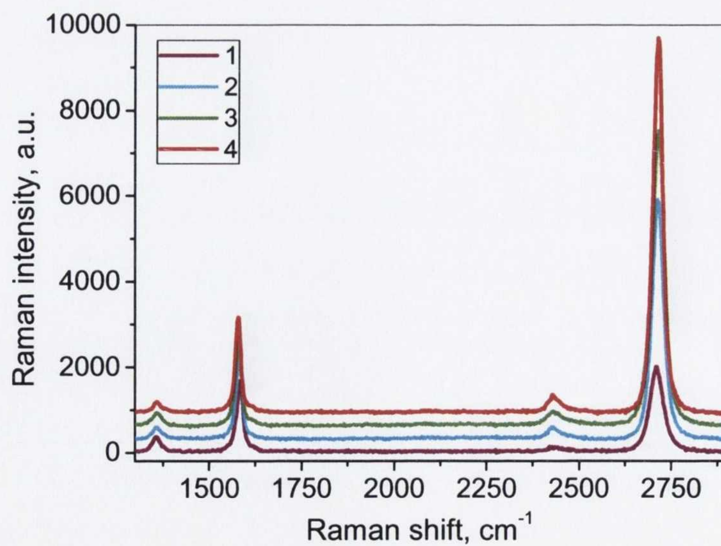

Fig. 10.15. Raman spectra from different spots of graphene on SiO_2/Si. The spectra 1-4 correspond to spots of the sample presented in Fig. 10.16 (b).

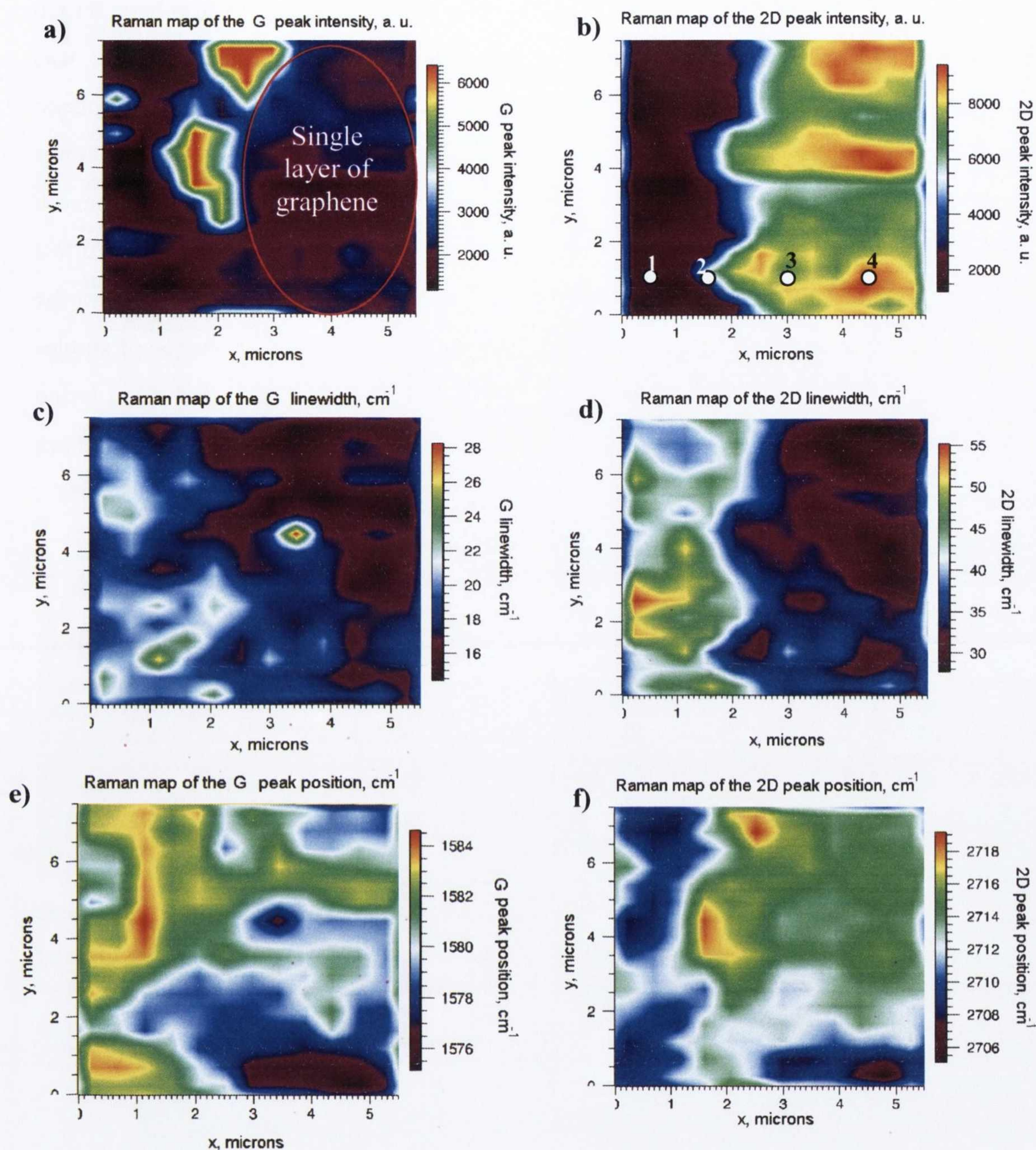

Fig. 10.16. Raman area maps of graphene transferred from $Ni/SiO_2/Si$ onto SiO_2/Si. (a), (c), (e) Raman maps of the intensity, linewidth and peak position of the G peak, respectively. (b), (d), (f) Raman maps of the intensity, linewidth and peak position of the 2D peak, respectively.

In the following paragraph, further results for graphene deposited on Cu films with improved CVD growth conditions are presented. Figure 10.17 presents the optical microscopy images of mapped area from graphene on Cu foil and after transfer onto SiO_2/Si substrate. The arrows indicate the direction and mapped area (50 μm^2). Figure

10.19 and 10.20 show the Raman area maps of the G and 2D peak for graphene on Cu and SiO_2/Si respectively. A higher structural uniformity for graphene on Cu was achieved after improving the growth conditions. In this case, a single-layer graphene was detected on an area of 20 μm x 40 μm. The linewidth of the 2D peak for mono-layer of graphene is relatively large, i.e. ~60 cm^{-1} due to the background signal from Cu and due to interaction of metal-graphene. In addition, it has to be noted that the Cu foil was not smooth but was bended in many places. An evolution of the Raman spectra for graphene on Cu with mapping distance is shown in Fig. 10.18. The existence of single-layer of graphene after transfer onto the SiO_2/Si substrate was detected on a twice bigger area 40 μm x 50 μm (see Fig. 10.20). Linewidths of the 2D peak in this area are from 30 to 45 cm^{-1}, while the peak position is in the range from 2678 to 2690 cm^{-1}. Raman spectra of uniform monolayer of graphene on SiO_2/Si are shown in Fig. 10.21.

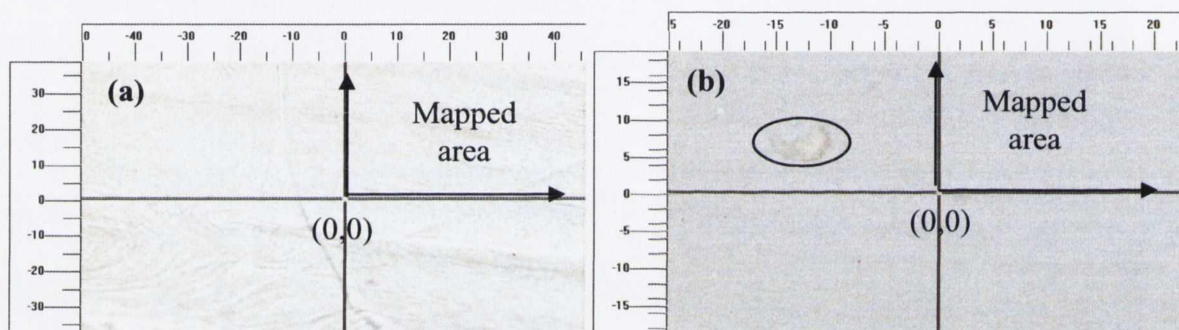

Fig. 10.17. Optical microscopy image of (a) graphene deposited on Cu and (b) graphene transferred onto SiO_2/Si (black arrows shows direction of mapping). In circle (b) - the grain of Cu remained after PDMS transfer.

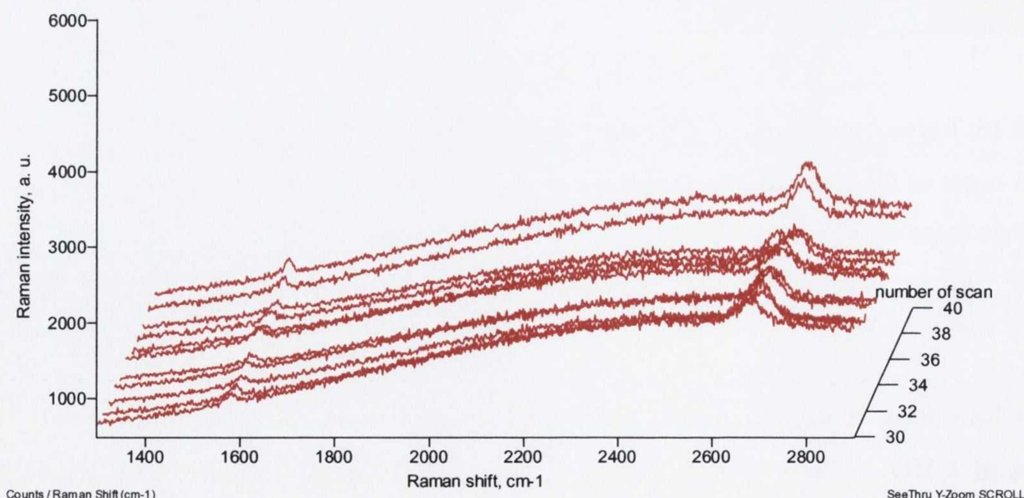

Fig. 10. 18. Evolution of the 2D and G peaks for graphene on Cu with scanning distance.

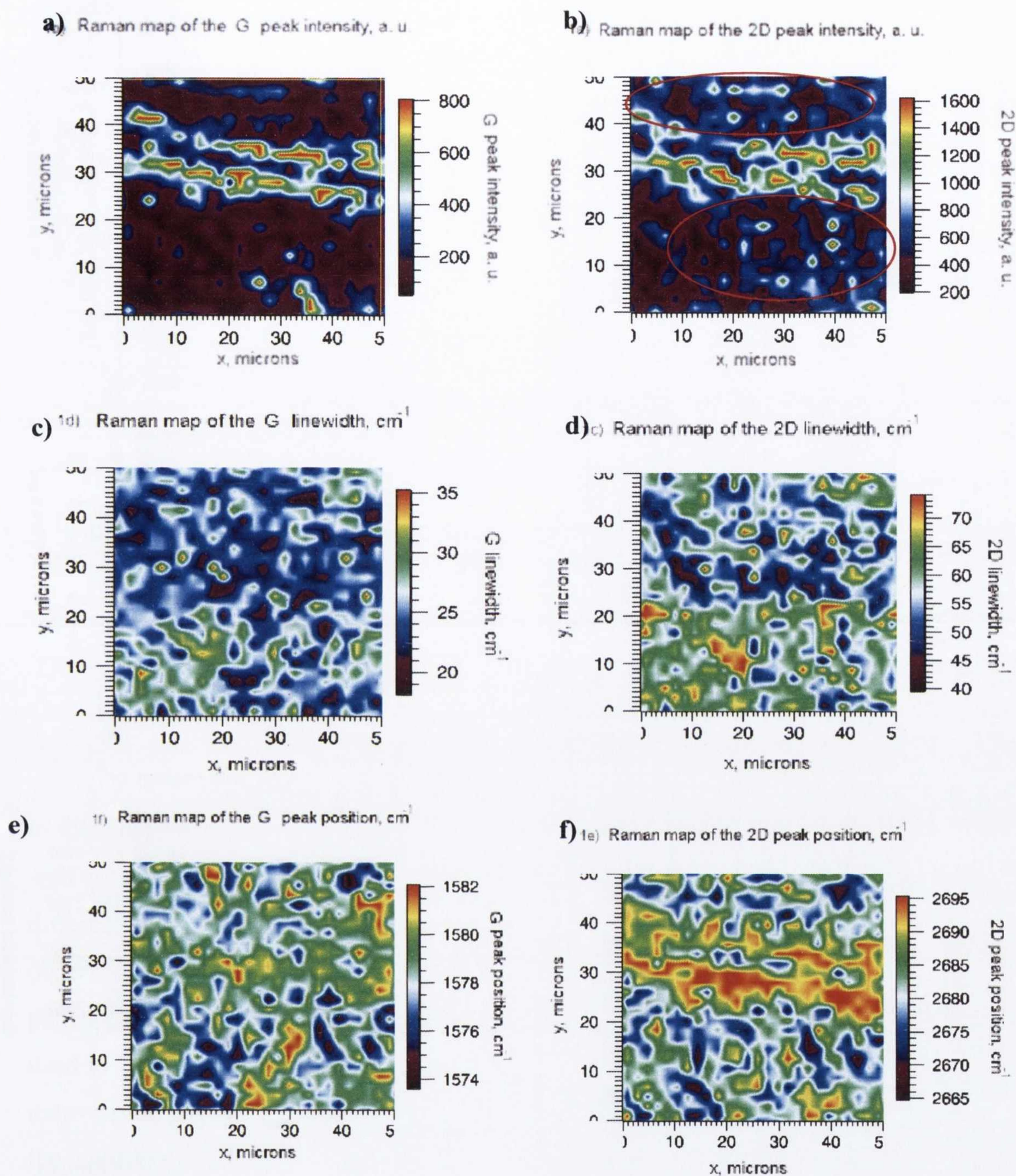

Fig. 10.19. Raman area maps of graphene deposited on Cu. (a), (c), (e) Raman maps of the intensity, linewidth and peak position of the G peak, respectively. (b), (d), (f) Raman maps of the intensity, linewidth and peak position of the 2D peak, respectively. Red circles indicate the flakes of graphene mono-layer.

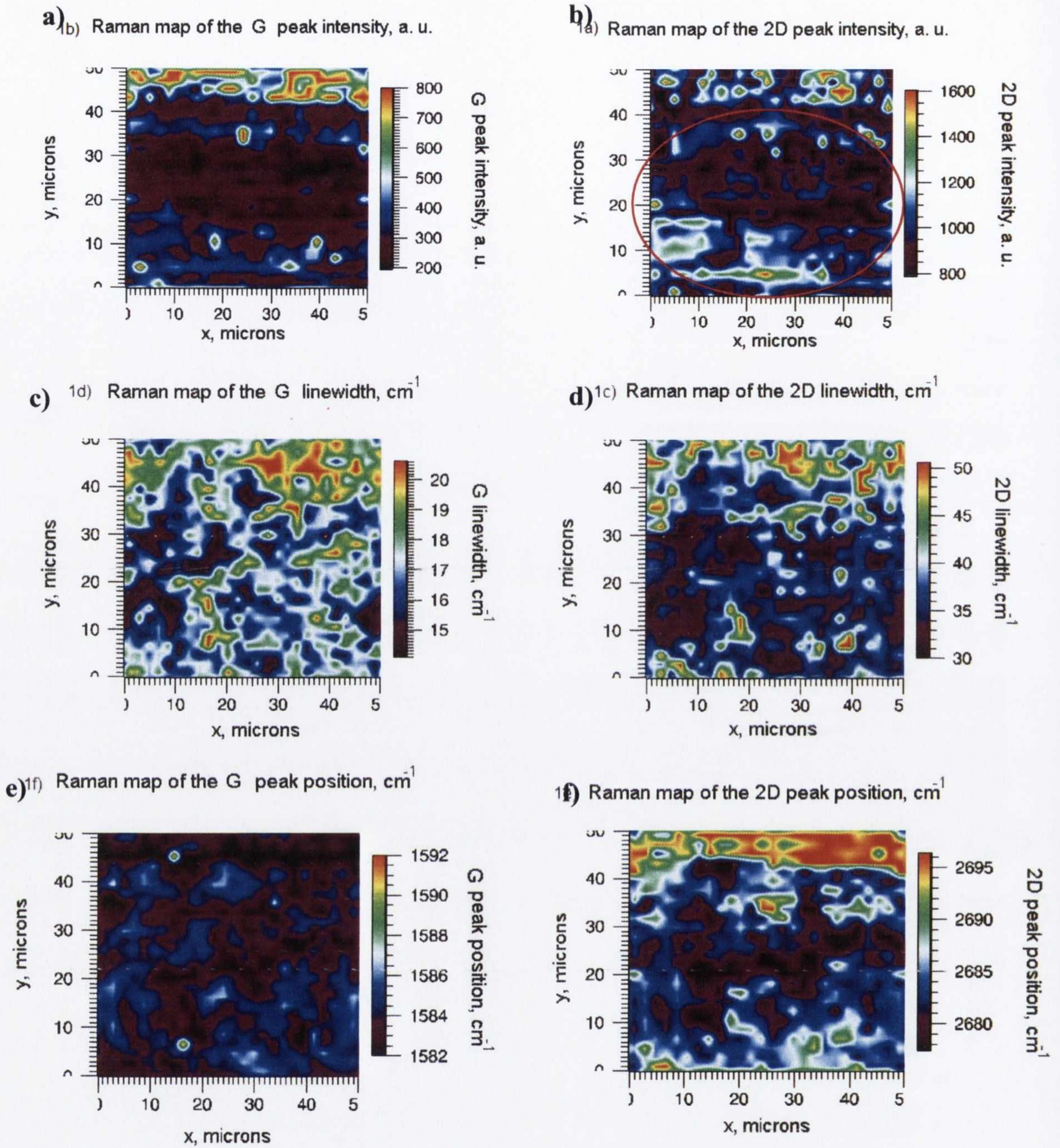

Fig. 10.20. Raman area maps of graphene transferred from Cu onto SiO_2/Si. (a), (c), (e) Raman maps of the intensity, linewidth and peak position of the G peak, respectively. (b), (d), (f) Raman maps of the intensity, linewidth and peak position of the 2D peak, respectively. Red circle indicates the flake of graphene mono-layer.

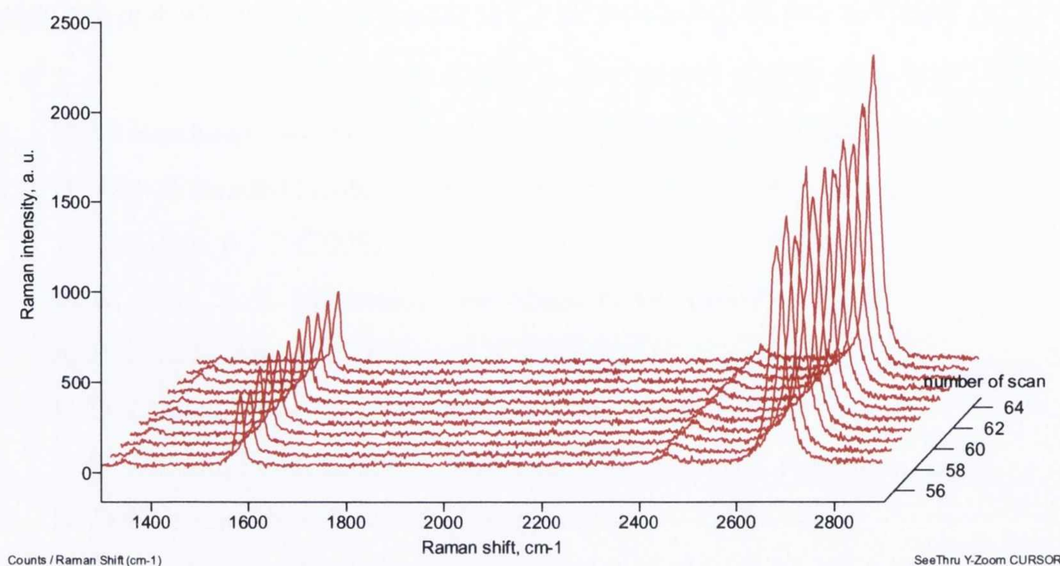

Fig. 10.21. Evolution of the 2D and G peaks for graphene on Cu with scanning distance.

10.5. Conclusions

In this chapter, the Raman spectra of mono-layer, multi-layer and disorder graphene as well as those of graphite are presented and discussed. The spectra were measured using different excitation energies in the visible range. A linear dispersion of the 2D band was observed for different excitation wavelengths, which is in agreement with results published earlier [37,38]. It was shown that the Raman area mapping technique can be used to distinguish graphene flakes of different thicknesses. In particular, the Raman maps of the intensity of 2D and G peaks and FWHM of the 2D peak clearly highlight the contribution from single-layered graphene. The Raman results were compared between the graphene samples on different substrates (metal and SiO_2/Si). The highest structural uniformity was observed for graphene grown on Cu after transfer on SiO_2/Si substrate. A single-layer of graphene was detected in the area of 40μm x 50μm. An enhancement of Raman signal was observed for graphene on SiO_2/Si due to the effects of multi-reflection and interference as described by the Fresnel equations [42]. This depends on the thickness of the silicon oxide layer as it was reported in Ref [42]. Results presented in this chapter indicate that single-layered graphene with a large area

and uniform thickness can be fabricated by CVD deposition on Cu and transfer onto SiO_2/Si.

References

1. ITRS Roadmap Process Integration Devices and Structures 2005
2. H. Iwai, Extended Abstracts of the International Workshop on Junction Technology, p 1-2 (2008)
3. A. K. Geim, K. S. Novoselov, Nat. Mater. 6, 183 (2007)
4. R. E. Peierls, Ann. I. H. Poincare 5, 177 (1935)
5. L. D. Landau, Phys. Z. Sowjetunion 11, 26 (1937)
6. L. D. Landau, E. M. Lifshitz, Statistical Physics, Part I, Pergamon, Oxford, 1980
7. N. D. Mermin, Phys. Rev. 176, 250 (1968)
8. J. A. Venables, G. D. T. Spiller, M. Hanbucken, Rep. Prog. Phys. 47, 399 (1984)
9. K. S. Novoselov, A. K. Geim, S. V. Morozov, D. Jiang, Y. Zhang, S. V. Dubonos, I. V. Grigorieva, A. A. Firsov, Science 306, 666 (2004)
10. J.C. Meyer, A. K. Geim, M. I. Katsnelson, K. S. Novoselov, T. J. Booth, S. Roth, Nature, 446, 60 (2007)
11. Y. Zhang et al., Appl. Phys. Lett. 86, 073104 (2005)
12. N. M. Peres et al., Phys. Rev. B 73, 125411 (2006)
13. C. Berger et al., J. Phys. Chem. B 108, 19 912 (2004)
14. K. Nakada et al., Phys. Rev. B 54, 17 954 (1996)
15. Y.-M. Lin, C. Dimitrakopoulos, K.A. Jenkins, D.B. Farmer, H.-Y. Chiu, A.Grill, P. Avouris, Science, 327, 662, (2010)
16. X. *Wang*, L. J. Zhi, and K. Mullen, Nano Lett. 8, 323 (2007)
17. G. Eda, G. Fanchini, M. Chhowalla, Nat. Nanotechnol. 3, 270 (2008)
18. Y. C. Wang, Z. Xiaohong, Z. Yulin, L. Furong, Y. Wang, Appl. Phys. Lett. 95, 063302 (2009)
19. J. Wu, M. Agrawal, H. A. Becerril, Z. Bao, Z. Liu, Y. Chen, P. Peumans, ACS Nano, 4, 43 (2010)
20. J. Hofrichter,B. N. Szafranek, M. Otto, T. J. Echtermeyer, M. Baus, A. Majerus, V. Geringer, M. Ramsteiner, H. Kurz, Nano Lett., 10, 36 (2010)
21. X. Liang, Z. Fu, and S. Y. Chou, Nano Lett. 7, 3840 (2007)
22. C. Berger, Z. M. Song, X. B. Li, X. S. Wu, N. Brown, C. Naud, D. Mayo, T. B. Li, J. Hass, A. N. Marchenkov, E. H. Conrad, P. N. First, and W. A. de Heer, Science 312, 1191 (2006)

23. K. V. Emtsev, A. Bostwick, K. Horn, J. Jobst, G. L. Kellogg, L. Ley, J. L. McChesney, T. Ohta, S. A. Reshanov, J. Rohrl, E. Rotenberg, A. K. Schmid, D. Waldmann, H. B. Weber, T. Seyller, Nat. Mater. 8 (3), 203 (2009)
24. C. Oshima and A. Nagashima, J. Phys.: Condens. Matter 9, 1 (1997)
25. A. N. Obraztsov, E. A. Obraztsova, A. V. Tyurnina, and A. A. Zolotukhin, Carbon 45, 2017 (2007)
26. S. Gilje, S. Han, M. Wang, K. L. Wang, and R. P. Kaner, Nano Lett. 7, 3394 (2007)
27. X. L. Li, X. R. Wang, L. Zhang, S. W. Lee, and H. J. Dai, Science 319, 1229 (2008)
28. Q.Yu, J.Lian, S. Siriponglert, H. Li, Y. P. Chen, S.-S. Pei, Appl. Phys. Lett. 93, 113103 (2008)
29. K. S. Kim, Y. Zhao, H. Jang, S. Y. Lee, J. M. Kim, K. S. Kim, J.-H. Ahn, P. Kim, J.-Y. Choi, B. H. Hong, Nature 457, 706 (2009)
30. X. S. Li, W. W. Cai, J. H. An, S. Kim, J. Nah, D. X. Yang, R. D. Piner, A. Velamakanni, I. Jung, E. Tutuc, S. K. Banerjee, L. Colombo, R. S. Ruoff, Science 324, 1312 (2009)
31. W. Liu, C.-H. Chung, C.-Q. Miao, Y.-J. Wang , B.-Y. Li, L.-Y. Ruan, K. Patel, Y.-J. Park, J. Woo, Y.-H. Xie, Thin Solid Films 518, S128 (2010)
32. L.M. Malard, M.A. Pimenta, G. Dresselhaus, M.S. Dresselhaus, Physics Reports 473, 51 (2009)
33. A.W. Moore, in: P.L. Walker, P.A. Thrower (Eds.), Chemistry and Physics of Carbon, Marcel Dekker Inc., New York, 17, 233 (1981)
34. F. Tuinstra, J. Koenig, J. Chem. Phys. 53, 1126 (1970)
35. C. Casiraghi et al., Nano Lett. 9, 1433 (2009)
36. Z. H. Ni, H. M. Wang, J. Kasim, H. M. Fan, T. Yu, Y. H.. Wu, Y. P. Feng, Z. X. Shen, Nano Letters 7, 2758 (2007)
37. I.Calizo, I. Bejenari, M. Rahman, G. Liu, A. A. Balandin, J. Appl. Phys. 106, 043509 (2009)
38. D. L. Mafra, G. Samsonidze, L. M. Malard, D. C. Elias, J. C. Brant, F. Plentz, E. S. Alves, M. A. Pimenta, Phys. Rev. B 76, 233407 (2007)
39. A.V. Baranov, A.N. Bekhterev, Y.S. Bobovich, V.I. Petrov, Opt. Spectrosk. 62, 1036 (1987)
40. R. Saito, A. Jorio, A.G. Souza Filho, G. Dresselhaus, M.S. Dresselhaus, M.A. Pimenta, Phys. Rev. Lett. 88, 027401 (2002)

41. J. Kurti, V. Zolyomi, A. Gruneis, H. Kuzmany, Phys. Rev. B 65, 165433 (2002)
42. Y. Y. Wang, Z.H. Ni, Z. X. shen, H. M. Wang, Y. H. Wu, Appl. Phys. Lett. 92, 043121 (2008)

11. Conclusions and suggestions for future work

11.1. Conclusions

In this work a number of Si/Ge based materials and carbon related materials were examined using micro-Raman spectroscopy developed for applications in nanotechnology. It was shown that micro-Raman spectroscopy can be used as a non-destructive and highly accurate tool for direct analysis of different properties of the very thin layers. The investigation of the following materials were undertaken: ion implanted Ge and Ge On Sapphire, SiGe and s-Si layers, SiGeC thin films, SiC layers, Diamond Like Carbon, a-C:Pt and graphene.

Various applications of spectroscopic technique for nano-materials characterisation are presented. It was shown that micro-Raman spectroscopy provides information on strain, composition, crystalline quality, structural defects, a number of monolayers, polytypism and clustering.

For the first time a structural damage in the bevelled, ion implanted Ge was investigated using micro-Raman mapping technique. It was shown that the bevelling process allows for Raman probing with nano-scale depth profile. A comparison and correlation of the electrical and structural properties of implant-related defects has been performed for "smart-cut type" doses of hydrogen and helium in Ge. Spreading Resistance Profiling (SRP) results show the maximum of the carrier concentration at the middle of projected range (~300 nm) for Ge samples implanted with a dose of H^+ $\sim 3\times 10^{16}$ atoms/cm^2 and annealed at 450°C. The maximum structural damage detected with Raman line mapping corresponds exactly to the maximum carrier concentration. This was also confirmed by presented SRIM simulations. Using SRP, it has been found that, for both ion species, a quantity of 1×10^{16} defects/cm^2 electrically active defects still remain after annealing at 600°C. Raman data shows that at 600°C, the crystal damage have been fully repaired, which suggests that these remaining acceptor states are due to point defects.

In Chapter 5, the application of micro-Raman spectroscopy for determination of Ge content, x, and relaxation factor, r, of SiGe buffers layers is presented. The x and r were estimated from the set of equations for Si-Si, Si-Ge and Ge-Ge Raman vibrational modes modified in this work for thin SiGe layers. The Ge content in SiGe layers was

calculated using both frequency and intensity methods. It was shown that even for very thin SiGe films micro-Raman spectroscopy is a very valuable and enough accurate characterisation tool. It was also presented that visible light Raman spectroscopy can be reliably used for the characterisation of strained Si on ultra-thin SiGe virtual substrates.

A detailed study of Raman and infrared spectra of the $Si_{1-x-y}Ge_xC_y$ layers with different Ge and C content was performed in Chapter 6 in order to gain a better understanding of carbon incorporation and its influence on SiGeC structures. This is the first investigation on SiGeC layers which was undertaken for a range of samples with different Ge content and in a wide range of possible for these structures C content. An increase of the linewidth and intensity of the Si-C peaks with the carbon content was observed in both the infrared and the Raman spectra. FTIR analysis shows that the integrated intensity of the Si-C peak increases linearly with the C concentration and is independent of the Ge content up to 16%. The linear dependence of the relative Raman intensity $I(C_{local})/I(Si\text{-}Si_{layer})$ versus C content of the SiGeC samples was also obtained. The relative Raman intensities increase linearly with C content and are independent of the Ge content up to 16%. Therefore, both FTIR and Raman spectroscopy can be used as non-destructive analytical methods for the determination of the amount of substitutional carbon in SiGeC layers, which influence the electrical performance of SiGe devices. The established relationship of Infrared and Raman intensities of Si-C peak versus C content are important in semiconductor engineering as these spectroscopic methods allows for a non-destructive and relatively fast estimation of the substitutional carbon content in SiGeC layers.

The thin SiC layers grown by a new method of solid-gas phase epitaxy were investigated using MRS, SEM, AFM and EDX techniques. It is shown that the SiC layer on Si (111) investigated here is composed of a cubic polytype of SiC with a small amount of 6H-SiC. The presence of the voids has been experimentally confirmed by micro-Raman spectroscopy and scanning electron microscopy. The strong enhancement in the peak intensity of the TO and LO modes is observed for the Raman signal measured in the void area. The intensity of TO Si-C peak increases with void depth. The enhancement of the electromagnetic field at the voids was also confirmed by theoretical calculation based on Fresnel's equation. This enhancement of the Raman signal is advantageous as it allows micro-Raman measurements to be used for the detection of different polytypes in ultra thin SiC layers.

A systematic UV and visible Raman analysis of very thin a-C films with sp^2 content varying from ~20% to ~90% were presented in Chapter 8. It was shown that the UV Raman spectra can provide direct evidence for the presence of sp^3 bonds, while visible Raman spectra present a powerful way to follow the evolution and ordering of the sp^2 sites. A sharp transition between sp^2-rich and sp^3-rich forms of a-C films was observed. This observation provides strong evidence that stress is the driving force behind the formation of the sp^3-rich ta-C phase. The dispersion of the G peak is a crucial parameter to distinguish between different structures of amorphous carbon. It was confirmed that the bigger dispersion of G peak observed for ta-C films with high sp^3 content indicates the larger disorder in these films. The a-C films with Pt content were also investigated using Raman and Rutherford backscattering spectroscopy. An understanding of Pt interaction with a-C matrix is important for a catalyst in fuel cell applications. It was found that the graphene clusters increase in size as the Pt concentration increases to $\sim 0.5 \times 10^{22}$ at/cm^{-3}. As the platinum concentration increases further, size of graphene clusters decreases. A comparison between the Raman spectra for Pt-free a-C and a-C:Pt films confirms that the presence of Pt in the a-C matrix leads to an increase in the fraction of the sp^2 phase within the matrix.

Finally, it was demonstrated that Raman area mapping technique can be used to distinguish between various numbers of monolayers of graphene and to investigate structural uniformity of graphene flakes.

11.2. Future work

The miniaturization in microelectronics, allowing more efficient and less energy-consuming devices, has been mainly relied on the continuous decrease of MOS features, usually based on Si. Since we are reaching the physical limits of Si technology, new structures and compatible materials are considered for improving devices performances in the near future. I believe, germanium appears as the most promising candidate, because of its similarities with Si and of the higher charge carrier mobility. Therefore, the scientific efforts are going to be required for improving the Ge based solutions such as advanced doping methods (new implantation methods or novel annealing strategies). Micro-Raman spectroscopy is a promising technique for further investigation of dopant-

defect interactions underlying diffusion and precipitation phenomena in Ge. The relative softness of Ge leads to heavier radiation damage than for Si and causes problems when both materials are used within the same device. This structural damage can be monitored by Raman mapping technique with combination of sample bevelling. The great possibilities are opened also for GeSn alloys, which offer a promising perspective of becoming a direct band gap semiconductor for modest Sn concentration. One of the important applications of GeSn would be the embedded source/drain stressors for Ge channels in future pMOS devices. For this purpose, the information on the composition and stress of grown GeSn alloys is required. This opens the door for future application of micro-Raman spectroscopy as a non-destructive and accurate characterisation technique.

The future work includes investigation of promising materials for 'post-silicon electronics' such as Ge, GeSn and graphene. The origin of the observed amorphization in hydrogen implanted Ge after layer transfer is going to be further studied. The deeper understanding of the Raman enhancement process for monolayer of graphene is needed. For this purpose, the reflection measurements are going to be conducted for graphene samples. Future work involves also the improvement of the performance and applications of the experimental technique. Raman spectroscopy has been significantly improved for the last decades to be an effective method for the investigation of nanostructures in the form of thin layers, quantum dots and quantum rods. This was achieved thanks to development of tuneable laser sources and the laser sources of different excitation wavelengths as well as sensitive detectors (CCD cameras) for advanced micro-Raman systems. However, the technique can be further modified to give greater sensitivity and higher resolution using a specific method of the sample preparation as well as new approach for system configuration. The two improvement of Raman spectroscopy were presented in this work. Firstly, it was shown that bevelling process of samples allows for nano-scale Raman depth profiling. Secondly, the enhancement of Raman signal due to interference and multi-reflection of laser light allows for quick and high resolution measurement of ultra thin layers. Other development of Raman spectroscopy can be investigated in the future work related to Tip-Enhanced Raman spectroscopy (TERS), which allows for spectroscopic measurements of single nano-structures such as single carbon nanotube or single quantum dot. Micro-Raman signal is relatively weak compared to techniques such as fluorescence. Surface enhanced Raman scattering (SERS) has helped overcome this

problem, offering signal enhancements of several orders of magnitude over conventional Raman scattering. However, the heterogeneity of metallic SERS substrates creates variable electromagnetic field enhancement across the surface. This limits the utility of the technique and renders quantitative measurements unreliable. As an alternative to conventional SERS, apertureless scanning near-field optical microscopy can be employed, in which a modified with metal AFM tip can be brought into contact with a sample surface. This approach utilizes highly localized enhancement providing spatial resolution of <50 nm (compares with resolution of ~1 μm micro-Raman spectroscopy) and offers more uniform enhancement up to several orders of magnitude when scanning the sample. All these achievements placed Raman spectroscopy to a unique position of becoming an advanced characterisation technique for investigation of nanostructures.

Appendix I

Surface profiler results

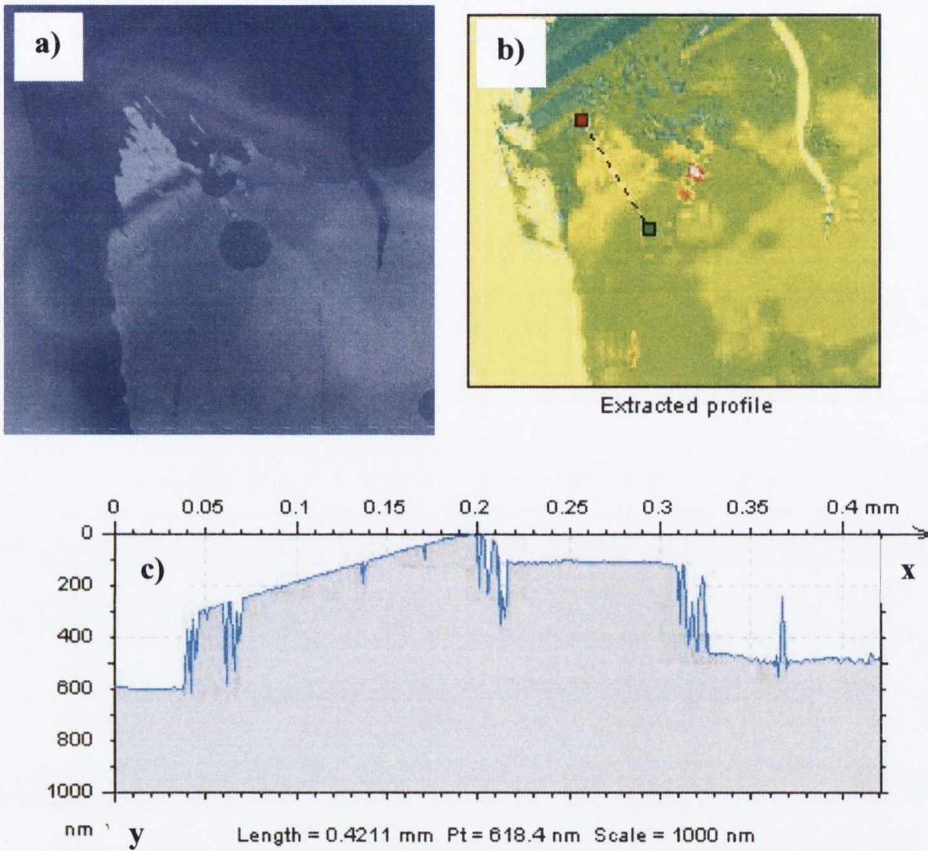

Fig. I.1. Surface profile results of the sample GeOS annealed at 600°C. (a) Optical image of the corner bevel of the sample. (b) Position of extracted profile. (c) Extracted cross-sectional profile.

The angle of bevel was calculated based on the following trigonometric function:

$$tg\alpha = \frac{y}{x}$$

The angles of ~0.002 rad and ~0.0016 rad were obtained for sample Ge600 and Ge800, respectively.

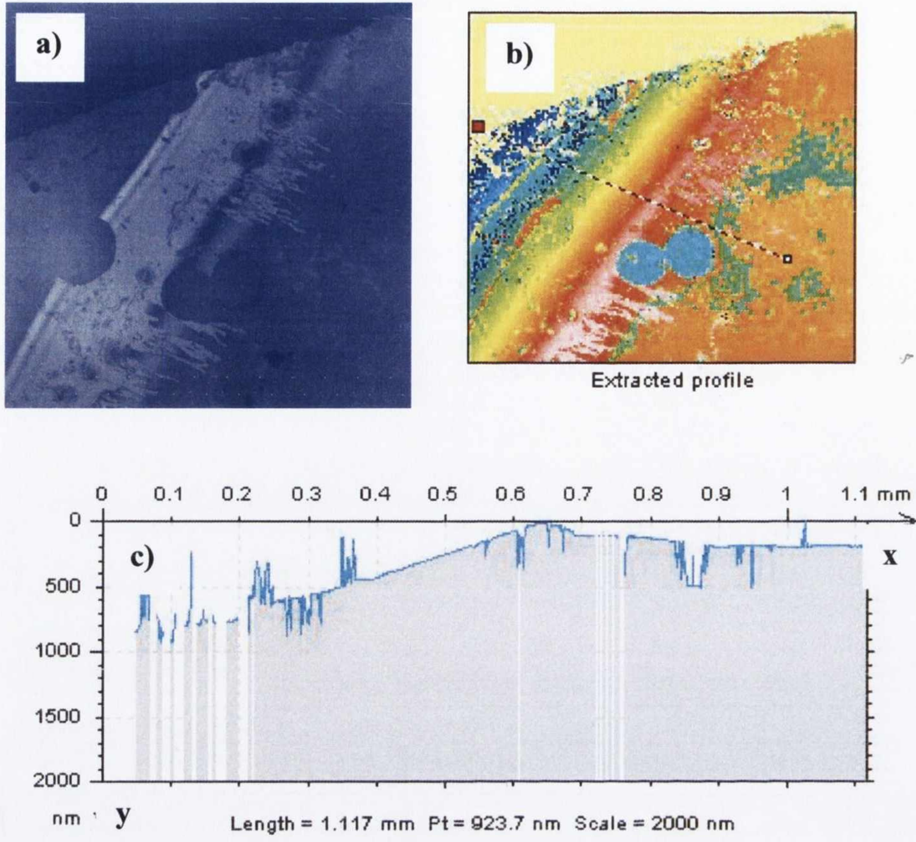

Fig. I.2. Surface profile results of the sample GeOS annealed at 800°C. (a) Optical image of the corner edge of the sample. (b) Position of extracted profile. (c) Extracted cross-sectional profile.